Universidade de Lisboa

Instituto de Geografia e Ordenamento do Território



Large deep-seated landslides in the northern Rif Mountains (Northern Morocco): inventory and analysis

André Filipe de Paxiuta Sá Couto Fonseca

Doutoramento em Geografia

Especialização em Geografia Física

2014

Universidade de Lisboa

Instituto de Geografia e Ordenamento do Território



Large deep-seated landslides in the northern Rif Mountains (Northern Morocco): inventory and analysis

André Filipe de Paxiuta Sá Couto Fonseca

Tese orientada pelo Professor Doutor José Luis Zêzere e pelo Professor Doutor José Eduardo Madeira, especialmente elaborada para a obtenção do grau de doutor em Geografia, área de especialização de Geografia Física.

This work was funded by *Fundação para a Ciência e Tecnologia* through PhD grand SFRH / BD / 65019 / 2009.

Esta dissertação foi financiada pela Fundação para a Ciência e Tecnologia integrando-se no âmbito da bolsa de Doutoramento SFRH / BD / 65019 / 2009.

Agradecimentos

Aproveito este momento para agradecer a todos aqueles que, directa ou indirectamente, contribuíram para a realização deste trabalho.

Aos meus orientadores, Professores José Luís Zêzere e José Madeira, por todo o apoio e disponibilidade no decorrer deste projecto, pela orientação, dedicação e companheirismo.

Institucionalmente, ao Centro de Estudo Geográficos, enquanto unidade de acolhimento da investigação realizada e ao Instituto de Geografia e Ordenamento do Território, enquanto unidade que confere o grau. À Fundação para a Ciência e a Tecnologia pelo apoio financeiro para o desenvolvimento desta dissertação.

Ao professor João Catalão (IDL-Fcul) pela modelação dos dados InSAR e pela sua disponibilidade para a discussão de resultados. Ao Professor Bouchta El Felah (Institute Scientifique - Université Mohammed V Rabat) pelo apoio institucional em Marrocos, pela sua ajuda na aquisição de dados e pelos momentos de discussão saudável no decorrer das campanhas de campo. Ao Professor Ali Faleh (Faculté des Lettres et de Sciences Humaine Saïs-Fès) pelo suporte logístico durante a fase inicial deste projecto.

À Aldina Piedade, Cristina Henriques, Inês Fonseca, Mário Neves, Raquel Paixão, Ricardo Garcia, Sérgio Oliveira e Susana Pereira, pelos saudáveis momentos de convívio que esta investigação proporcionou e pelo auxilio na recolha de dados de campo.

À população da aldeia de Azaib Beni Salah, em particular a Mohamed Salah, por abrirem a porta das suas casas e me fazerem sentir como um membro das suas famílias.

Aos meus pais, por me incentivarem a terminar esta etapa da minha vida. Sou eternamente grato pelo vosso amor incondicional, apoio nos momentos mais difíceis e presença nos tempos de maior felicidade.

Aos meus mais queridos, Rita e Mateus, pelo vosso amor, compreensão e presença constante.

Obrigado!

Abstract

This work aims to contribute to the knowledge of large-scale slope instability phenomena in the northern Rif Mountain, whose setting is presented in the first chapter. On a second chapter we analyse the topography of the Rif belt resorting to morphometric parameters extracted from digital terrain data. Our results indicate a concentration of surface uplift and tectonically induced drainage network incision along the Internal Domain and southern sector of the Ketama Unit, defining two zones of distinct deformation that are consistent with the transpression models for northern Africa.

In the chapter 3 we study the frequency-size and spatial distribution of 3610 bedrock landslides (La> 0.01km^2). The results show that while the precipitation related to humid climatic condition throughout the Quaternary has certainly favoured the triggering of very large landslides (>1km^2) along the south-western sector of the mountain chain, the importance of deep-seated bedrock fracturing in close proximity to active tectonic structures and high relief sites clearly outlines the role of seismic ground acceleration in producing large-scale slope instability events.

The fourth chapter constitutes a preliminary approach to study slope instability based on PSInSAR technique. The velocity and density of persistent PSs was analyzed to refine the classification of the activity status of the inventoried landslides using the PSI-based matrix approach. Furthermore, we used Hotspot and Cluster analysis (PSI-HCA) in order to detect PSs clusters associated with slow gravitational movement. The comparison between the results that were obtained through the PSI-HCA and PSI-based matrix approach confirm the capability of both methods to detect landslide activity.

The final chapter focuses on a detailed study of a complex deep-seated landslide. Field data collection enabled the identification of paleoseismic activity in landslide triggering. Furthermore, according to Holocene climatic reconstructions, the age constrains for the landslide reactivations are placed during one of the driest and hottest phases of the Holocene, which suggests that slope deformation is decoupled from the Holocene climatic trends.

Keywords: Bedrock landslides; Magnitude-frequency distribution; Tectonic and bedrock control; Seismic triggering; Rif Mountains; Morocco

Resumo

As cadeias montanhosas alpinas são laboratórios privilegiados para o estudo dos mecanismos de feedback entre processos morfogénicos endógenos e exógenos. Neste contexto, os deslizamentos profundos constituem um dos processos mais rápidos de reajuste gravítivo das vertente após a sua instabilização por levantamento tectónico e incisão da rede de drenagem. As Montanhas do Rif localizam-se-se ao longo da costa noroeste do continente Africano, formando o sector ocidental do orógeno Bético-Rif-Tell. O presente projecto de investigação assenta em dois objectivos principais: 1) compreender as relações de *feedback* entre o levantamento da cadeia montanhosa, a incisão da rede hidrográfica e a a ocorrência de movimentos de vertente profundos; 2) realizar um inventário de movimentos de vertente procurando identificar os principais factores de predisposição que controlam a ocorrência e a variabilidade espacial de movimentos de vertente profundos com diferente magnitude.

Numa primeira fase, a topografia das montanhas do Rif é analisada recorrendo a parâmetros geomorfométricos obtidos a partir de um modelo digital de terreno com o objectivo de: i) detectar variações espaciais na morfometria do relevo reflectindo a interferência da actividade tectónica pós-Tortoniana; ii) ajustar as observações tectónico-geomorfológicas aos modelos tectónicos Plio-Quaternário de evolução da cadeia montanhosa descritos na bibliografia; iii) analisar o papel da litologia no controlo da variabilidade espacial do relevo. Os resultados obtidos mostram uma concentração de evidências tectono-geomorfológicas no domínio Interno do Rif e a sul da Unidade de Ketama, definindo duas zonas de deformação distintas compreendidas entre as falhas de Jebha e Nekkor. Este padrão de deformação é consistente com o regime tectónico transpressivo identificado por diversos autores.

Umas das contribuições mais relevante desta dissertação resulta da elaboração de um inventário de movimentos de vertente realizado a partir da análise de fotografias aéreas na escala 1:40.000 e de imagens de satélite, permitindo a identificação de mais de 10.000 movimentos de vertente com áreas entre $3x10^{-5}$ e $9,4 \times 10^{6}$ km^2. O terceiro capítulo deste trabalho estuda a relação de magnitude - frequência do inventário e analisa detalhadamente a distribuição de 3.610 deslizamentos profundos (La> $0.01km^2$), com o objectivo de discriminar o papel dos principais factores de predisposição e dos mecanismos de desencadeamento na concentração espacial de deslizamentos de grandes dimensões (La>$1km^2$). A fiabilidade estatística do inventário é confirmada para movimentos com área entre 0,01 e $1km^2$ por ajuste gráfico à distribuição de magnitude-frequência proposta por Mallamud et al. (2004a). Enquanto a identificação de deslizamentos de menor

dimensão é dificultada pela variação espacial da qualidade das imagens de satélite, os deslizamentos de maior dimensão são sistematicamente capturados, não revelando lacunas significativas ao longo da extensão leste-oeste da cadeia montanhosa. No que se refere à distribuição espacial dos movimentos de maior dimensão (La>1km^2), estes tendem a ocorrer associados às formações litológicas mais compactas das unidades de Tiziren, Dorsal Calcária e Numidiana, que se sobrepõem por carreamento a formações margosas e argilosas. A assinatura topográfica destes eventos gravíticos manifesta-se através da redução do declive modal em cerca de 8 graus nas unidades mais compactas. Dentro deste contexto estrutural, os movimentos de grandes dimensões surgem ainda a curta distância de falhas netectónicas. Sendo seguro que a precipitação terá favorecido a ocorrência movimentos de vertente de grandes dimensões, enquanto factor desencadeante, no decurso de fases climáticas mais húmidas do Quaternario, o controlo imposto pela fracturação produnda das unidades mais compactas, aliada à proximidade a estruturas tectónicas ativas e a condições de relevo energético, enfatiza a importância da actividade sísmica no desencadeamento de deslizamentos de dimensão superior a 1km^2.

O quarto capítulo constitui uma abordagem preliminar ao estudo da instabilidade de vertentes com base na técnica de PSInSAR. A velocidade e a densidade de persistent scatterers (PSs) é analisada em relação às propriedades do terreno (declive, exposição e litologia) e à distribuição de deslizamento profundos, com o objectivo de refinar a classificação do estado de actividade dos mesmos. Além disso, recorreu-se à tecnica PSInSAR – Hotspot and Cluster Analysis (PSI-HCA), com o objectivo de detectar clusters de PSs associados a um movimento gravitacional lento. A comparação entre os resultados obtidos através do método PSI-HCA e de classificação do estado de actividade confirmam a capacidade de ambos os métodos para detectar atividade em deslizamentos profundos. Os resultados mostram ainda que o método PSI-HCA se ajusta à detecção de actividade em grandes deslizamentos profundos, sobretudo em locais onde a magnitude do movimentos tende exceder os limites predefinidos para a aplicação dos métodos de classificação do estado de actividade.

O quinto capítulo analisa as características geológicas e geomorfológicas de um movimento de vertente profundo – o deslizamento de Beni Derkoul - com o objetivo de i) definir o modelo estrutural de deformação; ii) definir a profundidade da superfície de ruptura, iii) analisar o comportamento cinemático da massa deslizada e iv) identificar diferentes fases de evolução a partir da análise crono-estratrigrafica de sedimentos lacustres. O deslizamento de Beni Derkoul é um movimento profundo complexo, composto por quatro áreas de ruptura profunda (30-70m),

apresentando uma importante componente de fluxo que se extende ao longo de 5 km. A deformação na área de ruptura é caracterizada por um forte controlo estrutural imposto pela atitude e composição das bancadas mais argilosas e margosas associadas a variação lateral de faciés dentro da mesma unidade geológica ou como fácies de transição entre unidades de cavalgamento. Neste contexto, a geometria e profundidade dos planos de ruptura são controlados pela ocorrência de estruturas tectónicas de orientação E-W a NW-SE, pela profundidade a que as formações mais brandas ocorrem relativamente às unidades mais compactas sobrejacentes e pela concordância entre a atitude do substrato e a inclinação e exposição da superfície topográfica. A complexidade da evolução do deslizamento de Beni Derkoul é testemunhada pela presença de duas unidades de deslizamento na secção inferior do vale. Além disso, a consistência da altitude da superfície basal estimada e a altitude dos terraços quaternários posicionados a jusante da massa deslizada sugerem uma adaptação do deslizamento a uma superfície topográfica pré-existente que se relacional com a evolução fluvial da região. A idade referente à primeira fase de desencadeamento não foi determinada neste estudo. No entanto, foram identificadas cinco reativações ocorridas durante o Holocénico médio a partir da datação de sedimentos lacustres, para as quais foram obtidas idades mínimas por AMS14C compreendidas entre 6.868 Cal BP e 6.046 Cal BP. Os níveis lacustres mais antigos apresentam evidências de deformação associadas a paleosismicidade (i.e. estruturas de tipo *flame*). As reactivações detectadas nos níveis mais recentes enquadram-se numa tipologia de deformação gravítica do estilo *creep*. De acordo com os modelos de reconstrucção do clima do Holocénico do norte de Marrocos, os períodos de reativação do deslizamento estão enquadrados numa das fases mais secas e mais quentes do Holocénico. Os resultados obtidos questionam assim a capacidade dos padrões de precipitação actuais em desencadear reactivações (que não as superficiais) no deslizamento de Beni Derkoul. O facto de este movimento de vertente estar localizado numa das áreas de maior aceleração sísmica do Rif, aliado à presença de indicadores de paleosismicidade no interior da massa deslizada, leva-nos a associar as principais fases de reactivação à ciclicidade sísmica da região. No entanto, face ao controlo imposto pelos materiais de elevada plasticidade e à forte componente de fluxo identificada, somos tentados a colocar a fase inicial de desencadeamento nas fases húmidas do Pleistocénico médio-superior, em resposta a chuvas fortes e prolongadas, fusão da cobertura nival (sazonal ou induzida por alteração do clima) ou actividade sísmica.

Palavras chave: deslizamentos profundos; Magnitude-frequência; Controlo estrutural; Rif Mountains; Morocco.

Table of Contents

ABSTRACT ..... **I**

RESUMO ..... **II**

TABLE OF CONTENTS ..... **VI**

LIST OF FIGURES ..... **IX**

LIST OF TABLES ..... **XI**

LIST OF ABBREVIATIONS ..... **XII**

INTRODUCTION **1**

1 THE NORTHERN RIF MOUNTAINS **7**

1.1 GEOGRAPHICAL SETTING 7

1.2 GEOLOGICAL SETTING 9

1.3 TECTONIC SETTING 11

1.4 POST-TORTONIAN LANDSCAPE EVOLUTION IN THE RIF: AN OVERVIEW OF MAJOR GEOLOGICAL EVENTS 14

2 TECTONIC AND BEDROCK SIGNATURE ON THE TOPOGRAPHY OF THE NORTHERN RIF INFERRED FROM DEM-BASED GEOMORPHOMETRY **17**

ABSTRACT 17

2.1 INTRODUCTION 17

2.2 DIGITAL DATABASE 18

2.3 GEOSPATIAL ANALYSIS OF TOPOGRAPHY 20

2.3.1 Summit, base level and mean elevation 20

2.3.2 Local relief and mean slope 23

2.3.3 Elevation-relief ratio 26

2.3.4 Post-Tortonian uplift and drainage incision 27

2.4 DRAINAGE NETWORK AND DRAINAGE BASIN ANALYSIS 29

2.4.1 Drainage network orientation 29

2.4.2 Drainage basin analysis 32

2.5 RIVER PROFILE ANALYSIS 36

2.5.1 Profile concavity 36

2.5.2 Knickzones 37

2.6 PEARSON CORRELATION STATISTICS 39

2.7 DISCUSSION 42

2.8 CONCLUSION 46

3 DISTRIBUTION OF LARGE BEDROCK LANDSLIDES **51**

ABSTRACT 51

3.1. INTRODUCTION 52

3.2. METHODS AND DATASET PROPERTIES 52

3.1.1 Structural data: lithology and tectonic 52
3.1.2 Topographic data 54
3.1.3 Climatic data 55
3.1.4 Landslide inventory 55
3.1.5 Landslide density and spatial distribution 60
3.2 Results 61
3.2.1 Landslide frequency area 61
3.2.2 Landslide spatial distribution 63
3.2.3 Landslide height and runout 63
3.2.4 Landslides and bedrock structure 65
3.2.5 Landslides and topography 67
3.2.6 Landslides and precipitation 71
3.3 Discussion 72
3.4 Conclusion 76

4 ACTIVITY OF LARGE BEDROCK LANDSLIDES IN THE NORTHERN RIF MOUNTAINS DURING THE PERIOD 2004-2010 DETECTED THROUGH PERSISTENT SCATTERER INTERFEROMETRY, HOTSPOT AND CLUSTER ANALYSIS 79

Abstract 79
4.1 Introduction 79
4.2 Available triggering mechanisms for the SAR image timeframe 81
4.3 Dataset and methodology 82
4.3.1 PSInSAR dataset 82
4.3.2 Definition of the landslide activity status 84
4.3.3 Hotspot Getis-Ord analysis 86
4.4 Persistent scatterer distribution outside landslide areas 87
4.5 PSs distribution and landslide activity 90
4.6 Hotspot and cluster analysis 92
4.7 Landslide cases 93
4.7.1 Jebel Sougna: Tiarta and El Marhza landslides 93
4.7.2 Beni Haoulane landslide 95
4.7.3 Tazakht landslide 99
4.7.4 Beni Mizar landslide 100
4.7.5 Agni Beni Boufra landslide 101
4.7.6 Hadada landslide 102
4.7.7 Atress landslide 102
4.8 Discussion and conclusion 103

5 AN EXAMPLE OF COMPLEX DEEP-SEATED SLOPE DEFORMATION IN THE NORTHERN RIF: THE BENI DERKOUL LANDSLIDE 111

Abstract 111
5.1 Introduction 111
5.2 Study area 112

5.3 METHODS 115
5.3.1 Geological and geomorphological analysis 115
5.3.2 Field sampling and laboratory techniques 115
5.3.3 Landslide morphometry and depth estimation 117
5.3.4 Persistent scatterer interferometry 122
5.4 RESULTS 122
5.4.1 Bedrock structure and mechanical properties 122
5.4.2 Landslide geomorphology 123
5.4.3 Landslide depth estimation 126
5.4.4 Slope tectonics 128
5.4.5 Taghfart gully sections 129
5.4.6 Village of Azaib section 129
5.4.7 Azaib Café road-cut 132
5.4.8 Lake Azaib road-cut 132
5.5 EVIDENCE FOR PRESENT-DAY ACTIVITY 132
5.6 INTERPRETATION AND DISCUSSION 133
5.6.1 Active Beni Derkoul landslide 133
5.6.2 Structural, lithological and tectonic control 133
5.6.3 Landslide kinematics and slope tectonics 134
5.6.4 Middle Holocene activity and the Lake Azaib sedimentary record 135
5.6.5 Present-day activity 139
5.6.6 Landslide deposition units 1 and 2: record of past landslide activity 140
5.7 CONCLUSION 142

6 CONCLUDING REMARKS 145

REFERENCES 149

ANNEXES 171

List of figures

Figure 1.1 - Topographic setting of the northern Rif Mountains. 7
Figure 1.2 - Distribution of precipitation in the northern Rif Mountains. 9
Figure 1.3 - Simplified structural outline of the northern Rif Mountains. 11
Figure 1.4 – Tectonic setting of the northern Rif. 12
Figure 2.1 Tectonic setting of the Northern Rif. 19
Figure 2.2 Geospatial analysis of topography. 23
Figure 2.3 - Swath profiles. 24
Figure 2.4 – Slope distribution. 28
Figure 2.5 – Drainage network orientation. 30
Figure 2.6 Rose diagrams for each sampled zone around topographic gradients. 32
Figure 2.7 – Drainage basin morphometry. 33
Figure 2.8 – Stream long profiles and knick point analysis. 40
Figure 2.9 – Synthesis of geomorphic evidences of active tectonics. 48
Figure 3.1 Detachment and neotectonic faults. 53
Figure 3.2 – Criteria for landslide-to-fault distance calculation. 54
Figure 3.3 – Examples of landslide detection from satellite images provided by the GoogleEarth platform. 56
Figure 3.4 – Landslide inventory of the northern Rif Mountains. 58
Figure 3.5 – Magnitude-frequency distribution for the complete landslide inventory. 62
Figure 3.6 Landslide density mapping in the northern Rif. 64
Figure 3.7 - Landslide morphometry. 67
Figure 3.8 - Mean bedrock dip and landslide runout azimuth for each structural unit of the Rif. 68
Figure 3.9 Landslide distribution. 70
Figure 3.10 - Frequency distributions of surface-slope angles normalized by area and stratified by landslide area for each structural unit of the Rif. 71
Figure 3.11 - Frequency of slope failures per seismic acceleration class following the work of Benchekroun et al. (2013). 76
Figure 4.1 - Limits to the PS2005 and PS2007 datasets. 82
Figure 4.2 – Mean annual precipitation at the meteorological station of Chefchauen for the SAR image timeframe (2003/2010). 82
Figure 4.3 – Extreme precipitation event during the winter of 2009-2010. 83
Figure 4.4 - Infrastructures affected by landslide reactivations during the winter period of 2009-2010. 84
Figure 4.5 – PSs density within landslide limits. 86
Figure 4.6 – PSs deformation rate along the satellite LOS 92
Figure 4.7 - Landslide activity status reclassification following the PSI-based matrix approach. 94
Figure 4.8 - PSI hotspot map of the northern Rif Mountains. 95
Figure 4.9 – Tiarta landslide. 96

Figure 4.10 - El Marhza landslide. 97
Figure 4.11 - Beni Haoulane landslide. 98
Figure 4.12 - Tazakht landslide. 99
Figure 4.13 - Beni Mizar landslide. 100
Figure 4.14 - Agni Beni Boufra landslide. 101
Figure 4.15 - Hadada landslide. 102
Figure 4.16 - Atress landslide. 104
Figure 4.17 - Landslide area vs. Average Kernel density estimation. 105
Figure 5.1 – Location of the Beni Derkoul landslide in the context of the Rif. 112
Figure 5.2 - Overview of the Beni Derkoul valley looking south. 113
Figure 5.3 Simplified geomorphological map of the Beni Derkoul landslide. 114
Figure 5.4 - DEM first order derivatives. 116
Figure 5.5 - Stratigraphy of stable bedrock units. 117
Figure 5.6 Longitudinal and transverse profiles. 119
Figure 5.7 - Shaded relief image of the Beni Derkoul landslide. 121
Figure 5.8 - Plasticity chart for the bedrock clay samples. 123
Figure 5.9 – Bird-eye view of the Beni Derkoul landslide. 125
Figure 5.10 - Longitudinal profiles of the streams incising the landslide body, inferred subsurface paleo-topography and landslide stratigraphy. 128
Figure 5.11 - Altitudinal distribution of the fluvial terraces of the Maâmala River. 129
Figure 5.12 - Slope tectonic structures of the Beni Derkoul landslide. 131
Figure 5.13 - Geomorphic features of past and present-day activity. 138
Figure 5.14 - Reconstructed climatic parameters according to present-day conditions (adapted from Cheddadi et al., 1998). 140
Figure 5.15 – Precipitation and data correlationa for the meteorological stations of Bab Taza and Chefchauen for the SAR image timeframe. 141

List of tables

Table 1.1 – Hydrological parameters of the main wadis of the Northern Rif. Figure 1.2 for location.. 8
Table 2.1 - Topographic and basin-scale morphometry. 35
Table 2.2 - Pearson correlation matrix for basin-scale morphometric parameters..... 47
Table 3.1 - Cartographic and published resources used in the work. 57
Table 3.2 – Total number of landslides for each morphostructural unit. 59
Table 3.3 - Landslide morphometry and morphostructural data for each structural unit of the Rif.. 66
Table 4.1 – Persistent scatterer distribution in stable and unstable areas and PSs movement rate outside and inside landslide limits for the PS2005 and PS2007 datasets. 88
Table 4.2 - PSs distribution per slope aspect class and PSs displacement rate statistics for the PS2005 and PS2007 datasets. 89
Table 4.3 - PSs distribution per hillslope slope angle class and PSs displacement rate statistics for the PS2005 and PS2007 datasets. 90
Table 4.4 - PSs distribution per lithological unit of the Rif (Suter, 1980) and PSs displacement rate statistics for the PS2005 and PS2007 datasets. 91
Table 4.5 - Landslide activity status classification and hotspot kernel density estimation. 106
Table 5.1 - Shear strength and Atterber limits for the bedrock samples. 117
Table 5.2 - Conventional and calibrated AMS 14C ages of the Azaib paleolake sediments (AUD-Area Under the Curve). 118
Table 5.3 - Morphometric properties and depth estimation of the landslide sectors..... 118

List of abbreviations

A	Catchment area
ANCFCC	Agence National de la Conservation Foncière, du Cadastre et de la Cartographie
Br	Basin relief
C	Concavity
CIAT	Center of Tropical Agriculture
DEM	Digital Elevation Model
DSGSD	Deep-seated gravitational slope deformation
E	Elevation
ENVISAT	NVIronmentalSatellites
Er	Elevarion-Relief ratio
ESA	European Space Agency
FAO	Food and Agriculture Organization
GHCN	Global Historical Climatology Network
Gi	Getis-Ord cluster analysis
GIS	Geographical Information System
H	Hack exponent
HeU	High Erodibility Units
Hi	Hypsometric Integral
Inc	Incision
InSAR	Interferometric Synthetic Aperture Radar
La	Landslide area
LeU	Low Erodibility Units
LOS	Line of Sight
Lr	Local relief
MDD	Main drainage divide
Ms	Surface-wave magnitude
Mw	Moment magnitude
NBF	Northern Boukkoya Fault
P	Precipitation
Pdf	Probability density function
PSI	Persistent-Scatterer Interferometry
PSI-HCA	Persistent-Scatterer Interferometry, hotspot and cluster analysis
PSInSAR	Persistent Scatterers derived from interferometric processing
PSs	Persistent scatteres
RWMF	Rifain West Mediterranean Fault
S	Slope
SAR	Synthetic Aperture Radar
ShF	Shape factor
SL	Stream length-gradient index
SRF	Southern Rif Fault
TM	Trade Mark
UTM	Universal Transverse Mercator
WMO	World Meteorological Organization

Introduction

While tectonic convergence builds-up topography through compression and thickening of the crust, surface processes tear it down through fluvial incision, mass wasting and glacial processes. The rate at which mountains are eroded depends on the rate of tectonic uplift, the nature and intensity of climatic processes and the physical and mechanical characteristics of bedrock (e.g. Willett, 1999; Sklar & Dietrich, 2001).

The study of active mountain belts has shown that orogen evolution is marked by drastic changes in relief production due to temporal and spatial variations in bedrock uplift and drainage network incision (Willett, 1999). On a temporal scale of 5-10 million years the Alpine orogens suffered substantial transformations in topography through migration of the main drainage divides in response to tectonic advection, increased precipitation along the windward flank and fluvial incision and regressive erosion (Koons, 1989; Willett, 1999). Furthermore, the spatial variability of intensity of building and destructive processes, expressed through variation in mean slope angle and local relief, has proven to exert a strong influence over long-term erosion rates (Montgomery and Brandon, 2002; Roe et al. 2003).

The importance of bedrock strength in landscape evolution has been thoroughly addressed in geomorphological studies (Molnar et al. 2007). In the early evolutionary stages of formation of compressional orogens, lithology controls the ability of topography to grow both vertically and laterally. As topography grows, rivers tend to get established along less competent materials and carve deep into bedrock along fault lines or fractured zones. As valleys get deeper adjacent slopes become steeper and respond through bedrock failures in order to maintain local equilibrium according to the mechanical strength of hillslope-scale rock masses (Clarke & Burbank, 2010). The spatial variability in erosional processes is further incremented by dissimilarities in the distribution of precipitation (Champagnac et al. 2012).

The study of the mechanisms and rates at which mountain landscapes are eroded through mass wasting processes enables a better understanding of the complex feedback between uplift and active denudation (e.g. Hovius et al., 1997; Shroder, 1998; Roering et al. 2005; Korup, 2005a & b; Korup, 2010) and allows the construction of statistical-based and physically-based models to evaluate landslide susceptibility and hazard (e.g. Varnes and IAEG, 1984; Soeters & van Westen, 1996; Carrara et al., 1999; Guzzetti et al., 1999, 2005).

The stability of hillslope rock masses is primarily influenced by its surface gradient, the density, cohesion and frictional properties of the parent rock, the depth of potential failure surfaces, and the gravitational acceleration (Carson and Kirkby, 1972). When prolonged precipitation or seismic ground acceleration occurs bedrock strength is reduced through loss of cohesion or reduction of frictional strength. Factors such as the intercalation of weaker (silty or clayish) lithological units together with variations in bedrock fracture density, depth, orientation, and spatial distribution, have proven to control both magnitude and frequency of slope failure in different geomorphological settings (e.g. Barton et al., 1974; Selby, 1992; Hoek and Brown, 1997; Clarke & Burbank, 2010).

The role of rainfall-induced pore pressure increase in landslide triggering has been addressed by several authors (e.g. Iverson and Major, 1987; Corominas et al., 2005; Schulz et al., 2009 & Calabro et al., 2010), with theoretical and empirical data showing that bedrock failures may occur, or reactivate, in response to precipitation events through delayed (from hours to days) increases in pore pressure from downward infiltration. The time-lag between a precipitation event and the hillslope response depends on the depth and geometry of the failure surface and on the permeable and mechanical characteristics of bedrock (Baum and Reid, 1995).

Earthquakes affect the stability of slopes by causing loss of cohesion and/or reduction of the frictional strength of the affected material by shattering of compact rock units, or liquefaction in soft, saturated soils (Meunier et al., 2008). Furthermore, topographic amplification of ground accelerations occurs when seismic waves entering the base of a topographic ridge are progressively projected upwards increasing the interference between reflections and the associated diffractions towards the ridge crest. These are partially reflected back into the rock mass and diffracted along the free surface forcing the amplification of ground accelerations (Davis and West, 1973; Geli et al., 1988; Benites and Haines, 1994; Meunier et al. 2008; Hovius and Meunier, 2012).

The initial stage in the investigation of landslides involves the inventory of the instability phenomena. Landslide mapping is a crucial procedure in geomorphological studies as it sets the precision of the morphometric data (i.e. area, run-out, depth and volume) used in the calculation of landslide driven erosion rates and to assess landslide hazard (e.g. Stark & Hovius, 2001; Mallamud et al. 2004a; Larsen, Montgomery & Korup, 2010).

Landslide inventories have been prepared worldwide with different objectives and using different techniques (Guzzetti et al. 2000, 2012). Based on the identification of key morphological features, the extent of slope failure can be mapped and landslide type can be determined, usually involving

flowing, sliding, spreading, toppling, falling, or the combination of two or more types of movements (Cruden and Varnes, 1996). From landscape evolution studies to the analysis of natural hazards, several landslide inventories have been published resulting from the analysis of aerial photos, satellite images and DEM interpretation, field surveys and the application of remote sensing techniques such as PSInSAR (i.e. Hovius et al., 1997; Guzzetti et al. 1999, 2008; Cigna et al. 2012). Over recent years the increasing availability of satellite imagery within online servers (i.e. Google-Earth; Bing) has provided earth scientists with new opportunities to detect and map landslides (Sato and Harp, 2009).

To analyze the statistical distribution and contribution of landslides to sediment yields researchers have resorted to the exploitation of the scaling properties of landslides. This approach is supported by evidence that frequency-size distributions of several landslide inventories have shown a functional relationship between landslide magnitude (area or volume) and frequency (spatial or spatio-temporal) where the abundance of slope failures increases with landslide area/volume up to a maximum value and rapidly decays along a power law (Pelletier et al., 1997; Hovius et al., 1997; Stark and Hovius, 2001; Guzzetti et al., 2002; Guthrie and Evans, 2004; Malamud et al., 2004). According to Brardinoni and Church (2004), if the exponential coefficient b of the power-law decay is greater than 2, then the majority of the cumulative landslide sediment volume is comprised of small failures. On the other hand, if b is smaller than 2, large landslides dominate the cumulative volume generated by gravitational processes.

The statistical behaviour of the functional relationship between landslide magnitude and frequency is despite large differences in landslide type, frequency and triggering mechanisms, suggesting a universal mean landslide area and a predictable population of failures for any given landslide event (Malamud et al., 2004). Nonetheless, the source of the rollover in landslide distribution has been attributed to an artifact of survey resolution (Hovius et al., 2000), to the scale of observation (Stark and Hovius, 2001), and to slope material strength (Pelletier et al. 1997). Furthermore, the position of the “roll-back” and the model fit for the power law decay for varying spatio-temporal inventories has proven to depend on the geological and geomorphological context and the depth of bedrock failure (Guzzetti et.al. 1996; Clarke & Burbank, 2010).

For the estimation of landslide driven erosion rates researchers have relied on empirical modeling connecting landslide volume with more easily obtained measurements of landslide geometry (e.g. area, width, length) (Innes, 1983; Hovius, Stark and Allen, 1997; Guthrie and Evans, 2004; Korup, 2005b; Guzzetti et al., 2008; Imaizumi et al. 2008). In such studies, landslide volume and erosion

estimates trust on scaling relationships where the predicted volume (V) for a given landslide area (A) depends on a scaling exponent γ and intercept α such that $V = \alpha A^{\gamma}$ (Guzzetti et al. 2009). Several studies focusing on landslide scaling relationships have been presented with γ tending to vary from 1.35 to 1.5 (e.g. Malamud et al. 2004; Guzzetti et al. 2009; Stark and Guzzetti 2009). Nonetheless, Larson et al. (2010) showed that small differences in γ lead to considerable variance in volume predictions, with errors becoming larger with increasing difference in γ, decreasing area–frequency scaling exponents and increasing maximum landslide area. Furthermore the authors highlight the importance of distinguishing between soil and bedrock landslides when estimating erosion rates due to significant variation of the scaling parameters for both landslide types. Any attempt to apply a scaling relationship outside the region it was developed should be performed with caution (Larson et al. 2010).

In the context of active mountain belts large bedrock landslides ($La>1km^2$) are one of the fastest geomorphic processes of hillslope adjustment to the local gravitational stress field after it has been unbalanced through tectonic uplift and glacial and/or fluvial incision, detaching almost instantaneously large amounts of sediment into the fluvial system (Korup et al. 2010). Therefore, discriminating between bedrock and shallow landslides is crucial as bedrock landslides are seen as the prevailing processes matching river incision and exhumation rates in rapidly uplifting terrains (Hovius et al., 2000; Clarke & Burbank, 2010; Larson et al. 2010). This is usually performed following the definition of a threshold depth of the failure surface based on field observations, taking into account different geological and geomorphic contexts and comprising different landslide typologies. Nonetheless, when considering large landslide inventories stretching over ten orders of magnitude (10^{-3} to $10^{7}km^2$), scaling relationships between landslide area-volume and area-depth have shown that a threshold value of $0.1km^2$ can be used to discriminate between large deep-seated/bedrock landslides and shallow/soil landslides (Larson et al. 2010).

In summary, the coexistence of medium to high rates of tectonic uplift, high relief slopes, fractured bedrock, heterogenic lithology, strong precipitation gradients and occasional seismic ground acceleration within active mountain belts creates the necessary conditions for the occurrence of high magnitude landslides events ($La>1km^2$). Nonetheless, the specific location to were such events tend to occur, or have occurred in the past, is commonly related to, or the combination of, specific bedrock and structural features, present/past climate conditions, and high relief setting capable of accommodating hillslope deformation and landslide propagation over several kilometres. Furthermore, large landslide clustering in different mountainous environments has been

successfully attributed to both precipitation and seismic events (Meunier et al. 2007; Qi et al. 2010). Thus distinguishing the relative importance of the different predisposing conditions and triggering mechanisms on landslide type, size and magnitude constitutes a difficult challenge (Roering et al. 2005).

This work aims to contribute to the knowledge of large-scale slope instability phenomena in the northern Rif Mountain combining geomorphologic, geomorphometric and laboratory techniques in the identification and analysis of large (>0.1km^2) bedrock landslides. The first regional landslide studies in the Rif were developed by Millès-Lacroix (1965, 1968), Mariotti & Milliès-Lacroix (1963) and Maurer (1962 & 1968), the later resulting in the publication of three geomorphological maps for the central part of the mountain chain, containing over 800 landslides identified through aerial-photo interpretation and field survey. In the following years, geologists responsible for geological survey of the Rif placed a significant effort in the identification of landslides deposits. Over the last decade, significant work has been undertaken in the study of slope instability in the Rif Mountains (e.g. Margaa, 1994; El Felah et al., 1996; Azzouz et al., 2002; Faleh & Sadiki, 2002; Faleh et al. 2002; Rouai & Jaaidi, 2003; Khattabi & Carlier, 2004; Mansour & Ait Brahim, 2005; Zêzere et al. 2009) but no comprehensive landslide inventory has been presented. One of the main contributions of this work is the presentation of the first regional landslide inventory (10,400 landslides spanning over six orders of magnitude, from 3x10^{-5} to 9,4×10^6 km^2) for the Northern Rif Mountains (north of Ouergha River).

This thesis is subdivided into five chapters. Following the geographical and geological overview of the northern Rif Mountains presented in chapter one, chapter two analyses the topography of the northern Rif belt using morphometric parameters extracted from digital terrain data. Due to its geographical position, the Rif mountain belt bears evidence of a complex geodynamical setting that relates to the Neogene evolution of the Africa-Iberia suture zone. Our goal is to detect spatial variations in landscape morphometry reflecting the interference of post-Tortonian tectonic activity and to fit the tectonic-geomorphic observations with the Plio-Quaternary tectonic models affecting mountain building. Moreover, we analyse the role of bedrock in controlling the spatial variability in topographic relief.

The third chapter studies the landslide size and spatial distribution of 3610 bedrock landslides (La> 0.01km^2) in the Central Rif Mountains with the objective of analysing how large landslide clusters relate to the structural (tectonics and bedrock) and topographic architecture and climatic setting of

the mountain belt and to discuss the geomorphic implications of large landslides located along the tail end of the frequency-size distribution.

The fourth chapter constitutes a preliminary approach to the study of slope instability analysis based on PSInSAR technique. The velocity and density of persistent PSs are analyzed with respect to terrain properties and landslide distribution to refine the classification of the activity status of the inventoried landslides. Furthermore, we resort to Hotspot and Cluster analysis in order to detect PSs clusters associated with slow gravitational movement.

In the fifth and final chapter we analyse the geological and geomorphological features of a complex deep-seated landslide – the Beni Derkoul landslide. The main objectives are: i) to analyse the landslide surface geology and geomorphology; ii) to define the structural model of deformation and the depth of the failure surface; iii) to analyse landslide kinematics; iv) to identify different stages of landslide evolution; v) and to analyse present-day landslide activity.

1 The Northern Rif Mountains

1.1 Geographical setting

The Rif Mountains extend along the northern coast of Africa forming the south western-end of the Betic-Rif-Tell orogen. This mountain system has been uplifting over the last 70 million years due to the convergence between the African and Eurasian plates, resulting in the formation of a 250 km wide E-W trending collisional prism. From Tangiers in the North, to Fes in the south and Mellila in the east, the Rif Mountains follow the geometry of the fold-thrust belt (Fig. 1.1). The Northern Rif (north of Ouerha River) comprises the highest sector of the mountain belt, forming parallel sets of NW-SE to W-E oriented fault bounded ridges reaching over 1500 meters above sea-level (asl).

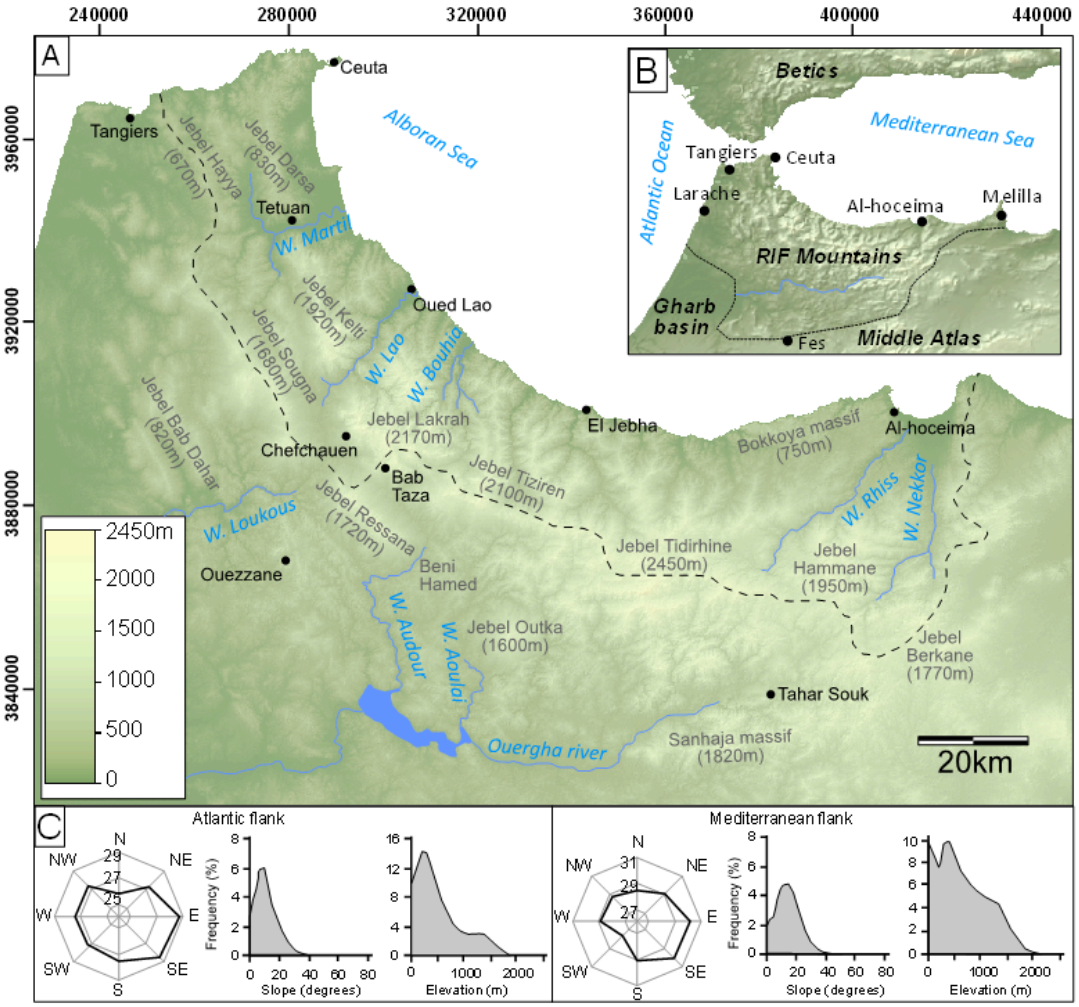


Figure 1.1 - Topographic setting of the northern Rif Mountains.
A) Topography of the northern Rif Mountains (north of Ouergha river) identifying the main mountain peaks. B) Overview of the Rif Mountain in the context of northern Morocco. C) Slope aspect and histograms showing elevation and slope distribution for the Atlantic and Mediterranean flanks of the mountain belt.

The main drainage divide (MDD) separates the Atlantic from Mediterranean flowing catchments. It stretches along the highest peaks east of Jebel Lakrah (Jebel Berkane, Hammane, Tidirhine and Tiziren), while to the north-west it is established along the top of Jebel Ressana and Sougna, reaching the Strait of Gibraltar east of the city of Tangiers (Fig.1.1). Slope distribution shows that the Atlantic flank has lower modal slope values when compared to Mediterranean side. Mean hillslope angles are higher by a factor of two degrees along the northeastern flank, with east and southeast facing slopes reaching mean values of 30 degrees (Fig.1.1). In both flanks, north, west and southwest facing slopes tend to be less steep (Fig. 1.1).

The present-day climate of the Rif is under Atlantic and Mediterranean influences. Together with the proximity to the ocean, the climatic characteristics of the region are set by its geometry and location blocking air masses traveling from the west and north-west creating orographically-enhanced rain-fall on the south-western flank and a rain-shadow effect on the northern and north-eastern side. Mean annual precipitation differences of 300 to 400mm/yr occur between the southern and northern and north-eastern flanks. In the highest peaks of the southern and south-western flanks annual precipitation reaches 1800mm/yr and is strongly concentrated during the Autumn-Winter months (November to February) (Fig. 1.2), with occasional snowfall above 1300m asl.

The valleys of the Rif present a torrential regime fitting the strong seasonality of precipitation. Catastrophic flooding is a common feature of the wadis, with maximum flood discharge rates reaching maximum values of 1500 to 7000 m^3/s (Table 1.1).

Table 1.1 – Hydrological parameters of the main wadis of the Northern Rif. Figure 1.2 for location.

Wadi	Drainage basin area (km2)	Annual rainfall (mm)	Maximum discharge (m^3/s) (1960-2008)	Source
Aoudour	985	1263	2000	Maurer 1968
Aoulai	775	1300	1825	Maurer 1968
Ouerrha	6134	1031	7000	Maurer 1968
Loukous	4411	960	3204	water.gov.ma
Martil	1525	1300	3350	water.gov.ma
Lao	915	1150	2150	water.gov.ma
Rhiss	805	890	1530	water.gov.ma

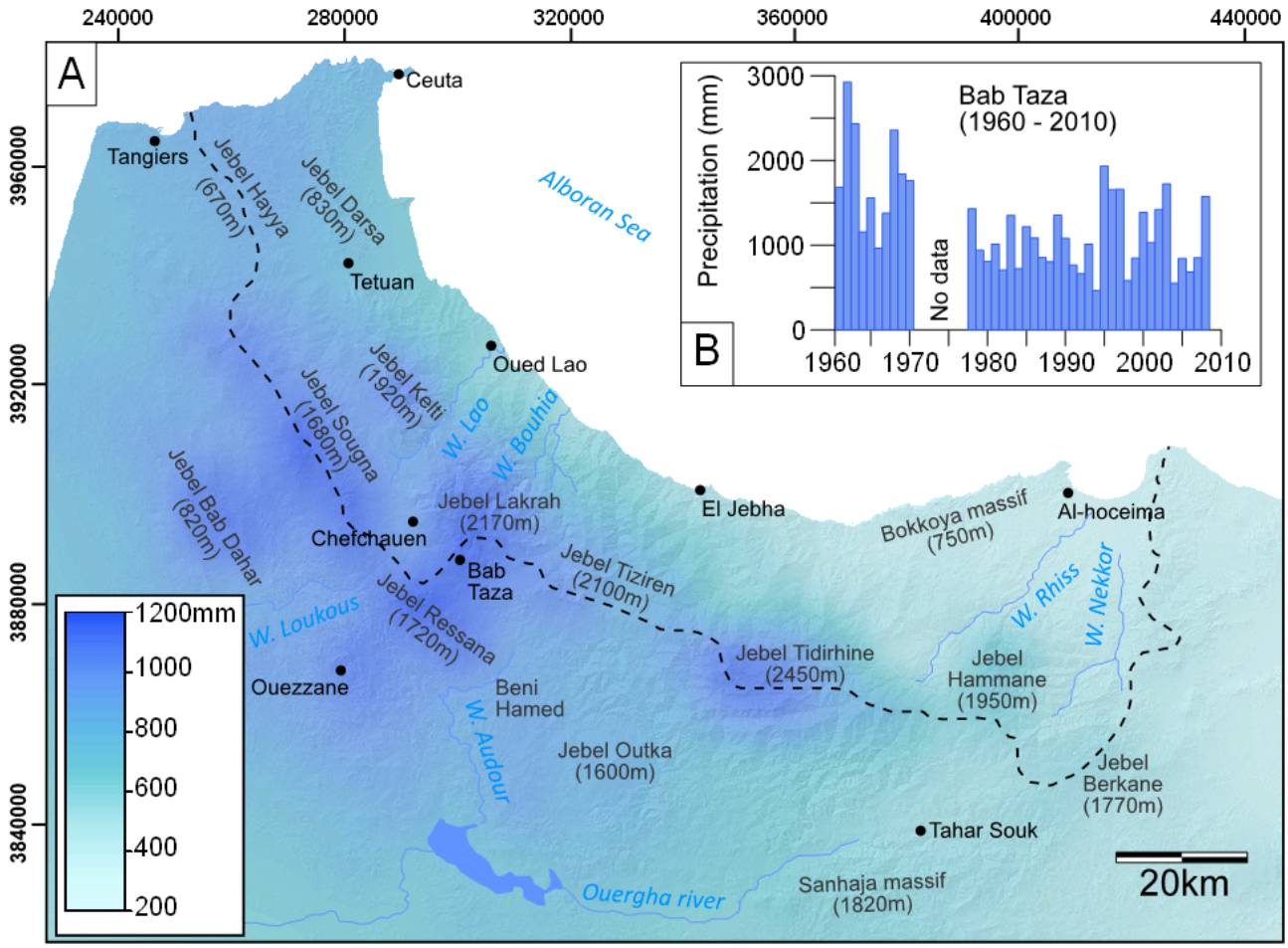


Figure 1.2 - Distribution of precipitation in the northern Rif Mountains.
A) Mean annual distribution of precipitation (WorldClim-Global Climate Database, http://www.worldclim.org/). B) Mean annual precipitation between 1960 and 2010 for the station of Bab Taza (see figure 1.2A for location).

1.2 Geological setting

The structure of the Rif belt is characterized by northward dipping detachment faults defining three main structural domains (Suter, 1980a, 1980b; Chalouan et al., 2001) (Fig. 1.3): i) the Internal Zones; ii) the Maghrebian Flysch; iii) and the External Zones. The NE-SW trending Nekor and Jebah transfer faults played a crucial role in the tectonic emplacement of the Internal Zones and Maghrebian Flysh, constituting lateral ramps to NW-SE to W-E thrust systems (Andrieux, 1971; Olivier, 1981-82; Benmakhlouf et al., 2005) (Fig. 1.3 and 1.4).

The Internal zones are subdivided into three tectonic units, namely the Sebtides, Ghomarides and the Dorsal Calcaire (Limestone Dorsal) (Durand-Delga et al. 1962) (Fig. 1.3). Taking into account the grade of Alpine metamorphism, two complexes can be recognized forming the upper (Sebtides) and

lower (Gomarides) plates of a metamorphic core complex (Chalouan et al. 2006). The Sebtides unit consists of mica-schist, migmatite and granulite associated with mantle peridotite. This unit is overthrust through a regional detachment by the Ghomarides, which includes schist and greywacke affected by Variscan metamorphism and by weak Alpine recrystallization (Chalouan & Michard, 1990; Chalouan et al., 2001). The Dorsal Calcaire occupies a more internal position forming thrust sheets of Triassic-Liassic carbonates composed of compact limestone, dolomite and breccia, overlain by Eocene-Lower Miocene unconformable formations (El Kadiri et al. 1992).

The Maghrebian Flysch was progressively deformed during the late-Oligocene - Early Miocene, forming a nappe stack of marine and turbiditic sediments (Sanz de Galdeano & Vera, 1992; Sanz de Galdeano et al., 2006). These units are overthrust by the Internal Zone and overlay the External Zone (Fig. 1.3). The more internal and higher units are known as the Mauritanian nappes and are subdivided into the Jebel Tisiren and Beni Ider nappes. From bottom to top the Jebel Tisiren nappe is composed of marly-limestone, followed by turbiditic levels consisting of graded siliciclastic sandstones with argillaceous horizons of Berriasian – middle Albian age (Durand-Delga et al., 1999). The Beni Ider nappe comprises black shales, pelite, schist and sandstone of upper Albian–Eocene-Oligocene age (Zaghloul et al. 2002). The more external and lower units belong to the Massylian nappe, which is formed by the Chouamat-Melloussa (Aptian-Albian to Senonian siliciclastic flysch, calcareous microbreccia and clay) and the Numidian nappe (Oligocene-Aquitanian compact sandstone) (Lespinasse, 1975).

The External Zones of the Rif (Fig. 1.3) are subdivided into three structural units from north to south and top to bottom (Suter, 1980a, 1980b; Chalouan et al., 2001): the Intrarif, Mesorif and Prerif. The northernmost sector of the Intrarif is subdivided into the Ketama (Lower Cretaceous folded carbonate-siliciclastic turbidites) and the Tanger and Loukkous units (Cenomanian-Eocene marly-pelitic formations) (Suter, 1980a; Andrieux, 1973).

The Mesorif and Prerif are the southernmost tectonic units along the Rif front extending from the western-central Rif to east of the Nekor fault. The central sector consists of Miocene turbidites and is overthrust by limestones, pelites and sandstones of Mesozoic age (Suter, 1980a). To the east, a volcano-sedimentary sequence of Liassic to upper Cretaceous age (lava flows and limestone intruded by gabbro) crops out. These units are unconformably overlain by middle Miocene turbidites. The Prerif contains marly-argillaceous formations extending from upper Cretaceous-Eocene to middle-upper Miocene (Suter, 1980a; Chalouan et. al., 2008).

1.3 Tectonic setting

The first compressional phase leading to the formation of the Rif Mountains occurred during Late Eocene-Oligocene, mostly concentrated in the Internal (Alboran) Domain. The presence of clastic sediments belonging to the Ghomarides within the Flysch and Intrarif units testify to this initial uplift phase (Chalouan et. al., 2008). From Lower to Middle Miocene, shortening inside the Flysch and Intrarif created NW-SE and NNW-SSE oriented folds, while in the Internal Zone prevailed the formation of extensional faults in response to the collapse of the Alboran Sea (Wildi et al. 1977; Nold et al. 1981; Ait Brahim et al., 2002). This event is further marked by the deformation of Oligocene to Burdigalian "post-nappes" intramontane basins and by backthrusting of the Dorsale and Flysch units on the Ghomaride units.

During Early-Miocene the tectonic setting was characterized by N50°E to N90°E-trending sinistral and N20°E to N160°E-trending dextral strike-slip faulting, evidencing a stress pattern with N25°E to N40°E striking compressive stress axis (**σ**1). During Late-Miocene and through the Plio-Quaternary the deformation was characterized by N170°E to N20°E-trending sinistral and N90°E to N140°E-

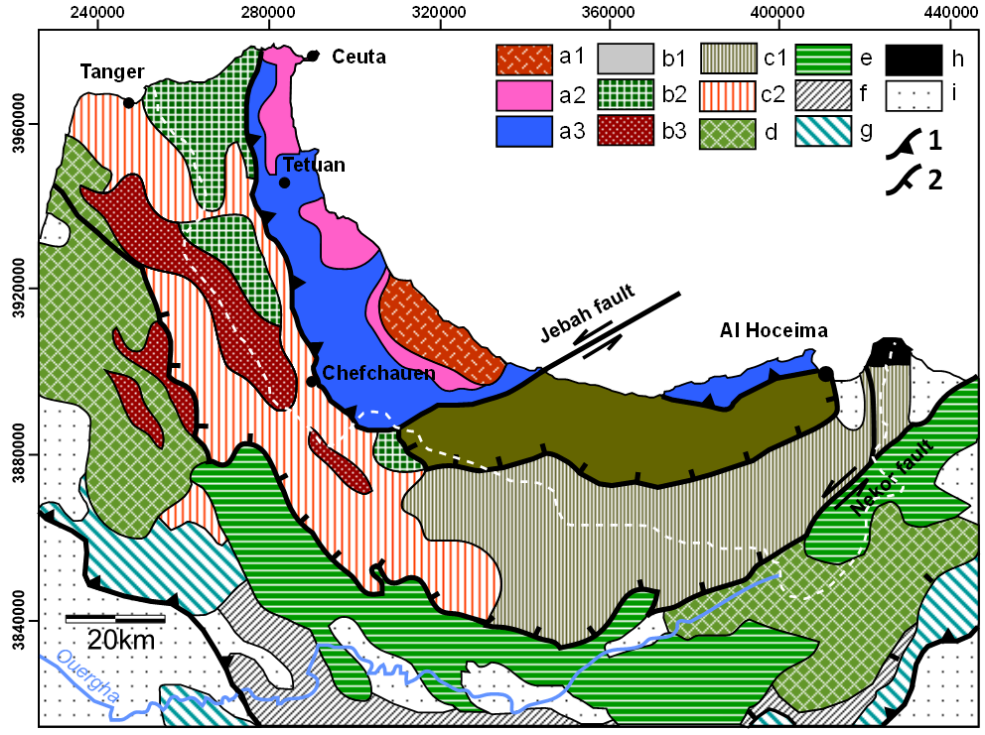


Figure 1.3 - Simplified structural outline of the northern Rif Mountains.

1 – First order thrust fault; 2 – Second order thrust fault; a – Internal Zones; a1 – Sebtides; a2 – Ghomarides; a3 – Dorsal Calcaire; b – Maghrebian Flysch; b1 – Tiziren nappe; b2 – Beni Ider nappe; b3 – Numidian nappe; c – Intrarif; c1 – Ketama unit; c2 – Tanger unit; d – Thrust nappes of Intrarif origin; e - Mesorif; f – Internal Prerif; g – External Prerif; h – Volcanic; i – Gharb basin.

trending dextral strike-slip faults in response to N – S to N140°E compression (Ait Brahim et al., 2002). Thermochronological data (Romagnya et al. 2014) indicate that during the 18–15 Ma interval (Burdigalian–Langhian), the Internal Zone experienced a slight reheating or a thermal stase, which may be linked to a renewal in thrusting activity and momentaneous burying of the inner zones. From 15 to 13 Ma, the exhumation resumed at a rate of around 0.8 mm/y in response to the ongoing NE-SW extension in the Alboran Sea.

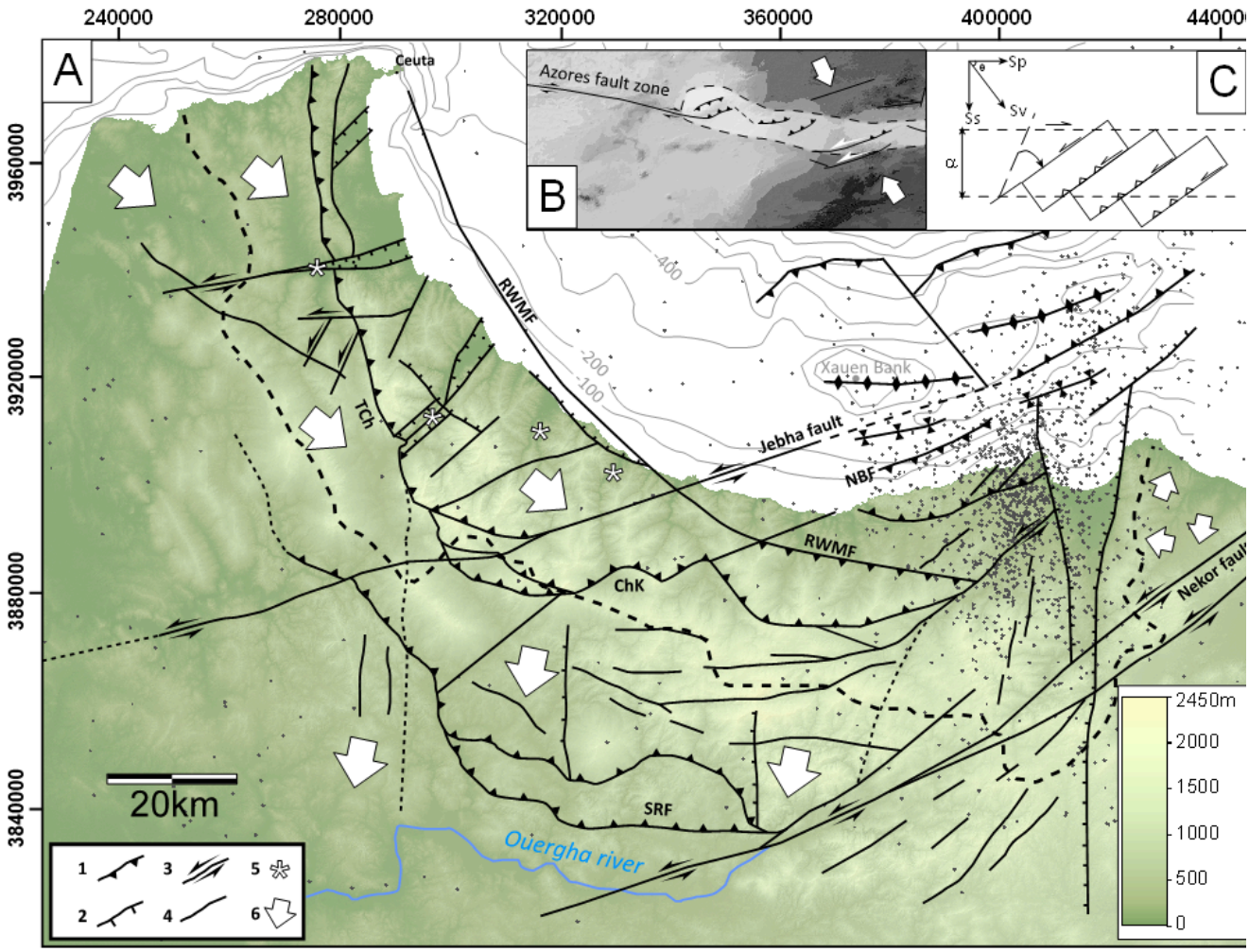


Figure 1.4 – Tectonic setting of the northern Rif.
Tectonic setting of the northern Rif following the work of Suter (1980), Morel (1992) and Faure-Muret & Morel (1992): 1) detachment fault; 2) normal fault; 3) strike-slip fault; 4) fault (unknown component); 5) Southwestern limit of the Pliocene reflooding along the Mediterranean flank of the Rif (see section 2 for explanation). RWMF – Rif West Mediterranean Fault; TCh – Tetuan-Chefchauen fault; ChK – Chefchauen-Ketama fault; NBF – Northern Bokkoya fault; SRF – Souther Rif thrust. Earthquake epicenters (USGS database 1973 to 2012) are represented by dark-grey dots. B & C) Transpressional and block rotation model for the Trans-Alboran shear zone according to Morel & Meghraoui (1996) and Meghraoui & Pondrelli (2012).

At present, the Betic-Rif thrust belt appears as a zone of diffuse deformation, where the low level of seismic activity and the superimposition of different Tertiary tectonic phases hinder the definition of a clear interplate limit (Serpelloni et al. 2007). Nonetheless, the seismic activity in the northern Rif emphasizes the convergence and collision of Africa and Eurasia tectonic plates. This process is marked by high frequency seismic activity in the north-eastern Rif and by the occurrence of high magnitude earthquakes such as the Al-hoceima 6.324 magnitude (Mw) event of February 24, 2004.

GPS data (Fadil et al. 2006; Tahayt et al., 2008) reveal that the Rif Mountains are divided into three blocks displaying different kinematical behaviour (Fig. 1.4): (I) the north-western block, which moves at an approximate speed of 1.6 to 1.2mm/y to the south-east; (II) the central Rif block, which moves southwards at a rate of approximately 3.4 ±1.2 mm/y, shows compression in the central-southern region and extension in the north; and (III) the eastern block, which is limited to the west by the N-S trending Al-Hoceima fault, rotates clock-wise .

Presently, Meghraoui & Pondrelli (2012) suggest that the right-lateral faulting mechanism observed on the Atlantic side (e.g. Azores fault zone) also affects crustal deformation along the North African margin through strike-slip and high-angle reverse faults, in association with transpression and block rotation (Fig. 1.4). The most significant (Ms>4) shallow seismicity shows a good correlation with onshore and offshore compressional Quaternary structures (Morel & Meghraoui, 1996).

Figure 4 shows the main tectonic structures affecting the Northern Rif. Four main structural trends are identified (Deffontaine et al., 1992): i) a NE-SW set, represented by the Jebah and Nekor faults; ii) a N-S set of structures controlling topography, which acted as normal faults with a minor strike-slip component during the Pliocene and Quaternary; iii) a group of NW-SE oriented structures within the Internal Zone; and iv) a E-W set affecting the north-western (Tangiers Peninsula, Tetuan valley) and south-eastern portion of the Rif (Southern Rif Fault - SRF) (Fig. 1.4).

In the context of the Rif, the Jebah and Nekor faults assume regional importance as transfer faults within the trans Alboran shear zone, extending inland from the Mediterranean coast (Figs. 1.3 and 1.4). The Jebah fault extends towards the northeast beneath the Xauen bank and Alboran Ridge (Chalouan et al. 1997). Offshore seismic data show ENE-WSW trending antiform folds along the Xauen bank related to SE and NW verging thrust systems (Northern Boukoya Fault – NBF; Fig. 1.4) connected to NE-SW oriented strike-slip faults (Chalouan et al. 1997). Seismic profiles and well data suggest bank formation by compression and uplift of Early Miocene reworked deposits and Langhian to Pliocene sedimentary units that were previously deposited in the deep Western Alboran Basin (Gensous et al., 1986; Bourgois et al., 1992; Morley, 1993; Chalouan et al., 1997). The

presence of unconformities affecting the Quaternary deposits on the anticline limbs confirms the progressive growth of the Xauen - Alboran ridge lineament (Woodside & Maldonado, 1992).

Recent gravimetry studies of the Moroccan crust outline the existence of deep-seated tectonic structures (Khattacha et al., 2013). Concerning the Rif, this study confirmed the SW extension of the Jebah fault and the position of the Tanger-Ketama fault along the southern edge of the Tiziren unit. Furthermore, a NW-SE to WNW-ESE structure along the Mediterranean coast was identified (Rifain West Mediterranean Fault – RWMF) extending for 150km, from Ceuta to the southernmost part of Al-Hoceima (Fig. 1.4). According to Khattacha et al. (2013), this arcuate NW-SE structure with a south-westward convexity is vertical from Ceuta to Jebah and dips to the southwest in its easternmost part, while crossing the Flysch domain.

Although the tectonic setting of the northern Rif is well established it lacks consistent data on spatial variations in uplift rates. Late-Miocene to Quaternary uplift rates have been estimated by fission-track dating and from the analysis of seismic profiles and Plio-Quaternary deposits along the Mediterranean coast (Morel & Meghraoui 1996; Romagnya et al. 2014). Seismic profiles northeast of the Internal Zone in the Alboran Sea reveal significant tilting of the Moroccan margin towards the Mediterranean, suggesting a post-Messinian uplift of approximately 1km (Mauffret et al., 2007). Estimated uplift of Quaternary deposits and slip-rates of NE-SW trending left-lateral faults in the Rif Mountains reach a maximum of 1 mm/y and 2.3 mm/y, respectively (Morel and Meghraoui 1996).

1.4 Post-Tortonian landscape evolution in the Rif: an overview of major geological events

On the onset of the Messinian, the Rif had already established its overall physiography, with southwest and northeast facing flanks draining towards the Atlantic Ocean and Mediterranean, respectively. Similarly to the Betics and the Apennines, the Rif preserves evidence of an erosional phase – the Pontian erosional surface - placed within the Upper-Tortonian-Messinian boundary and generally described as gentle topography representing an early stage of sub-aerial evolution of the mountain topography (Maurer, 1968).

The Pontian surface in the Rif precedes the Pliocene re-flooding of the Mediterranean, as testified by the presence at a lower altitude of Pliocene marine sediments along the wadi Lao gorge, and post-dates the tectonic movements that affected the Internal Zone and the Maghrebian Flysch during Middle-Upper Miocene (Maurer, 1968). Its remnants reach a maximum altitude of 1500m and are preserved along valley flanks of both the Atlantic and Mediterranean side. In the south-central and north-eastern sectors it occupies the top of the Beni Hamed and Boukkoya massifs

(Maurer, 1968) (Fig. 1.1 for location). Recent studies (Romagnya et al. 2014; Cornée et al. 2014) suggest that the Pontian surface within the Internal Domain is in fact a marine planation surface of Late Miocene – Early Pliocene age, as demonstrated by the presence of intense bioerosion of lithophagid molluscs.

One of the key moments in the geological history of the Mediterranean corresponds to the Messinian Salinity Crisis (MSC) (5.9 to 5.3 Ma). The progressive uplift of the External Zones of Rif corridor by middle-late Miocene led to the exhumation of the marine gateways closing the connection between the Atlantic and the Mediterranean Sea (Chalouan et al., 2008). The absence of oceanic water inflow triggered the desiccation of the Mediterranean, inducing a dramatic sea level drop of up to 1500 meters below present sea level and subsequent incision of the continental margins by regressive erosion (Loget & Driessche, 2006). Three models have been proposed to explain this event: (1) rollback beneath the Alboran region (Zeck, 1996; Lonergan & White, 1997), (2) lithospheric mantle delamination beneath the crust of the Alboran region (Comas et al., 1993) and (3) convective removal of the lower part of the over-thickened crust/lithosphere of the Alboran domain (Platt & Vissers, 1989).

Willett et al. (2006) suggest that the strong stratigraphic signature of the Messinian might express a positive feedback between tectonic, climatic and surface processes. In fact, in the western Mediterranean, the increase in both sedimentation rates and total sediment volumes have been associated to an increase in the accommodation space in response to the tectonic subsidence of the Alboran Sea (Iribarren et al., 2009). From early to middle Miocene sedimentation rates are of the order of 0.24 mm/y, nearly doubling towards the upper-Miocene (Iribarren et al., 2009). While first order tectonic processes (mainly the collapse of the Alboran domain) can be responsible for the increase in sedimentation rate, the contribution of the MSC to the observed increased sedimentation rates is poorly constrained. However, Romagnya et al. (2014) show that vertical motions were low within the Internal Domain since 13Ma and that AHe thermochronology could not detect any accelerated denudation during the MSC.

By early Pliocene, the opening of the Strait of Gibraltar allowed Atlantic waters to re-enter the Mediterranean basin. This event has been attributed to normal faulting within the Strait of Gibraltar or to tectonic subsidence in response to the westward roll-back of the underlying subduction, together with regressive erosion of fluvial systems towards the west, eventually capturing Atlantic waters (Chalouan et al., 2008). The presence of Pliocene sediments trapped within the deeply incised valleys of the Internal Zone indicates that these valleys functioned as rias during the re-

flooding of the Mediterranean (Wildi & Wernli, 1977; Morel, 1987) (Fig. 1.4). These basins were later affected by normal faulting along NW-SE structures in response to the late Pliocene - Pleistocene extensional episode on the Alboran Sea (Romagnya et al., 2014).

Surface uplift persisted throughout the Quaternary as testified by the presence of Pliocene sediments within the core of the mountain belt presently situated at 500-600m asl (Wildi & Wernli, 1977; Morel, 1987) (Fig. 1.4) and through the uplift of fluvial and marine terraces along the Atlantic and Mediterranean flanks (Maurer, 1968; Morel and Meghraoui 1996).

2 Tectonic and bedrock signature on the topography of the Northern Rif inferred from DEM-based geomorphometry

Submitted articles:
Fonseca, A.F., Zêzere, J.L., Madeira, J., Bouchta, EF. (submited). Tectonic and bedrock signature on the topography of the Northern Rif inferred through DEM based geomorphometry (Morocco). International Journal of Earth Sciences.

Abstract

The present day topography of the Rif mountain belt bears evidence to the Post-Tortonian interaction between tectonic and climate induced surface processes. In this work the topographic signature of both tectonics and bedrock control is captured over different length-scales of landscape analysis through DEM-based geomorphometry. Post-Tortonian uplift occurs in response to the on-going convergence between the African and Eurasian plates. Uplift and sea level fluctuations played a strong role in the way drainage systems evolved through bedrock incision and regressive erosion, with bedrock lithology favouring river dissection along less resistant lithological units. Geomorphic evidence for the north-western sector of the mountain chain indicate drastic changes in relief production imposed by tectonic uplift and drainage incision, resulting in migration of the main drainage divide during middle to late Pliocene. Furthermore, the combination of geomorphic and geological evidences indicates a concentration of surface uplift and tectonically induced drainage incision within the Internal Domain and the southern sector of the Ketama Unit, defining two distinct zones of deformation. To the east of the Jebah fault, the position of major knick zones and spatial variations in basin-scale morphometric data reveals a broad NE-SW trending deformation zone in response to NW-SE shortening that is consistent with transpression models for the Western Mediterranean. Northwest of the Jebah fault, tectonic deformation is associated to normal faulting in response to the collapse of the Alboran Sea, with nearly one third of the available relief being formed in response to Plio-Quaternary surface uplift.

Keywords: tectonic geomorphology; landscape evolution; geomorphometry; Pontian-Quaternary; Rif Mountains; Morocco.

2.1 Introduction

Over recent years the increasing availability of digital terrain data and the evolution of GIS and programing techniques has allowed earth scientists to look at landform evolution in a more precise and quantitative way. In this context, the study of landscape morphometrics resorting to digital terrain data has proven to capture the topographic signature of tectonic, bedrock and climate induced surface processes over different temporal and spatial scales (e.g. Montgomery et al., 2001; Jordan, 2003; Stolar et al., 2007).

In this section we analyse the topography of the northern Rif belt using morphometric parameters extracted from digital terrain data. Due to its geographical position, the Rif mountain belt bears evidence to a complex geodynamical setting that relates to the Neogene evolution of the Africa-Iberia suture zone. Our goal is to detect spatial variations in landscape morphometry reflecting the interference of post-Tortonian tectonic activity and to analyse the role of bedrock in sustaining relief conditions in this active mountain belt.

The topography of the Rif was inspected through two scale-time dependent morphometric approaches. First we analysed the first order derivatives (i.e. elevation, local relief, and slope) for the entire mountain range with the objective of identifying both tectonic and bedrock related influences on the physiography of the Rif. On a second stage we focused our attention on a drainage basin scale analysis (a total of 21 catchments) (Fig.2.1) to detect spatial anisotropies connected with differential uplift and to variations in inferred bedrock strength. While the first approach aims for a coarser detection of the tectonic signature on topography acting over the earliest stages of landscape dissection (Late-Tortonian-Pliocene), the later helps to extract information for a later geological timeframe that extends through the Pleistocene.

2.2 Digital database

A digital database was constructed combining a digital elevation model, climatic data and geological information. Lithological data was extracted from Suter (1980a) and complemented through the analysis of 1:50,000 scale geological maps of the Rif. Tectonic data was compiled from Suter (1980a, 1980b), Chalouan et al. (1997), Deffontaine et al. (1992) and Ait Brahim & Sossey (2003).

Precipitation data was acquired online through the WorldClim-Global Climate Database (http://www.worldclim.org/). The dataset follows the work of Hijmans et al. (2005) and results from the compilation of climatic data between 1950 and 2000 from the Global Historical Climatology Network (GHCN), the FAO, the WMO, the International Centre for Tropical Agriculture (CIAT) and the R-Hydronet. The data is interpolated using a thin plate smoothing spline, placing latitude, longitude and elevation as independent variables. Even though the WorldClim database underestimates precipitation values when compared to gauge station data, the dataset expresses the overall control of topography in the distribution of precipitation, thereby fitting present objectives.

To quantify the first order characteristics of the present topography of the Rif, eight tiles of the ASTER GDEM2 covering northern-central Morocco and the Strait of Gibraltar were used in this study. ASTER GDEM2 is a product of METI and NASA and is available on a 1 arc-second (approximately 30m at the equator) grid and referenced to the 1984 World Geodetic System (WGS84)/1996 Earth Gravitational Model (EGM96) geoid.

In order to improve the DEM quality and ensure the continuity of the drainage systems, sinks were filled through specific GIS tools. Sinks were individually inspected on satellite images and published geomorphological maps in order to eliminate false artifacts expressing lakes, closed karts features and depressions within large landslide bodies. A single flow drainage direction (steepest descent)

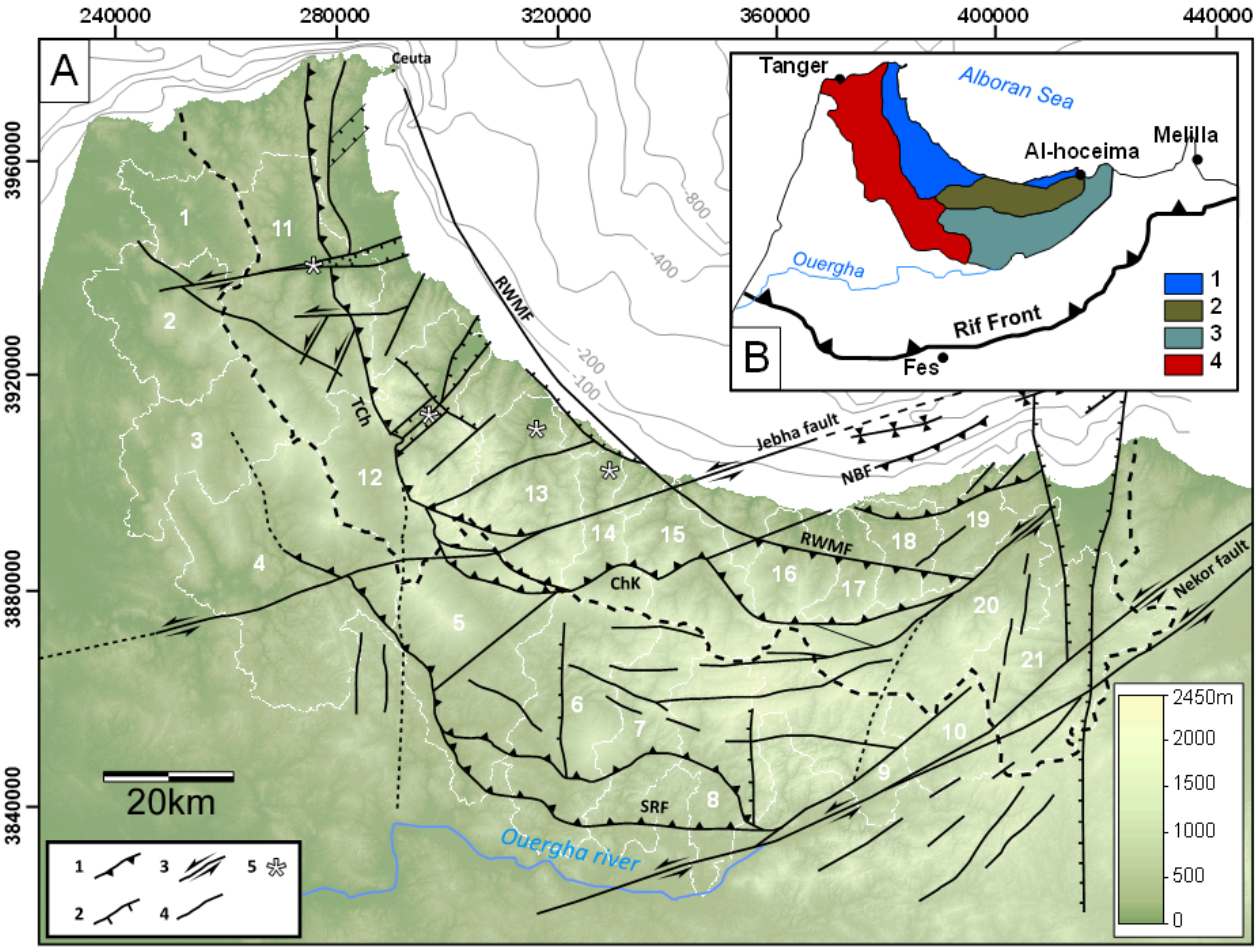


Figure 2.1 Tectonic setting of the Northern Rif and location of the drainage basins.
A) Onshore and offshore tectonic structures according to Suter (1980a, 1980b), Chalouan et al. (1997), Deffontaine et al., (1992); Ait Brahim & Sossey (2003). 1) Thrust fault; 2) Normal Fault; 3) Strike-slip fault; 4) Fault; 5) Southwestern limit of the Pliocene reflooding along the Mediterranean flank of the Rif (see text for explanation); White lines and numbers locate the 21 catchments analyzed in this study. B and C) Transpressional and block rotation model for the Trans-Alboran shear zone according to Meghraoui & Pondrelli (2012) and Morel & Meghraoui (1996). B) Location of the morphostructural units for which slope histograms were calculated. 1) Internal Zone; 2) Tiziren Unit; 3) Ketama Unit; 4) Tanger/Beni Ider units.

was calculated for each cell of the grid, followed by the calculation of flow accumulation. The channel network was extracted by applying a constant threshold area, defined as 0.2176 km^2 following the work of Chen et al. (2003). The resulting drainage map was compared with 1:50,000 scale topographic maps of the Rif to confirm drainage consistency.

2.3 Geospatial analysis of topography

The present section focuses on a small-scale analysis using geomorphometric parameters derived from digital terrain data. Specifically we analysed the mean elevation, summit and base level topography, local relief, mean slope, and terrain hypsometry (Fig. 2.2). Furthermore, we analysed the spatial variability in post-Tortonian drainage network incision resourcing to the remnants of the Pontian erosional surface.

Cross-range swath profiles were created combining summit and base-level data, mean elevation, local relief and precipitation (see Burbank, 1992; Fielding et al., 1994 for methodology) (Fig. 2.3). The traverses are perpendicular to the main axis of the orogen and swath position was chosen to cover spatial variability in morphometric data.

A similar approach using summit level topography was used by Deffontaine et al. (1992) to detect structural discontinuities throughout Morocco. Nonetheless, in this work, summit level mapping results from compilation of spot-heights on slopes with less than 5 % and on planar surfaces with more than 4 km^2 in area, retrieved from 1:500.000 scale topographic maps. At present, the existence of medium resolution DEMs for the Moroccan territory allows the validation of previous results through the application of GIS based methods.

2.3.1 Summit, base level and mean elevation

To analyse the distribution of maximum, minimum and mean elevation, summit level, base level and mean elevation maps were extracted from the digital elevation model. The average or mean elevation mapping technique is useful to detect locally averaged maxima within a landscape. This was performed by applying a smoothing (lowpass) filter to the DEM using a 10x10 and 5x5km moving window.

The summit level and the base level map contain the highest and the lowest point elevation within a given area, respectively. These are generally seen as dynamic levels of erosion (Deffontaines et al., 1994) representing proxies to past and present evolutionary stages of the mountain belt. The main objective behind these methods is to smooth topography around maximum and minimum height

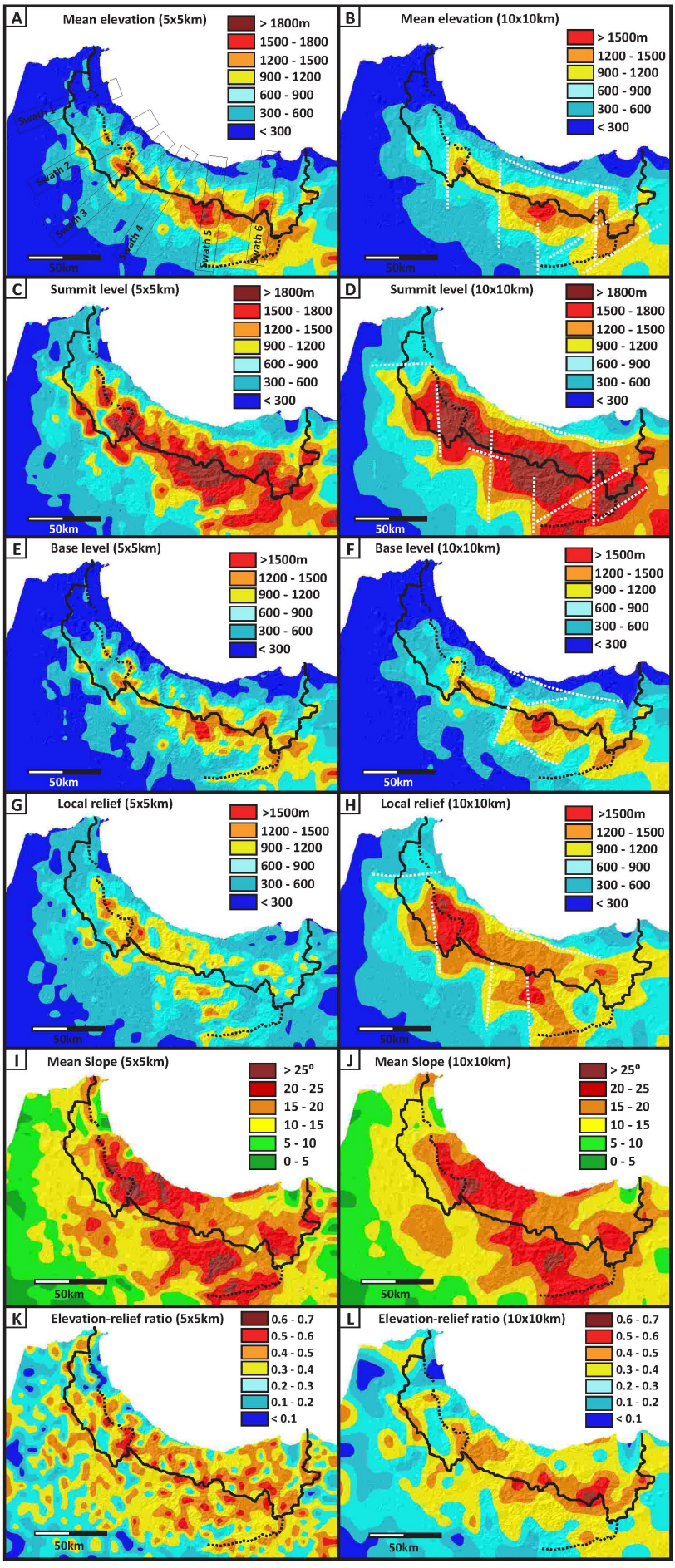
values in order to detect local anisotropies reflecting the interference of tectonics and bedrock lithology in landscape morphology. Base level mapping is particularly useful in landscape studies as it illustrates the slope and major knickpoints within the drainage network and allows an estimation of the available (local) relief (Dury, 1951).

The summit level map was calculated on a 10x10 and 5x5km moving window. For each length-scale the coordinates of the points with the highest elevation were stored and interpolated with a standard kriging method. The base level map follows the same premises as the later and was obtained through the interpolation of height data collected along valley bottoms (Fig. 2.2).

Figures 2.2 and 2.3 show the distribution of mean elevation, summit and base level topography. The summit level map shows four sectors with altitude above 1500m associated with the summit areas of Jebel Lakra, Jebel Rhesana, Jebel Tidirhine and Jebel Hammane. The MDD is consistently positioned along the highest sectors ESE of Jebel Lakra following competent rock-bodies of the Tiziren sandstone and Ketama carbonates. Towards the northwest, while present day drainage divide is positioned along the top of Jebel Rhesana and Sougna, the summit level map exhibits higher altitudes along the compact limestones of the Dorsal Calcaire (Fig. 2.2 and 2.3).

A strong contrast in summit level is observed between the Atlantic and Mediterranean flanks. Along the Atlantic side both the 10x10 and 5x5km summit level maps define a sharp but sinuous limit between summits above and below 900m, capturing the south-western base of Jebel Sougna, Rhesana and Outka and extending towards the east following the Ouerga River (Fig. 2.2). This altitudinal boundary is associated with the northern limit of the Tanger Unit, while limited to the east and west by sharp NE-SW and N-S gradients that relate to previously identified tectonic structures (Deffontaine et al., 1992).

Along the Mediterranean flank, the summit level above and below 600m is set by a rectilinear and sharp contrast that extends from the north-central sector towards the east and south of the Boukkoya massif. The lack of geological contacts associated with this topographic signature leads towards the definition of a tectonic control in summit level that relates to the geomorphic expression of the Rifain West Mediterranean Fault (Fig. 2.1 for location). Within the Internal Zone a NW-SE oriented gradient is captured along the northern flank that is consistent with normal faults described by several authors (e.g. Wildi & Wernli1977; Morel, 1987; Romagnya et al. 2014).


A
Mean elevation (5x5km)
> 1800m
1500 - 1800
1200 - 1500
900 - 1200
600 - 900
300 - 600
< 300
Swath 1
Swath 2
Swath 3
Swath 4
Swath 5
Swath 6
50km
B
Mean elevation (10x10km)
> 1500m
1200 - 1500
900 - 1200
600 - 900
300 - 600
< 300
50km
C
Summit level (5x5km)
> 1800m
1500 - 1800
1200 - 1500
900 - 1200
600 - 900
300 - 600
< 300
50km
D
Summit level (10x10km)
> 1800m
1500 - 1800
1200 - 1500
900 - 1200
600 - 900
300 - 600
< 300
50km
E
Base level (5x5km)
>1500m
1200 - 1500
900 - 1200
600 - 900
300 - 600
< 300
50km
F
Base level (10x10km)
> 1500m
1200 - 1500
900 - 1200
600 - 900
300 - 600
< 300
50km
G
Local relief (5x5km)
>1500m
1200 - 1500
900 - 1200
600 - 900
300 - 600
< 300
50km
H
Local relief (10x10km)
>1500m
1200 - 1500
900 - 1200
600 - 900
300 - 600
< 300
50km
I
Mean Slope (5x5km)
> 25°
20 - 25
15 - 20
10 - 15
5 - 10
0 - 5
50km
J
Mean Slope (10x10km)
> 25°
20 - 25
15 - 20
10 - 15
5 - 10
0 - 5
50km
K
Elevation-relief ratio (5x5km)
0.6 - 0.7
0.5 - 0.6
0.4 - 0.5
0.3 - 0.4
0.2 - 0.3
0.1 - 0.2
< 0.1
50km
L
Elevation-relief ratio (10x10km)
0.6 - 0.7
0.5 - 0.6
0.4 - 0.5
0.3 - 0.4
0.2 - 0.3
0.1 - 0.2
< 0.1
50km

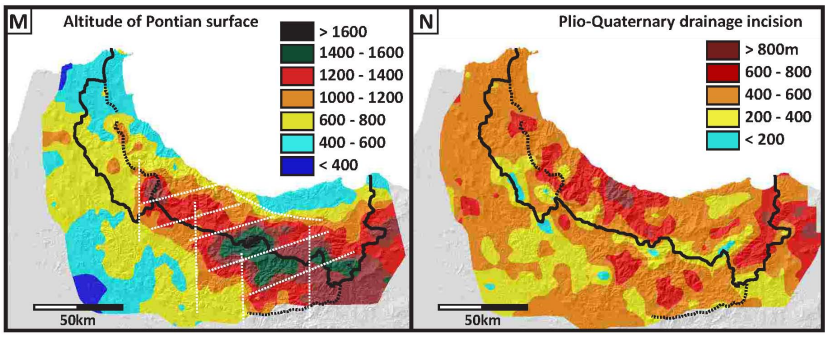


Figure 2.2 Geospatial analysis of topography.
Geospatial analysis for different length scales (5x5km and 10x10km) and location of swath profiles (A). Dashed white lines identify the topographic gradients described in the text. Solid black line indicated the position of the main drainage divide (MDD). Black dashed line indicates secondary divides.

The mean elevation map depicts a similar spatial trend as the summit level, with mean elevation above 1200m defining the highest peaks of the Northern Rif. A sharp contrast between the Atlantic and Mediterranean flanks is also apparent. Although it captures the summits of Jebel Rhesana and Jbel Sougna, the Dorsal Calcaire still maintains its altitudinal dominance. Interestingly enough, while the north-eastern flank of Jbel Sougna drains towards the Mediterranean Sea through the wadi Lao gorge, the mountain pass between Sougna and Rhesana, while established within the marls of the Tanger Unit, presents a mean and summit level altitude about 150m lower than its northern connection with the Dorsal Calcaire.

The base level map captures the present day position of the MDD, connecting the Numidian ridges with the mountaintops to the east. Base-level altitude increases towards the east, reaching a maximum altitude at the top of Jebel Tidirhine. An interesting feature of the present day drainage network topography is the definition of sharp gradients along N-S to NNE-SSW striking slopes east of Jebel Lakra – Jebel Sougna and west of Jebel Tidirhine – Jebel Outka (Fig. 2.2).

2.3.2 Local relief and mean slope

Local relief is a morphometric parameter defining the difference in height in a region between the highest peaks and the valley bottoms. While expressing the competition between tectonic and climate-driven geomorphic processes, local relief has been widely used in the description of mountain topography (e.g. Ahnert, 1970; Burbank, 1992; Roe et al. 2003).

Spatial variations in bedrock strength impose a significant impact in local relief distribution by limiting the ability of detachment-limited geomorphic processes to erode mountainous terrain. Therefore, the interpretation of local relief data is hindered by the complexity of physical based processes that interplay in relief production.

Mean slope angle, while calculated over different length scales has proven to be linearly correlated

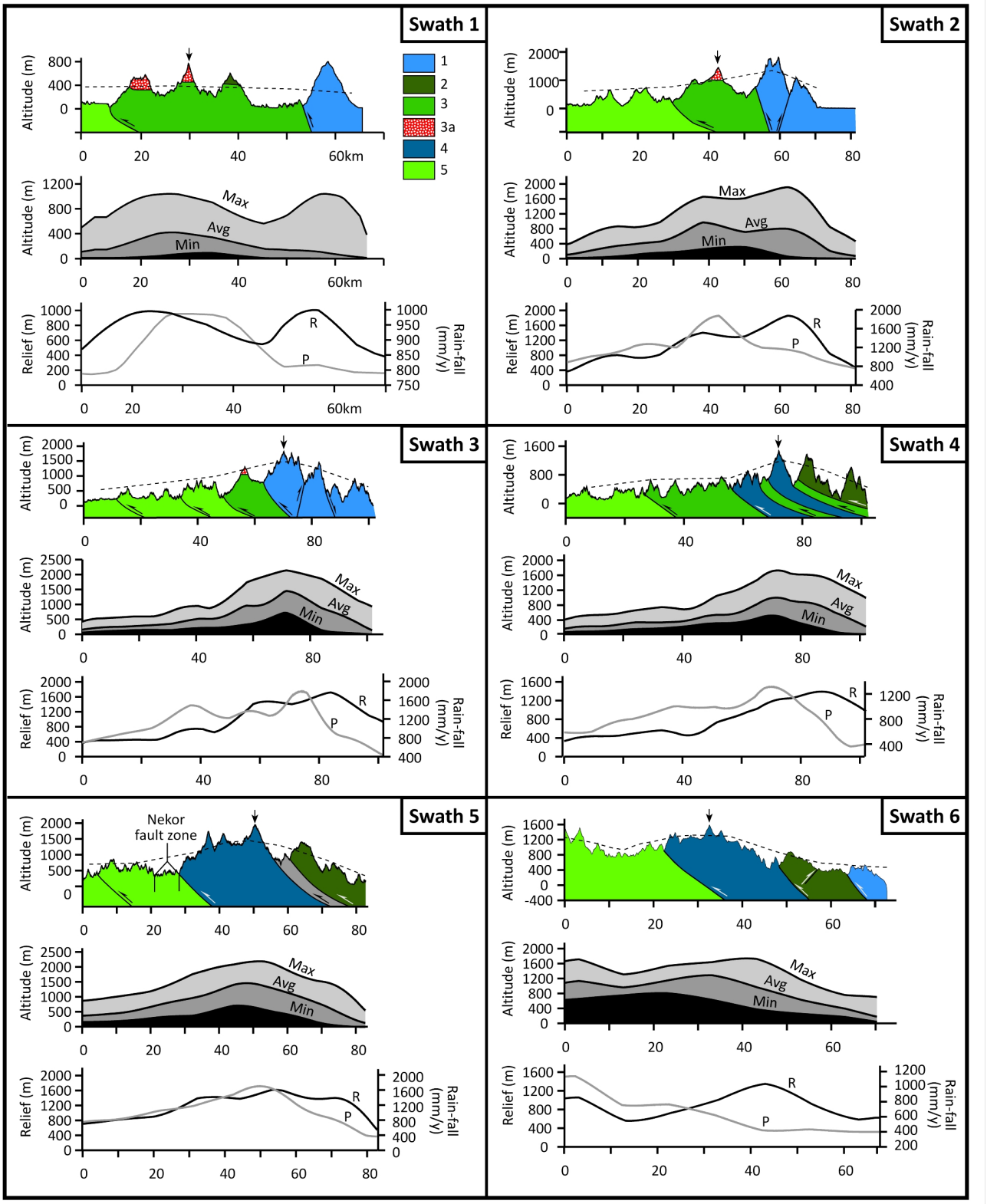


Figure 2.3 - Swath profiles.
Swath profiles running perpendicularly to the mountain range (figure 2.2 for location), created for elevation (Summit, base-level and mean elevation), local relief and mean annual precipitation. Dashed lines indicate the mean altitude of the Pontian surface. Arrows locate the present-day position of the MDD. 1) Internal Zone; 2) Tiziren Unit; 3) Tanger/Beni Ider Unit; 3a) Numidian sandstone; 4) Ketama Unit; 5) External Zone.

with local relief (Montgomery and Brandon, 2002). Several studies show that landscape-scale erosion rates are correlated with both local relief and mean slope angle (Ahnert, 1970; Summerfield & Hulton, 1994; Montgomery & Brandon, 2002). Furthermore, where incision rate keeps pace with rock uplift, hillslopes display a normal distribution about a modal slope value that depends on the mechanical strength of hillslope-scale rock masses (Burbank et al., 1996; Montgomery, 2001).

For the purpose of this study, local relief and mean slope angle where extracted from the digital elevation model. Local relief was calculated by subtracting the previously calculated Base-level map from the Summit level map for each of the selected length-scales. The mean slope map was obtained by averaging the slope map over a 10x10 and 5x5km moving window using aggregate statistics. Furthermore, slope histograms were calculated for four morphostructural units to the north of the SRF (Fig. 2.1 for location) (Internal zone, Tiziren, Ketama and Tanger, the latter comprising the Tanger, Numidian and Beni Ider units) as well as for low (compact limestone, dolomite, compact sandstone) and high (clay, marl, poorly consolidated sand) erodibility units according to Suter (1980a).

Figure 2.2 shows two areas with mean local relief above 1500m associated with the deeply incised valleys along the southern flank of Jebel Tidirhin and within the Internal Zone. Reaching over 1800m, the wadi Lao gorge depicts one of the highest mean local reliefs in the Northern Rif.

Low relief areas are mainly concentrated in the External Zone and north of Jebel Sougna. With the exception of the southern Tidirhin sector, the majority of the available relief is concentrated in the Mediterranean flank (Figs. 2.2. and 2.3), expressing a sharp gradient that strikes along the coast from WNW to ESE and leaves the low relief area of the Boukkoya massif to the north. Furthermore, swath profiles reveal that local relief is decoupled from mean annual distribution of precipitation (Fig 2.3).

The mean slope map depicts a similar spatial distribution as the later, displaying a sigmoidal concentration of high (>20 degrees) slope values along the north-central and southern flanks of the mountain chain in association with the compact carbonate and metamorphic units of the Internal Domain and Ketama unit (Fig. 2.2). High slope values occur along the Mediterranean coast west of the Jebah fault. The lowest mean slope values occur along the southwest facing Atlantic flank, with striking low values around the peaks of Jebel Rhesana and Sougna in association with the marly and clay domain of the Tanger Unit.

A strong variability in slope distribution is observed for each structural unit of Northern Rif. Figure 2.4 shows slope distribution normalized by area for four morphostructural units - the Internal Zone,

Tiziren, Ketama and Numidian-Tanger Units (Figure 2.1 for location) - as well as for high and low erodibility units according to Suter (1980a). Modal slope values within the Internal Zone, Ketama and Tiziren units reach 18 to 19 degree, while for the Tanger Unit modal values drop to 11 degrees. A similar tendency is observed when considering bedrock strength, which indicates a probable hillslope adjustment to the strength of the undelaying bedrock material while responding to long-term base-level lowering. Bedrock strength plays a crucial role in mean slope distribution, with competent rock bodies effectively sustaining higher mean hillslope angles within areas with mean local relief above 1000 meters.

2.3.3 Elevation-relief ratio

Analysis of the distribution of the horizontal cross-sectional area of a landmass with respect to elevation is generally described as hypsometric analysis (Strahler, 1952). The use of hypsometric curves and integrals (area beneath the curve) helps differentiating erosional landforms according to three evolutionary stages (Strahler, 1952, Schumm, 1956): Convex-up curves and high integrals (I>0.70) are typical of youthful, undissected (disequilibrium stage) landscapes; smooth, s-shaped curves crossing the centre of the diagram characterize mature (equilibrium stage) landscapes; and concave up with low integrals (I<0.30) typify old and deeply dissected landscapes (Strahler, 1952). Several studies have successfully associated landform evolutionary stages to differences in tectonics, bedrock strength and erodibility, and climate (Strahler, 1951; Stoler et al. 2007). Furthermore, Strahler (1952) showed that the hypsometric integral is inversely correlated with local relief, slope steepness, drainage density and channel gradients.

While the hypsometric curve and integral are widely applicable at a landform scale, when covering large portion of the territory it becomes a very time-consuming task. Pike and Wilson (1971) showed that the Elevation-relief ratio (Er) is identical to the hypsometric integral. According to the authors Er is defined as

$$\mathrm{Er} = \frac{\mathrm{ElevAvg} - \mathrm{ElevMin}}{\mathrm{ElevMax} - \mathrm{ElevMin}}$$

where the average, minimum and maximum elevation are calculated over a predefined length scale In this work we use Er to analyse the spatial variability in landscape maturity. Calculations were performed using the summit-level, base-level and mean elevation maps for each of the selected length-scales.

Elevation-relief ratio values range from 0.2 to 0.7 with a spatial distribution that reflects the co-existence of two distinct geomorphic domains (Fig. 2.2). Higher E values are concentrated north of Jebel Lakra, Tiziren, Tidirhin and Hammane, with the latest reaching Er values over 0.6. Taking into account bedrock lithology, higher values tend to occur in clear association with the competent rock bodies of the Internal Zone (in particular the Dorsal Calcaire) and Ketama Unit. Furthermore, low Er values tend to be concentrated further to the west were precipitation and bedrock erodibility are higher. The south-western sector of the Atlantic flank has the lowest E values in the Rif, defining a broad area east of Jebel Outka with Er values under 0.4, consistently reproducing the NW-SE extension of the marly domain of the Tanger-Numidian morphostructural unit.

2.3.4 Post-Tortonian uplift and drainage incision

Available data on uplift rates of the Rif Mountain are limited to the Internal Domain and to particular sites along the Mediterranean coast (Morel & Meghraoui, 1996). The lack of spatially distributed information of uplift rates makes it impossible to incorporate uplift data within landscape morphometric studies.

The analysis of bedrock-rivers within active mountain belts suggest that long-term incision rates match measured uplift rates (Burbank et al. 1996; Rockwell et al., 1988; Lave & Avouac, 2000). Nonetheless, other factors such as base level fall, increase in precipitation and discharge, decrease in sediment load and spread of vegetation cover may all influence incision by enhancing rivers erosional capacity (Schumm, 1965). As incision rates are governed by a complex interaction between bedrock strength and stream power, the possibility of using it as a proxy to surface uplift is hindered by the difficulty in fully constraining the uplift history, the geological complexity and the climatic influences over space and time.

In order to analyse spatial variations of drainage network incision within a defined timeframe we used the remnants of the Pontian erosional surface (Maurer, 1968). Assuming that in the early stages of surface formation base-level topography did not express significant spatial variations along the highest sectors, we made an attempt to use its present day altitude to analyse the accumulated tectonic deformation since the Early Messinian (Fig. 2.2M). Furthermore, by using this geomorphic marker as a proxy for local base level during Early Messinian, we analyse the spatial variability in drainage network incision by comparing it with present day base-level topography (Fig. 2.2N).

We mapped the remnants of Pontian surface within a GIS environment following the work of Maurer (1968). The average altitude of each polygon was extracted from the DEM using cross and aggregate statistics. The final map was interpolated and data in-between points were extracted using a standard kriging method. By subtracting the base level map from the Pontian surface we were able to roughly estimate the spatial variability in drainage network incision and the tectonic deformation of the Pontian surface since the Early-Messinian.

Figure 2.2M represents the present-day altitude of the Pontian surface and magnitude of post-Messinian drainage network incision. Present-day altitude and incision values along the western,

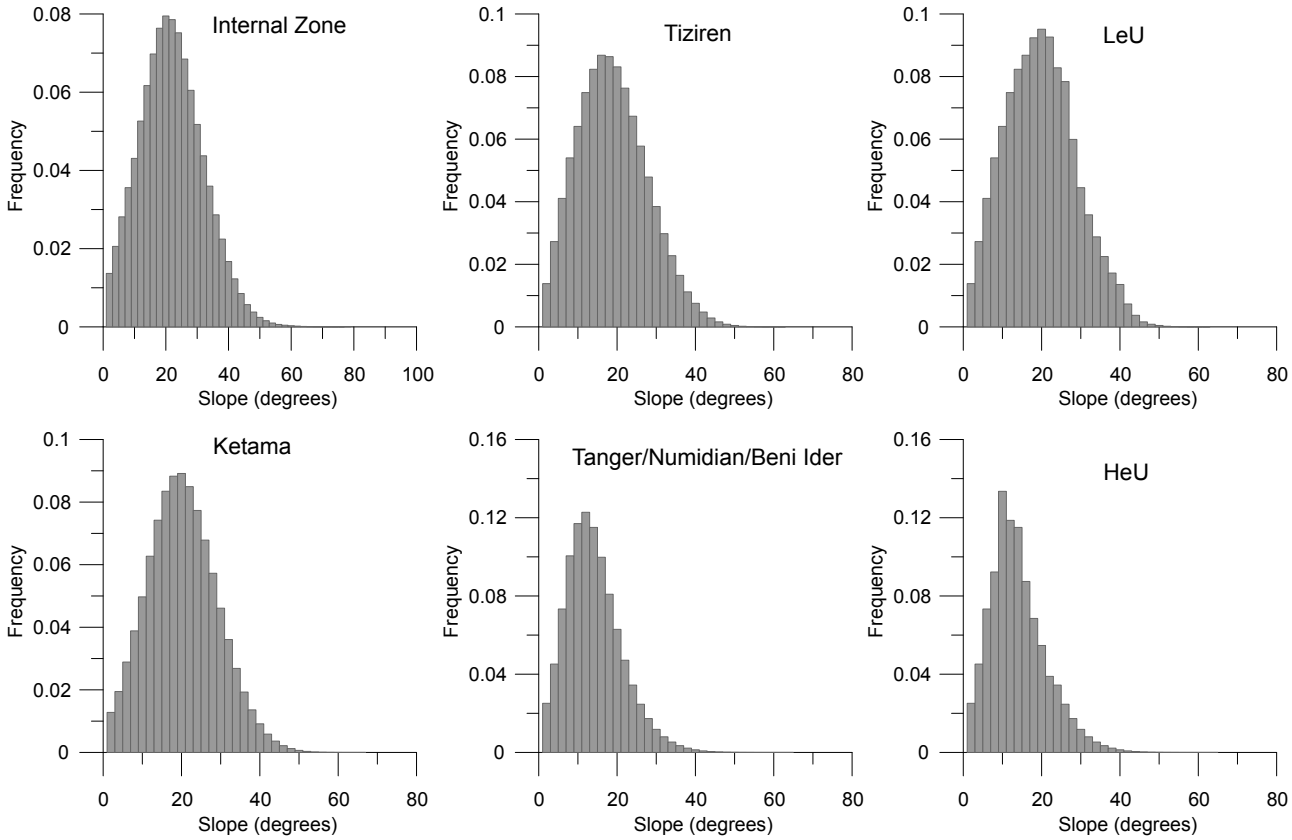


Figure 2.4 – Slope distribution.
Slope distribution for each structural unit of the Northern Rif and for high (HeU)and low (LeU) erodibility units according to Suter (1980a).

southern and eastern edge of the mountain range should be interpreted with caution as it reflects an interpolation adjustment to low-density data.

The present day altitude of the Pontian surface expresses a similar spatial trend as the summit level and mean elevation topography, with maximum altitudes (>1000m) extending from the east around the Jebel Hammane to the west and into Internal Domain. Similarly to the summit level, the present-day drainage divide east of Jebel Lakra is consistently captured by this method. To the west,

the connection between Jebel Rhesana and Sougna is nearly 100m lower than the saddle points connecting Jebel Sougna to the Dorsal Calcaire.

Differences between the Atlantic and Mediterranean coasts are also apparent. Along the southern flank, higher (750 to 1000m) pontian surface values are concentrated near the drainage divide extending further south towards the Jebel Rhesana and Jebel Outka domain. To the west, the altitude of the Pontian surface increases to 1000-1500m and extends into the upper sectors of the Ouerga valley along a WNW-ESE trend.

Along the Mediterranean flank the remnants of the Pontian surface are preserved at a higher altitude north of Jbel Tiziren and towards the edge of the Mediterranean coast. Additionally, a sharp E-W to NE-SW striking gradient is observed along the northern and north-western flanks of the Jebel Tidirhin domain, respectively. The extension of these topographic boundaries beyond any geological contact favours its association with NE-SW trending tectonic structures.

By comparing present base-level topography with the altitude of the Pontian erosional surface it is possible to analyse the spatial variability in drainage network incision (Fig. 2.2N). As expected, the lowest relief is observed along the highest sectors of the mountain belt. Intermediate relief areas (200-600m) delineate the majority of the northern Rif defining the incised regions associated with south flowing Ouerga tributaries and the deeply incised valleys of the Mediterranean flank. Strong NE-SW striking gradients tend to limit the high relief areas north of Jebel Tiziren and South of Jebel Tidirhin, were over 800m of drainage network incision has been produced since the Early-Messinian. Bedrock lithology seems to be unrelated to high values of incision, as it tends to concentrate within the hanging-wall of major thrust units (e.g. Internal and Tiziren domains). This fact re-enforces the notion that the nature and magnitude of endogenous and exogenous processes acting in landscape formation are fairly distinct between both flanks of the Rif and that tectonic processes play a crucial role in controlling landscape dissection.

2.4 Drainage network and drainage basin analysis

2.4.1 Drainage network orientation

The drainage network is among the fastest geomorphic systems to respond to tectonic processes. As fluvial systems tend to follow the path of least resistance while incising into bedrock, drainage orientation typically depicts the structural imposed on drainage network evolution. For this reason, drainage network orientation studies have proven to successfully capture the tectonic interference over different spatial and temporal scales (Jarvis, 1976; Pelletier et al., 2009).

In this study, the orientation of each drainage segment was extracted according to Strahler classification. Low order streams (1 & 2) were previously tunnelled to reduce segment sinuosity. In order to facilitate data interpretation we analyse drainage orientation for each morphostructural unit (see Fig. 2.1 for location). Additionally, with the objective of validating and analysing the nature of the previously identified topographic gradients, a 20km (10km on each side) wide sample zone was defined (see Figs. 2.2 and 2.6 for location), for which drainage orientation was extracted (Fig. 2.5).

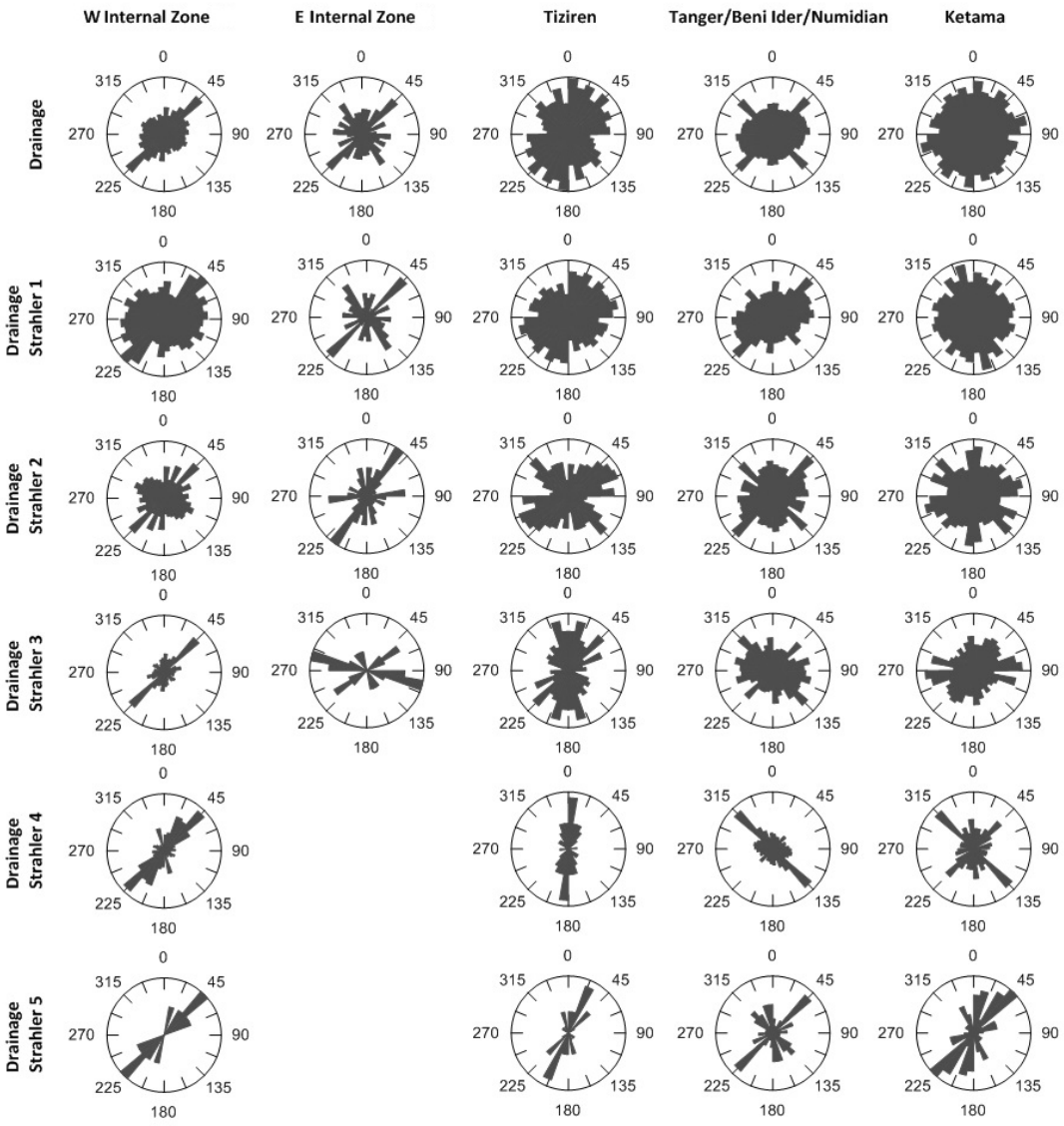


Figure 2.5 – Drainage network orientation.
Drainage network orientation (10°bin) for each structural unit of the Northern Rif, per Strahler order. The sector referring to the Internal Zone cropping out west of Al-hoceima (E Internal Zone) is separately analyzed.

Figure 2.5 presents the rose diagrams showing drainage network orientation within each morphostructural unit of the Rif and per Strahler order. The first observation regards the dominance of the N45°E±20° or/and N135°E±20° orientations in the majority of diagrams and independently of the structural unit. Only for 3rd, 4th and 5th order stream of the Tiziren and Ketama units did we obtain a N20°E±20° dominance.

Along the south-western and southern flanks, NW-SE and E-W drainage segments are related to bedrock strike of the Tanger-Numidian and Ketama Units, respectively. The tectonic control associated with these orientations is difficult to ascertain as it is masked by the control imposed by less competent geological units. As for the NE-SW orientation, although locally associated to downsl ope flow from NW-SE oriented ridges within the Tanger Unit, its persistency on high order streams along the Atlantic flank suggests fault-oriented bedrock incision.

On the Mediterranean side a similar pattern is observed in the Internal Zone and Tiziren Unit, with a clear dominance of the NE-SW orientation. It is particularly striking that within the Internal domain, while 5th and 4th order streams flow from SW to NE, dominant low order streams do not reveal a typical stream bifurcation pattern. This is particularly odd due to the deeply incised valleys that crosscut the compact limestone and metamorphic units of the Internal Zone.

Within the Tiziren unit, although high order streams follow a N-S to NNE-SSW pattern, low order streams display a similar arrangement as in the Internal Zone with NE-SW oriented segments dominating throughout the sample-set. Locally, the NE-SW orientation gains relevance along the upper sector of drainage basins 16 through 20 (Fig. 2.1), were low order streams strike obliquely to the main drainage divide.

As for the sampled areas along the previously identified topographic gradients, rose diagrams for drainage orientation (Fig. 2.6) show that the N-S anomalies (diagrams A and B) does not seem to have any repercussion on drainage network orientation. Although the dataset displays some dispersion, it clearly outlines a dominance of NNW-SSE and NNE-SSW trends.

Diagrams C, D and E in figure 2.6 present the drainage orientation along ENE-WSW sample zones. The N45±20° orientation seems to consistently replicate the existence of tectonic discontinuities affecting the topography of both flanks of the Northern Rif. These tectonic structures seem to form a conjugate set together with N90 to N135E±20°oriented structures.

2.4.2 Drainage basin analysis

In this section we focus our attention on 21 main drainage basins with headwaters along the main divide of the Northern Rif (Fig. 2.1). Each morphometric parameter was plotted against basin ID (Fig. 2.7), thereby representing a west to east variation of each index along the Atlantic and Mediterranean flanks. Table 2.1 summarizes the data for the 21 catchments of the Northern Rif.

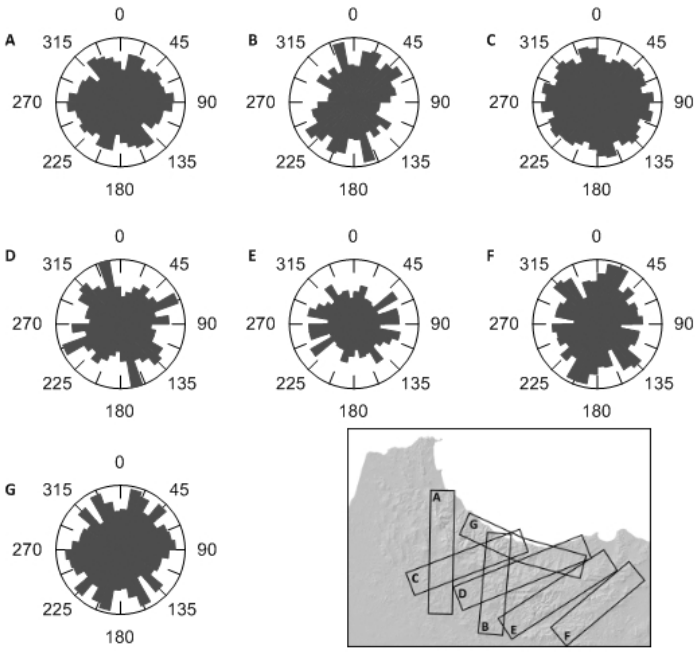


Figure 2.6 Rose diagrams for each sampled zone around topographic gradients.
Rose diagrams for drainage network orientation (10°bins) for each sampled zone around previously identified topographic gradients.

2.4.2.1 Basin shape

Empirical landscape evolution models have shown that drainage basin size and shape tend to vary over time, given similar substrate, climate, and rate of base level fall (Parker & Schumm, 1982; Ritter & Gardner, 1993; Densmore et al., 2005). Variation in bedrock uplift exert influence in drainage basin shape and consequently on basin hydrology.

We use the Shape factor (Sf) (Horton, 1932) to analyse the spatial variability in drainage basin geometry, namely its elongation. The shape factor can be seen as a simple width-to-length ratio where values close to 1 represent near-circular basins. Depending on the geometry of the elongation vector with respect to the main stem-river flow azimuth, values may range from close to zero to higher than 1. While the later values are uncommon in natural fluvial setting, Sf values close

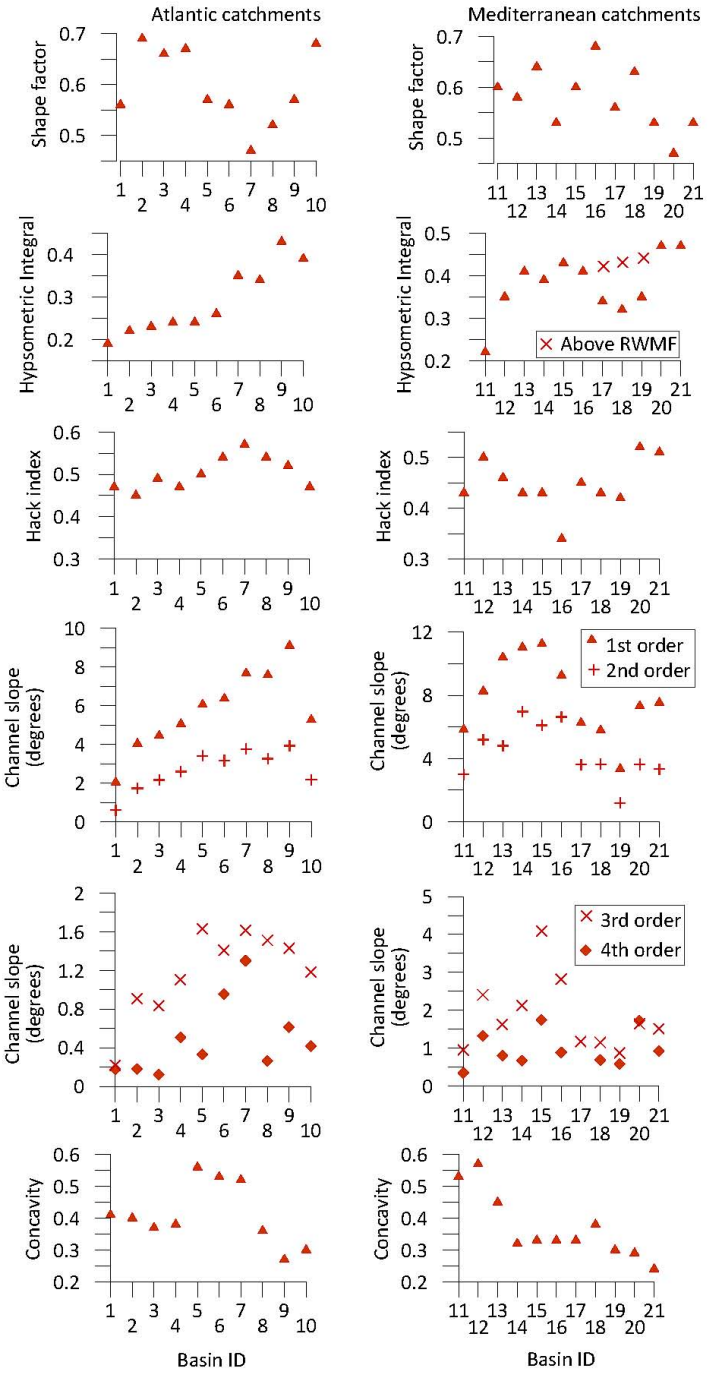


Figure 2.7 – Drainage basin morphometry.
Drainage basin morphometric parameters plotted against basin ID for both the Atlantic and Mediterranean flanks of the Rif. Note that basin ID reflects west to east variation in basin morphometry.

to zero have been associated with active mountainous setting were uplift outpaces the ability of the drainage basin to propagate laterally (Keller & Pinter, 1996).

For this study, basin width was extracted by averaging three equally spaced measurements perpendicularly to the main channel. For basin length we used the longest channel length from

outlet to divide. Figure 2.7 shows the spatial variation of Sf for both the Atlantic and Mediterranean flanks. Values reflecting highly elongated basins occur within the central Atlantic flank associated with catchments established within the Ketama Unit. Further to the west and east, values increase to 0.65-0.69. In contrast, although the data along the northern flank present significant fluctuations between basins, it illustrates an increase-decrease tendency with a maximum value of 0.68 on catchment 16. On average, Mediterranean basins are more elongated than its Atlantic counterparts.

2.4.2.2 Basin hypsometry

As described in section 4.3, hypsometric data is thought to reflect the maturity of the landscape, mirroring the spatial dominance of tectonic and erosional processes (Strahler, 1952). We quantified the hypsometry of the 21 catchments using the hypsometric integral (Hi), and results were plotted against basin ID (Fig. 2.7).

The Mediterranean basins show higher Hi values when compared to the Atlantic catchments. With the exception of basin 11 (Hi=0.22), central and eastern drainage basins located along the northern flank show Hi values higher than 0.32. Nevertheless, the overall eastward increase in Hi values that is detected along the southern flank of the Rif is not displayed along the Mediterranean flank due to the occurrence of low Hi values on catchments 17 (Hi=0.34), 18 (Hi=0.32) and 19 (Hi=0.35). However, the lower section of these catchments is developed within the low region of the Bokkoya massif, extending north and beyond the W-E trending RWM fault. This way, if we only consider the upper section of these catchments (above the RWMF, see Fig. 2.1 for location) Hi values increase to 0.40, 0.42 and 0.49, respectively (Fig. 2.7), expressing a similar tendency as the catchments along the southern flank with a consistent eastward increase of Hi values.

Considering Figure 2.7, the Atlantic basins can be subdivided into two populations with a marked transition between basins 6 and 7. Hypsometric integrals are constant west of basin 6, depicting a slight increase towards the east to a maximum value of 0.26. The eastern population has higher hypsometric integrals, reaching a maximum value of 0.43 on basin 9.

Table 2.1 - Topographic and basin-scale morphometry.
A – Catchment area; Br – Basin relief; H – Hack exponent; C – Concavity; HI – Hypsometric integral; ShF – Shape factor; E_avg – Mean elevation; S_Avg – Mean slope; P_Avg – Mean rain-fall; Lr_Avg – Mean local relief; Inc_Avg – Mean Pontian-Quaternary incision.

	ID	A (km2)	Br (m)	H	H R^2	ShF	C	C R^2	HI	E_Avg (m)	S_Avg (°)	P_Avg (mm)	Lr_Avg (m)	Inc Avg (m)
Atlantic catchments	1	336	396	0.47	0.96	0.56	0.41	0.72	0.19	316	19.81	833	493	461
	2	563	881	0.45	0.92	0.69	0.4	0.53	0.22	514	23.05	880	586	620
	3	567	778	0.49	0.95	0.66	0.37	0.55	0.23	745	24.33	951	867	435
	4	1353	607	0.47	0.96	0.67	0.38	0.53	0.24	831	27.04	955	942	338
	5	956	1986	0.5	0.94	0.57	0.56	0.73	0.24	1058	28.37	932	981	374
	6	829	1525	0.54	0.93	0.56	0.53	0.62	0.26	1056	27.4	887	939	366
	7	501	1890	0.57	0.95	0.47	0.52	0.45	0.35	1068	28.07	842	1035	371
	8	543	1996	0.54	0.96	0.52	0.36	0.35	0.34	1307	29.3	807	1167	389
	9	535	1314	0.52	0.96	0.57	0.27	0.31	0.43	1400	30.1	760	1122	438
	10	310	946	0.47	0.97	0.68	0.3	0.61	0.39	1278	24.89	623	933	337
Mediterranean catchments	11	1051	1639	0.43	0.98	0.60	0.53	0.64	0.22	851	30.02	903	1146	431
	12	936	1972	0.5	0.98	0.58	0.57	0.43	0.35	1040	33.94	837	1196	444
	13	588	1979	0.46	0.96	0.64	0.45	0.59	0.41	1013	34.29	811	1324	583
	14	285	1413	0.43	0.90	0.53	0.32	0.68	0.39	916	29.5	748	1231	503
	15	505	1893	0.43	0.97	0.60	0.33	0.56	0.43	998	28.59	698	1278	406
	16	251	1828	0.34	0.91	0.68	0.33	0.68	0.41	871	25.94	625	1058	593
	17	163	1569	0.45	0.87	0.56	0.33	0.63	0.34	812	24.34	599	938	487
	18	211	1434	0.43	0.95	0.63	0.38	0.70	0.32	677	26.06	426	900	402
	19	220	1186	0.42	0.91	0.53	0.3	0.51	0.35	528	25.91	388	821	395
	20	787	1742	0.52	0.96	0.47	0.29	0.51	0.47	1005	27.09	612	963	466
	21	771	1518	0.51	0.97	0.53	0.24	0.51	0.47	1011	29.68	537	1149	476

2.4.2.3 Hack exponent

Hack (1957) proposed a functional relationship between basin area (A) and divide-to-outlet length (L) of the main river channel,

$$\mathrm{L} \, \alpha \, A^{H}$$

where H is known as the Hack exponent. Several studies have shown that variations in the Hack exponent are associated to differences in basin elongation (Rigon et al., 1996). According to Stolar et al. (2007), when applied to individual drainage basins, Hack's law can be inverted so that it expresses the upstream area as a function of downstream distance.

$$\mathrm{A} \, \alpha \, \mathrm{x}^{1/H}$$

For this study we extracted the Hack exponent for the 21 basins by linear regression of the logarithms of contributing area and downstream distance. The correlation coefficients for all 21

basins exceed 0.87.

Figure 2.7 shows Hack values for each of the studied drainage basins of the Northern Rif. Hack values range from 0.34 to a maximum of 0.57. Along the Atlantic flank values are relatively similar up to basin 4, progressively increasing towards the east to a maximum of 0.57 on catchment 7. From that point on, values decrease to 0.47. In the Mediterranean flank Hack values display a parabolic tendency with a minimum value of 0.34 on basin 16, with higher values towards the west and east.

2.4.2.4 Channel slope

Low order streams bear evidence to the most recent phases of landscape evolution. Spatial variations in slope of low order streams have been successfully associated to non-uniform surface uplift, incision rates and precipitation (e.g. Stoler et al., 2007). Furthermore, within structurally controlled landscapes, anti-dip low order streams tend to present higher mean slope values.

Mean channel slope of 1st through 4th order Strahler streams was automatically extracted for each catchment and plotted from west to east according to drainage basin ID (Fig. 2.7).

Along the southern flank of the Northern Rif the mean slope of 1st and 2nd order streams increases from west to the east, reaching a maximum value on basin 9. Mean slope distribution is consistent with bedrock lithology as higher values occur within the Ketama Unit. As for 3rd and 4th order streams, although a similar distribution pattern is observed, maximum values occur on basins 5 and 7.

Along the northern flank of the Rif channel slope distribution allows the definition of two distinct populations. Maximum slope values are observed on the western basins 12 through 15. To the east mean channel slope values drop considerably in all considered Strahler orders.

2.5 River profile analysis

2.5.1 Profile concavity

Longitudinal river profiles show slope variations along their length. For graded streams, longitudinal profiles tend to be concave, with high gradients near the source and progressively less steep portions towards the mouth. The predictability of river profile evolution has led geomorphologists to describe mountain rivers through a power-law relationship between channel slope (S) and upstream contributing area (A);

$$S = K_s A^{-\theta}$$

where θ is the profile concavity and K_s is the steepness index (Whipple and Tucker, 1999; Van Laningham et al. 2006).

Variations in profile concavity are thought to express differential tectonic uplift and spatial variations in the climatic and hydrological setting (Whipple and Tucker, 1999; Zaprowski et al., 2005). While in the absence of variable rock uplift or precipitation concavity values range between 0.4 and 0.6 (Whipple and Tucker, 1999), regions affected by non-uniform patterns of rock uplift and precipitation express concavity values from 0.2 to 2.0 (Kirby and Whipple, 2001; Roe et al. 2002; Van Laningham et al. 2005). Furthermore, high θ values have been successfully linked to less competent geological units (Van Laningham et al. 2005).

Concavity indexes for the 21 river profiles were calculated in order to quantitatively compare longitudinal profile forms along the extension of the mountain belt. Concavity values were extracted through the calculation of the slope of the elevation-distance (log/log) profile for main channel streams through linear regression. We chose a 1km window length to filter any resulting noise from DEM filling. Nonetheless, the presence of prominent knickzones in some of the segments hampers the significance of the power-law relation. With the exception of basins 8, 9 and 12 the dataset presents correlation coefficients above 0.50.

Concavity values for the studied catchments range from 0.24 to 0.57 (Fig. 2.7 and Table 2.1). Nonetheless, considering best-fit values (R^2>0.6) for smooth profiles, concavity ranges from 0.3 to 0.56. Highest values occur in catchments 5, 6 and 11 in clear association to the less competent geological formations of the Tanger Unit.

2.5.2 Knickzones

The ability of a stream to transport sediments and to erode its bed is strongly dependent on the available stream power. Stream power expresses the rate of energy dissipation along channel bed and banks and depends on channel slope, channel width, discharge, density of water and acceleration due to gravity (Hack, 1973). Tectonic perturbations together with imposed bedrock limits to riverbed erosion have proven to exert strong influence on channel slope (Keller and Pinter, 1986). Base level changes due to fault rupture or due to sea level variations along the mouth of a river force fluvial systems to adapt to renewed, usually increased, channel slope conditions. While erosion takes place, channel-slope deformation tends to progress upstream. As bedrock strength

imposes limits the stream erosion, the upstream migration of high slope reaches can be temporarily frozen in time along highly competent rock bodies.

According to Hack (1973), the Stream length-gradient index (SL Index) correlates with stream power and is a practical tool for measuring channel slope perturbations along stream longitudinal profiles (Burbank and Anderson, 2001). Tectonic and bedrock related anomalies along channel slope have proven to be successfully identified through the use of the SL index (Merritts & Vincent, 1989; Keller & Pinter, 1996; Brookfield, 1998; Chen et al., 2003; Zovoili et al., 2004). The SL Index is defined as

$$\mathrm{SL} = \mathrm{L}(\Delta\mathrm{H}/\Delta\mathrm{L})$$

where L is the length of the stream from the point of interest, ΔH is the change in elevation of the reach and ΔL is the length of the reach (Hack 1973).

Due to the coarse resolution of the DEM, the ability to detect changes in channel slope are hindered by the presence of artifacts. With the objective of avoiding misinterpretation of false SL values, the drainage network was divided into 500m segments and all calculation was limited to high order (>4) Strahler streams. Furthermore, based on the detection of dam structures and bridges along channel profiles, we established a threshold value of 200m to differentiate between true and probable channel-slope anomalies. Although this method is fairly qualitative and excludes real profile irregularities below a certain scale, the threshold of 200m is sufficiently large to avoid most artifacts and to identify significant slope anomalies along individual channels.

To facilitate data interpretation SL values are plotted against channel profiles. The integration of tectonic and bedrock data within each plot allows the differentiation between tectonic and bedrock related knickpoints. Furthermore, the altitude of the Pontian surface and magnitude of Post-Tortonian drainage network incision is plotted against SL values (Fig. 2.8).

Figure 2.8 shows along-channel length variation in SL index for basins with knickzones above the defined threshold. Dam construction within catchments 3, 8 and 21 was successfully captured with this method. For the purpose of interpretation, as dam construction usually takes advantage of narrow valley sections associated with compact geological units, it is likely that along channel-slope variations existed at these locations prior to channel anthropization.

The majority of high SL index values occur in the transition between competent and less competent geological units. On average, mapped knick zones account for 10-12% of the available relief,

reaching maximum values along the eastern catchments of the Atlantic flank, where nearly 20% of the basins relief in captured along major knick zones.

Only catchment 9 exhibits a prominent knick zone with clear association to a mapped fault striking along the Ketama Unit. Nonetheless, as most geological transitions are associated with north and south verging detachment faults, the bedrock versus tectonic nature of fluvial knicks is difficult to ascertain.

By comparing the spatial distribution of SL values with the altitude of the Pontian surface and calculated Post-Tortonian incision, we can observe that knickzones are strongly associated with abrupt changes in both the altitude and incision of the Pontian surface. This is particularly relevant along the eastern and central catchments of both the Atlantic and Mediterranean flanks, respectively.

2.6 Pearson correlation statistics

In this section we use the Pearson linear correlation analysis to assess how drainage basin morphometric parameters correlate with 1^{st} order topographic and climatic variables. For each catchment the following topographic and basin-scale variables were extracted: i) mean elevation, mean and modal precipitation, mean and maximum local relief, mean slope, mean altitude of the Pontian surface, mean and maximum incision of the Pontian surface; ii) basin area, basin relief, shape factor, Hack exponent, hypsometric integral, concavity index and mean slope of 1^{st} through 4^{th} order streams.

The significance of each correlation was determined by Pearson probabilities with a 5% level of significance (Summerfield & Hulton, 1994; Hurtrez et al., 1999). Table 2.2 presents the Pearson correlation coefficients for the Northern Rif and for the Atlantic and Mediterranean flanks, respectively. Correlation coefficients with P<5% are highlighted in grey.

The first observation regarding the data presented in table 2.2 refers to the fact that morphometric variables characterizing basin geometry are correlated (i.e. basin shape, basin relief, Hack index) present medium to high correlation coefficients. This observation is most probably related to the scale dependency of the dimension of the investigated basin areas. This is particularly evident along the Mediterranean flank of the Rif were drainage basin size increases from east to west.

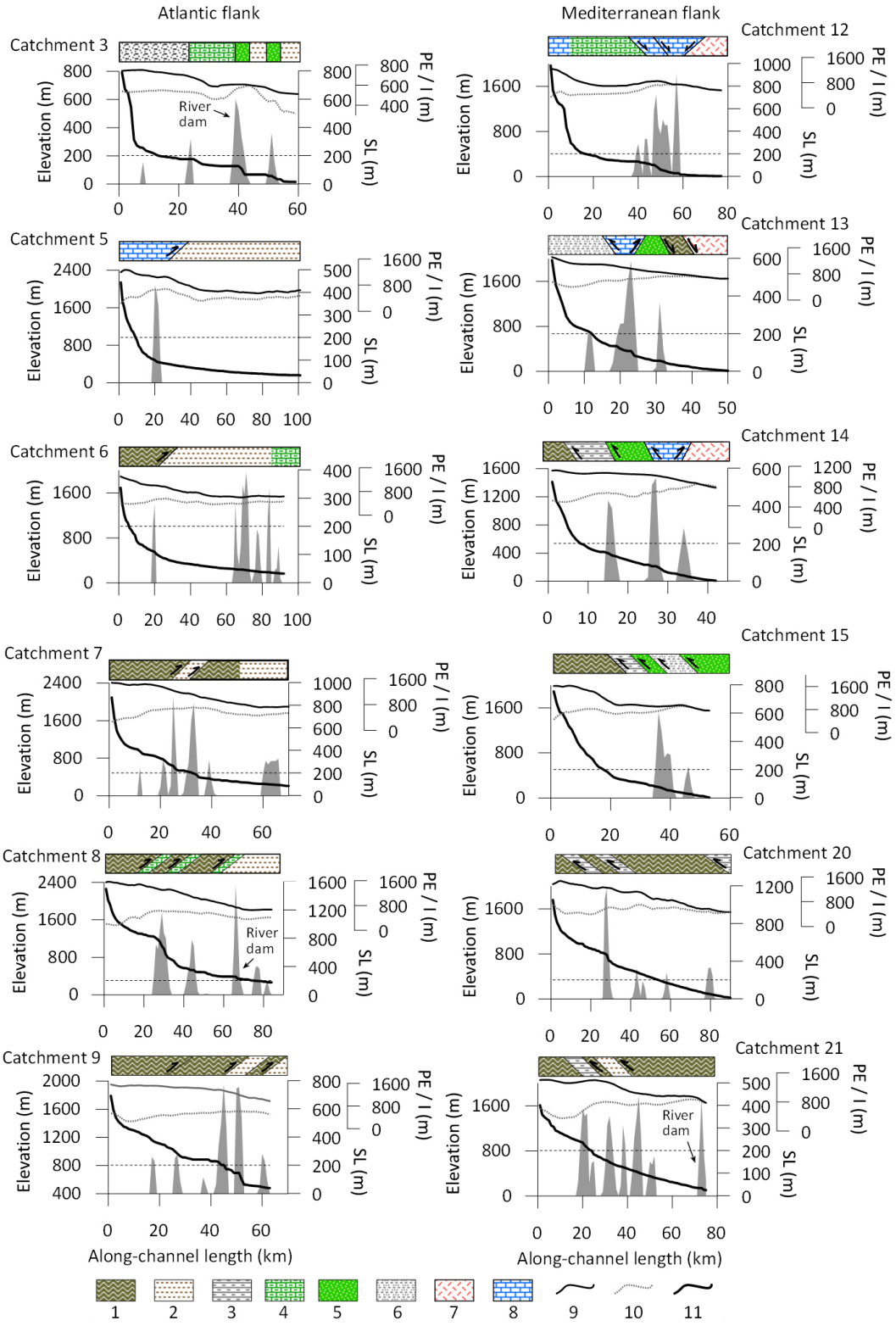


Figure 2.8 – Stream long profiles and knick point analysis.
Along-Channel profiles and stream-gradient index for selected catchments of the Northern Rif. Dashed line indicates selected SL-Index threshold (see text for explanation). Bedrock lithology and tectonic structures are plotted in the upper section of the graph: 1) Metamorphic carbonates (Ketama Unit); 2) Clay (Tanger Unit); 3) Marls and clay (Tanger Unit); 4) Marly-limestone (Tanger Unit); 5) Sandstone (Tiziren); 6) Sandstone and clay (Tiziren Unit); 7) Metamorphic complex (Internal Zone); 8) Compact limestone and dolomite (Dorsal Calcaire); 9) Altitude of the Pontian Surface; 10) Post-Pontian drainage incision; 11) River longitudinal profile.

Taking into account first order topographic variables, a strong correlation between elevation, precipitation, local relief and mean slope is observed for both the Northern Rif and its Atlantic and Mediterranean counterparts. For the Atlantic flank, modal precipitation is negatively correlated (r=-0.82) with mean elevation, expressing the eastward decrease in precipitation despite the increase in elevation towards the top of Jebel Tidirhin. The increase in mean slope angle and mean local relief along with mean elevation suggests a westward rejuvenation of topography in response to surface uplift. Furthermore, the presence of competent rock formations of the Ketama units towards the east effectively maintains hillslopes at higher angles of stability.

As for drainage basin and channel scale morphometric parameters, the most significant positive correlations are observed in basin relief, channel slope, basin hypsometry and concavity, in association to morphometric variables characterizing topographic relief and precipitation. The hypsometric integral is positively correlated to mean elevation, relief and mean slope. Only for the Atlantic flank we observe a negative correlation between Hi and precipitation, which is in accordance with an eastward increase in bedrock strength and decrease in precipitation. The lack of significance for the correlation between the hypsometric integral and precipitation along the Mediterranean flank is an indicator that other factors such as bedrock strength and tectonic processes control landscape maturity.

Only few morphometric parameters correlate to the incision of the Pontian surface, namely local relief, mean slope, basin relief and slope of 1^{st} order streams. Interestingly enough, these only seem to hold for the Mediterranean flank. Nonetheless, by eliminating Atlantic catchments 1 through 4 from the analysis, correlations are significantly improved. In this case I_Avg and I_Max are positively correlated to mean slope (r=0.90) and maximum local relief (r=0.84), respectively, indicating that the spatial variability in Post-Pontian drainage network incision is fully captured by Local relief.

The absence of a meaningfull correlation between I_Max and Lr indicates spatial anisotropy in dataset, resulting from increased incision within low relief sites. This is outlined along the central sector of the Mediterranean flank were the highest incision values are spatially offset from high relief sites, extending towards the east along the upper sectors of basins 17 and 18.

The strong positive correlation between the slope of 1^{st} order streams and I_max along the Mediterranean flank suggests an on-going adjustment to base-level lowering. If we assume that higher incision reflects prevailing surface uplift, the higher slope of 1^{st} order streams may indicate that tectonic uplift persisted at these sites throughout the Quaternary.

2.7 Discussion

The first aspect to notice while analysing the summit, Pontian and base-level topography, is the ability of each method to capture the present day position of the MDD. While the Post-Tortonian tectonic deformation is difficult to ascertain on local scale, both the summit and Pontian topography suggest that during the early stages of mountain building the MDD was positioned along the Internal domain, rather than further to the southwest along the top of the Numidian ridges. In fact, the position of the MDD is decoupled from the travel direction of predominant air masses that reach the barrier of the Rif, which would expectedly maintain its position along the highest north-eastern peaks of the mountain belt due to increased erosion along the windward flank. Furthermore, the MDD is currently positioned within the marly and sandstone domain of the Tanger and Numidian units, rather than along the compact limestone of the Internal Zone. Although both the summit-level and Pontian topography accumulate Post-Tortonian tectonic deformation, these observations suggest a dramatic shift in the position of the north-western portion of the MDD in response to the recent uplift of the Internal Domain and drainage network incision.

The presence of clastic sediments belonging to the Ghomarides within the Flysch and Intrarif units (Chalouan et. al., 2008) indicate that during the early stages of mountain building the MDD was positioned within the Internal Zone. The shift in the position of the MDD might have occurred within two specific timeframes: I) in response to the development of NW-SE oriented folds within the Flysch domain and accompanied by the reactivation of the southeast extension of the Jebah fault during Lower to Middle-Miocene; II) or as a consequence of Post-Pontian drainage network incision, in response to both sea level variation and surface uplift. While the first hypothesis suggests that the Post-Tortonian incision of the Internal Zone is related to antecedent SW-NE flowing river systems, the later implies a progressive growth of Mediterranean catchments towards the southwest after the Pontian erosional phase, accompanied by deep river incision into the compact limestone of the Dorsal Calcaire in response to uplift of the Internal Domain and collapse of the Alboran Sea.

Landscape evolution models for the Western Mediterranean reveal that during the MSC a strong re-incision of the drainage network took place along the coast of Morocco and Spain, eventually leading to the capture of Atlantic waters through regressive erosion within the Gibraltar area (Loget & Driessche, 2006). Nonetheless, according to Romagnya et al. (2014) vertical motions were low within the Internal Domain since 13Ma and AHe thermochronology could not detect any accelerated denudation during the MSC.

During the Pliocene re-flooding (Zanclean, between 5.33 and 3.8 Ma) of the Mediterranean the valleys of the Internal Zone functioned as rias (Wildi & Wernli, 1977; Rampnoux et al., 1979; Morel, 1987). Nonetheless, only in the Wadi Martil (Tetuan valley) do the evidences of the Pliocene marine transgression extend further inland and beyond the western edge of the Internal Domain (Fig. 2.1). Along the northern flank, the confirmed extension of Pliocene marine transgression is further positioned to the east and closer to the Mediterranean coast (Fig. 2.1), disappearing east of the Jebah fault and reappearing east of Al-Hoceima.

The inexistence of Pliocene sediments southwest of the Wadi Lao gorge reveals that most of the valley lowering postdates the Pliocene flooding of the Mediterranean and establishes circumstantial evidence to the recent nature of the incision. In fact, Wildi & Wernli (1977) suggest that the Wadi Lao valley was formed along NE-SW trending normal faults that lowered the valley floor by about 200 meters. Based on stratigraphic and geomorphological data the authors suggest that the Pliocene re-flooding of the Wadi Lao valley did not extend beyond the SW limit of the Internal Domain as it was constrained to a smaller paleo-drainage basin within the Dorsal Calcaire. Uplift data produced by Romagnya et al (2014) indicate that in the 5Ma to present-day interval the Pliocene basins were tilted towards the north-east by 0.2–0.3◦ and underwent differential uplifts at a rate between 0.03 and 0.1 mm/y. According to the authors late Messinian and early-Pliocene deposits are uplifted in a same order of magnitude, 580 and 570 m respectively.

The fact that the modelled Pontian topography locates the MDD along the Internal Domain indicates that the capture of the south-draining basin occurred most probably after the Zanclian reflooding and that nearly one third of the available relief was formed in response to Pliocene and Quaternary surface uplift. Once established within the marly and sandstone domain of the Tanger and Numidian units, the position of the MDD would have been effectively maintained due to sharp differences in bedrock lithology between the Tanger and Dorsal unit. Precipitation captured between Jebel Sougna and the Internal Domain would flow towards the Mediterranean, therefore increasing stream power and erodibility of valley floors.

The geospatial analysis of topography further reveals the existence of sharp topographic gradients that relate to previously identify tectonic structures (Olivier, 1981-82; Deffontaine et al., 1992; Khattacha et al. 2013). The fact that these anomalies are captured on both of the chosen length-scales (10x10 and 5x5km) supports the feasibility of the results. Along the W-E extension of the mountain belt a set of N-S to NNE-SSW faults are systematically shown on both the summit and base-level as well as in the Pontian topography. While the topographic signature of the Jebah fault

is barely identified, the southwest extension of the Nekor fault is clearly visible along the upper sectors of the Ouergha River.

Previous work (Deffontaine et al., 1992) suggests an association of N-S striking topographic gradients with Plio-Quaternary normal faults controlling the definition of tectonic compartments. The fact that our data captures the anomalies along different length-scales of landscape analysis indicates a probable tectonic nature. Nonetheless, since its southern extension is spatially coincident with the lithological boundaries of the Dorsal Calcaire and Ketama Unit with the marly domain of the Tanger Unit, the vertical step along the observed gradients mimics both fault reactivation and differences in erodibility of the bedrock units.

Additionally, the use of landscape smoothing techniques allowed the identification of a topographic anomaly consistent with the geomorphic expression of the RWMF striking along the northern flank of the Rif. The eastern edge of the RWMF crosses catchments 16, 17 and 18. Differences in along-channel hypsometric integral reflect the uplift of the southern compartment of the RWMF. The lack of along-channel slope variations for these catchments is most probably connected to the low angle geometry of the fault. The RWMF is intersected by a set of NE-SW to ENE-WSW oriented structures that clearly deform the Pontian topography. Magnitude of deformation seems to increase from NW to SE until the north-western edge of the Nekor fault.

The tectonic control over landscape dissection is further emphasised by the study of drainage network orientation. Drainage segments seem to be fairly organized along three major trends defining a conjugated set of N-S, N45°E±20° and N130°E±20° structures. The fact that these orientations are systematically captured independently of stream order supports the existence of a tectonic pre-design in drainage orientation extending through the Plio-Quaternary. Furthermore, these azimuths are consistent with previously identified tectonic trends in the northern Rif (Ait Brahim et al., 2002).

The spatial distribution of local relief and mean slope angle are strongly dependent on bedrock lithology, with competent structural units of the Internal Zone and Ketama effectively maintaining higher relief and mean slope values. Nonetheless, the distribution of Post-Pontian relief derived from drainage network incision seems to be fairly concentrated along the same areas of the north-western and south-eastern sector of the Mediterranean and Atlantic flanks, respectively. These observations indicate probable rejuvenating of the available relief through tectonic uplift, being mostly concentrated between the Jebah, the RWMF and the Nekor faults along a NW-SE trend. These observations are further validated by high hypsometric integrals and presence of prominent

tectonically controlled knick zones along the central and eastern catchments of both the Mediterranean and Atlantic flanks.

Base level variations throughout the Neogene played a crucial role in the upstream propagation of knick zones. Competent rock bodies along the northern and southern flank of the Rif seem to have blocked knick migration by imposing limits to bedrock incision. However, the consistency between high SL values and the deformation of the Pontian surface indicates the prevailing action of tectonic processes through effective surface uplift and fault reactivation along the frontal part (SRF) of the Northern Rif. This notion if further emphasised through the spatial coincidence of both the SL index and magnitude of Post-Tortonian drainage network incision.

The marked transition in Hi values along the catchments of the Atlantic flank is a first order signature of bedrock control in basin morphometry. While the western population is established within the Tanger Unit (marls, clays and marly-limestone) the eastern population develops within the metamorphic-carbonate setting of the Ketama unit. Nonetheless, the higher incision and higher present day position of the Pontian surface indicates that differential uplift over intermediate time scales (≈5m.y.) contributed to the higher elevation of the upper portions of the eastern Atlantic flank, thereby affecting terrain hypsometry. Moreover, it is striking that within the Mediterranean domain the highest Hi values occur within the sandstone and marly-limestone context of the Tiziren unit, especially if we take into account that to the west lays the compact bedrock domain of the Internal Zone.

Over the Pliocene and Quaternary, deformation was concentrated along N45°E and N-S trending structures in clear association to the context of the Trans-Alboran shear zone. Normal faulting is particularly relevant along NE-SW structures of the Internal Zone in association with the collapse of the Alboran Sea and along N-S trending faults that bound the Al-Hoceima region. While fault activity in the RWMF during the Plio-Quaternary is uncertain, fault geometry and present-day stress field data indicates probable strain accumulation along its southern extension where it strikes approximately W-E.

The combination of geological and geomorphological data suggests the existence of two tectonic domains separated by the Jebah fault, portraying distinct kinematical behaviours throughout the Plio-Quaternary. To the north-west, landscape evolution was controlled by uplift along the frontal part of the Internal Domain and normal faulting along NW-SE structures in association to the collapse of the Alboran Sea. To the east, we argue that during the earliest stages of Post-Tortonian landscape evolution, deformation was mostly concentrated along N135°E oriented structures, with

the RWMF and SRF (Fig.II for location) assuming regional importance as conjugated thrusts to the NE-SW oriented Jebah and Nekor strike slip faults. The fact that the Pliocene sediments are absent east of the Jebah fault supports these observations as it indicates probable higher base-level altitude during sea level rise for the sector between the Jebah fault and Al-Hoceima. At the beginning of the Pliocene re-flooding, the sector east of the Jebah fault had already emerged or was not affected by extension in response to the collapse of the Alboran Sea. The presence of contrasting tectonic settings west and east of the Jebah fault further explains the preservation of higher relief condition within the Internal Domain where active tectonic subsidence and compact bedrock units occurs.

Therefore, the combination of geomorphic evidences indicate a concentration of surface uplift and tectonically induced drainage network incision along the Internal Domain and southern sector of the Ketama Unit, defining two distinct zones of deformation. To the east, the position of major knick zones and spatial variations in basin-scale morphometric data reveals a broad NE-SW trending deformation zone between the Jebah, the RWMF and Nekor fault (Fig.2.9) that is consistent with present transpression models for the Western Mediterranean (Morel & Meghraoui, 1996; Meghraoui & Pondrelli, 2012), with surface uplift being fairly concentrated at the intersection of NE-SW and NW-SE trending faults with regional detachment faults. Northwest of the Jebah fault, tectonic deformation is associated to normal faulting in response to the on-going collapse of the Alboran Sea, as suggested by Romagnya et al. (2014). Furthermore, these observations are in accordance with GPS surveys, which suggest the existence of two distinct kinematic patterns of deformation for the northern Rif (Fadil et al. 2006; Tahayt et al., 2008) (Fig. 1.4).

2.8 Conclusion

The present day topography of the Rif belt bears evidence to the Post-Tortonian interaction between tectonic and climate induced surface processes. In this work the topographic signature of both tectonics and bedrock control is effectively captured over different length-scales of landscape analysis. Nonetheless, the superimposition of factors controlling landscape evolution and spatial variations in bedrock lithology hinders data interpretation for particular sectors of the mountain belt. For these sites only field data could contribute to draw further conclusion. This is particularly notorious along the south-western extension of the Northern Rif, where geomorphic evidences are masked by less competent geological formations of the Tanger Unit and by intense erosion along the windward flank of the Rif.

Table 2.2 - Pearson correlation matrix for basin-scale morphometric parameters.

Pearson correlation matrix for 3 regional sub-sets (Northern Rif, Atlantic flank and Mediterranean flank). Correlation coefficients with P<5% are highlighted in grey. A – Catchment area; Br – Basin relief; E_Avg – Mean elevation; P_Avg – Mean rain-fall; P_Mo – Modal rain-fall; R_Avg – Mean relief; R_Max – Maximum relief; S_Avg – Mean slope; Pont_E – Mean elevation of the Pontian Surface; Inc_Avg – Mean Pontian-Quaternary incision; Inc_Max – Maximum Pontian-Quaternary incision; ShF – Shape factor; H – Hack exponent; HI – Hypsometric integral; C – Concavity; S_ord1 – Mean slope of 1st order streams; S_ord2 – Mean slope of 2st order streams; S_ord3 – Mean slope of 3st order streams; S_ord4 – Mean slope of 4st order streams.

	Variables	A	Br	E_Avg	P_Avg	P_Mo	R_Avg	R_Max	S_Avg	Pont_E	I_Avg	I_Max	ShF	H	HI	C	S_ord1	S_ord2	S_ord3	S_ord4
Northern Rif	A	1.00	0.06	0.21	0.61	0.53	0.19	0.45	0.40	-0.17	-0.28	0.24	0.03	0.37	-0.28	0.46	-0.03	-0.09	-0.02	0.06
	Br		1.00	0.55	-0.10	-0.39	0.74	0.76	0.70	0.48	0.08	0.49	-0.38	0.12	0.49	0.29	0.69	0.65	0.63	0.56
	E_Avg			1.00	0.11	-0.07	0.69	0.70	0.62	0.85	-0.31	0.11	-0.20	0.47	0.53	-0.02	0.61	0.42	0.39	0.29
	P_Avg				1.00	0.90	-0.01	0.20	0.12	-0.22	-0.05	0.25	0.18	0.36	-0.59	0.62	-0.04	-0.07	-0.10	-0.29
	P_Mo					1.00	-0.34	-0.13	-0.17	-0.35	-0.21	-0.05	0.20	0.41	-0.76	0.55	-0.41	-0.45	-0.41	-0.53
	R_Avg						1.00	0.90	0.88	0.58	-0.01	0.47	-0.17	0.04	0.61	0.02	0.88	0.77	0.67	0.47
	R_Max							1.00	0.89	0.42	-0.08	0.52	-0.20	0.22	0.42	0.26	0.72	0.63	0.54	0.47
	S_Avg								1.00	0.41	0.01	0.59	-0.19	0.21	0.45	0.27	0.71	0.58	0.46	0.41
	Pont_E									1.00	-0.11	0.11	-0.18	0.27	0.76	-0.32	0.66	0.47	0.54	0.43
	I_Avg										1.00	0.65	0.25	-0.46	0.16	-0.16	0.24	0.30	0.11	-0.02
	I_Max											1.00	0.06	-0.02	0.26	0.23	0.56	0.49	0.45	0.38
	ShF												1.00	-0.54	-0.31	0.00	-0.15	-0.05	-0.02	-0.41
	H													1.00	-0.01	0.25	-0.05	-0.27	-0.22	0.12
	HI														1.00	-0.57	0.70	0.57	0.57	0.66
	C															1.00	-0.09	-0.02	-0.05	-0.03
	S_ord1																1.00	0.92	0.81	0.59
	S_ord2																	1.00	0.84	0.56
	S_ord3																		1.00	0.71
	S_ord4																			1.00
	Variables	A	Br	E_Avg	P_Avg	P_Mo	R_Avg	R_Max	S_Avg	Pont_E	I_Avg	I_Max	ShF	H	HI	C	S_ord1	S_ord2	S_ord3	S_ord4
Atlantic flank	A	1.00	0.05	0.00	0.67	0.45	0.22	0.38	0.36	-0.34	-0.32	0.11	0.17	-0.05	-0.34	0.34	0.07	0.28	0.28	0.11
	Br		1.00	0.67	-0.03	-0.37	0.71	0.73	0.77	0.56	-0.32	0.18	-0.68	0.79	0.41	0.47	0.75	0.81	0.88	0.46
	E_Avg			1.00	-0.48	-0.82	0.93	0.83	0.86	0.91	-0.57	-0.25	-0.30	0.58	0.86	-0.19	0.89	0.83	0.83	0.40
	P_Avg				1.00	0.88	-0.17	0.05	-0.02	-0.77	0.15	0.43	0.03	-0.02	-0.74	0.54	-0.23	-0.01	-0.07	-0.08
	P_Mo					1.00	-0.58	-0.39	-0.48	-0.97	0.30	0.32	0.17	-0.32	-0.94	0.46	-0.64	-0.46	-0.49	-0.27
	R_Avg						1.00	0.97	0.95	0.71	-0.63	-0.16	-0.40	0.69	0.72	-0.07	0.91	0.90	0.86	0.43
	R_Max							1.00	0.96	0.55	-0.58	-0.02	-0.39	0.69	0.56	0.07	0.87	0.92	0.88	0.43
	S_Avg								1.00	0.64	-0.48	0.07	-0.42	0.68	0.63	0.07	0.94	0.97	0.93	0.49
	Pont_E									1.00	-0.39	-0.27	-0.30	0.48	0.95	-0.29	0.77	0.64	0.67	0.40
	I_Avg										1.00	0.72	0.29	-0.43	-0.34	-0.15	-0.36	-0.44	-0.46	-0.43
	I_Max											1.00	-0.05	0.08	-0.25	0.19	0.09	0.09	0.08	0.00
	ShF												1.00	-0.86	-0.27	-0.45	-0.50	-0.50	-0.42	-0.57
	H													1.00	0.47	0.37	0.76	0.76	0.68	0.74
	HI														1.00	-0.46	0.79	0.63	0.58	0.41
	C															1.00	-0.05	0.19	0.28	0.42
	S_ord1																1.00	0.95	0.87	0.57
	S_ord2																	1.00	0.94	0.62
	S_ord3																		1.00	0.57
	S_ord4																			1.00
	Variables	A	Br	E_Avg	P_Avg	P_Mo	R_Avg	R_Max	S_Avg	Pont_E	I_Avg	I_Max	ShF	H	HI	C	S_ord1	S_ord2	S_ord3	S_ord4
Mediterranean flank	A	1.00	0.46	0.60	0.63	0.74	0.44	0.79	0.65	0.05	-0.12	0.49	-0.18	0.58	-0.08	0.52	0.05	-0.11	0.00	0.21
	Br		1.00	0.78	0.66	0.40	0.65	0.81	0.57	0.50	0.43	0.87	0.42	0.13	0.23	0.48	0.63	0.54	0.59	0.55
	E_Avg			1.00	0.65	0.40	0.78	0.82	0.63	0.73	0.40	0.82	-0.04	0.48	0.49	0.18	0.74	0.57	0.52	0.58
	P_Avg				1.00	0.90	0.78	0.92	0.72	0.10	0.30	0.71	0.21	0.10	-0.24	0.70	0.53	0.46	0.28	0.05
	P_Mo					1.00	0.61	0.81	0.71	-0.21	0.06	0.50	0.14	0.14	-0.49	0.79	0.19	0.11	-0.03	-0.24
	R_Avg						1.00	0.78	0.79	0.56	0.37	0.82	0.26	0.12	0.20	0.35	0.84	0.64	0.56	0.18
	R_Max							1.00	0.80	0.28	0.23	0.83	0.13	0.38	-0.03	0.67	0.52	0.38	0.34	0.31
	S_Avg								1.00	0.20	0.21	0.82	0.13	0.40	0.03	0.63	0.46	0.26	0.17	0.04
	Pont_E									1.00	0.36	0.52	0.01	0.18	0.83	-0.41	0.77	0.60	0.73	0.65
	I_Avg										1.00	0.54	0.38	-0.25	0.35	-0.04	0.51	0.51	0.14	-0.09
	I_Max											1.00	0.26	0.30	0.32	0.44	0.68	0.47	0.42	0.35
	ShF												1.00	-0.67	-0.30	0.41	0.26	0.38	0.28	-0.27
	H													1.00	0.30	0.04	-0.06	-0.30	-0.22	0.41
	HI														1.00	-0.64	0.48	0.31	0.45	0.65
	C															1.00	0.02	0.07	-0.04	-0.18
	S_ord1																1.00	0.91	0.77	0.41
	S_ord2																	1.00	0.78	0.31
	S_ord3																		1.00	0.66
	S_ord4																			1.00

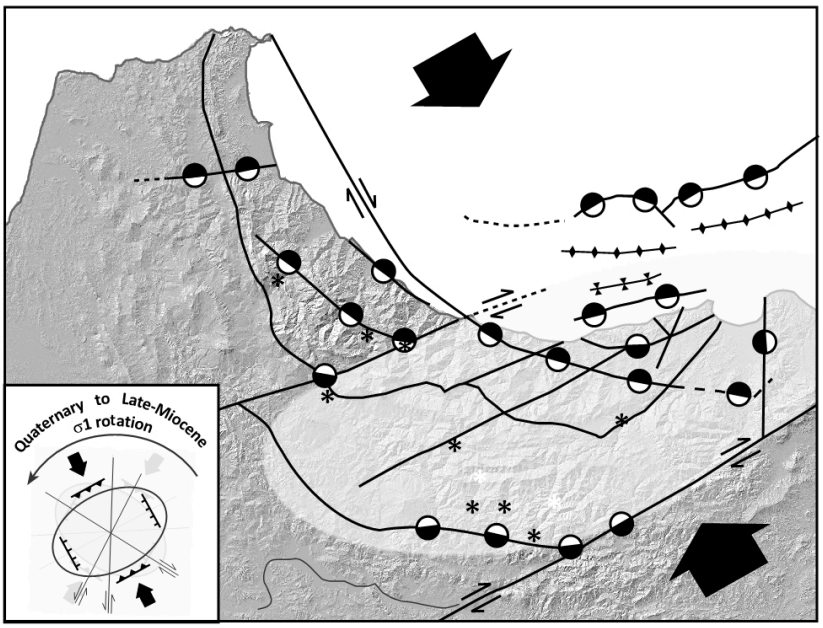


Figure 2.9 – Synthesis of geomorphic evidences of active tectonics.
Geomorphic evidences of active tectonics in the transpressional setting of the Northern Rif and Alboran Sea. Active tectonic structures with half circles indicating vertical tectonic component: White – uplift; Black – subsidence. Asterisks indicate the location of major knick zones. White ellipse outlines the region where the geomorphic evidences of tectonic uplift relate to the transpressional setting of the Northern Rif and (see text for explanation). Inset shows Late---Miocene to Quaternary rotation in σ1.

Post-Tortonian surface uplift of the Rif occurred in response to the ongoing convergence between the African and Eurasian plates. Uplift and sea level fluctuations played a strong influence in the way drainage systems evolved through bedrock incision and regressive erosion, with bedrock lithology favouring river dissection along less resistant strata.

The topography of the Rif was affected by significant changes in relief production due to spatial variation in bedrock uplift and base-level change. Our data indicate a dramatic shift in the position of the MDD during the Plio-Quaternary in response to uplift of the Internal Domain and collapse of the Alboran Sea. Although landscape evolution models indicate that during the Messinian Salinity Crisis the continental margins of the Western Mediterranean suffered significant erosion through drainage network incision, our data suggests that the major phase of relief production along the northern sector of the Rif Mountains results from surface uplift during the Pliocene and Quaternary. The combination of geomorphic and geological evidence indicates a concentration of surface uplift and tectonically induced drainage network incision along the Internal Domain and southern sector

of the Ketama Unit, defining two zones of distinct deformation. In the central and eastern sectors of the Northern Rif deformation is limited by the Jebah and Nekor faults, respectively, forming a broad NE-SW zone affected by transpressive deformation. To the northwest the action of normal faults in response to the collapse of the Alboran Sea and thrusting in the frontal part of the Internal Zone prevails. Our data is in accordance with tectonic models for the Alboran region (Meghraoui & Pondrelli, 1996 & 2012; Ait Brahim et al., 2002; Fadil et al. 2006).

3 Distribution of large bedrock landslides

Submited articles:

Fonseca, A.F., Zêzere, J.L., Madeira, J., Bouchta, EF. (accepted). Landslide inventory of the Northern Rif Mountains: a regional overview of large gravitational processes. Journal of Maps.

Fonseca, A.F., Zêzere, J.L., Madeira, J., Bouchta, EF. (accepted). Distribution of large bedrock failures in the Northern Rif Mountains. Geomorphology.

Abstract

Landslide inventories are crucial tools in the study of short to long-term landscape evolution and to the analysis of landslide hazard and risk. The ability to produce complete landslide inventories depends on the availability of cartographic data, satellite imagery, aerial photos and the possibility to perform field surveys. The recent emergence of free satellite image archives such as Google-Earth (TM Google) and Bing (TM Microsoft) and the ability to use the datasets within specific GIS tools has revolutionized the way earth scientist look at the globe by allowing a straightforward interpretation of landscape geomorphology and geology. In this paper, a landslide inventory for the northern sector of the Rif Mountains (north of the Ouergha river) is presented, obtained from published data and from the analysis of aerial photos at the scale of 1:40,000 and satellite images from the Google-earth (TM Google) and Bing (TM Microsoft) archive. While the complete landslide inventory is composed of over 10.000 landslides, covering more than six orders of magnitude ($3x10^{-5}$ to $9,4 \times 10^{6}$ km^2), in this paper we focus our attention on the spatial distribution of large gravitational processes with a platform area over 0.01km^2.

The specific location where large (>1km^2) bedrock failures tend to occur expresses particular topographic, structural and hydrogeological features, past climate conditions and specific time-dependent, short-term, triggering events (i.e. earthquake, rainfall, snow-melt). The presence of landslide cluster with similar size-magnitude or typology is a strong indicator of the presence of specific terrain conditions capable of accommodating large slope deformation events. In this section we take advantage of the complete landslide inventory to I) analyse the spatial distribution of large bedrock failures, II) study how large landslide clusters relate to the structural (tectonics and bedrock) and topographic architecture and climatic setting of the mountain belt, and III) discuss the geomorphic implications of large bedrock landslides. In the northern Rif mountains landslide distribution is primarily controlled by bedrock lithology, with high plasticity geological units within the Tanger and Chaumat-Mellousa units congregating nearly 75% of the of the landslide cases. Nonetheless, the critical location of very large (>1km^2) landslides, occurring in close association to high local relief sites and in the vicinity of active tectonic structures along the thrust fronts of the Rif, provides evidence to the topographic site effect for landslide triggering through amplification of seismic acceleration along the thrust fronts of the Rif.

Keywords: bedrock landslides; magnitude-frequency distribution; topography; tectonic and bedrock control; Rif Mountains; Morocco

3.1. Introduction

The present section studies the landslide size and distribution of 3610 bedrock landslides (La> 0.01km^2) in the Central Rif Mountains. Our objectives are I) to analyse how large landslide clusters relate to the structural (tectonics and bedrock) and topographic architecture and climatic setting of the mountain belt, II) and to discuss the geomorphic implications of large landslides situated along the tail end of the frequency-size distribution.

3.2. Methods and dataset properties

3.1.1 Structural data: lithology and tectonic

To examine the role of the geological structure in landslide distribution, lithological and bedrock dip data was extracted from Suter (1980a) and complemented through the analysis of 1:50.000 geological maps, aerial photos and satellite images of the Rif. To facilitate data handling and analysis we divided the Rif belt into 6 units based on its structural and morphological setting (inset on Fig. 1): 1) Internal Zone; 2) Tiziren Unit; 3) Ketama Unit; 4) Tanger Unit (comprising the Tanger, Beni Ider and Numidian nappe); 5) External zone west (west of Ouergha river); 6) External zone east (east to the Ouergha river) (Fig. 3.1).

Less competent-high plasticity geological units with thick marly, clay and pelitic intercalations were separately mapped (Fig. 3.1). These are present within the Tanger, Beni Ider, Chouamat-Melloussa and External Zones, as well as within the Triassic diapiric complex. A stretch of the Chouamat-Melloussa pelites and schists is present along the thrust zone opposing the Tiziren and the Ketama units, establishing connection with the south-western extension of the Riss valley (Fig. 3.1). Laboratory data on the plasticity and liquidity limits for some of these materials (Mariotti & Milliès-Lacroix, 1963) reveals a high variability in the mechanical properties of the Tanger Unit, showing medium to high plasticity characteristics.

Tectonic data was compiled from different sources (Suter 1980a, 1980b; Chalouan et al. 1997; Deffontaine et al., 1992 & Ait Brahim & Sossey, 2003) distinguishing between detachment and neotectonic faults according to Morel (1992**)**, Faure-Muret & Morel (1992), Morel & Meghraoui (1996) and Meghraoui & Pondrelli (2012). Fault mapping was limited to deep-seated structures crossing multiple geological units. The majority of these faults are formed by several parallel structures forming a fault zone with geometrical consistency. Furthermore, visual inspection of aerial photographs, satellite images and published data (Morel, 1992; Ait Brahim & Sossey, 2003; Mansour & Ait Brahim, 2005; Benmakhlouf et al. 2012) allowed the identification of secondary

structures affecting the hanging-wall of the compact units of the Internal, Tiziren and Numidian formations, as well as conjugated systems to the Jebah and Nekor strike-slip faults (Fig. 3.1).

Specifically, to analyze the spatial correlation between landslides and fault distribution, the distance

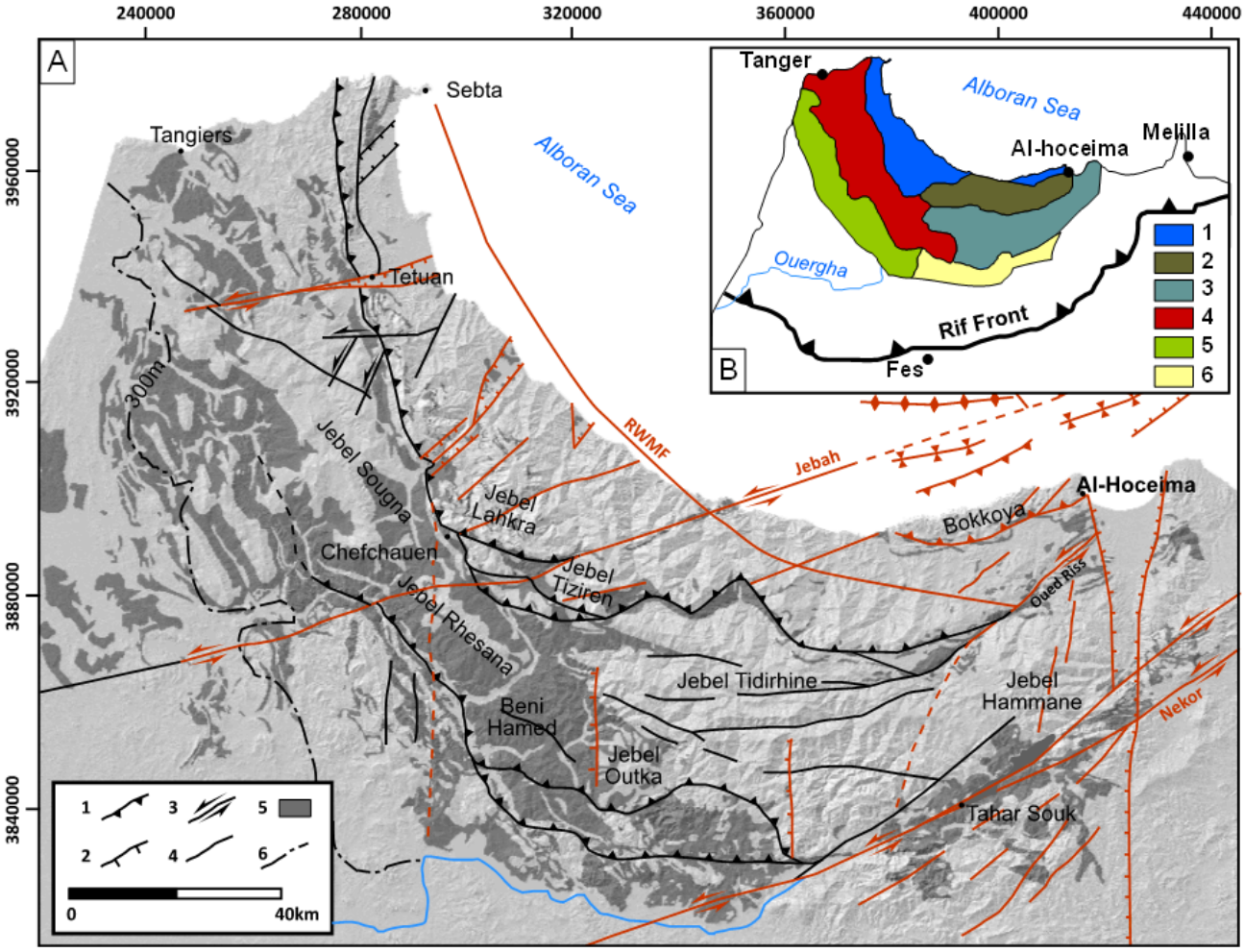


Figure 3.1 Detachment and neotectonic faults.
Tectonic structures following the work of Morel (1992) and Faure-Muret & Morel (1992): 1) Detachment fault; 2) normal fault; 3) strike-slip fault; 4) fault (unknown component). Red faults represent neotectonic faults; 5) marly-pelitic units. Inset shows the limit to the morphostructural units used in this study: 1 – Internal Zone; 2 – Tiziren; 3 – Ketama; 4 – Tanger; 5 – Eastearn External zone; 6 – Western External Zone.

from each landslide to both detachment and neotectonic faults was calculated. While distance calculations to neotectonic faults were performed in a straightforward manner by computing the shortest distance to fault using GIS tools, the distance to detachment faults was calculated for the section comprising the hanging wall (Fig. 3.2). This way, landslides positioned close to a detachment fault but within the footwall block will show higher fault distance values. We use this method so that we can limit the analysis of landslide distance to fault based on the knowledge that I) most of

the topographic relief is accommodated along the front of the hanging wall; II) widespread bedrock shattering has been reported from the epicentral areas of many large earthquakes associated with thrusting, particularly in topographic slopes located on the hanging wall (Brune, 2001); III) unexpectedly large peak vertical accelerations have been recorded at ridge crests during several earthquakes (Spudich et al., 1996).

Moreover, using the seismic acceleration map produced by Benchekroun et al. (2013), we computed the total number of landslides per seismic acceleration class ranging from 0.02 to 0.33g (1 g = 9.81 m/s^2), with a 0,02g equidistance. We calculated the total number of landslides taking into account the complete landslide inventory as well as for two landslide datasets: landslides >0.5km^2 and landslides > 1km^2.

3.1.2 Topographic data

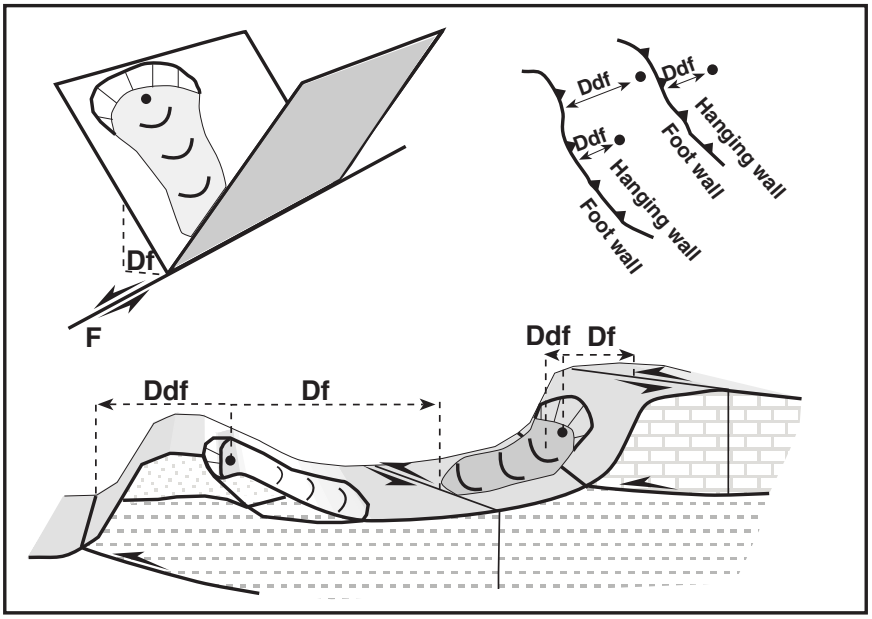


Figure 3.2 – Criteria for landslide-to-fault distance calculation.
Df – distance to neotectonic fault; Ddf – distance to detachment fault.

To quantify the first order characteristics of the present topography of the Rif, we use eight tiles of the ASTER GDEM2 covering northern-central Morocco and the Strait of Gibraltar. The ASTER GDEM2 is a product of METI and NASA and is available on a 1 arc-second (approximately 30m at the equator) grid and referenced to the 1984 World Geodetic System (WGS84)/1996 Earth Gravitational Model (EGM96) geoid.

Local relief, defined by the difference in height in a region between the peaks of highest elevation and the valley bottoms, is a parameter describing the maximum dissection of a landscape. While expressing the competition between tectonic and climate-driven geomorphic processes, local relief has been widely used to describe mountain topography (Ahnert, 1970; Burbank, 1992; Roe et al. 2003) and to study large bedrock failures (Korup et al., 2010). We extracted local relief (Lr) by subtracting the base-level altitude from the summit elevation within a moving window of 10km following the method described in section 2. Furthermore, we use the elevation-relief ratio parameter calculated over a 10x10 grid to analyse the role of large landslides in moderating landscape maturity.

Slope frequency distribution for stable and unstable areas for each morphostructural unit of the Rif were also obtained. We excluded the fluvial plains and low gradient intra-mountain basins from the analysis given that large bedrock failures are not expected to occur at these sites.

3.1.3 Climatic data

Precipitation data was collected for the mountainous area of the Rif in order to understand how landslide distribution correlates with mean annual rainfall. Precipitation data was acquired online through the WorldClim-Global Climate Database (see point 2.2 for data description). Even though the WorldClim data underestimates precipitation values when compared to gauge station data, the dataset expresses the overall control of topography in the distribution of precipitation, thereby fitting present objectives.

3.1.4 Landslide inventory

Landslide inventories are crucial tools in the study of short to long-term landscape evolution and to the analysis of landslide hazard and risk. The ability to produce complete landslide inventories depends on the availability of cartographic data, satellite imagery, aerial photos and the possibility to perform field surveys.

For the present work we compiled a landslide inventory for the northern sector of the Rif (north of the Ouergha River) from published papers, thesis, geological and geomorphological maps (Table 1), resulting in a total of 1820 landslides ranging from $5x10^{-5}$ to $7.4x10^{0}km^{2}$. In the case of the geological maps of the Rif, landslide mapping was originally performed focusing on landslide deposits, which forced a detailed analysis of each landslide in order to include both crow and depletion areas. Furthermore, some of the polygons referring to gravitational processes identify

broad sectors were slope deformation occurs, rather than mapping specific landslide bodies. In the processes of validation we limited landslide mapping to clearly identifiable landslide cases.

The landslide database was augmented through the interpretation of 1994 aerial photos at the scale of 1:40,000 (Agence Nationale de la Conservation Foncière, du Cadastre et de la Cartographie, ANCFCC) and satellite images within free online image databases. The emergence of Google Earth (Google) and Bing (Microsoft) revolutionized the way earth scientists look at the globe (Hengl, 2007). These tools provide worldwide high-resolution coverage, in some cases multi-temporal, of optical satellite images (Sato and Harp, 2009). Nonetheless, the consistency of landslide detection over large areas is hampered by the spatial variation in the quality and date of image collection and by the inability to use pre-processing techniques that allow image enhancement. For the northern Rif, image resolution varies from 1 to 5 meters depending on the image provider (i.e. Digital Globe, GeoEye, Cnes/SPOT) (Fig. 3.3). Furthermore, the Google-Earth image archive has an average of 2 (maximum 4) images from the year 2001 to 2012. Images within the Bing database are temporally limited to one set of images and provide lower image resolution.

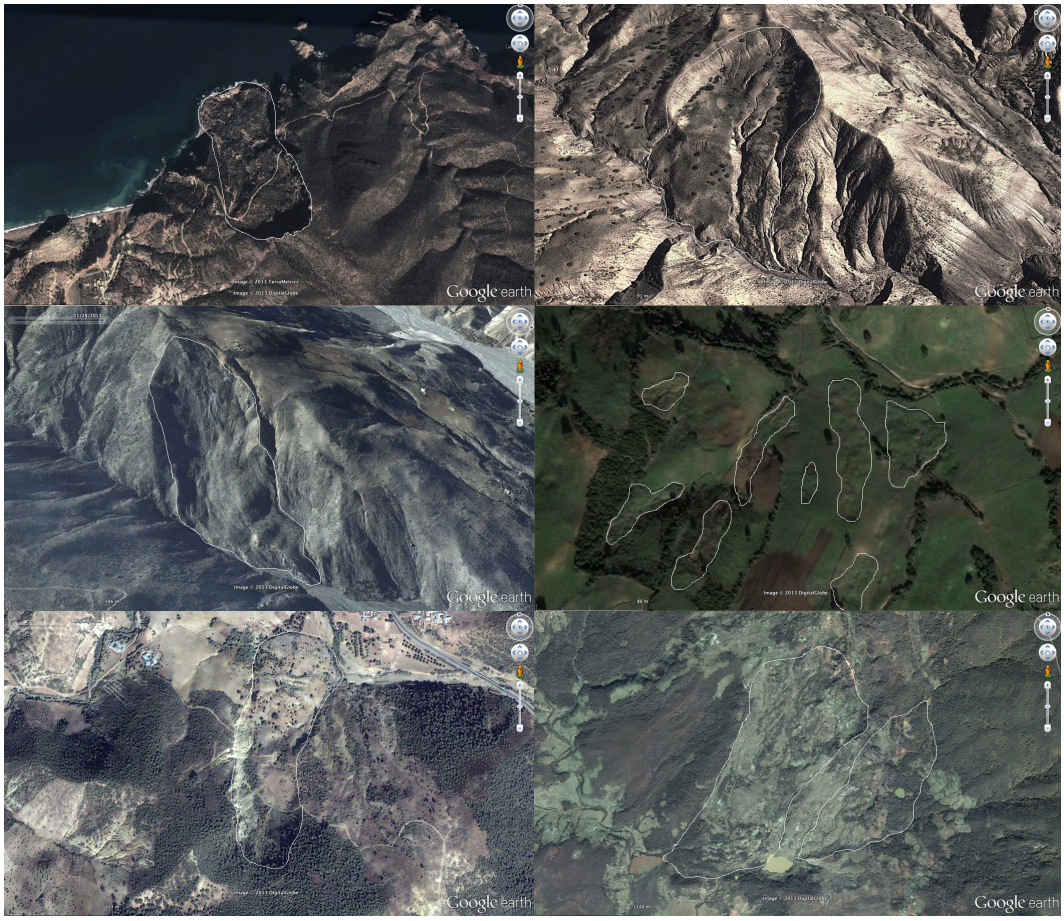


Figure 3.3 – Examples of landslide detection from satellite images provided by the GoogleEarth platform.

Landslide examples captured with Google-Earth image database. The available image resolution changes throughout the northern Rif, but allows the identification and precise mapping of large gravitational processes.

To ensure the accuracy of the mapping procedure, the Google-Earth and Bing images where automatically imported into Quantum GIS (V.1.7.3) using the "OpenLayers plugin" (source: http://hub.qgis.org/projects/openlayers). Landslides were individually mapped and classified according to landslide typology. The combination of aerial photo interpretation with the analysis of Google-earth images allowed the identification of further 8660 landslides ranging between $3x10^{-5}$ and $9.4km^2$.

Table 3.1 - Cartographic and published resources used in the work.
The references to the number of landslides results from the computation of the total number of polygons identifying gravitational processes. In the case of the geological maps of the Rif a great number of polygons refer to sectors affected by slope deformation rather than to specific landslide events (see text for explanation).

Published maps used in this work	Year of publication	Scale of publication	Nº of landslides
Maurer	1963	1:100,000 & 1:50,000	800
Suter	1966b	1:50,000	66
Suter & Mattauer	1967	1:50,000	65
Andrieux et al.	1973	1:100,000	30
Lespinasse et al.	1978	1:50,000	138
Kornprobst	1980	1:50,000	5
Suter	1980	1:500,000	67
Kornprobst et al.	1980	1:50,000	67
El Gharbaoui	1981	1:100,000	148
Leblanc et al.	1983	1:50,000	44
Vidal	1983	1:50,000	63
Choubert & Faure-Muret	1984	1:50,000	12
Leblanc et al.	1986	1:50,000	26
Choubert et al.	1987	1:50,000	6
Suter	1990	1:50,000	58
Bouhdadi	1999	1:50,000	50
Chenakeb & Bendkik	2004	1:50,000	23
Khattabi & Carlier	2004	1:100000	28
Didoon	2004	1:50,000	54
Mansour & Ait Brahim	2005	≈1:50,000	70

The final landslide inventory is composed of 10.400 landslides comprising crown and deposition areas (Fig. 3.4). The area of the individual landslides spans more than six orders of magnitude, from $3x10^{-5}$ to $9{,}4\times10^{6}$ km^2, and the cumulative area affected by all mapped landslides is 630 km^2.

Based on its morphological signature, landslides where classified according to Cruden and Varnes (1996) (Table 3.2). We distinguish four main landslide typologies: complex (slide-flow or rotational-translational sliding), slide (rotational and translational), flow and hillslopes affected by deep-seated gravitational slope deformation (DSGSD). The later refers to sectors were slope deformation is accommodated by trenching in the crow area, but the horizontal component is absent or less apparent. Moreover, landslides that could not be delineated with confidence due to post failure erosion were classified as probable. Landslides for which typology could not be identified were classified as uncertain.

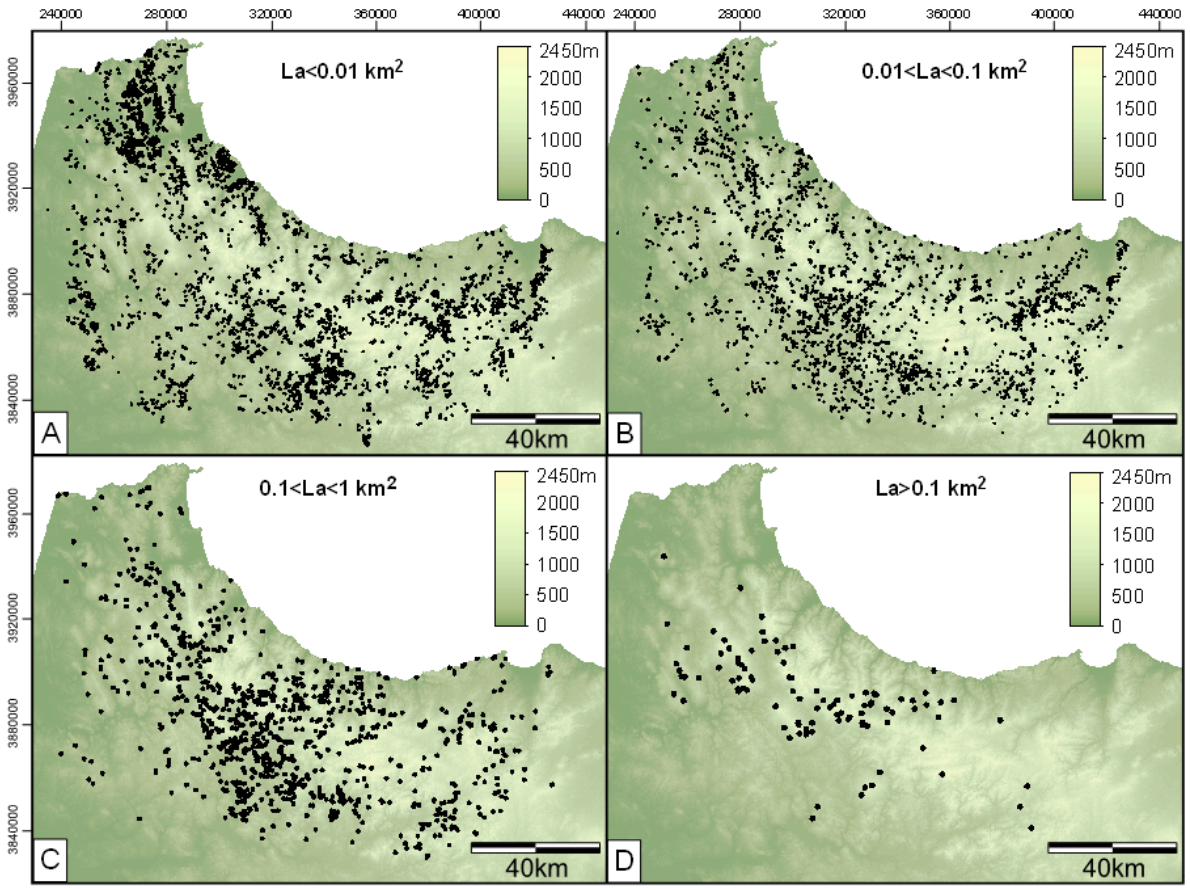


Figure 3.4 – Landslide inventory of the northern Rif Mountains.
Landslide spatial distribution according to landslide size. A) La<0.01km^2; B) 0.01<La<0.1km^2; C) 0.1<La<1km^2; D) La>1km^2.

The relative age of the landslides was assessed from the inspection of the morphological characteristics and vegetation cover. Nonetheless, taking into account the complete dataset, only 2% of the landslide inventory can be dated with relative certainty from the comparison of the satellite image archive of the Google-Earth database with the aerial photos. To aid landslide classification we resorted to published data on particular landslides that were triggered or reactivated by intense precipitation or seismic activity (i.e. Al-hoceima earthquake in 2004) (Maurer, 1968; El Felah et al., 1996; Tahayt, 2008). For the landslides identified in the geological maps of the Rif a relative chronology was already established, with the oldest landslides identified as upper Pleistocene (Soltanian in the Moroccan chronology). The oldest landslide in our dataset dates back to 1962, setting the temporal boundary for the definition of active landslides.

Table 3.2 – Total number of landslides for each morphostructural unit.

Structural Unit	Landslide inventory	Number of landslides	
		Total	N > 1km2
Internal Zone	All landslides	314	7
	Complex	54	3
	Slides	202	1
	Flow	39	0
	DSGSD	3	3
Ketama	All landslides	809	36
	Complex	129	3
	Slides	572	26
	Flow	69	6
	DSGSD	7	1
Tiziren	All landslides	339	30
	Complex	79	14
	Slides	201	7
	Flow	34	7
	DSGSD	2	2
Tanger	All landslides	1273	50
	Complex	388	38
	Slides	684	4
	Flow	139	3
	DSGSD	5	5
External W	All landslides	346	14
	Complex	66	10
	Slides	210	4
	Flow	46	0
External E	All landslides	375	2
	Complex	78	1
	Slides	224	0
	Flow	49	1

In order to compare our results with the statistical distribution of Mallamud et al. (2004a) we computed the distribution of landslide areas using the probability density function $p(A_L)$ defined by the authors as

$$p(A_L) = \frac{1}{N_{LT}} \frac{\delta N_L}{\delta A_L}$$

with the normalization condition

$$\int_0^\infty p(A_L) dA_L = 1$$

where A_L is landslide area, N_{LT} is the total number of landslides in the inventory, and δN_L is the number of landslides with area between A_L and $A_L + \delta A_L$. Following the work of Garcia (2012) δA_L was defined as 1.5.

Furthermore, in order to compare our results with the work of Rouai and Jaaidi (2003) we computed the cumulative frequency–size distribution by counting the number of landslides of area A larger tha a specified area a. Data is ploted on a logaritimic scale on the inset of figure 3.5.

For the purpose of this study we limit our analysis to bedrock failures with a platform area over 0.01km^2, which includes 3456 landslides (annex 1); i.e. 30% of the complete inventory. We chose the threshold value of 0.01km^2 by taking into account the magnitude-frequency distribution of the complete landslide inventory (Fig. 3.5), which presents a robust fit above 0.01km^2 that is comparable with the work of Malamud et al. (2004a). Furthermore, taking into account the work of Larsen et al. (2010), we consider the threshold values of 0.1km^2 for the distinguishing between true bedrock (>0.1km^2) and bedrock/soil failures (<0.1km^2).

3.1.5 Landslide density and spatial distribution

The presence of landslides clusters with similar magnitude or typology is a strong indicator of the presence of particular terrain conditions capable of accommodating large deformation events. This notion allows geomorphologists to integrate landslides in landscape evolution models and to study landslide hazard following the assumption that similar terrain properties, when reproduced over different landscape scales and exposed to analogous triggering mechanisms, will respond with similar instability phenomena.

The detection of landslide clusters is therefore of extreme importance allowing a better understanding of landscape dynamics. A typical method used in the analysis of landslide clustering is the application of the landslide density method by calculating the total number of landslides per a

user-defined length scale. The problem with this method is that it gives no indication of the concentration of large magnitude events.

On a first attempt to analyse the regional patterns of landslide distribution, we computed landslide density by calculating the total number of landslides per length scale (5.38x5.38km grid = mean distance between landslides in the dataset) (Fig. 3.6A). Furthermore, in order to visually inspect spatial variations in landslide magnitude, we resorted to the Getis-Ord (*Gi*) method, using landslide area as a morphometric variable indicative of landslide size. The Getis-Ord (*Gi*) (Getis and Ord, 1992; Ord and Getis, 1995), is a local spatial statistic method that represents the association of a particular variable (in this case landslide area) up to a specified distance d

$$Gi^*(d) = \frac{\Sigma\, x_j + x_i - n_{ij}\overline{x}^*}{S^*\left\{\left[\left(n \times n_{ij}\right) - n_{ij}^2\right] / (n-1)\right\}^{0.5}}$$

where, n is the total number of landslides in the data set, n_{ij} is the number of landslides in the vicinity of the searching distance d (5.38km), x is the landslide area, x_j *is* the mean landslide area and S^* is the standard deviation of landslide area for whole data set. This statistical method identifies spatial clusters of high values (hotspots) and spatial clusters of low values (cold spots) based on the output of the *Gi scores*. A high *Gi score* for a feature indicates a spatial clustering of high values, while a low negative *Gi score* indicates a spatial clustering of low values. The higher (or lower) the *Gi score*, the more intense is the clustering. A *Gi score* near zero indicates no apparent spatial clustering. To facilitate data interpretation and hotspot identification a smoothed surface was applied to the obtained *Gi* scores through Kernel density estimation (Fig. 3.6B).

3.2 Results

3.2.1 Landslide frequency area

As it was discussed in the introduction, magnitude-frequency distributions of several landslide inventories have shown a functional relationship between landslide magnitude (area or volume) and frequency (spatial or spatio-temporal) where the abundance of slope failures increases with landslide area up to a maximum value and rapidly decays along a power law (Pelletier et al., 1997; Hovius et al., 1997; Stark and Hovius, 2001; Guzzetti et al., 2002; Guthrie and Evans, 2004; Malamud et al., 2004). According to Malamud et al. (2004) this behaviour is despite large differences in landslide types, sizes, distributions, patterns, and triggering mechanisms. Nonetheless, the position

of the "roll-back" and the model fit for the power law decay for spatio-temporal inventories has proven to vary depending on the geological and geomorphological context and the depth of bedrock fracturing (Guzzetti et.al. 1996; Clarke & Burbank, 2010).

The landslide frequency-area distribution for the northern Rif exhibits the typical trend were the abundance of slope failures increases with the landslide area up to a maximum value (330m^2), where landslides are most frequent, and then it decays along a power law with a slope (r) of –1.36 for landslide under 1km^2 (Fig. 3.5). When considering the pdf distribution for each structural unit of the Rif the consistency of the inventory is slightly diminished, but preserves the similar rollover pattern and power-law decay along the tail end (Fig. 3.5).

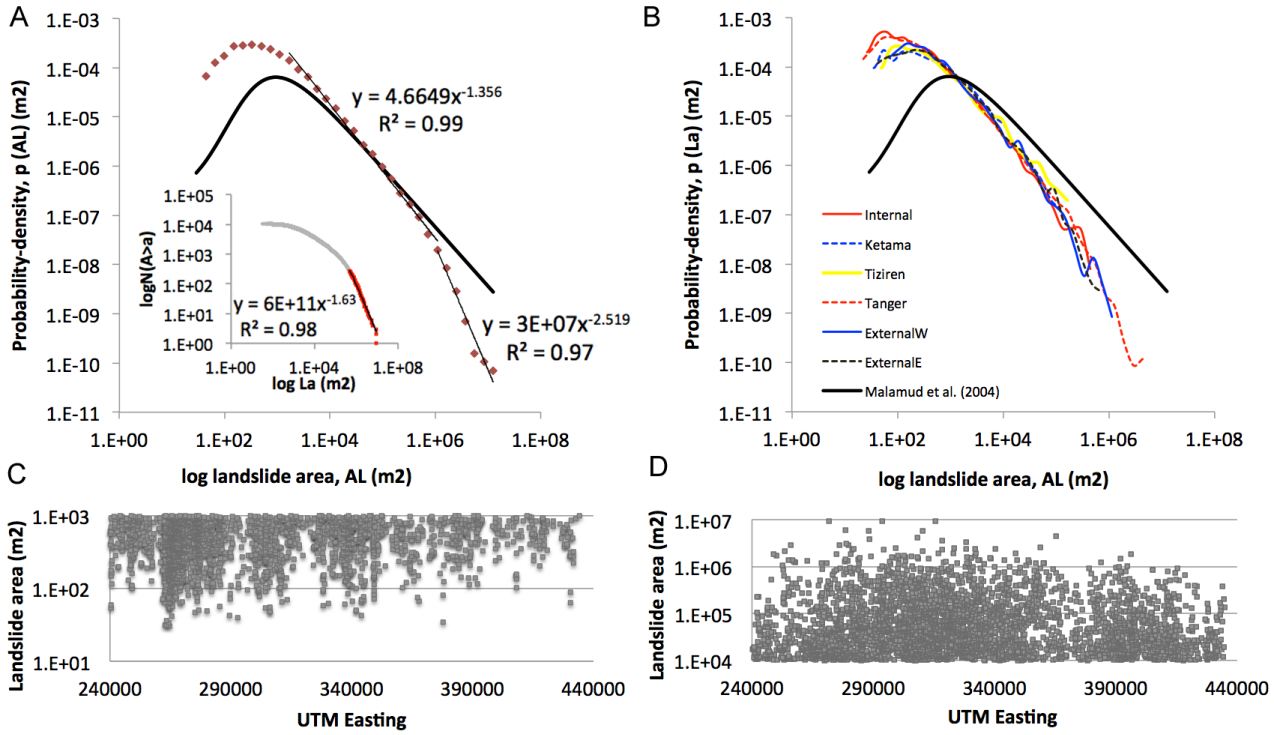


Figure 3.5 – Magnitude-frequency distribution for the complete landslide inventory.
A) Statistics of landslide area in the northern Rif. Black line, maximum likelihood estimation of inverse Gamma function (Malamud et al., 2004a). Dotted grey line shows the probability density for the complete landslide inventory, with a power-law fit along the tail end of the distribution. Inset shows the cumulative frequency–size distribution (i.e., number of landslides of area A larger than a given area a).
B) Spatial distribution of landslide area along UTM Easting for landslides with a platform area under 1000m2. Note I) the presence of vertical bands with high and low point density, referring to sectors were image quality is best; II) the irregularity of point density along the lower end of the distribution. C) Spatial distribution of landslide area along UTM Easting for landslides with a platform area over 1000m2.

Above the threshold value of 1km^2 the distribution falls rapidly along a power law fit with a slope (r) of -2.52 (Fig. 3.5), losing statistical consistency when compared with the work of Malamud et al. (2004).

3.2.2 Landslide spatial distribution

The results of landslide spatial distribution mapping through point density mapping and Getis-Ord statistical method (Fig. 3.6) reveal that the landslide phenomena in the northern Rif, although present through the entire mountain belt, tends to be clustered along particular sites.

The output of the Getis-Ord method is a hotspot map (Fig. 3.6) that highlights areas that concentrate landslides cases. The results are displayed based on the kernel density estimation.

Pixels with high positive values are shown with the red color, while clustering of low negative pixels is displayed with the blue color. Both blue and red hotspots indicate where landslides tend to concentrate and the color of the hotspots provides information on the magnitude of the landslide cases. Red-yellow hotspots indicate concentration of high magnitude landslide and blue hotspots indicate sites concentrating low magnitude cases. In our dataset the concentration of large landslides is expressed by a rapid increase in Gi scores for a threshold value close 1km^2 (Fig. 3.6C).

Visual inspection of figure 3.6 shows that both methods provide similar result showing higher landslide densities along the contact between the Internal Zone and the Tanger unit, extending to south-east to Jebel Outka and further to the east towards Al-hoceima along the Riss Valley. Low-density sites are also clearly defined using both methods, outlining the central sector of the mountain belt between Jebal Outka and Jebel Hammane.

Nonetheless, the use of the Getis-Ord method reveals sharp differences in landslide size distribution. Larger (La>1km2) landslides tend to be clustered along the contact between the Internal Zone - Tiziren and the Tanger-Numidian unit and around the flanks of Jebel Sougna, Ressana and Outka. Furthermore, high-density sites north and south of Jebel Hammane and around Jebel Ressana and Outka are in fact characterized by smaller magnitude events (Fig. 3.6).

3.2.3 Landslide height and runout

Landslide morphometric properties provide relevant information regarding the horizontal and vertical travel distance and depth of failure, allowing a better understanding of slope instability kinematics and implications in landslide hazard and risk mapping (Cruden & Varnes, 1996; Dewitte & Demoulin, 2005).

Figure 3.7 and table 3.2 shows the morphometric properties of the landslide inventory for each structural unit of the Rif. We extracted landslide height (altitude difference between head scarp and

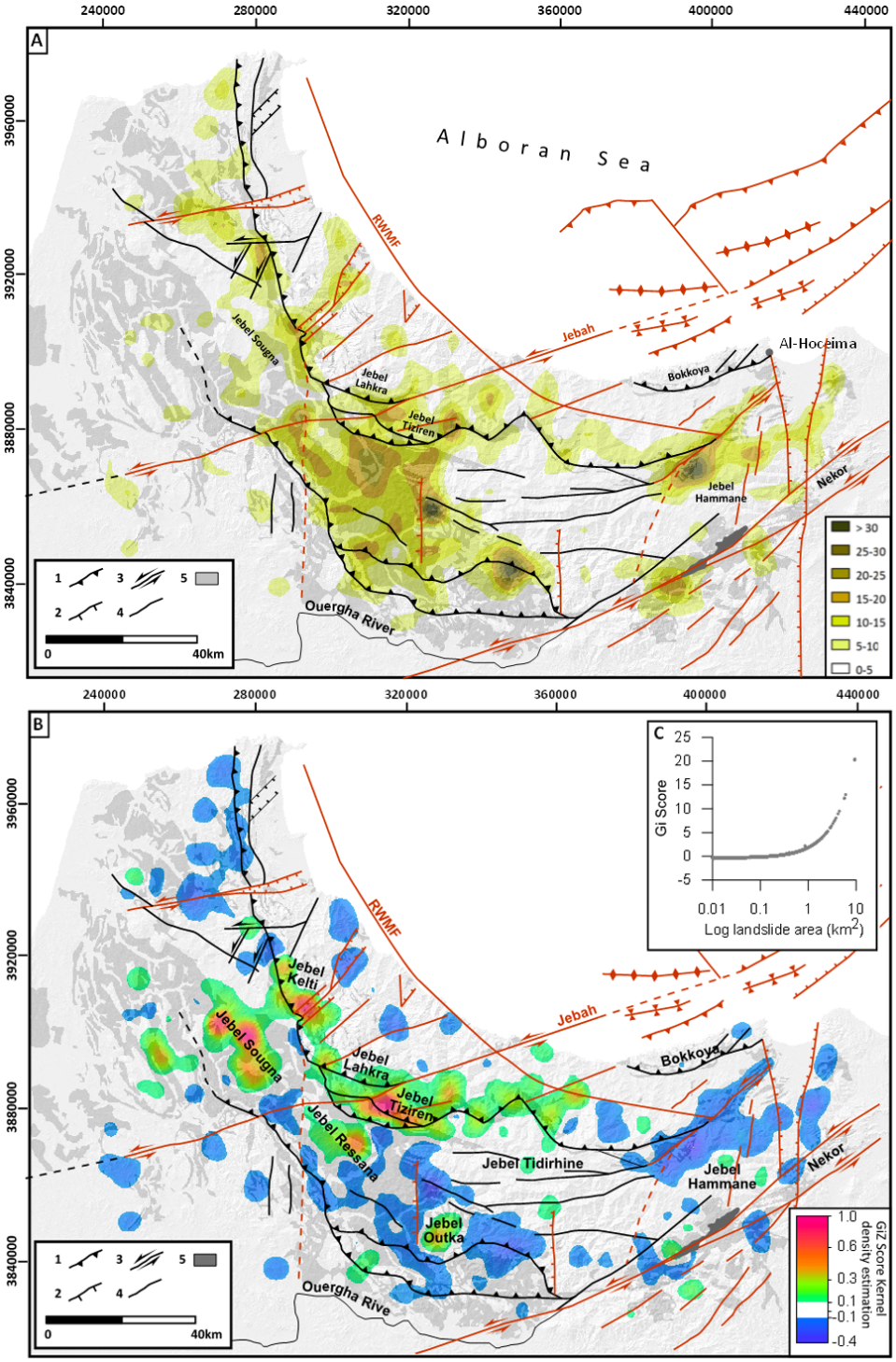


Figure 3.6 Landslide density mapping in the northern Rif.
A) Landslide density through box counting in a 5x5km matrix; B) Kernel density estimation of GiZ Scores based on landslide size; C) Landslide area vs. Gi scores. Note the increase in landslide clustering above 1km^2.

toe) and landslide runout (distance between head and toe). Differences in landslide height and

runout are outlined by a general power-law fit to the distribution (Fig. 3.7 & Table 3.2). Ploted against landslide area, both parameters express similar distributions for each structural unit of the Rif. Nonetheless, considering similar landslide area, landslides within the Tanger unit and External zone W of the Rif display lower landslide heights.

For the majority of the landslide inventory, landslide height is lower than the mean local relief and only 0.5% exceeds Lr (Fig. 3.7), a fact explained by the selected moving window for the calculation of Lr, which is in some cases lower than landslide length. These landslide cases are typically large complex or flow slides with a runout length exceeding 5km. Moreover, in areas with low to medium Lr (400 to 800m) the vast majority of the landslide inventory tends to propagate within 1/2 to 1/5 of the available relief (Table 3.2).

The propagation azimuth of bedrock failures in the rupture area indicates the prevalence of the S-N, SE-NW, SW-NE, E-W and W-E orientations for both the complete landslide inventory (above 0.01km^2) and ridge failures (Fig. 3.8). However, if we take into account the larger (>1km^2) portion of the inventory, the NE-SW and N-S orientation gains relevance over the latter.

3.2.4 Landslides and bedrock structure

Nearly 74% of the landslide cases occur under a 2km window from marly-clay outcrops. Furthermore, the predominant S-N, SW-NE and SW-NE propagation azimuth for the landslide dataset is consistent with mean bedrock dip and overall geometry of the nappe stratigraphy (Fig. 3.8). Landslides propagating to the south and southwest are limited to large (>1km^2) failures positioned along the north and northeast dipping thrust fronts of the Rif and along the NW-SE oriented ridges of the Jebal Sougna, Ressana and Outka. Larger bedrock failures (>1km^2), particular those with rupture area within the Dorsal Calcaire, Tiziren thrust fronts and Numidian ridges, have deep-seated detachment surfaces affecting both the hanging and foot-wall blocks. Furthermore, our dataset indicated that large landslides tend to be located close to both neotectonic and detachment faults, in association to areas with a mean local relief between 1200-1600mm (Fig. 3.9). As shown in figure 3.9A, this is particularly relevant for landslide with area between 0.01 and 0.1km^2 and for the largest landslide in the dataset (La>1km2; Fig. 3.9A raw data)

Table 3.3 - Landslide morphometry and morphostructural data for each structural unit of the Rif.

	Stat	Landslide area (km2)	Landslide runout (m)	Landslide height (m)	Propagation azimuth (deg)	Local relief (m)	Precipitation (mm)	Distance marly-clay units (m)	Distance neotectonic faults (m)	Distance detachment faults (m)
Inventory	Average	0.16	556	153	193	728	732	1382	3395	11136
	Mode	0.40	1871	52	349	499	602	0	436	465
	Stdev	0.46	554	150	153	263	189	2262	3091	8542
	Max	9.43	6003	1409	359	1453	1149	19370	20874	42398
Internal zone	Average	0.19	555	185	207	899	735	1904	3451	10313
	Mode	0.40	1871	138	359	1137	640	0	29	610
	Stdev	0.68	637	185	153	258	168	1883	3820	7187
	Max	9.43	5605	1364	359	1447	1108	9856	20618	26316
Tiziren	Average	0.25	687	209	190	948	610	2035	2217	9686
	Mode	0.38	870	71	5	1056	720	0	1249	285
	Stdev	0.47	624	188	154	215	166	2203	1986	10960
	Max	4.47	3791	1105	359	1375	1043	10269	8352	42398
Ketama	Average	0.10	460	156	194	820	580	2593	3494	14083
	Mode	0.86	1569	52	335	725	755	0	1045	13341
	Stdev	0.21	390	140	155	210	166	2686	3337	9326
	Max	2.55	3789	1099	359	1357	1052	13068	15478	42125
Tanger	Average	0.20	632	136	191	675	873	658	3639	11225
	Mode	0.50	197	100	350	500	856	0	465	3444
	Stdev	0.58	653	137	152	251	100	1650	2667	7484
	Max	9.35	6003	1109	359	1453	1149	10989	15211	33640
W External	Average	0.12	490	126	185	459	859	1131	4554	11342
	Mode	0.18	543	60	24	494	716	0	116	4269
	Stdev	0.31	478	149	152	122	88	2868	4350	8455
	Max	2.87	3195	1499	359	757	1064	19370	20874	36498
E External	Average	0.09	463	145	195	647	597	475	2464	4706
	Mode	0.03	320	111	318	500	630	0	668	58
	Stdev	0.15	342	122	152	215	112	1097	2071	3252
	Max	1.50	2534	972	359	1299	836	8079	11994	12296

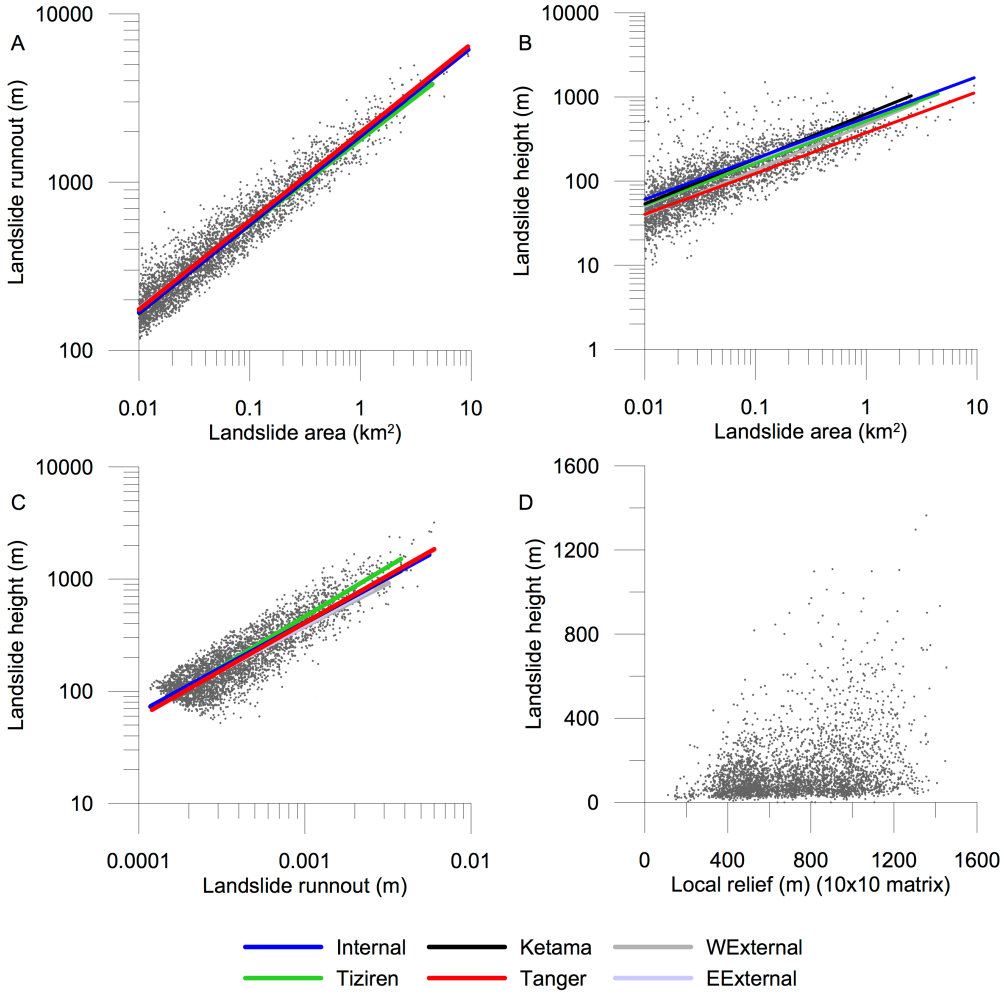


Figure 3.7 - Landslide morphometry.
A) Landslide area vs. landslide runout; B) Landslide area vs. landslide height. C) Landslide runout vs landslide height. Colored lines represent the linear fit to the distribution for each structural unit of the Rif; D) Local relief vs landslide height. Colored lines represent the power-law fit to the distribution for each structural unit of the Rif. Power-law fit expressions and R^2 adjustment are presented in table 3.

3.2.5 Landslides and topography

Our dataset shows that large bedrock landslides occur in areas with a mean local relief from 200 to 1600m, with a tendency to concentrate around 500m (Fig. 3.9A). Larger failures (>1km^2) occur almost exclusively in areas with Lr above 1000m. Bedrock failures associated to high relief sites occur under a 10km window from both neotectonic and thrust faults.

A strong variability in slope distribution is observed for each structural unit of the Northern Rif. Figure 3.10 shows slope distribution normalized by area for each structural unit of the Rif. Modal slope values within the Dorsal, Ketama and Tiziren units reach 18 to 20 degrees, while for the

Tanger Unit and External Zones modal slope values drop to 16 and 11 degrees, respectively. A similar tendency is observed considering bedrock erodibility, which indicates a probable hillslope adjustment to the strength of the undelaying bedrock material. As we saw in section 2, bedrock strength plays a crucial role in mean slope distribution, with competent rock bodies effectively sustaining higher mean hillslope angles within areas with mean local relief above 1000 meters.

When considering slope distribution for unstable sectors, our data indicates that for the complete landslide inventory, bedrock failures tend to reduce modal slope values by 3 degrees in the compact structural domain of the Internal Zone and Tiziren Unit. This observation gains consistency when considering large (>1km^2) bedrock failures, which tend to drastically reduce modal slope values by 4 to 6 degrees (Fig. 3.10). In the Tanger and External Zones of the Rif, slope variations are not detected.

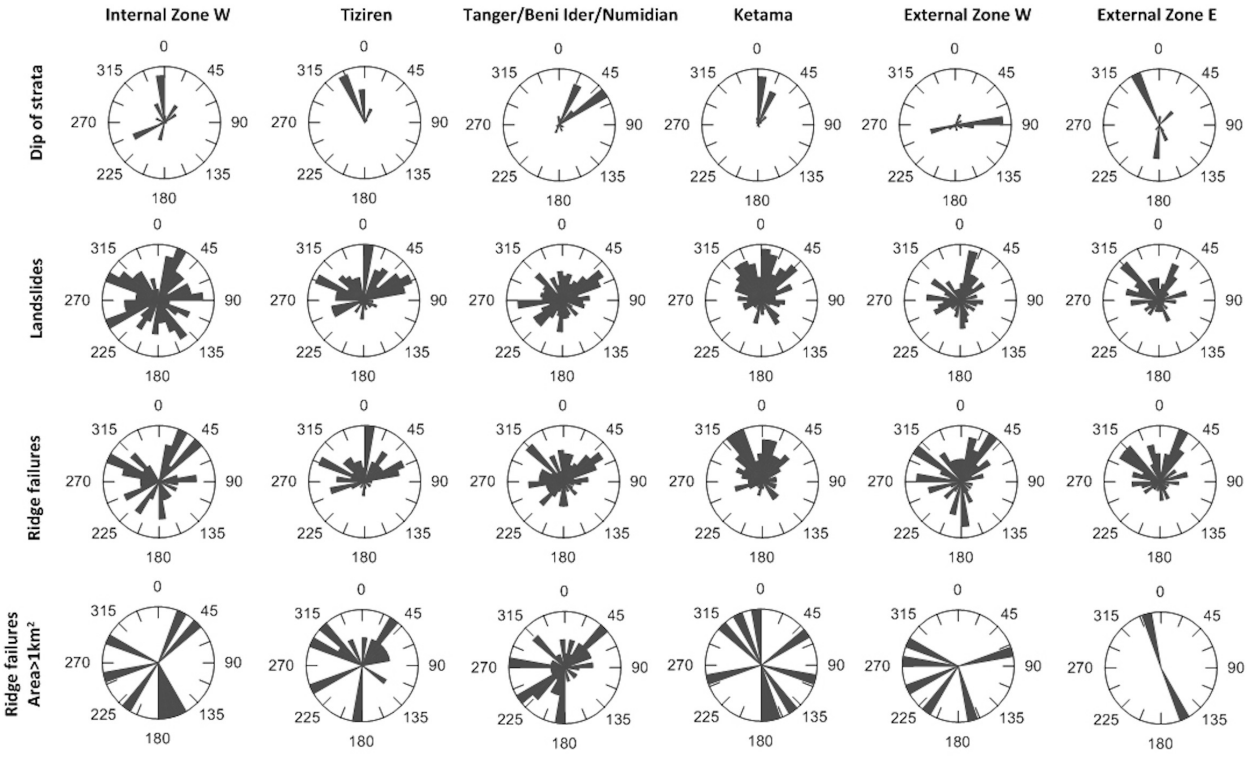
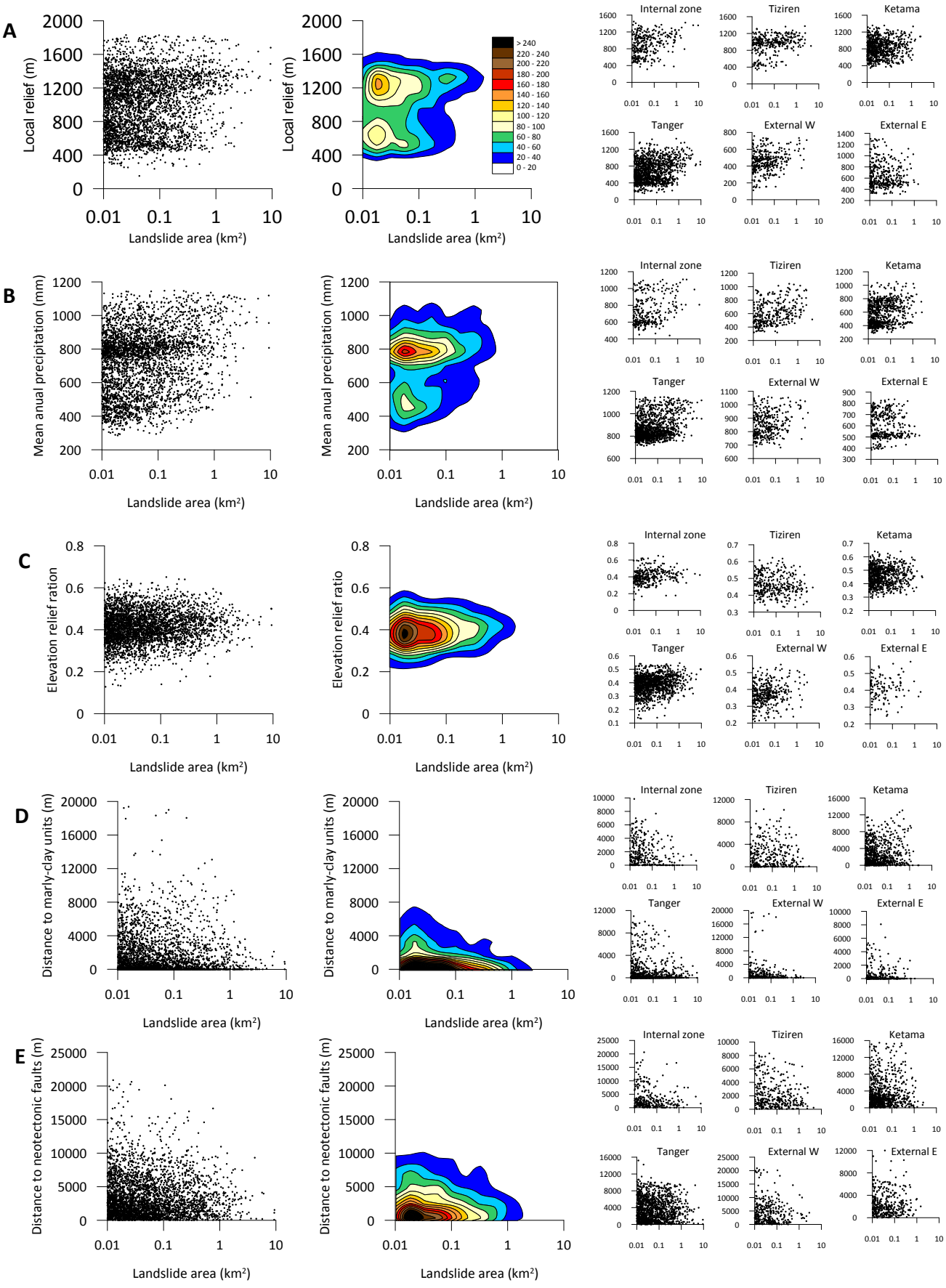


Figure 3.8 - Mean bedrock dip and landslide runout azimuth for each structural unit of the Rif.


A
Local relief (m)
Landslide area (km²)
> 240
220 - 240
200 - 220
180 - 200
160 - 180
140 - 160
120 - 140
100 - 120
80 - 100
60 - 80
40 - 60
20 - 40
0 - 20
Internal zone
Tiziren
Ketama
Tanger
External W
External E
B
Mean anual precipitation (mm)
C
Elevation relief ration
Elevation relief ratio
D
Distance to marly-clay units (m)
E
Distance to neotectonic faults (m)

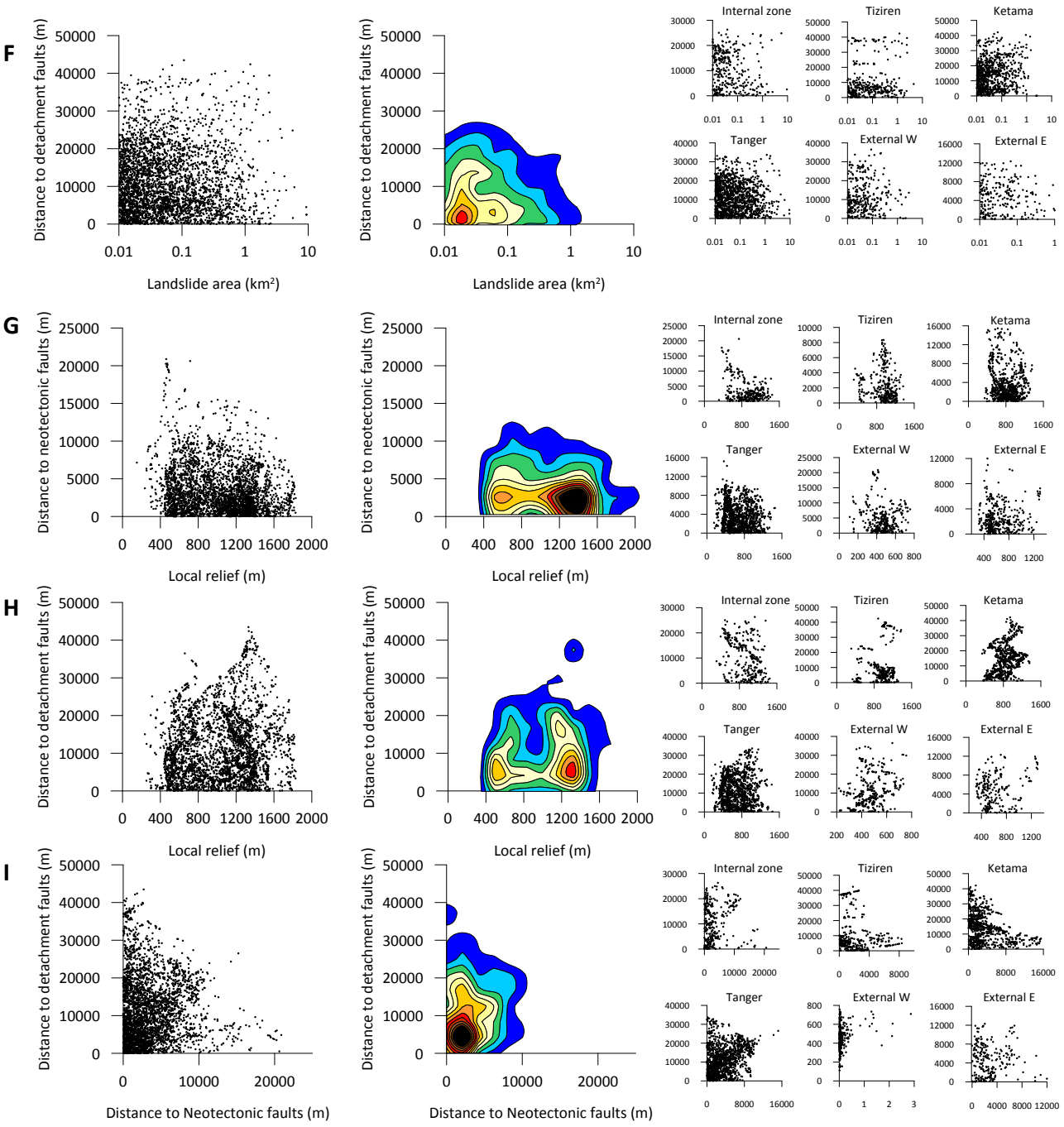


Figure 3.9 Landslide distribution.

Landslide distribution (raw data and contour-plots) for the complete landslide inventory (La>0.01km^2) and structural units of the northern Rif. A) Landslide area – Local relief; B) Landslide area – mean annual precipitation; C) Landslide area – Elevation-relief ratio; D) Landslide area - distance to marly-clay units; E) Landslide area – distance to neotectonic faults; F) Landslide area – distance to detachment faults; G) Local relief at landslide site - distance to neotectonic faults; H) Local relief at landslide site - distance to detachment faults; I) distance to neotectonic faults - distance to detachment faults.

3.2.6 Landslides and precipitation

A significant portion of the landslide inventory is concentrated in areas with a mean annual precipitation of 800mm, corresponding to the lower sectors around Jebel Sougna, Ressana and Outka (Fig. 3.9B). Larger landslides (>1km^2) are not limited to high mean annual precipitation sites, although the largest landslides in the inventory occur in areas with annual precipitation of over 1000mm.

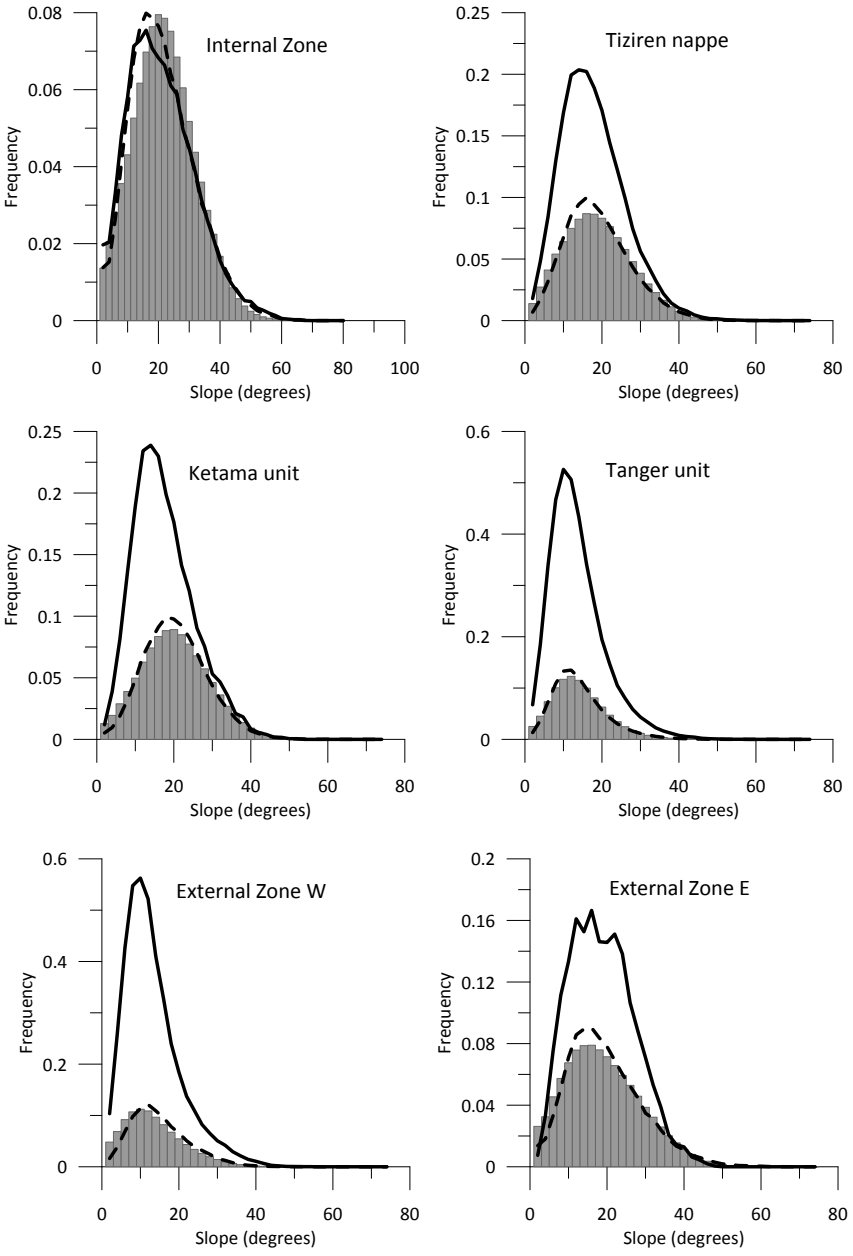


Figure 3.10 - Frequency distributions of surface-slope angles normalized by area and stratified by landslide area for each structural unit of the Rif.
Dashed line represents slope frequency for the complete landslide inventory (La<0.01km^2). Black line represents slope frequency for large (>1km2) bedrock failures**.**

3.3 Discussion

Presently, slope instability in the Rif is closely related to the intense and prolonged precipitation events occurring during autumn-winter months and to occasional seismic shaking (i.e. Lisbon and Meknes, 1755 - Vogt, 1984; Northern Morocco, 1801 - Jabour et al. 2004; Northern Rif - Maurer, 1968; Al Hoceima, 1994 and 2004 - Akoglu et al., 2006 & Tahayt, 2008). However, with the oldest and largest datable landslide in our dataset occurring in 1962 and having a platform area of 0.65km^2, nearly 39% of the largest landslides in our inventory have occurred in an earlier period and under unknown triggering conditions. The relative chronology used in the geological maps of the Rif places some of these large events in the middle-upper Pleistocene, which inevitably relates slope instability to a distinct, more humid, climatic setting, or to time-independent triggering processes such as seismic events.

The landslide probability density function for the landslide inventory of the northern Rif exhibits the typical trend were the abundance of slope failures increases with the landslide area up to a maximum value (330m^2), and then it decays along a power law with a slope of –1.36 for landslides under 1km^2 (Fig. 3.5). By comparing our results with the work of Mallamud et al. (2004a) we can observe that our dataset is well adjusted for landslides with a planimetric area between 0.01 and 1km^2.

In what concerns the frequency-size distribution (number of landslides of area A larger than a specified area a) our dataset shows a curve–like pattern revealing a slope of -1.63 for the power-law decay of the upper end of the dataset (inset on figure 3.5). Similar results have been presented for the Rif by Rouai & Jaaidi (2003) with a slope of -1.57 for the power-law decay. The different obtained results are a consequence of the methods used for landslide mapping. While these authors use the polygons mapped in the geological map of Beni Hamed (Lespinasse et al., 1978) to compute landslide areas, we limit our dataset to clearly identifiable landslide bodies. Since the geological maps of the Rif tend to represent broad areas were slope deformation occurs, rather than differentiating between individual landslides, the data used by Rouai & Jaaidi (2003) tends to overestimate the importance of large events.

In our pdf dataset, the lack of adjustment to the data produced by Mallamud et al. (2004a) along the lower end of the distribution is explained by the inconsistency of image quality and date of image collection throughout the northern Rif. While the detection of smaller landslides is hampered by the spatial variability in image quality, larger landslides are systematically captured with both aerial photos and Google-Earth images, not showing significant gaps in the inventory along the

west-east extension of the mountain chain (Figs. 3.4 and 3.5). While for some sectors the image quality allows the identification of smaller (La< 0.01km^2) slope instabilities, areas with poorer image quality, or lacking images that were taken prior, or close, to an event, present higher minimum landslide areas (Figs. 3.4 and 3.5). This results in a band-like distribution when plotting landslide occurrences along the east-west UTM grid (Figs. 3.4 and 3.5C e D).

Above the threshold value of 1km^2 the distribution falls rapidly along a distinctive power law fit with a slope of -2.52 (Fig. 3.5). As very large landslides tend to have longer residence time in the landscape than smaller landslides, it is unlikely that our dataset expresses the inability to detect larger (older) landslides due to post failure erosion. Nonetheless, geomorphological and geological data (Maurer, 1968) indicate the presence of thick multi-event landslide deposits for which the topographic signature in the rupture area is completely obliterated. This fact provides evidence that slope deformation persists at these sites and extends beyond the geological time frame of the inventory produced in this study.

Another approach is to interpret the rapid decay of the probability density function for landslides with La>1km^2 as an expression of a distinc landslide population associated with specific terrain conditions. The hotspot mapping and cluster analysis of landslide area support this notion as the spatial clustering of large landslides is expressed by a rapid increase in *Gi scores* for a threshold value close 1km^2 (Fig. 3.6C). Furthermore, taking into account figures 3.4 and 3.6 we observe that very large (La>1km^2) bedrock failures tend to occur along the edge of the Internal Zone, the flanks of Jebel Sougna, Ressana and Outka and along the Tiziren thrust (ChK fault; Fig. 1.4). The fact that these processes tend to appear in association with distinctive surface bedrock conditions is expressive of critical triggering and predisposing conditions (either than lithology), capable of producing high magnitude, low frequency events.

The consistency between high *Gi scores* and the location of both marly-clay outcrops and tectonic structures is clearly outlined within the Tanger domain and along the thrust front of the Internal Zone and Tiziren unit (Fig. 3.6). With the exception of the hotspots located within the topographic domain of Jebel Sougna, Ressana and Outka, very large bedrock failures tend to be grouped along the southern boarder of the structural units of the Rif. Outside these areas medium sized landslide clusters (0.7-1km^2) tend to occur along the NE-SW extension of the Nekor fault and in central sector of the Ketama Unit in clear association to deeply incised valleys.

The relevance of bedrock lithology in landslide distribution is further outlined in figure 3.9D, where nearly 74% of the landslide cases occur under a 2km window from marly-clay outcrops. In fact, the

rupture area for the majority of the landslides identified in this study is either located within softer lithologies or in the compact limestone and sandstone of the Dorsal and Tiziren, which overlay the latter by stratigraphic concordance or regional detachment faults. Furthermore, the predominant S-N, SW-NE and SW-NE propagation azimuth of large landslides is consistent with mean bedrock dip. Landslides propagating to the south and southwest are limited to large (>1km^2) failures positioned along the north and northeast dipping thrust fronts of the Rif and along the NW-SE oriented ridges of the Jebal Sougna, Ressana and Outka.

Larger bedrock failures (>1km^2), particular those with rupture area within the Dorsal Calcaire, Tiziren thrust fronts and Numidian ridges, have deep-seated detachment surfaces affecting both the hanging and foot-wall blocks. At these sites, deep-seated bedrock fracturing allows rainfall to infiltrate in depth, increasing pore-water pressure and reducing the sheer strength of the less competent units (normally marls and clay) located in the foot-wall of major thrust fronts. Similar conditions have been presented by Khattabi & Erick Carlier (2004) for the northeastern sector of the mountain belt, where the schists of the Chaumat-Mellousa undergo transformations, modifying their mechanical properties in response to the increase in water content.

The northern Rif depicts two areas with mean local relief above 1500m associated with the deeply incised valleys along the southern flank of Jebel Tidirhin and within the central sector of the Internal Zone. Reaching over 1800m, the wadi Lao gorge shows one of the highest relief sites in the Northern Rif. With the exception of the mountainous sector surrounding Jebel Tidirhin, the majority of the available relief is concentrated in the Mediterranean flank, with low relief areas mainly concentrated in the External Zone and N and NNW of Jebel Sougna. Large landslides are strongly associated with local relief values of 500 to 600m occurring along the lower flanks of Jebel Sougna and Ressana and in the Beni Hamed region. The largest landslides in the dataset occur along the wadi Lao valley or along the southern flank of the Tiziren thrust in association with Lr values of 1200 to 1500m.

From a geomorphological perspective, large bedrock failures tend to occur in association with Er values ranging from 0.4 to 0.5 (Strahler disequilibrium stage), which highlights the importance of large gravitational processes in moderating the transition between youthful and mature landscape stages.

Furthermore, very large landslides occurring in the Internal domain, Tiziren and Ketama units tend to reduce modal slope values by 8 degrees. However, slope changes produced by large bedrock failures in the Tanger and External Zones were not detected, which is partially explained by the low

resolution of the DEM. Nonetheless, differences in slope frequency between morphostructural units are explained by: i) the presence of low angle-rectilinear to concave slope profiles carved within the high plasticity units of the Tanger domain allows large complex and flow landslides to propagate over large distances without preforming significant changes in the preexisting topography in the runout area; ii) slope frequency variations between the depletion and accumulation areas is masked by the large slope frequency associated with complex slides experiencing large runout lengths; iii) the ratio between the thickness of the compact units occurring within the hanging-wall of the thrust fronts of the Rif and the altitude difference bewtween the ridge and valley floor; iv) by the length and slope angle of the hillslopes within the foot-wall blocks.

Large bedrock failures occurring along the tectonic scarps of the Dorsal and Tiziren thrust tend to reduce slope angles by removing material in the depletion area and producing large debris accumulations in the runout sector. We take this as an indication that very large landslides have reduced the modal terrain slope from the regional value in stable areas of ϕmode = 20° to ϕmode = 15°/13°. Similar observations have been reported for Southwest New Zealand (Korup, 2005b) and for the Apennines (Guzzetti et al., 2008).

One of the most relevant observations in this study regards the role of active tectonic structures in controlling landslide distribution. The critical location of large (>0.01km^2) landslides occurring in close association to high local relief sites and in the vicinity of active tectonic structures provides circumstantial evidence to the topographic site effect in triggering earthquake-induced landslides, through probable amplification of seismic accelerations along the thrust fronts of the Rif and along NE-SW and NW-SE valleys ridges. The increase in number of large bedrock failures along the highest classes of seismic acceleration supports this observation, with potencially high magnitude earthquakes effectively producing large scale slope deformation through rock shattering of highly and deeply fractured bedrock units positioned along the hanging-wall of the Rif thrust fronts. Additionally, while present-day earthquake density (Fig. 1.4) shows no particular relevance on landslide distribution, the number of bedrock failures with a platform area over 0.5 and 1km^2 increases towards the upper-end of the dataset (Fig. 3.11). In fact, nearly 72% of the detected landslide clusters occur under a 15km window to the Jebah fault, a sector defined by Benchekroun et al. (2013) as having one the highest seismic accelerations (0.27-0.33g) in the northern Rif.

Moreover, as it was discussed in chapter 2, the tectonic-geomorphic setting of the northern Rif exhibits a pattern of deformation that is consistent with the tranpressive deformation bounded by NE-SW oriented structures in response to NW-SE compression. The fact very large bedrock failures

tend to cluster in close proximity to these structures further outlines the importance of regional seismicity in landslide triggering.

3.4 Conclusion

In this section we presented a landslide inventory of the northern Rif Mountains focusing our attention on the spatial distribution and geomorphic signature of very large (>1km^2) gravitational processes. The completeness of the landslide inventory for landslides with a planimetric area

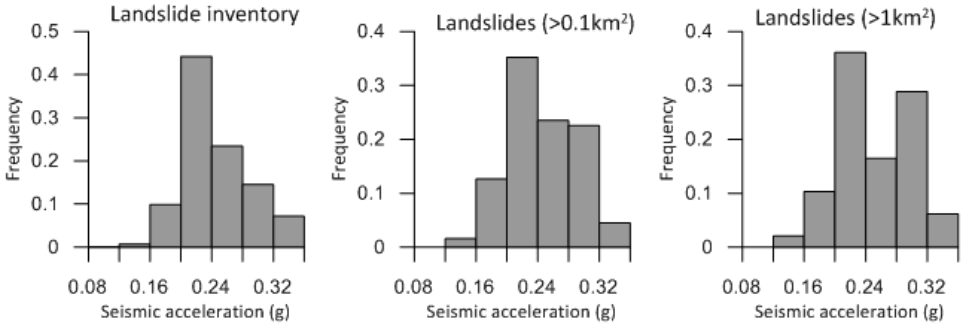


Figure 3.11 - Frequency of slope failures per seismic acceleration class following the work of Benchekroun et al. (2013).

between 0.01 and 1km^2 is confirmed by the adjustment of the pdf of large landslides to the inverse-gama distribution presented by Mallamud et al. (2004a). While the distribution of smaller landslides is hampered by the spatial variation in image quality, larger landslides are systematically captured, not showing significant gaps in the inventory along the west-east extension of the mountain chain.

While the role of precipitation related to humid climatic condition throughout the Quaternary might have favoured the concentration of slope deformation along the southwestern sector of the mountain chain, the importance of deep-seated bedrock fracturing in close proximity to active tectonic structures and high relief sites is clearly outlined in this study.

Future studies should try to perform a detailed analysis of the geometry and chronology of large and very large failures in order provide information of the volumetric and spatio-temporal contribution of large bedrock landslides to degradation of mountain topography.

4 Activity of large bedrock landslides in the northern Rif Mountains during the period 2004-2010 detected through Persistent Scatterer Interferometry, Hotspot and Cluster analysis

Abstract

A preliminary approach of slope instability analysis in the northern Rif Mountains based on Persistent Scatterer Interferometry (PSInSAR) technique is presented. The velocity and density of persistent scatterers (PSs) is analyzed in respect to terrain properties and landslide distribution to refine the classification of the activity status of inventoried landslides following the work of Cigna et al. (2012). Furthermore, Hotspot and Cluster analysis (Lui et al., 2011) were used to detect PSs clusters associated with slow gravitational movement.

Slope deformation expressed as high velocity hotspots is consistent with sectors previously identified as presenting deep-seated slope deformation. Very large landslides (>4km^2) show a lower density of higher velocity PSs when compared to smaller landslides. This fact is interpreted taking into account the relationship between landslide size and the ability of a precipitation event to produce reactivation. In our dataset, while smaller landslides present evidence of reactivation along significant portions of the landslide body, very large landslides tend to suffer partial reactivations, either through the slow downward propagation of a secondary landslide mass on top or along its margins in response to lateral or frontal gullt/river incision. Nevertheless, this observation is hindered by the fact that PSs are not always evenly distributed within the landslide body, but gathered around particular sites where reflectance is consistently captured by the satellite. Therefore, the nature of partial reactivations of large landslide is difficult to discriminate when simply referring to PSs data and further field data collection and detailed geomorphological mapping should be performed in order to avoid misinterpretations of landslide kinematics.

Keywords: landslide activity; PSInSAR ; Hotspot and cluster analysis ; Getis-Ord ; Rif ; Morocco

4.1 Introduction

Landslide hazard zonation and the implementation of early warning systems for slope instability depend on the existence of complete and regularly updated landslide inventories (Guzzetti et al., 2000). These can be achieved through different field and laboratory techniques, usually involving the analysis of aerial photos and satellite imagery, digital elevation models (contour-line based and high-definition such as LIDAR) and time-consuming field campaigns.

The use of remote sensing data to study gravitational processes is becoming increasingly popular as it allows the inspection of large portions of the territory at relatively low costs. Moreover, these tools allow the extraction of quantitative data describing the geometrical and spatio-temporal evolution of gravitational landforms.

Among other techniques, the Persistent Scatterers technique (PSInSAR) has proven to be a useful tool to assess the activity and kinematics of slow moving landslides (<60 mm/yr, velocity scale proposed by Varnes (1978) and Cruden and Varnes (1996)), allowing the measurement of centimetric to millimetric surface displacements (Hanssen, 2005; Colesanti and Wasowski, 2006; Crosetto et al., 2010; Cigna et al., 2012).

It is beyond the scope of this work to elaborate on the PSInSAR method. A description of the conceptual approach and methodological procedure can be found in Ferretti et al. (2001) Colesanti et al. (2003) and Hooper et al. (2004) and references there in. Nonetheless, it is important to refer to the outputs provided by the PSInSAR method and the approach to data interpretation.

The PSInSAR method measures differences in the path of the wavelength between the satellite and the terrain target along the satellite Line-of-Sight (LOS). The generation of Persistent Scatterers (PSs) relates to the terrain scattering properties (Hooper et al., 2009). The consistency of the microwave scattering captured by the satellite mainly depends on the radar wavelength, terrain roughness, soil moisture and local incidence angle which, for a given radar line-of-sightLOS, is determined by the local terrain slope and aspect angles (Nico et al., 2009). Moreover, for a correct interpretation of deformation rates from PSs it is crucial to combine GPS data as control points in the terrain to account for the vertical component of movement (Colesanti *et al.,* 2006).

The identification of PSs is hampered by several constraints (Hanssen, 2005; Colesanti and Wasowski, 2006; Crosetto et al., 2010; Cigna et al., 2012): I) problems associated with the geometrical visibility between local topography and the LOS orientation; II) the temporal decorrelation as the result of time varying backscattering properties resulting from the presence of vegetation; and III) landslides moving at rates exceeding the employed SAR wavelengths and satellite revisiting times (Cigna et al., 2013). Furthermore, within remote areas, data acquisition is hindered by the fact that PSs are not always evenly distributed but gathered around particular sites with high backscattered intensity.

From an interpretative perspective, positive deformation values indicate movement towards the satellite along the LOS, while negative values suggest that movement is occurring in the opposite direction of the sensor (e.g. Righini *et al.,* 2012). Moreover, when applied to the study of gravitational processes, the spatial distribution of deformation depends on landslide typology and kinematics. In the case of translational landslides, PSs rates tend to be homogenous throughout the landslide surface, while for rotational slides the deformation rate tends to diminish towards the toe of the landslide (Colesanti *et al.,* 2006).

The use of remote sensing techniques to study landslides in the northern Rif is scarce. Mastere *et al*. (2009) combined photogrammetric and digital terrain analysis to study the evolution of a debris flow located 15km east of the village of Chefchauen. Tahayt (2008) detected probable co-seismic landslide activity in the Rhiss valley triggered by the 24 February 2004 Al-Hoceima earthquake through the analysis of interferometrically processed ENVISAT images.

This is a preliminary approach to analyze slope instability in the northern Rif Mountains based on PSInSAR technique applied to a six-year timeframe of SAR imagery. The velocity and density of persistent PSs is analyzed in respect to terrain properties and landslide distribution in order to refine the classification of the activity status of the inventoried landslides. Furthermore, Hotspot and Cluster analysis are used with the purpose of detecting PSs clusters associated with slow gravitational movements.

4.2 Available triggering mechanisms for the SAR image timeframe

According to the USGS database, during the considered SAR image timeframe, 25 earthquakes with magnitude above Mo 4 (reference magnitude for landslide triggering according to Keefer (2002) and Malamud *et al*. (2004)) occurred in the study area. The majority of the seismic events were located at Al-Hoceima region (Fig. 4.1) and occurred during spring and summer. In particular, the PS2007 dataset covers the seismic crisis of February 24, 2004 at Al-Hoceima, related to a Mo 6.4 earthquake that produced surface rupture along the western flank of the Riss valley. Several co-seismic landslide reactivations were identified during this period in the Al-Hoceima region (Tahayt, 2008).

Rainfall data for the SAR image timeframe shows that between 2003 and 2008 the mean annual precipitation did not surpass 300mm (Fig. 4.2), and the maximum daily rainfall did not exceed 65 mm/day. Nevertheless, during the 2009/2010 winter northern Morocco and the Iberian Peninsula were affected by a south-westerly low pressure system, with precipitation values reaching 567mm in December 2009 and 200mm in January 2010 at the meteorological station of Chefchuen, distributed over a period of twelve days. During this time, the maximum daily rainfall reached nearly 160 mm/day at Chefchauen (Figs. 4.33). Several landslide reactivations were identified in the field causing severe damage to roads and infrastructures (Fig. 4.4).

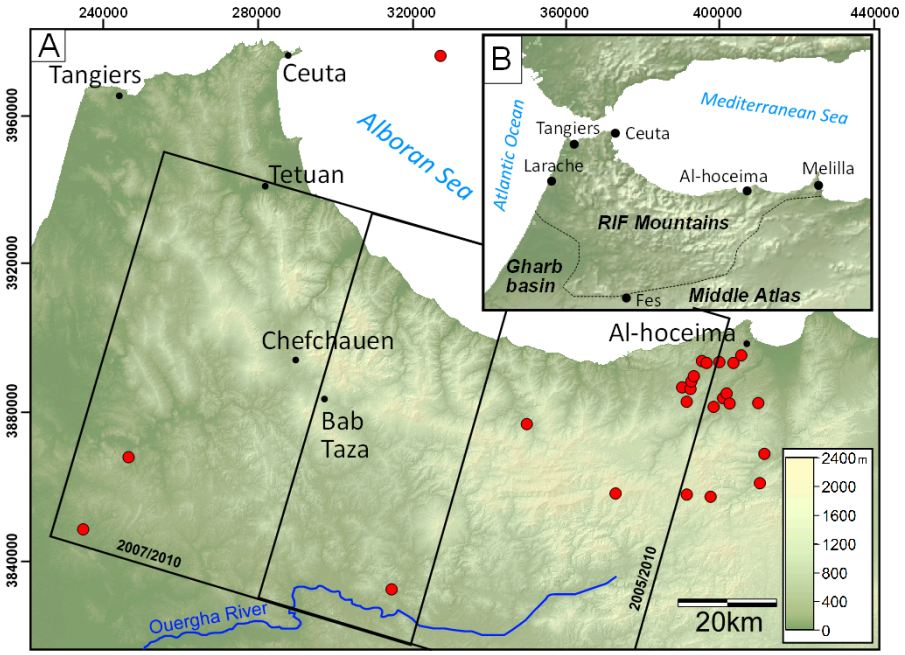


Figure 4.1 - Limits to the PS2005 and PS2007 datasets.
Red dots mark the epicentre to >4Mo (max 5.3) earthquakes (USGS database) for the SAR image timeframe. B) Geographical context of the Rif Mountain and location of the cities as reference to the precipitation data of the meteorological stations presented in figure 3.

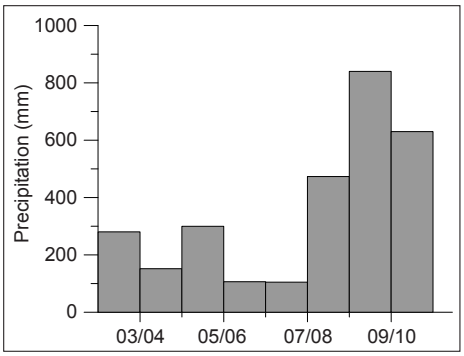


Figure 4.2 – Mean annual precipitation at the meteorological station of Chefchauen for the SAR image timeframe (2003/2010).

4.3 Dataset and methodology

4.3.1 PSInSAR dataset

This study is supported by a set of 41 SAR images, acquired between May 2003 and September 2010 by ENVISAT satellite along two tracks (descending track 51 – 21/05/04 to 4/6/10; descending track 323 – 5/2/03 to 1/9/10). The images were supplied by ESA in the scope of ESA Cat-1 (n.10338) Project "DSLRif - Detection, analysis and kinematics of deep-seated landslides in the central Rif

Mountains (Northern Morocco)". Image processing was performed under a partnership between the IDL-FCUL and the RISKAM-CEG- IGOT-UL. The 41 SAR images were interferometrically processed using one master image for each track resulting in a stack of interferograms that were further processed using the Persistent Scatterers technique producing two PSs dataset (PS2005 and PS2007).

At this stage, GPS was not included in data calibration, which hinders the definition of the vertical and horizontal components of movement.

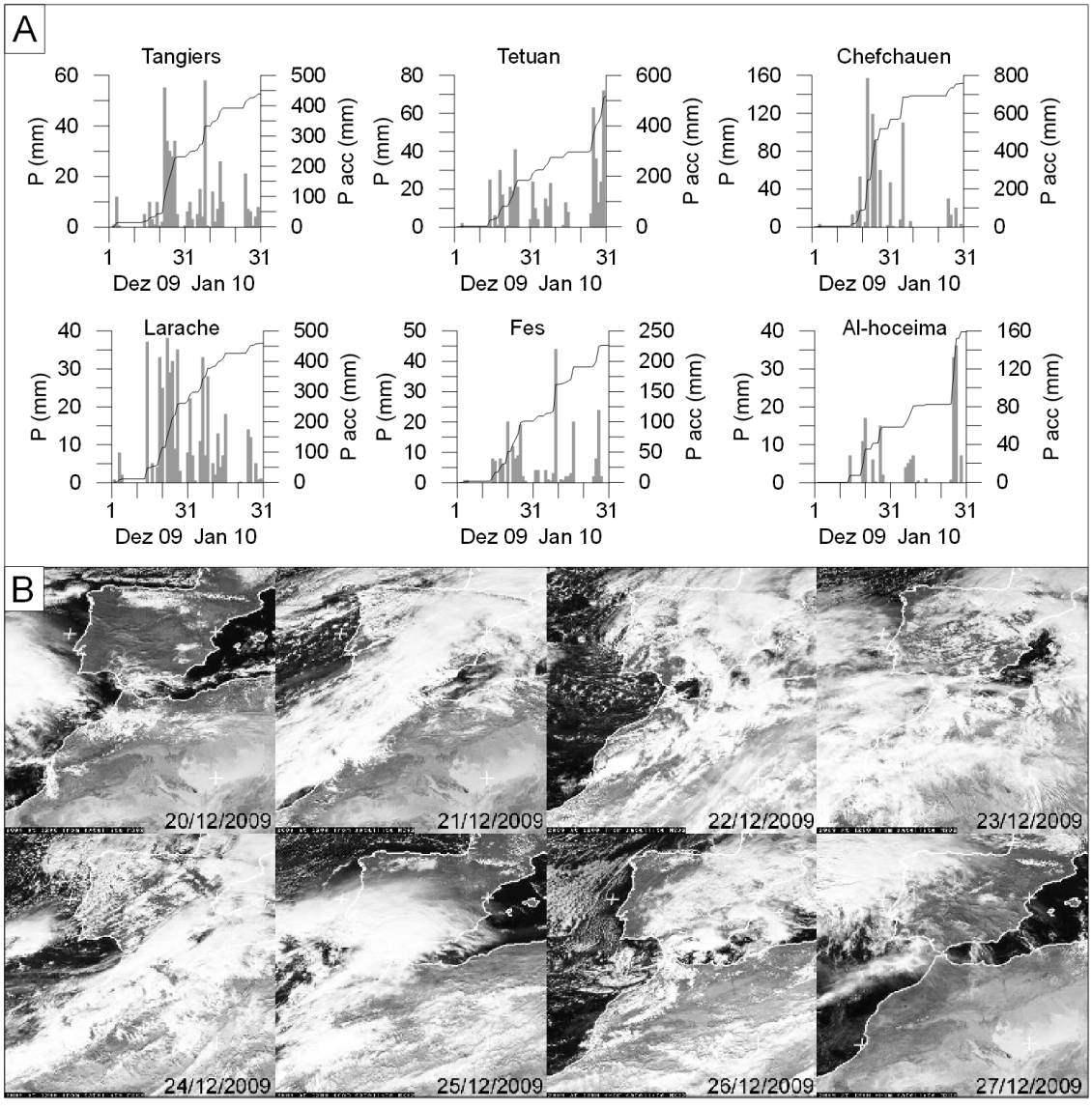


Figure 4.3 – Extreme precipitation event during the winter of 2009-2010.
A) Daily precipitation data for December 2009 and January 2010 at six meteorological stations (figure 1 for location) of the northern Rif. B) Cloud cover over northern Morocco captured by the EUMETSAT, NERC (University of Dundee) satellite from the 20th to the 27th of December 2009.

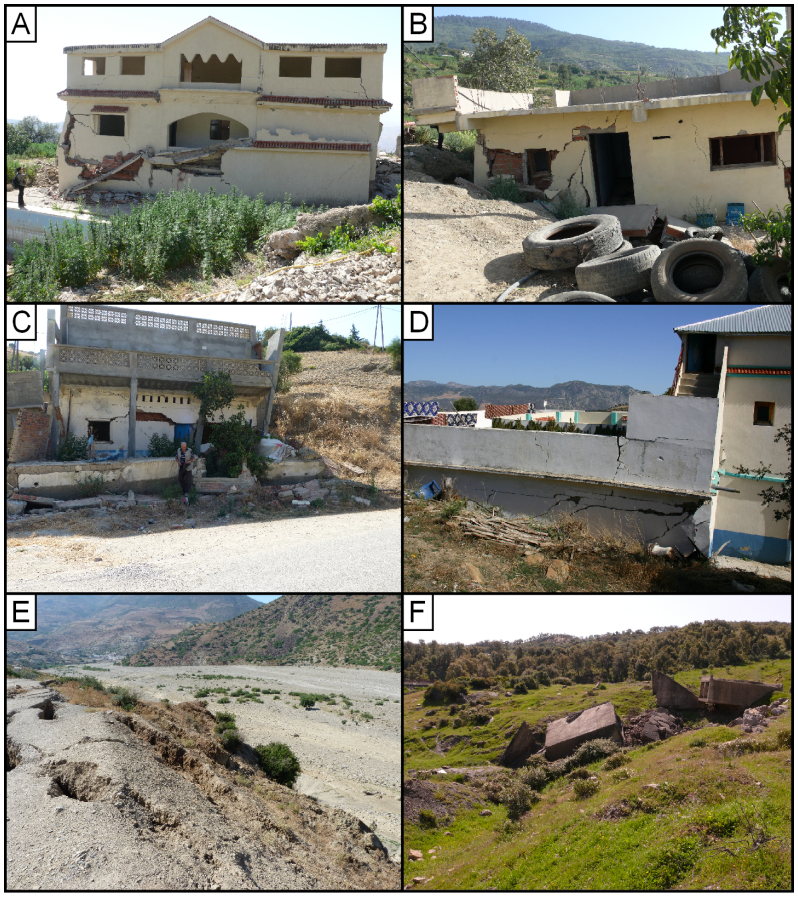


Figure 4.4 - Infrastructures affected by landslide reactivations during the winter period of 2009-2010.
A-D) Destroyed houses in the region of Bab Taza, Chefchauen and El Jebha; E) Tension fracture opening on an asphalt road caused by lateral river erosion (El Jebha); F) Water dike destroyed by landslide reactivation along the northern flank of Jebel Ressana.

4.3.2 Definition of the landslide activity status

The definition of the activity status of landslides is a crucial step for the straightforward evaluation of landslide hazard (Colesanti *et al.,* 2006). Classical studies have resorted to geomorphological criteria based on the freshness of the gravity-induced landforms through direct field observation or aerial photo interpretation. Nonetheless, these methods are strongly dependent on the expertise of the researcher performing the survey and are hindered by the spatial variability of geomorphic, geological, climatic and land cover specificities of each region.

Over the last decade, a significant effort has been made to apply remote sensing techniques in landslide studies. Among several procedures, the PSInSAR technique has been used to improve the completeness of landslide inventories and to aid the classification of the landslide activity status (e.g., Cascini et al. 2010; Farina et al. 2006; Herrera et al. 2009; Meisina et al. 2008; Righini et al.

2012; Bianchini et al. 2012; Cigna et al. 2012; Oliveira et al., 2014). The proposed methods exploit PSInSAR-derived multitemporal estimates of ground deformation as indicators of activity and magnitude of landslide processes (Cigna et al. 2012).

The PSI-based matrix approach (Cigna et al. 2012) is based on the integration of two matrixes combining historical and recent deformation records with landslide inventories and PSInSAR data post-dating the landslide-triggering event. For landslides with planimetric areas ranging from 0.007 and 2.107 km^2 Cigna et al. (2012) suggested that landslides must have at least 3 to 5 PSs depicting displacement rates of 2mm/yr (LOS), in order to distinguish stable from unstable areas.

Furthermore, the authors propose a threshold of ±13 mm/yr to discriminate extremely slow (<13mm/yr) from very slow (>13mm/yr) moving slides. The downsizing of the official threshold of 16 mm/year (Cruden and Varnes 1996) is to account for the difference between peak values and temporally averaged velocities (Cigna et al., 2012).

The PSI-based matrix approach was applied to the landslide inventory of the northern Rif. Taking into account that the landslide dataset constitutes an historical record of landslide activity stretching over a period of 46 years (1968-2014) and that only 2% of the inventory can be effectively dated by comparing aerial photos and satellite images, we assume that all large ($La>0.05km^2$) landslides precede the SAR image timeframe used in this study.

A preliminary assessment of the PSs density for each landslide was performed. Figure 4.5 shows the number of PSs plotted against landslide area (La). With the exception of 3 cases, landslides with a planimetric area larger than 0.05 km^2 show a higher concentration of PSs on both the PS2005 and PS2007 datasets. Following the thresholds (landslide area and number of PSs) proposed by Cigna et al. (2012) we limit our analysis to landslides ranging from 0.05 to $2km^2$ and with at least 5 PSs, allowing the classification of 45 landslides, approximately 1.3% of the inventory ($La>0.01km^2$). The activity status of the landslides was reclassified as follows: 1) Active landslides whose displacement rates are: i) lower than 2mm/yr, were classified as dormant/active; ii) higher than 2mm/yr, were classified as active; 2) Dormant landslides whose displacement rates are i) lower than 2mm/yr, were classified as stabilized; ii) higher than 2mm/yr, were classified as reactivated.

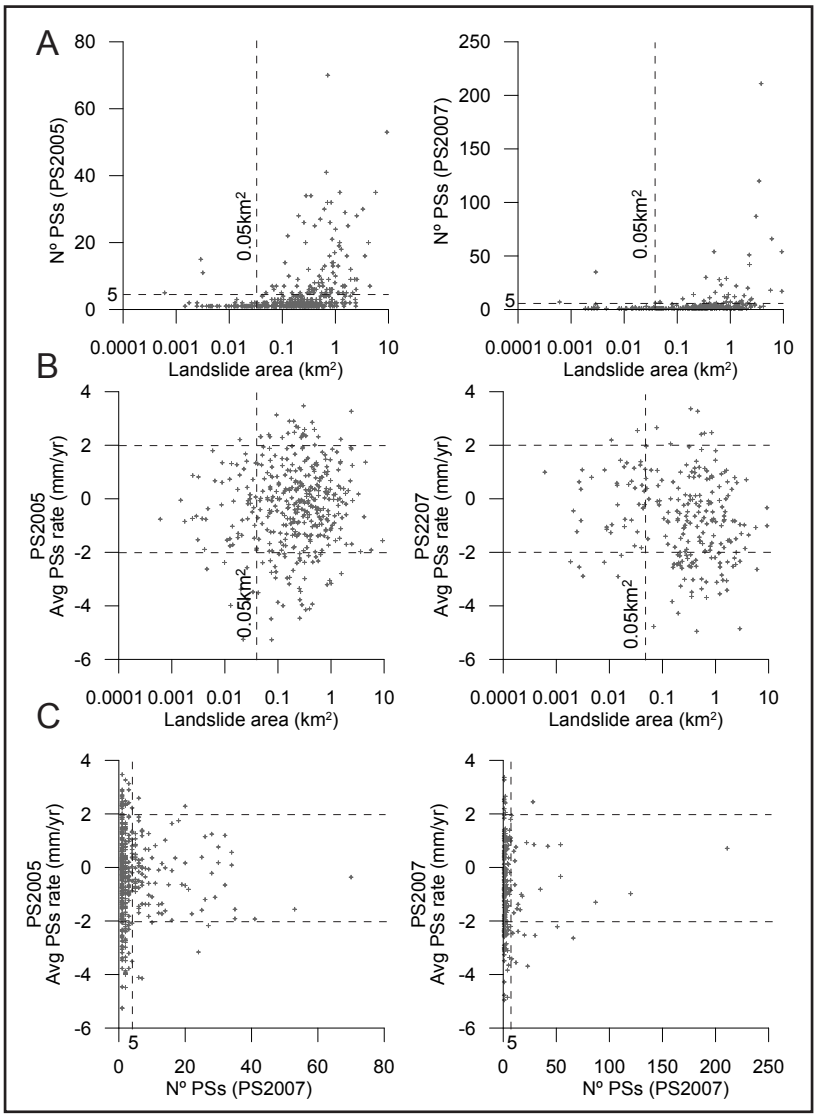


Figure 4.5 – PSs density within landslide limits.
Preliminary assessment of PSs density within landslide limits. A) Landslide area vs. Number of PSs for the PS2005 and PS2007 datasets; B) Landslide area vs. Average PSs rate (LOS) for the PS2005 and PS2007 datasets; Number of PSs vs. Average PSs rate (LOS) for the PS2005 and PS2007 datasets. Dashed lines indicate the thresholds for the application of the PS-based matrix approach (Cigna et al. 2012) for the classification of the activity status.

4.3.3 Hotspot Getis-Ord analysis

The extraction of information from the PSInSAR is sometimes difficult due to the possibility of obtaining a large number of PSs (Lu et al. 2011). Furthermore, in the scope of landslide hazard zonation and early warning system implementation, a rapid assessment of the data is needed. Lu et al. (2011) introduced a PSs spatial statistical approach – the PSI Hotspot and Cluster Analysis (PSI-HCA) – that is based on the Getis–Ord *Gi* statistical approach (Getis and Ord 1992, 1996; Ord and Getis 1995).

The Getis-Ord is a local spatial statistic method that represents the association of a particular

variable (in this case PSs) up to a specified distance (d). The method is applied in this context to evaluate the clustering level of PSs through the provided *Gi score*. The statistic specifies a single PS at a site *i,* and its neighbours *j,* within a searching distance *d.* For each single PS at a site *i,* the *Gi score* is calculated as

$$Gi^*(d) = \frac{\Sigma\, x_j + x_i - n_{ij}\overline{x}^*}{S^*\left\{\left[\left(n \times n_{ij}\right) - n_{ij}^2\right] / (n-1)\right\}^{0.5}}$$

where *n* is the total number of PSs in the data sets; *nij* is the number of PS in the vicinity of searching distance *d,* namely the summation of PS at site *i* and its neighbours *j; x* is the velocity of the PS; *x and s are* the mean value and the standard deviation of PSs velocity for whole data set, respectively.

The statistical method identifies spatial clusters of high values (hot spots) and spatial clusters of low values (cold spots) based on the output of *Gi scores*. A high *Gi* score for a feature indicates a spatial clustering of high values, while a low negative *Gi* score indicates a spatial clustering of low values. The higher or lower the *Gi* score, the more intense is the clustering. A *Gi* score near zero indicates no apparent spatial clustering.

To ensure that all calculations are performed within the same slope unit, d is normally defined (in the presence of high resolution DEMs) as the average of the shortest distance to channel and ridge (Lu et al. 2011). Nonetheless, due to the poor resolution of the available digital terrain data, Sd is here defined as the average over-land flow length from each PS to the ridge and channel (here assumed as proxy to slope length) obtained from an AsterGDEMv2 (pixel size=30.87m; AsterGDEM is a product of METI and NASA). Persistent scatterers located within intra-mountain basins and with displacement rates below 2mm/yr were not included. To facilitate data interpretation and hotspot identification a smoothed surface was applied to the obtained Gi scores through Kernel density estimation following the work of Lu et al. (2011).

4.4 Persistent scatterer distribution outside landslide areas

The PSInSAR technique enabled the identification of 43700 and 23833 PSs for the PS2005 and PS2007 datasets, respectively. Maximum and minimum deformations rates reach 4.4 and -5.2 mm/yr for the PS2005 and 4.9 and -5.7 for the PS2007 datasets (Table 4.1). The spatial distribution and rate along the LOS of PSs located outside landslide areas was analyzed taking into account terrain characteristics usually considered and landslide predisposing conditions, namely slope,

aspect and lithology (Tables 4.2, 4.3 and 4.4). Slope and aspect maps were obtained from the AsterGDEMv2. The lithological data used for the tabulation PSs density was extracted from the work of Suter (1980).

For both datasets, the aspect properties of the terrain seem to exert a similar control in the identification of PSs, with west facing (SW, W and NW) hillslopes congregating over 50% of the PSs in both datasets (Table 4.2). This observation is consistent with the fact that both datasets used in this study result from images that were captured along descending tracks.

Table 4.1 – Persistent scatterer distribution in stable and unstable areas and PSs movement rate outside and inside landslide limits for the PS2005 and PS2007 datasets.

Total number of PSs inside and outside landslides													
Data	**PSs total**	**PSs outside landslides**		**PSs inside landslides**		**Positive PSs outside landslides**		**Negative PSs outside landslides**		**Positive PSs inside landslides**		**Negative PSs inside landslides**	
PS2005	43700	41975	96%	1725	4%	21885	53%	20084	47%	710	41%	1015	59%
PS2007	23833	21449	90%	2384	10%	11680	54%	9764	46%	1220	51%	1162	48%
Total number of PSs inside and outside landslide ≥2 and ≤-2 mm/yr													
Data	**Total**	**PSs outside landslides**		**PSs inside landslides**		**PSs outside landslide ≥2 mm/yr**		**PSs outside landslide≤-2 mm/yr**		**PSs inside landslide ≥2 mm/yr**		**PSs inside landslide ≤-2 mm/yr**	
PS2005	8854	8507	96%	347	4%	4118	48%	4389	52%	92	27%	255	73%
PS2007	4242	3883	92%	359	8%	1685	43%	2198	57%	62	17%	297	83%

Statistics of PSs displacement rates inside and outside landslides								
Data	**PSs rate (mm/yr) outside landslides**				**PSs rate (mm/yr) inside landslides**			
	Max	**Min**	**Avg**	**Std**	**Max**	**Min**	**Avg**	**Std**
PS2005	4.4	-5.2	-0.2	2.3	4.4	-5.3	-0.4	1.6
PS2005	4.9	-5.7	-0.1	2.2	3.4	-5.7	-0.29	1.5

Slight differences in the distribution of PSs and hillslope angle are observed. For the PS2005 dataset, hillslope angle between 5 and 15 degrees gather 36% of the generated PSs, while for the PS2007 approximately 38% of the PSs occur in slopes ranging from 10 to 20 degrees (Table 4.3). These differences are related to the topographic conditions and to variations in the slope frequency distribution between the western and eastern sectors of the mountain belt. While the PS2005 dataset covers the eastern portion of the study area, a sector dominated by deeply incised into the compact bedrock units of the Ketama and Tiziren domain, the PS2007 extends further west covering an area dominated by larger and wider valleys incising the marly and clay domain of the Tanger

Unit. Furthermore, the PS2007 data extends into the low relief setting of the external zones were the slope is typically low.

In what concerns bedrock lithology, PSs tend to occur in association with compact limestone, dolomite and sandstone units (Table 4.4), which provide higher terrain roughness conditions and better backscattering properties. Nonetheless, marly and marly-limestone units gather the majority of the PSs in both datasets (PS2005 – 33%; PS2007 – 27%). The explanation to this fact lies in the characteristic of the human occupation and vegetation cover of the Rif. Marl and clay outcrops tend to occur in the lower sectors of the valleys and along the external zones of the Rif were buildings density is the highest and vegetation cover is lower. These conditions increase the backscattering quality of the signal captured by the satellite. Furthermore, the presence of limestone, schist and occasional limestone intercalations within the marly sequences are prone to scatter PS-like signal, particularly when associated to low dense vegetated areas. Similar results have been obtained in the regions of Arruda dos Vinhos and Fanhões-Trancão/Lousa (north of Lisbon, Portugal) (Nico et al 2009).

Table 4.2 - PSs distribution per slope aspect class and PSs displacement rate statistics for the PS2005 and PS2007 datasets.
The most relevant correlations are highlighted in grey.

Slope aspect	Number of PSs		%		Number of PSs >2 and <-2mm/yr		Avg. PSs rate (mm/yr)		Std. PSs rate (mm/yr)	
	PS2005	PS2007	PS2005	PS2007	PS2005	PS2007	PS2005	PS2007	PS2005	PS2007
North (337.6°-22.5°)	765	339	2	1	273	94	0.0	-0.2	1.5	1.3
North-East (22.6°-67.5°)	1588	974	4	4	580	319	-0.1	-0.3	1.6	1.5
East (67.6°-112.5°)	1964	1148	4	5	757	415	-0.1	-0.3	1.6	1.6
South-East (112.6°-157.5°)	2859	1573	7	7	1090	550	0.0	-0.2	1.6	1.6
South (157.6°-202.5°)	5946	2972	14	12	2205	1013	-0.1	-0.1	1.6	1.7
South-West (202.6°-247.5°)	10768	6238	**25**	**26**	3951	1948	0.0	0.0	1.5	1.6
West (247.6°-292.5°)	11945	7392	**27**	**31**	4516	2076	0.0	0.2	1.6	1.4
North-West (292.6°-337.5°)	7865	3197	18	13	2932	940	0.0	0.1	1.6	1.5

Table 4.3 - PSs distribution per hillslope slope angle class and PSs displacement rate statistics for the PS2005 and PS2007 datasets.
The most relevant correlations are highlighted in grey.

Slope angle	Number of PSs		%		Number of PSs >2 and <-2mm/yr		Avg. PSs rate (mm/yr)		Std. PSs rate (mm/yr)	
	PS2005	PS2007	PS2005	PS2007	PS2005	PS2007	PS2005	PS2007	PS2005	PS2007
0 - 5°	3203	2142	7	9	1256	755	0.2	-0.1	1.6	1.7
5 - 10°	6592	4552	**15**	**19**	2648	1515	0.0	-0.1	1.7	1.6
10 - 15°	8049	4601	**18**	**19**	3169	1518	0.0	-0.1	1.6	1.6
15 - 20°	7797	3890	**18**	**16**	2976	1174	0.0	-0.1	1.6	1.5
20 - 25°	6597	2973	15	12	2375	857	-0.1	0.1	1.5	1.5
25 - 30°	5032	2171	12	9	1716	605	0.0	0.0	1.5	1.5
30 - 35°	3248	1554	7	7	1152	404	0.0	0.2	1.5	1.4
35 - 40°	1883	999	4	4	625	288	0.0	0.3	1.5	1.4
40 - 45°	890	552	2	2	276	153	0.0	0.4	1.4	1.3
> 45°	409	399	1	2	132	104	0.1	0.5	1.4	1.3

4.5 PSs distribution and landslide activity

The set of georeferenced PSs was overlaid to the landslide inventory map of the northern Rif. Taking into account landslide typology and the terrain properties within landslides we observe that PSs follow a similar trend, concentrating along west facing slides (NW, W and SW) and in association to slopes less than 20 degrees (Fig. 4.6). Furthermore, PSs tend to be connected to large (>0.5km^2) complex, flow and slides. Deformation rates are highest within large complex slides reaching maximum rates of 3.7 and -5.7 mm/yr (Fig. 4.6). For the majority of the dataset, negative deformation rates exceed positive values by a factor of 1 to 2mm/yr. This is particularly evident for slopes less than 20 degrees for slides and complex slope movements, as well as for DSGSD cases in the PS2005 dataset (Fig. 4.6). Conceptually, the kinematical behavior of the landslide typologies gathering higher PSs concentration with rates ranging from 4.9 to -5.7 mm/yr is consistent with displacement rates of extremely slow moving landslides (Cigna et al. 2012).

Only 4% and 10% of the PSs within the PS2005 and PS2007 datasets, respectively, fall inside landslide limits (Table 4.1). For the PS2005 dataset nearly 60% of the PSs relate to negative deformation along the LOS and deformation rates inside and outside landslide bodies are comparable, ranging from 4.9 to -5.7 mm/yr (Table 4.1).

If we take into account the number of PSs with deformation rates above 2 mm/yr, only 4% and 8% of the PS2005 and PS2007 datasets respectively, occur within landslides and nearly 73% and 83% of those PSs refer to negative deformation (LOS) (Fig. 4.5).

The application of the PSI-based matrix approach enabled the reclassification of the landslide activity status for only 1.3% (45 landslides) of the inventory of large bedrock landslides with a planimetric area between 0.05 and 2km^2 (Fig. 4.7): 11 dormant landslide were reclassified as

stabilized; 8 active landslides were reactivated and classified as active; 2 active landslides were reclassified as dormant/active; 24 dormant slides were reactivated and classified as active.

Table 4.4 - PSs distribution per lithological unit of the Rif (Suter, 1980) and PSs displacement rate statistics for the PS2005 and PS2007 datasets.
The most relevant correlations are highlighted in grey.

Lithology (Suter 1980)	Number of PSs		%		Number of PSs≥2 and ≤-2 mm/yr		Avg. PSs rate (mm/yr)		Std. PSs rate (mm/yr)	
	PS2005	PS2007	PS2005	PS2007	PS2005	PS2007	PS2005	PS2007	PS2005	PS2007
Breccia	83	22	0.19	0.09	42	12	-1.5	-1.6	1.6	1.3
Breccia, sandstone and conglomerate	1223	749	2.80	3.14	427	230	0.30	-0.7	1.4	1.4
Clay	165	69	0.38	0.29	87	11	1.1	-0.3	1.5	1.2
Compact limestone	1954	4175	4.47	**17.52**	529	465	0.5	0.4	1.2	0.8
Compact limestone and flysch	2288	528	5.24	2.22	85	2	0.3	2.4	1.4	0.1
Compact sandstone	1398	1045	3.20	4.38	178	591	-1.2	-1.3	1.6	1.7
Compact sandstone and marls	7780	417	**17.80**	1.75	2706	230	0.1	-1.0	1.5	2.0
Compact limestone and oolitic limestone	2925	1491	6.69	**6.26**	791	539	-0.2	-0.1	1.2	1.4
Dolomite	428	1264	0.98	5.30	142	88	-0.2	0.2	1.4	0.9
Flysch	2144	1097	4.91	4.60	763	275	-0.4	-0.4	1.5	1.3
Flysch, clay and Schists	197	818	0.45	3.43	108	308	-0.7	0.6	1.8	1.4
Gnaisses	193	62	0.44	0.26	50	43	-0.3	-1.8	1.2	1.2
Limestone	1728	2074	3.95	8.70	50	11	-1.2	0.2	0.9	1.0
Marl and limestone	6096	281	**13.95**	1.18	2017	114	-0.3	0.1	1.6	1.6
Marl	8437	6404	**19.31**	**26.87**	3638	2159	-0.2	-0.2	1.7	1.6
Marl and marly-limestone	1672	591	3.83	2.48	768	172	-0.1	-0.1	1.8	1.4
Marly limestone	341	612	0.78	2.57	146	125	-0.5	-0.5	1.6	1.6
Micaschist	97	42	0.22	0.18	21	24	-0.1	-1.5	1.2	1.7
Olistolites	111	-	0.25	-	128	-	-1.1	-	1.5	-
Peridotites	133	45	0.30	0.19	53	31	-0.8	-2.0	1.1	1.4
Sandstone	381	-	0.87	-	36	-	-0.4	-	1.5	-
Sandstone and clay	156	98	0.36	0.41	32	54	-0.2	-0.9	1	2.0
Sandstone and conglomerate	22	384	0.05	1.61	178	185	-1.1	-1.4	0.7	1.6
Sandstone, clay and limestone intercalations	592	55	1.35	0.23	7	47	0.4	-2.9	1.4	1.0
Schist	118	1406	0.27	5.90	32	203	-0.6	0.4	1.2	0.9
Schist, clay with fine sandstone intercalations	202	104	0.46	0.44	52	81	0.0	1.5	1.2	1.7

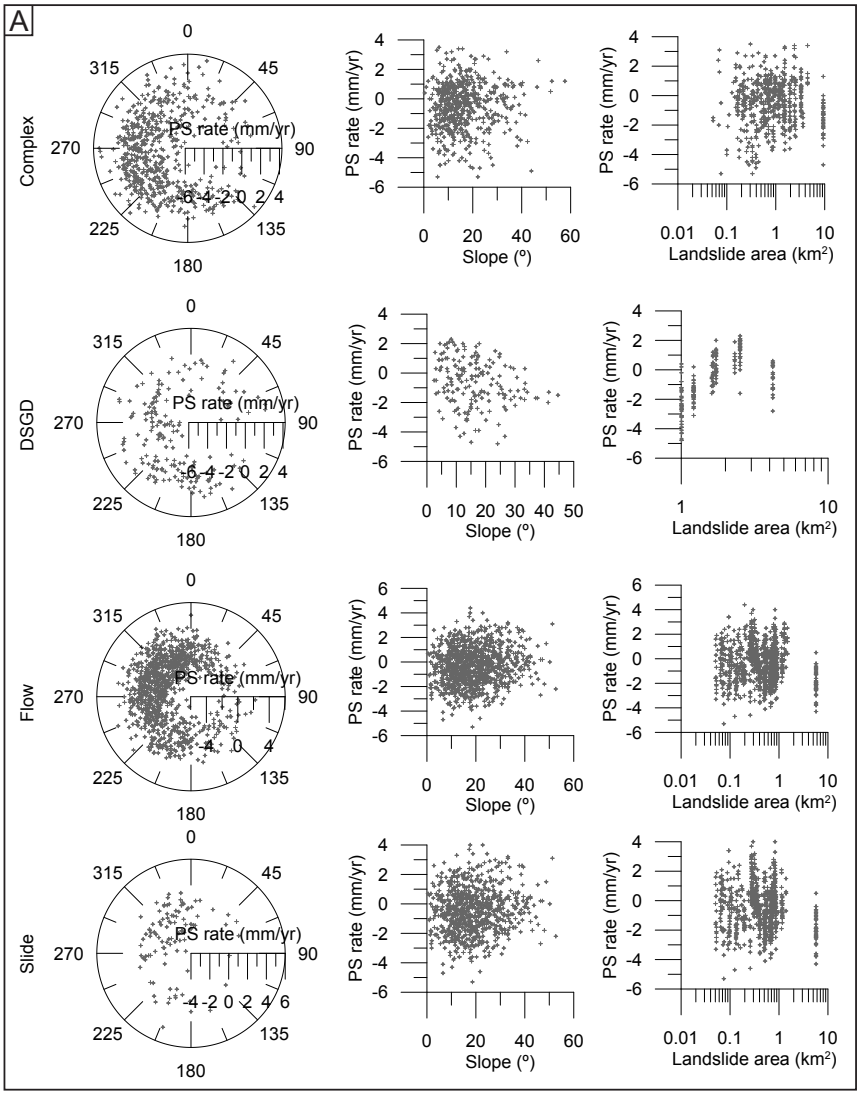


Figure 4.6 – PSs deformation rate along the satellite LOS
PSs deformation rate along the satellite LOS for the PS2005 (A) and PS2007 (B) datasets vs. aspect, slope and landslide area of large bedrock failures.

4.6 Hotspot and cluster analysis

The output of PSI-HCA is a hotspot map (Fig. 4.8) highlighting areas that are potentially affected by slow gravitational slope deformation. A total of 75 hotspots were obtained from the PS2005 (43) and PS2007 (32) datasets. The results are displayed based on the kernel density estimation. Pixels with high positive values are shown with the blue color, while clustering of low negative pixels are displayed with the red color. Potentially, both blue and red hotspots indicate where active slope deformation occurred. Furthermore, the color of the hotspots provides information of the moving direction. Blue hotspots indicate movement towards the LOS (positive velocity) and red hotspots indicate sites were PSs are moving away from the LOS (negative velocity).

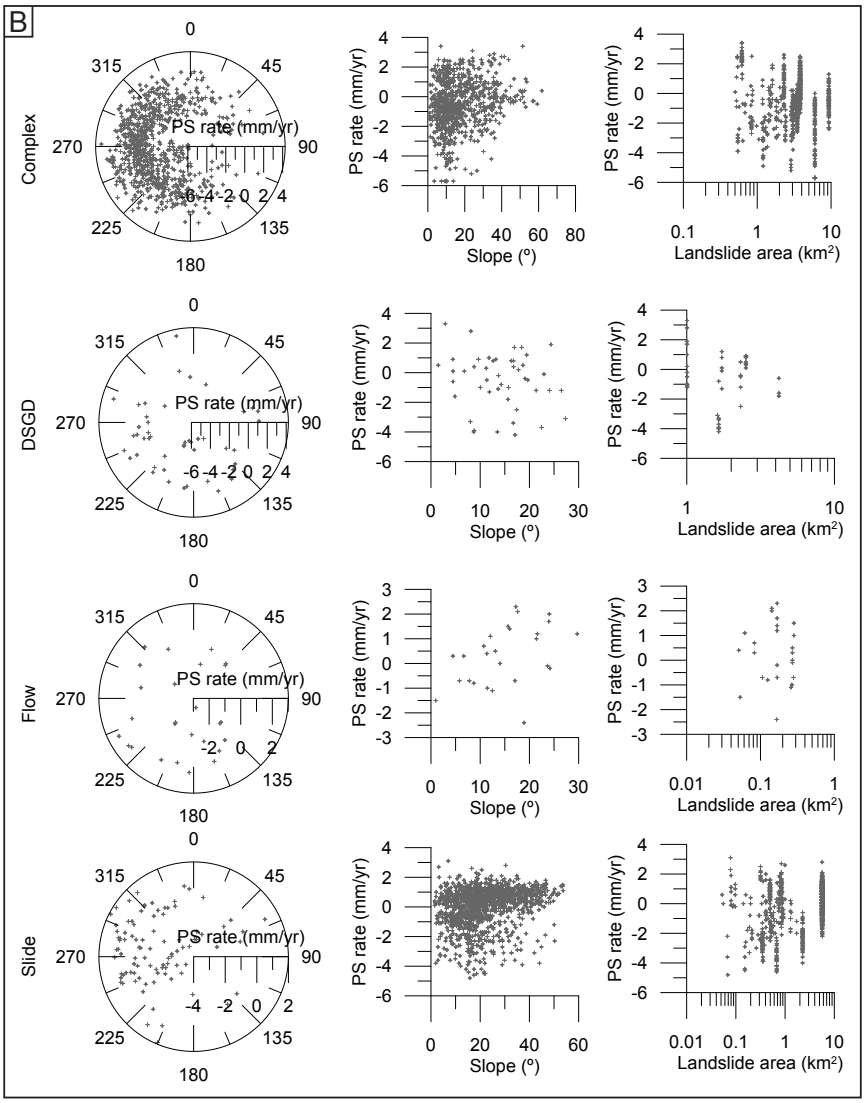


Figure 4.6 – (continued).

4.7 Landslide cases

Assuming that the PSI-based matrix approach and the PSI-hotspot cluster analysis enabled the identification of potential sectors experiencing active gravitational deformation, we now focus our attention on seven landslide cases to analyze the spatial distribution of PSs taking into account landslide geomorphology. The selected landslides are shown on figures 4.7 and 4.8.

4.7.1 Jebel Sougna: Tiarta and El Marhza landslides

The Tiarta and El Marhza landslides are located along the western flank of Jebel Sougna. Slope deformation occurs along the contact between the Numidian sandstone and the Tanger Unit.

Present-day landslide activity is detected by the presence of red colored hotspots indicating gravitational movement away from the satellite LOS (Fig. 4.8).

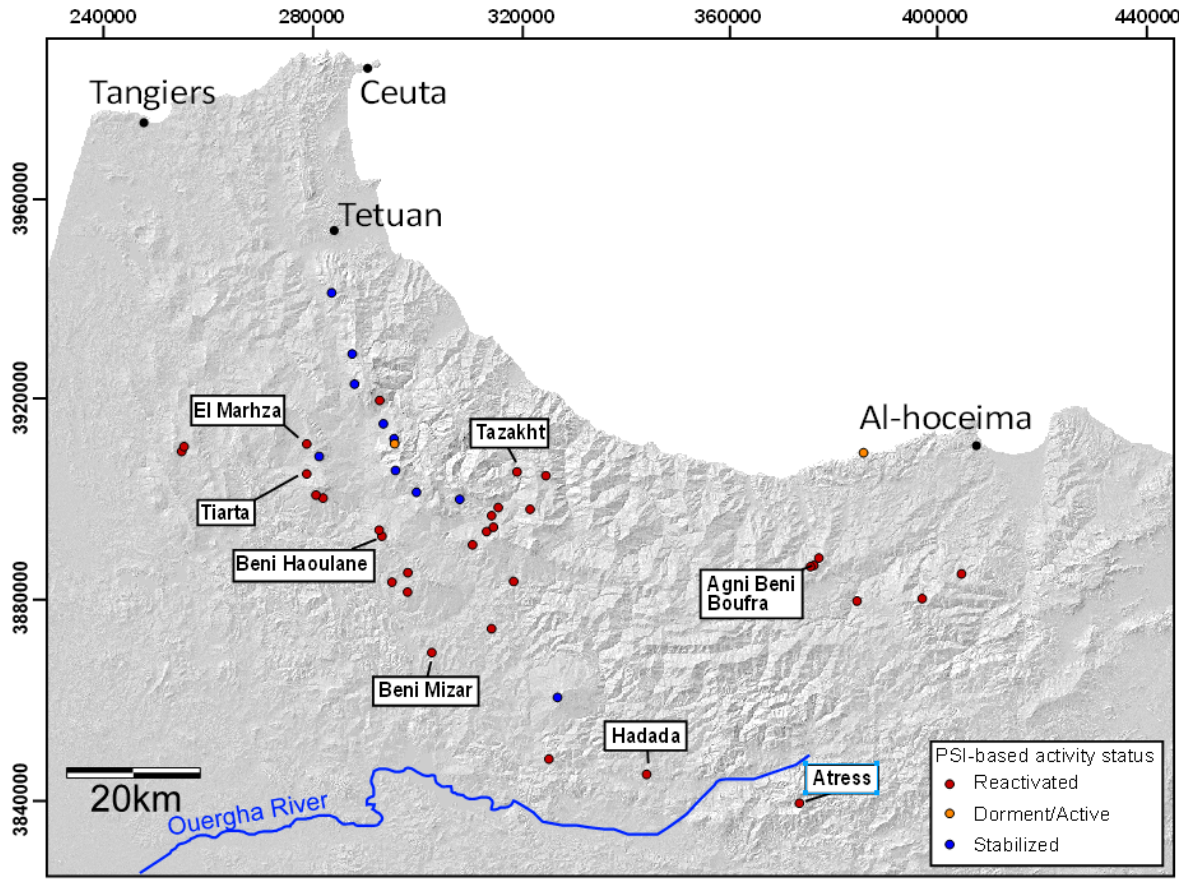


Figure 4.7 - Landslide activity status reclassification following the PSI-based matrix approach.

The Tiarta landslide (Fig. 4.9) is a complex deep-seated landslide. It has a runout distance of approximately 4.6km and reaches a maximum altitude of 1300 asl. Aerial photo interpretation and the analysis of satellite images enabled the identification of five landslide units (L1 through L5) within the runout area that relate to different evolution stages of the landslide (Fig. 4.9). The contact between units is established through gravitational thrusting along the toe of the landslide or through lateral propagation following a lower preexisting topography.

The spatial distribution of PSs is consistent with the landslide-affected area, showing deformation rates ranging from 2.5 to -4.5mm/yr. The consistency between the negative PSs rates indicates a slow gravitational movement away from the LOS. Nonetheless PSs are limited to the upper and most recent portion of the landslide, positioned above L5, and concentrated along the detachment area and frontal lobe.

The El Marhza landslide (Fig. 4.10) detaches from the Numidian ridges at approximately 1350 asl and extends over 4.3km down to the valley floor. It is composed of two main detachment areas

from which two landslide masses propagate and coalesce before reaching the valley bottom. The morphological evidence of slope deformation in the toe area is the hummocky topography and lateral-pressure ridges, which forms along the boundary between the two landslide bodies.

Similarly to the latter case, PSs distribution is consistent with the landslide-affected area, with deformation rate ranging from 1.5 to -4.5 mm/yr (Fig. 4.10). The consistency between the negative PSs rates along the LOS provides evidence to the present-day activity of the landslide. Nonetheless, the absence of PSs along the toe area hampers the association of the observed rates to movement along the whole length of the landslide.

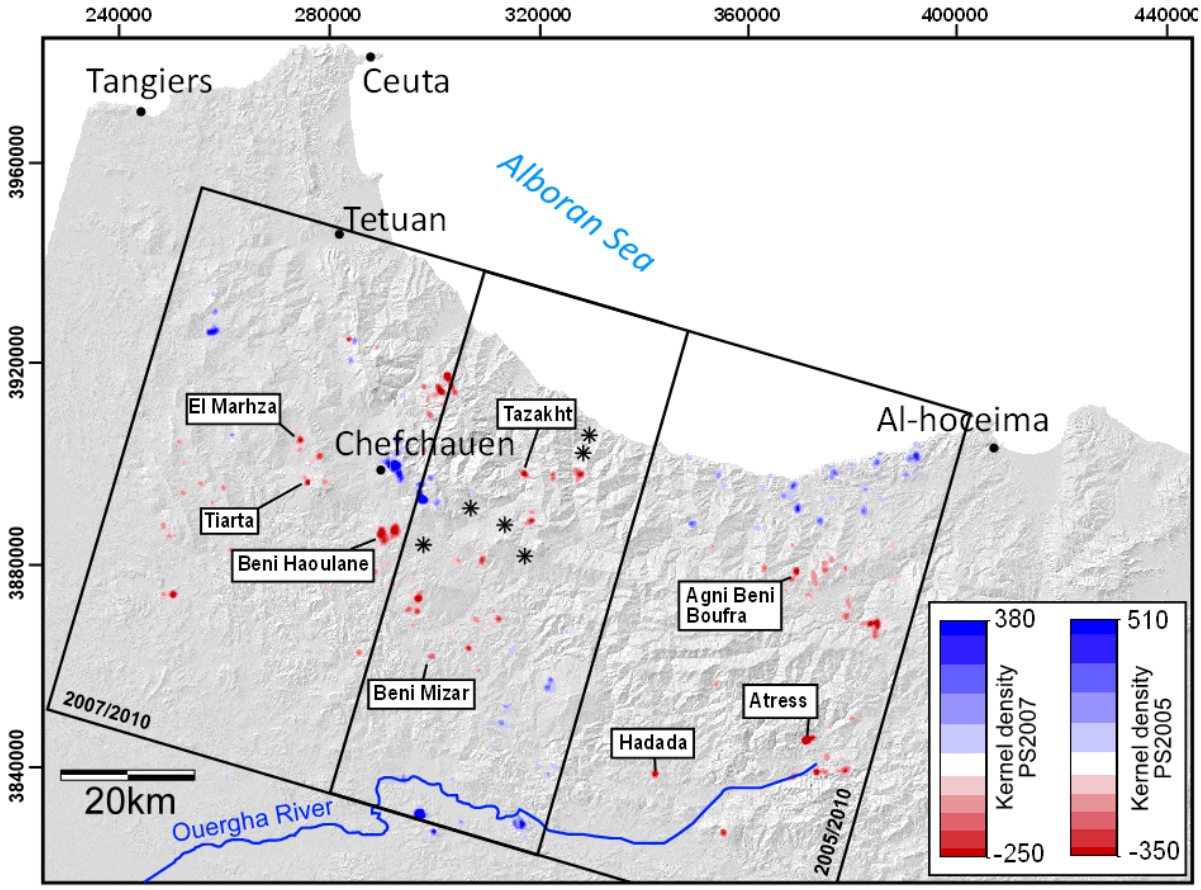


Figure 4.8 - PSI hotspot map of the northern Rif Mountains.
PSI hotspot map derived from kernel density estimation of Gi scores obtained from the PS2007 and PS2005 persistent scatterers (PSs). Red hotspots (low negative kernel density) indicate the clustering of high-velocity PSs moving away from the sensor, whereas blue hotspots (high positive kernel density) imply the clustering of high-velocity PSs moving towards the sensor. Asterixs locate the landslide reactivations identified during the winter of 2009-2010.

4.7.2 Beni Haoulane landslide

The Beni Haoulane landslide detaches from the Numidian ridge along the western flank of Jebel Ressana. Landslide activity is detected by the presence of a red hotspot indicating gravitational movement away from the satellite LOS (Fig. 4.7).

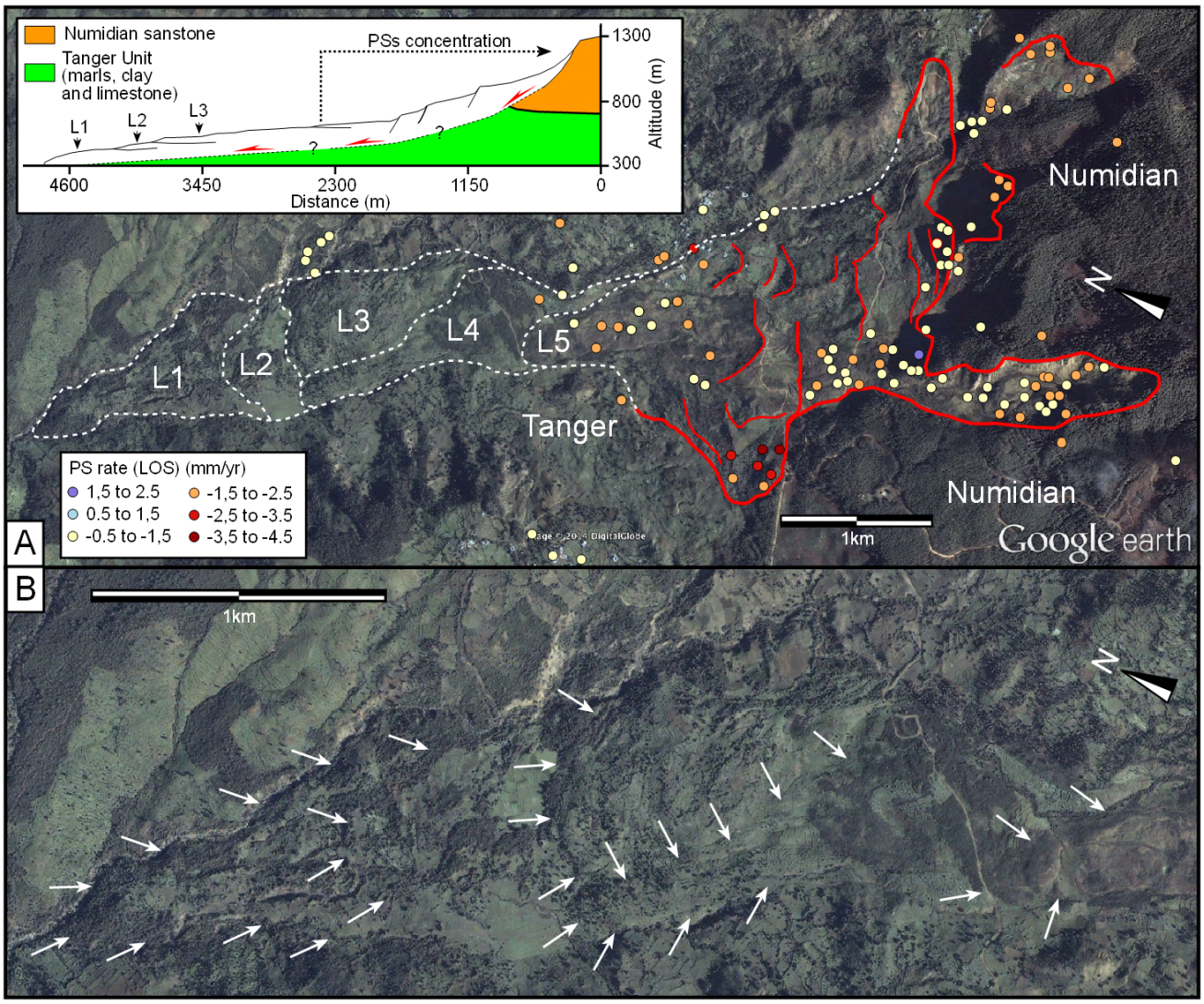


Figure 4.9 – Tiarta landslide.
A) Tiarta landslide geomorphology and PSs distribution. Red line marks the position of landslide scarps; dashed white line indicates the limit of the landslide body and landslide units (see text for explanation); B) Detail of the frontal lobe. White arrows indicate the limit to the landslide units.

The geological context in which slope deformation occurs is similar to the landslide cases of Jebel Sougna (Fig. 4.11). The landslide scarp is positioned close to the top of the Numidian ridges at a maximum altitude of 1390m asl. Within the detachment area the collapsed section of the Numidian sandstone is preserved. Below this point the landslide body is established within the bedrock context of the Tanger Unit and is composed of two tongues flowing to the north and west, which are separated by the drainage divide of the Wadi Loukous and Wadi Audour, respectively (Fig. 4.11). Geomorphic evidences of slope deformation are characterized by scarp formation within the mobilized sandstone unit and lateral ridges along the flowing units. However, it is unclear if these

features relate to a single landslide case or to the coalescence of the detachment areas through retrogressive sliding of the flowing tongs.

PSs distribution is consistent with the landslide-affected area, revealing deformation rates ranging from -0.5 to -3.5 mm/yr (Fig. 4.11). The high concentration of PSs in the main detachment area and along the north flowing tongue at rates of -2.5 to - 3.5 mm/yr indicates the presence of active gravitational deformation away from the satellite LOS.

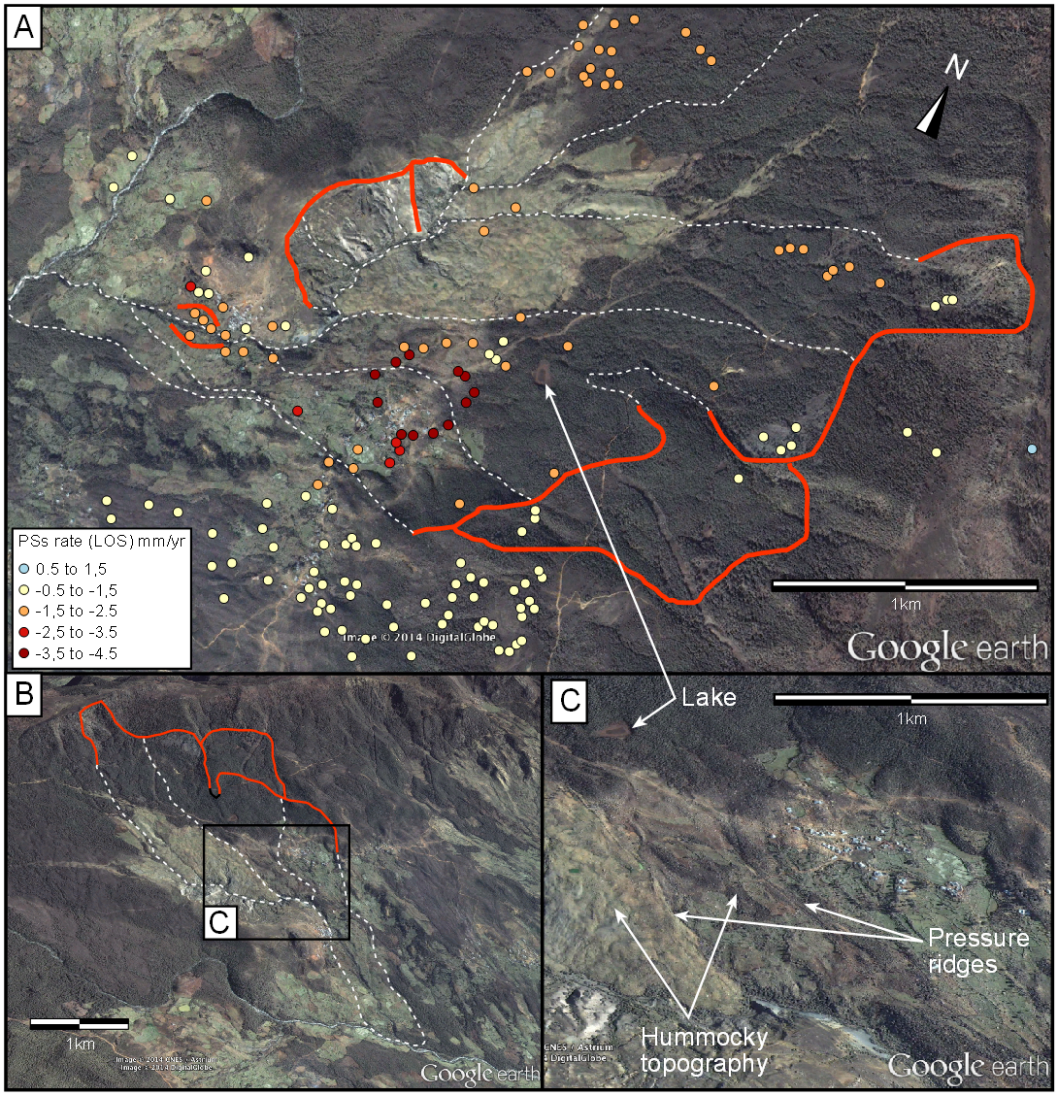


Figure 4.10 - El Marhza landslide.
Geomorphology and PSs distribution. Red line marks the position of landslide scarps; dashed white line indicates the limits of the landslide body and landslide units. A) Landslide overview and PSs distribution; B) Bird-eye view of the landslide; C) Detail of landslide units displaying geomorphic evidences of distinct displacement rates.

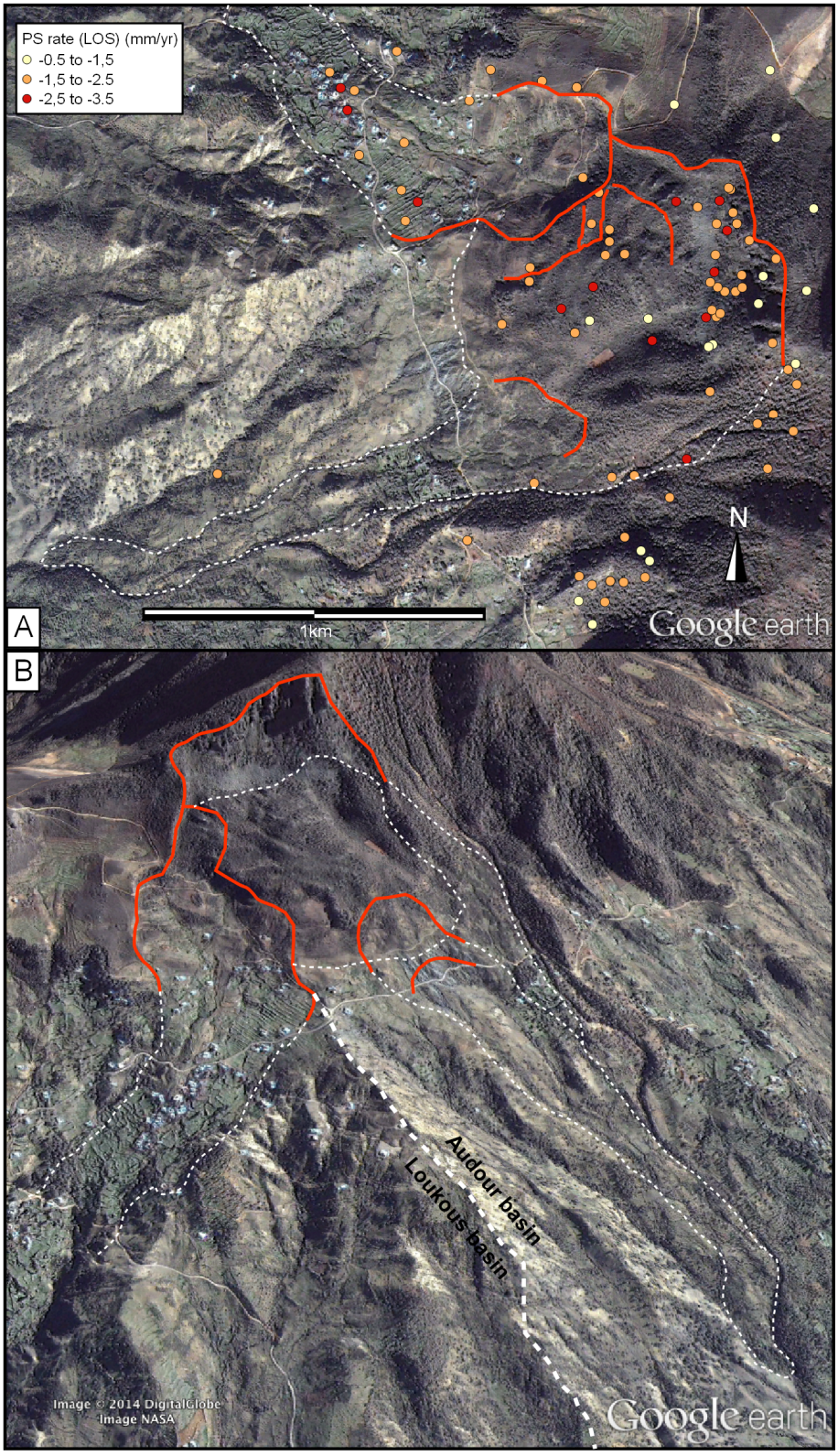


Figure 4.11 - Beni Haoulane landslide.
Geomorphology and PSs distribution. Red line marks the position of landslide scarps; dashed white line indicates the limit of the landslide body and landslide units. A) Landslide overview and PSs distribution; B) Bird-eye view of the landslide.

4.7.3 Tazakht landslide

The Tazakht rockslide is located in the Internal Domain, along the valley of the Wadi Bouhia. Slope deformation is detected through the presence of a red colored hotspot (Fig. 4.12). The landslide affects a nappe stack of dolomitic limestone, clay and flysch belonging to the Dorsal Calcaire, Sebtides and Ghomarides units, respectively. The rockslide covers and area of 0.3km^2 and extends over 740m in the runout sector. The collapsed debris reached the valley floor and created a 20 to 30 meter knick in the longitudinal profile of the river, suggesting river damming following the landslide event. Nonetheless, significant post failure erosion has already taken place through lateral fluvial erosion. This is evidenced by the presence of secondary slide scarps occurring at the base of the deposit (Fig. 4.12).

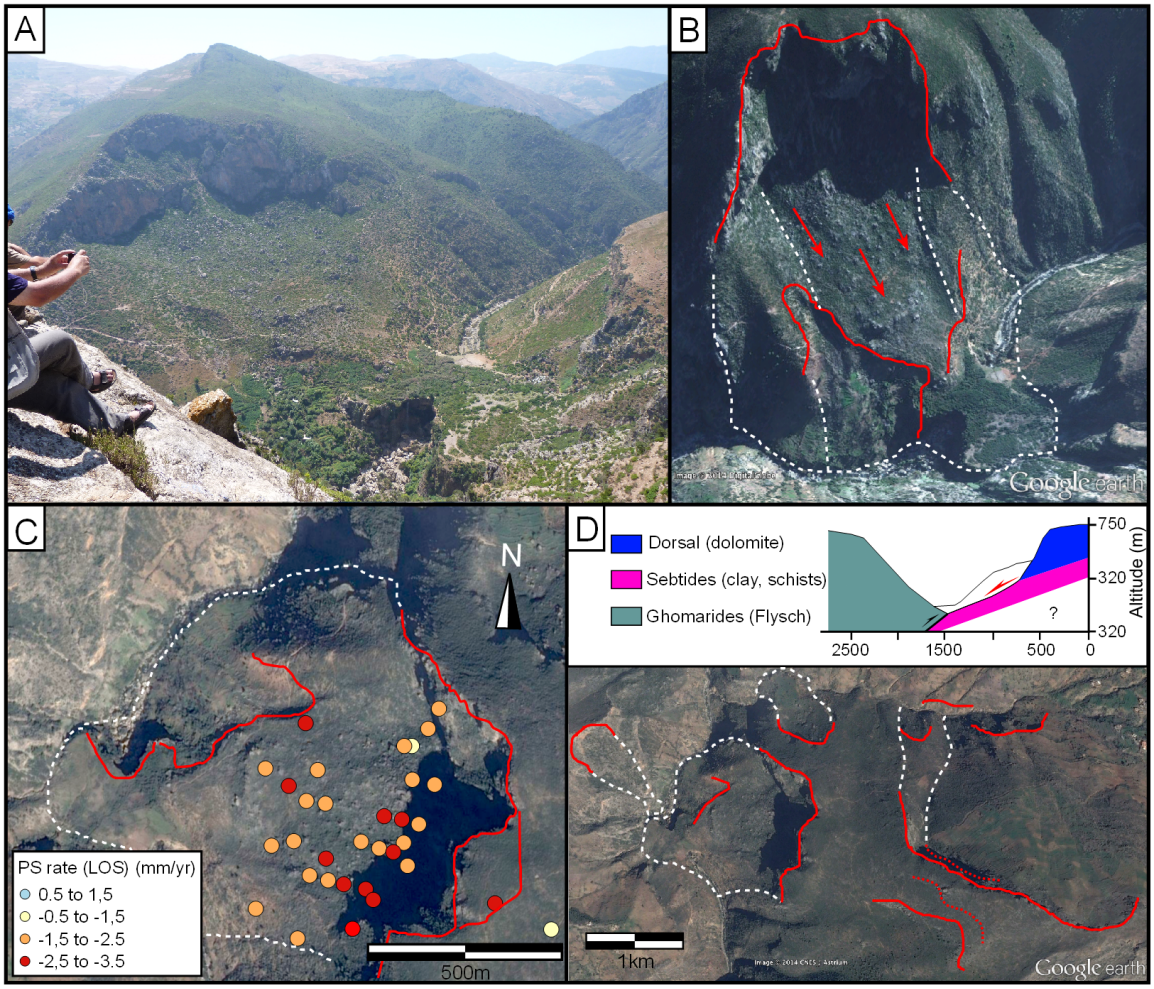


Figure 4.12 - Tazakht landslide.
Geomorphology and PSs distribution. A) Photo of the landslide deposit looking south-east; B) Bird-eye view of the landslide; C) Landslide overview and PSs distribution; D) Gravitational features around the Tazakht landslide. Red line marks the position of landslide scarps; dashed white line indicates the limit of the landslide body and landslide units.

PSs fall within the limits of the landslide-affected area. Deformation rates range from -0.5 to -3.5 mm/yr. Terrain roughness associated with the presence of limestone blocks inside the landslide body enabled the identification of PSs. Nonetheless, landslide activity as detected through PSInSAR seems associated with movement of the landslide debris in response to a gravitational destabilization process created by the lateral fluvial erosion along the base of the landslide body.

4.7.4 Beni Mizar landslide

The Beni Mizar landslide is a translational slide occurring in the context of the Tanger Unit. Slope deformation is consistent with the attitude of the marly and clay bed, which strike approximately W-E, dipping 15-20 degrees to the north (Lepinasse et al. 1970).

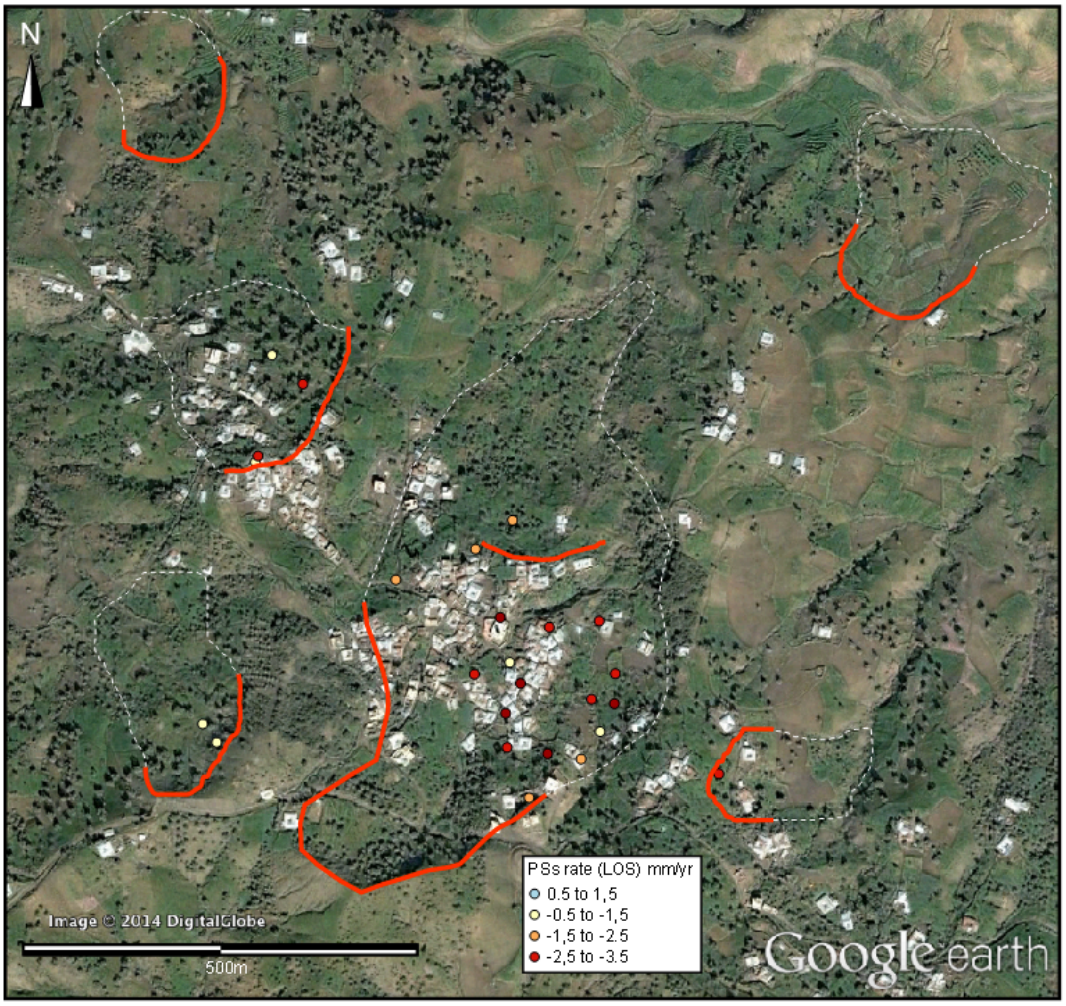


Figure 4.13 - Beni Mizar landslide.
Geomorphology and PSs distribution. Red line marks the position of landslide scarps; dashed white line indicates the limit of the landslide body and landslide units.

Slope deformation is detected through the presence of a red colored hotspot. The application of the InSAR method is clearly favored by the presence of the village inside the limits of the landslide as nearly 60% of the PSs are related to anthropogenic features. Locally, PSs distribution is consistent with the limits of the mapped landslide, experiencing deformation rates of –1.5 to -5.5 mm/yr in the crown area (Fig. 4.13).

4.7.5 Agni Beni Boufra landslide

The Agni Beni Boufra landslide is located in the northeastern edge of the study area. It is a complex deep-seated landslide established along the south-dipping thrust sheets of the Tiziren Unit and the Chouamat Formation (Fig. 4.14). Khattaby & Carlier (2004) studied the mechanical and hydrogeological conditions favoring slope deformation at this site and showed that the cohesion and angle of internal friction of the schists of the Chouamat Formation undergo transformations when water is present. According to the authors, the Chouamat schists form the substratum of the subsurface aquifer and may be considered as the rock horizon along which shear primarily occurs.
The distribution of PSs is consistent with the limits of the landslide. Nonetheless, deformation rates are low when compared with the previous examples (1.5 to -2.5 mm/yr) and the highest negative rates occur within secondary failures or associated with scree deposits within the landslide body (Fig. 4.14).

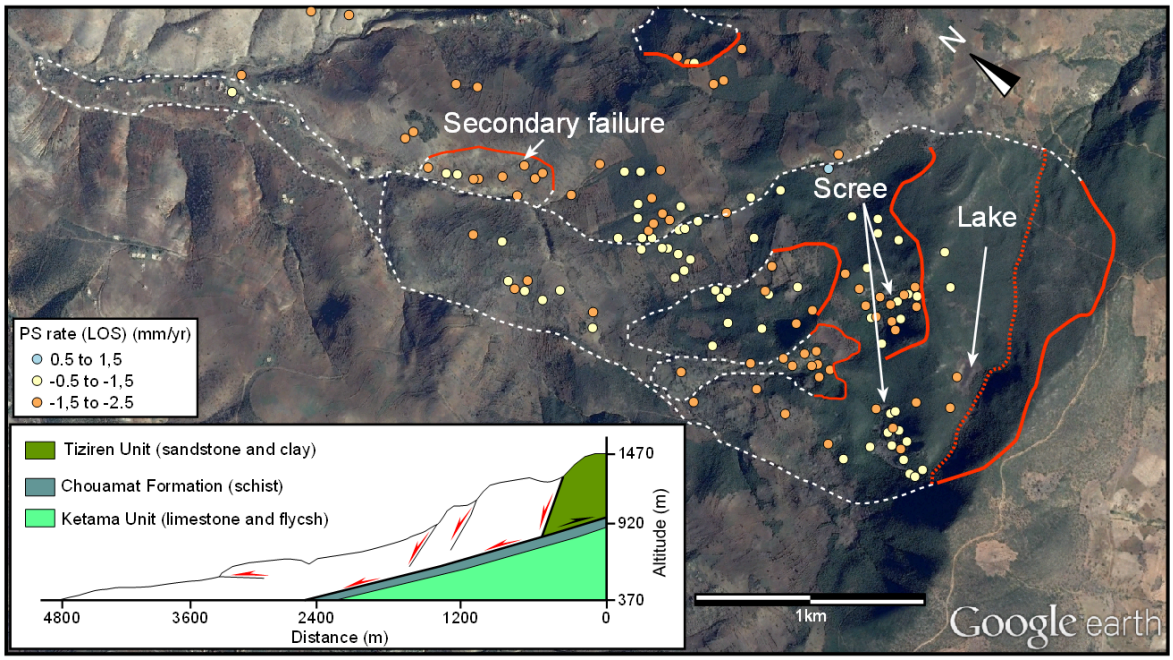


Figure 4.14 - Agni Beni Boufra landslide.
Geomorphology and PSs distribution. Red line marks the position of landslide scarps; dashed white line indicates the limit of the landslide body and landslide units.

4.7.6 Hadada landslide

Located on the northern boarder of the Mesorif zone, the Hadada translational landslide affects the marls and clays of the Upper and Lower Tanger Unit (Fig. 4.15). This particular landslide was not initially present in the inventory and was later detected through hotspot mapping. The inspection of aerial photos and satellite images enabled the definition of at least two landslide units (Fig. 4.15), with unit 2 representing a reactivation stage of the landslide unit 1.

PSs distribution is consistent with the limits of the landslide area showing deformation rates raging from -0.5 to -3.5 mm/yr, with the lowest values occurring within the upper sector of the landslide body. These observations are consistent with terrain morphology and with the translational component of the Hadada landslide, showing that active slope deformation is presently occurring in the crown area.

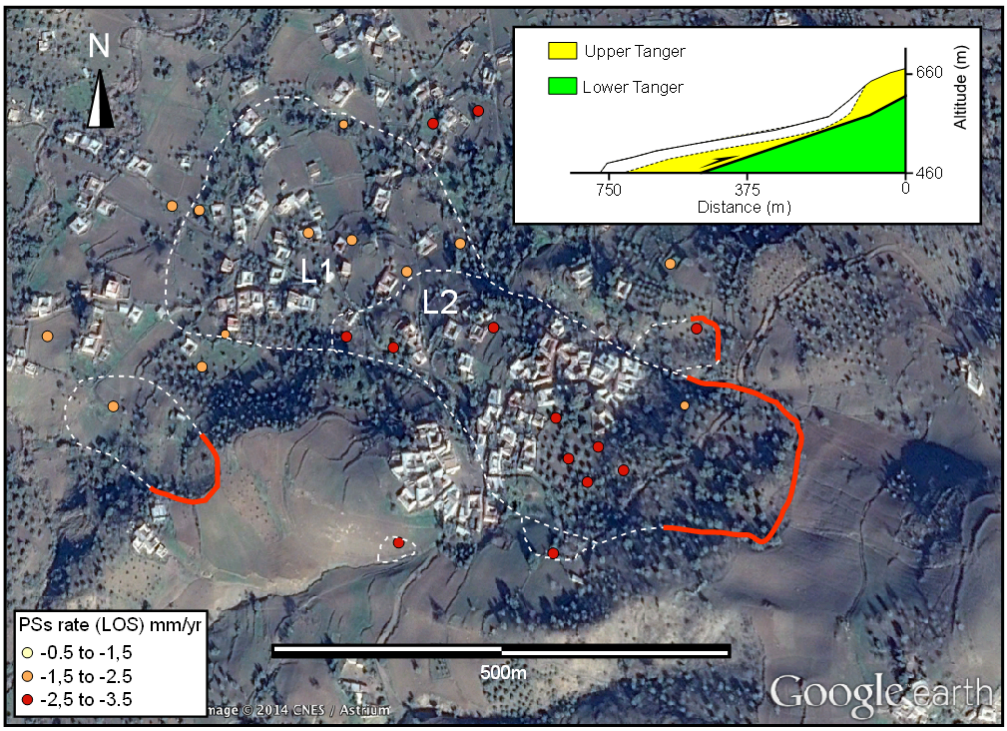


Figure 4.15 - Hadada landslide.
Geomorphology and PSs distribution. Red line marks the position of landslide scarps; dashed white line indicates the limit of the landslide body and landslide units.

4.7.7 Atress landslide

The Jebel Atress landslide covers an area of 0.7km^2 and a runout distance of over 1km. Slope deformation occurs along the tectonic contact between the Lower Ketama Unit and the Mesorif Zone, affecting a thrust sequence of marls and dolomitic limestone (Fig. 4.16).

Slope deformation is detected through the presence of red colored hotspots indicating terrain movement away from the satellite LOS (Fig. 4.7). The detection of PSs is favored by the presence of limestone blocks occurring on top the landslide body therefore increasing terrain roughness.

The distribution of PSs is consistent with the landslide morphology, depicting deformation rates of 1.5 to -3.5 mm/yr. The majority of the PSs positioned inside the landslide mass indicate low deformation rates (1.5 to -1.5 mm/yr), which most probably expresses gravitational stability. Nonetheless, the highest negative rates are obtained for the detachment area, showing active subsidence within the compact dolomitic limestone unit. The inspection of satellite images tends to confirm these observations showing a step-like morphology towards the top of the valley flank (Fig. 4.16).

4.8 Discussion and conclusion

From a methodological perspective, while the number of SAR images used in this study (PS2005 = 20 images; PS2007 = 21images) are within the recommended sample size for the application of the PSInSAR method (minimum of 20 images), the dataset presents a low temporal frequency considering the six-year SAR image timeframe used for PSs detection. This fact hampers the consistency of PSs detection and the definition of temporal deformation series for particular landslide cases or hotspot locations.

One of the most relevant factors obstructing PSs detection within landslides relates to the occurrence of triggering events during the winter period of 2009-2010. Since the employed SAR wavelengths and revisiting times of the ENVISAT satellite can only detect slope movement up to maximum value of 15cm/yr, it is probable that PSs acquisition is significantly hindered for the period in consideration.

Nonetheless, the application of the PSI-HCA method enabled the identification of sectors affected by deformation. Slope movement expressed as high velocity hotspots is consistent with sectors previously identified with deep-seated slope deformation. According to Lu et al. (2011), the radius of each hotspot implies the extent of a potential landslide-affected area. Nonetheless, in our dataset, some hotspots extend beyond the upper limits of the slope (Fig. 4.8). This is a result of the method used to calculate the parameter d (search distance) for the Getis-Ord statistic. By using a low resolution DEM and using the overland flow-length as a proxy to slope length, our results tend to over-cluster the PSs data sets. This methodological bias potentially results in an overestimation of landslides and makes difficult to differentiate landslides from other geomorphic

processes (Lu et al. 2011).

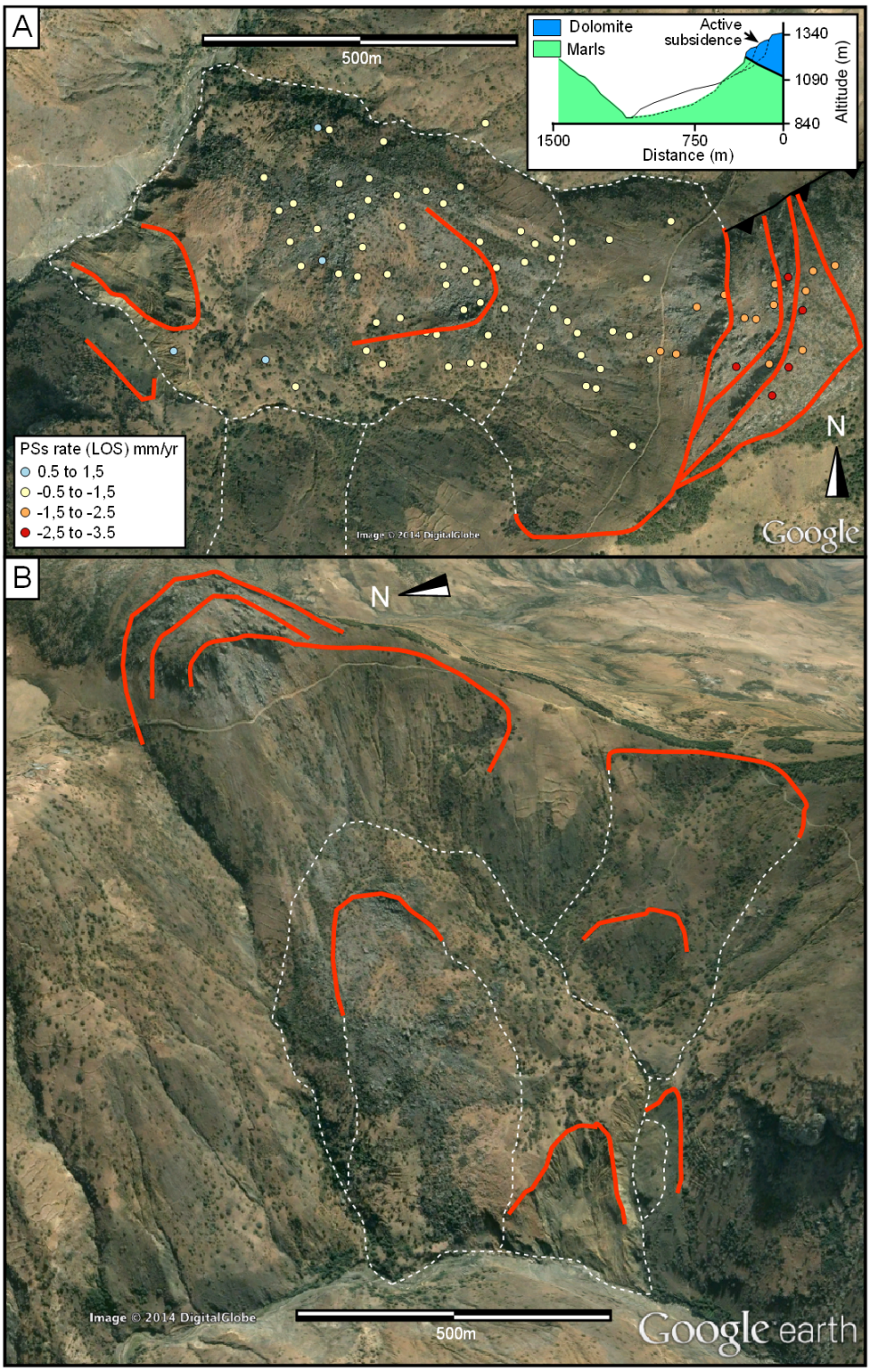


Figure 4.16 - Atress landslide.
A) Overview of landslide geomorphology and PSs distribution; B) Bird-eye view of the landslide mass. Red line marks the position of landslide scarps; dashed white line indicates the limit of the landslide body and landslide units.

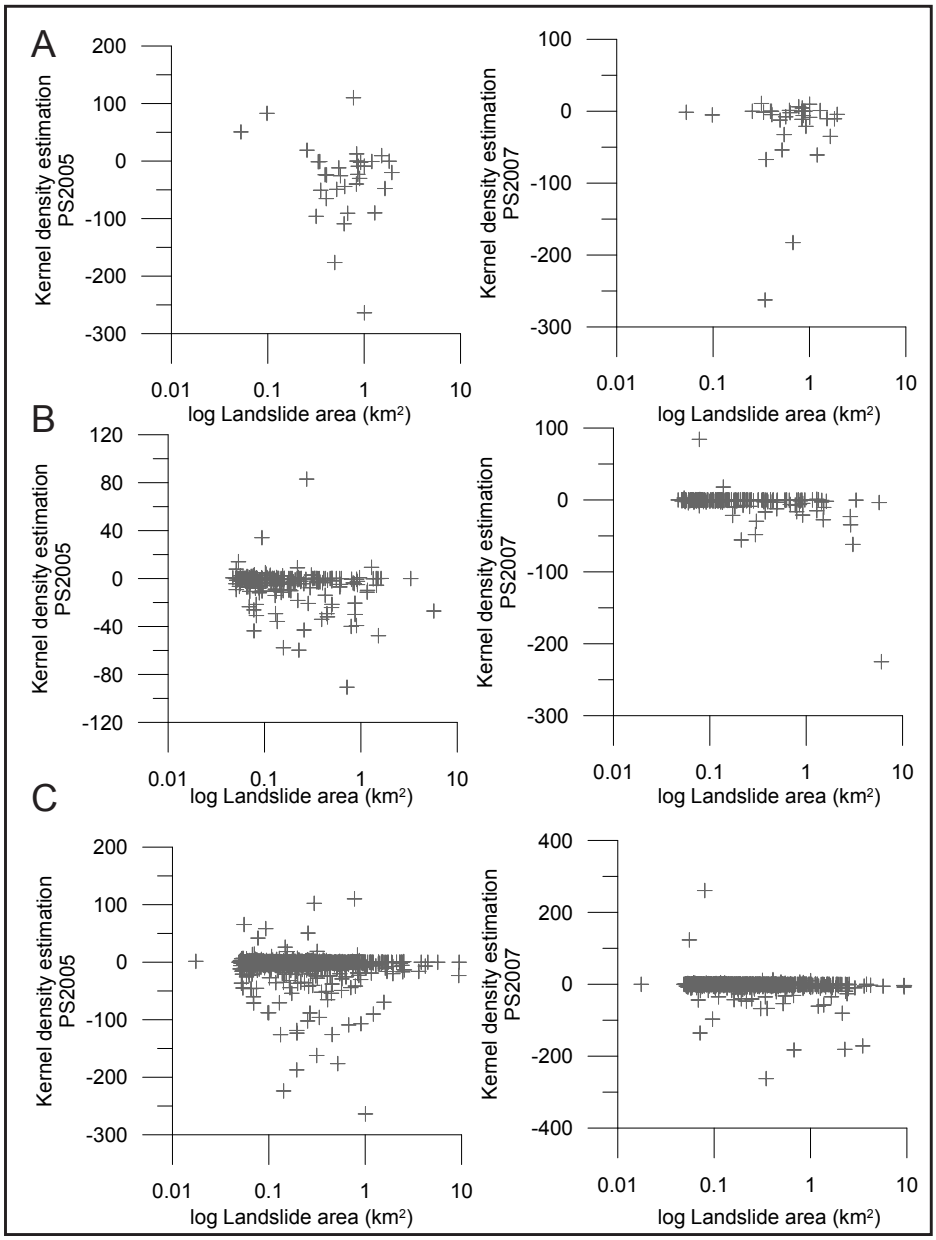


Figure 4.17 - Landslide area vs. Average Kernel density estimation.
A) Reclassified landslide through the PSI-based matrix approach; B) Active landslides (original inventory La>0.05km^2); C) Dormant landslides (original inventory La>0.05km^2).

A comparison between the hotspot data and the landslide inventory of the northern Rif indicates that only 23.2% of the generated hotspots are directly connected with existing landslides and only 12.3% are associated with newly detected landslides. Nearly 65% of the hotspots are connected to detection errors related to other geophysical and geomorphological processes that PSs could identify. This is particularly evident for blue hotspots were the misdetection rate reaches 17% and 21% for the PS2005 and PS2007 datasets, respectively. Furthermore, the fact that the kernel density

estimation overlaps several slope units hampers a clear association between the landslide cases and the obtained hotspots. This fact forces a detailed analysis of each hotspot to further discriminate the nature of the process behind surface deformation.

Table 4.5 - Landslide activity status classification and hotspot kernel density estimation.

Coordinate UTM	Typology	Area (km^2)	Activity status		PS2005 Hotspot Kernel density (Avg)	PS2007 Hotspot Kernel density (Avg)
			Geomorphic criteria	PSI based		
(413232.04, 3870761.96)	Translational	0.05	Dormant	Reactivated	-15.8	-1.4
(382439.56, 3872443.70)	Translational	0.13	Dormant	Reactivated	-126.0	-
(278820.27, 3891007.35)	Complex	0.15	Active	Reactivated	-	-61.8
(382933.80, 3872521.87)	Translational	0.20	Dormant	Reactivated	-123.2	-
(328468.85, 3832758.59)	Translational	0.26	Dormant	Stabilized	50.7	0.0
(393295.56, 3895535.52)	Translational	0.27	Active	Dorment/Active	83.0	-
(296552.29, 3898596.74)	Rotational	0.32	Dormant	Stabilized	18.9	10.8
(322131.85, 3891785.20)	Translational	0.35	Dormant	Reactivated	-1.2	-262.4
(296237.26, 3869164.97)	Translational	0.41	Dormant	Reactivated	-65.2	-4.7
(316555.15, 3882678.74)	Translational	0.50	Active	Reactivated	-24.2	-12.3
(294193.85, 3878261.68)	Translational	0.52	Dormant	Reactivated	-176.3	-53.9
(299395.76, 3870969.52)	Complex	0.57	Dormant	Reactivated	-49.1	-7.8
(300858.25, 3887562.50)	Complex	0.62	Dormant	Stabilized	-11.8	1.2
(316702.08, 3859304.15)	Translational	0.63	Dormant	Reactivated	-25.5	-2.0
(327887.27, 3890751.50)	Rotational	0.67	Dormant	Reactivated	-109.0	-182.7
(379886.97, 3823585.30)	Complex	0.71	Dormant	Reactivated	-44.2	-
(296958.81, 3892055.77)	Translational	0.77	Dormant	Stabilized	110.1	6.1
(391790.33, 3865183.65)	Translational	0.79	Active	Reactivated	-39.9	-
(330074.82, 3845369.85)	Translational	0.83	Dormant	Stabilized	12.4	0.00
(252909.79, 3895856.75)	Complex	0.84	Dormant	Reactivated	-	-11.3
(283859.74, 3928274.62)	Translational	0.84	Dormant	Stabilized	0.00	4.5
(405221.02, 3865548.67)	Translational	0.86	Dormant	Reactivated	-23.0	-6.0
(321180.21, 3869197.30)	Rotational	0.87	Dormant	Reactivated	-9.0	0.0
(312599.23, 3876626.49)	Complex	0.90	Dormant	Reactivated	-30.1	0.0
(318064.37, 3884372.46)	Rotational	0.92	Active	Reactivated	-2.3	-21.0
(310187.33, 3885948.66)	DSGSD	1.00	Dormant	Stabilized	-8.8	9.8
(293709.41, 3879610.15)	DSGSD	1.01	Dormant	Reactivated	-263.8	-8.5
(253614.19, 3896884.26)	Rotational	1.14	Dormant	Reactivated	-	-80.3
(324445.55, 3883952.55)	Complex	1.20	Dormant	Reactivated	-0.7	-60.8
(383774.11, 3874211.81)	DSGSD	1.21	Dormant	Reactivated	-90.1	-
(281231.05, 3894720.74)	Translational	1.27	Dormant	Stabilized	0.0	-180.9
(296786.71, 3897339.80)	Undefined	1.29	Active	Dorment/Active	9.4	1.0
(294416.39, 3901574.46)	Complex	1.30	Dormant	Stabilized	0.00	0.0
(315562.61, 3879309.24)	Complex	1.35	Dormant	Reactivated	-23.2	-7.6
(282010.06, 3886276.69)	Rotational	1.39	Dormant	Reactivated	0.00	-26.4
(293703.19, 3906250.23)	Rotational	1.43	Dormant	Reactivated	0.00	-4.4
(278511.18, 3897402.23)	Complex	1.48	Dormant	Reactivated	-	-171.5
(299294.53, 3866999.96)	Complex	1.52	Active	Reactivated	-47.7	-10.4
(316868.29, 3880406.22)	Translational	1.66	Dormant	Stabilized	0.00	-5.4
(288490.62, 3909645.03)	Complex	1.81	Dormant	Stabilized	0.00	0.0
(280568.42, 3886945.36)	Complex	1.82	Dormant	Reactivated	-	-10.6
(316868.29, 3880406.22)	Complex	1.94	Dormant	Reactivated	-19.9	-4.4
(280568.42, 3886945.36)	Complex	0.53	Active	Reactivated	-129.2	-100.4
(288490.62, 3909645.03)	Complex	0.59	Active	Reactivated	-132.0	-102.2
(288068.27, 3915730.91)	Translational	0.71	Active	Reactivated	-105.0	-184.7

For both the PS2005 and PS2007 datasets, large landslides (La>0.05km^2) show a higher density of high velocity (>2mm/yr) PSs when compared to smaller landslides (La<0.05) (Fig. 4.5). Several factors contribute to this observation: i) large landslide occurring in the contact between compact and marly units have higher terrain roughness due to the presence of large sandstone and limestone blocks in the deposit (e.g. Atress and Agni Beni Boufra landslides); ii) human infrastructures and houses occurring inside the limits of large landslides increase the terrain backscattering properties (e.g. Hadada, Beni Mizar and Jebel Sougna landslides); iii) smaller landslides tend to occur in association with marly and clay formations were the backscattering properties of the landslide body are hampered by the inexistence of terrain features capable of producing a PS signal.

Furthermore, field and PSs data suggests that during the triggering event of 2009/2010, while smaller landslides (<0.05km^2) suffered reactivation along significant portions of the landslide body, larger landslides tended to suffer only partial reactivations, either through the slow downward propagation of a secondary landslide mass or through sliding along its margins in response to gully incision and lateral erosion. This fact potentially expresses the dependency between landslide size and the ability of a precipitation event to produce a reactivation. Nevertheless, our conclusions are hindered by the fact that PSs are not always evenly distributed within large landslide bodies, but gather around particular sites where reflectance is consistently captured by the satellite. This is particularly evident in the Atress, Agni Beni Boufra, Tiarta and El Marhza landslides., confirming that the nature of partial reactivations of large landslide is difficult to discern when simply referring to PSs data and further field data collection and detailed geomorphological mapping should be performed in order to avoid misinterpretations of landslide activity.

The comparison between the results that were obtained through the PSI-HCA and PSI-based matrix approach confirm the capability of both methods to detect landslide activity (Table 4.5 and Fig. 4.17). Stabilized and dormant/stabilized landslides that were reclassified through the PSI-based matrix approach are characterized by low or positive hotspots. Only six landslides experiencing reactivation were not detected through the PSI-HCA. This is explained by the following reasons: i) the PSI-based matrix approach is landslide based, while the PSI-HCA depends on the definition of a parameter “d” defining slope length; and ii) the definition of parameter d in the PSI-HCA method is based on a low resolution DEM, resulting in an overestimation or underestimation of the landslide affected areas. Furthermore, in the overlapping sector of the SAR images used in this work, the occurrence of active landslides that are supported by a single hotspot is explained by the temporal

decorrelation created by the presence of image gaps in the PS2005 and PS2007 datasets. Nonetheless, our results show that the PSI-HCA method is suitable for detecting landslide activity within active mountain belts were the magnitude of gravitational processes tend to extend beyond the predefined thresholds for the application of the PSI-based matrix approach.

5 An example of complex deep-seated slope deformation in the northern Rif: the Beni Derkoul landslide

Submited articles:
Fonseca, A.F., Zêzere, J.L., Madeira, J., Fernandes, J.C., Bouchta, EF. (submited). Morphology, kinematics and activity of a complex deep-seated landslide in the northern Rif Mountains (Beni Derkoul, Morocco). Landslides. Springer.
Fonseca, A.F., Zêzere, J.L., Madeira, J., Bouchta, EF. (submited). Geomorphological map of the Beni Derkoul landslide (Northern Morocco). Journal of Maps. Taylor and Francis.

Abstract

The Beni Derkoul landslide develops along the northern slope of the Tisiren thrust front, approximately 50km southeast of Chefchauen, is 5km in length and covers an area of 5.02km^2. It displays characteristics of a deep-seated rotational landslide in the upper sectors of the slope, splitting in two tongues along the drainage divide of the Beni Derkoul valley. The landslide was analysed by combining geomorphologic, geomorphometric and remote sensing techniques, coupled with field observations and mapping.
The landslide is composed of four main detachment areas (D1, D2, D3, and D4) mainly controlled by bedrock structure and lithology. The favourable attitude of the geological units, the slope and aspect of the mountain flanks, and the occurrence of high plasticity clays in the sedimentary sequences explain slope deformation. Middle Holocene landslide activity was identified through the analysis of paleo-lake sediments radiocarbon dated between 6868 and 6046 Cal BP. The deformation of lakebeds and the presence of paleoseismite structures testify to the influence of paleoseismic activity in landslide triggering. Detailed geomorphological mapping and persistent scatterer technique indicate that present-day slope deformation is mostly associated with seasonal creep in response to heavy rainfall events during winter months. However, the activation of the complete Beni Derkoul landslide is not easy to consider without the aid of an earthquake event. The location in an area of high seismic acceleration, the evidence of paleoseismic deformation associated with geomorphic marker of slope instability, suggests a link between landslide triggering and past tectonic activity. Furthermore, and taking into account the relevant flow component within the runout area, favoured by the presence of high plasticity clays as one of the main predisposing condition controlling slope deformation, leads us to place of the initial triggering during the humid phases of the Upper-Pleistocene Lower Holocene boundary, in response to, or the combination of heavy prolonged rainfall and seasonal or climate-induced snow melting and seismic activity.

Keywords: deep-seated landslide; slope tectonics; landslide depth; landslide chronology; Rif Mountains; Morocco.

5.1 Introduction

In this section we analyse the geological and geomorphological features of a complex deep-seated

landslide – the Beni Derkoul landslide - in the Rif Mountains, northern Morocco. We know focus on a detailed analysis of a large deep-seated failure with the objective: i) to analyse the landslide surface geology and geomorphology; ii) to define the structural model of deformation and depth of the failure surface; iii) to analyse landslide kinematics; iv) to identify different stages of landslide evolution; v) to analyse present-day activity; V) to discuss the role of present-day available triggering mechanism in landslide reactivation.

5.2 Study area

The Beni Derkoul landslide is located along the south-western flank of the Rif, approximately 50km southeast of the village of Chefchauen (Fig. 5.1). The main topographic features of the region are the valley of Beni Derkoul and the mountain peaks of the Koudiet es Sbaa (1768m), Jebel Beni Salah (1504m) and the Azaib plateau (1472m) (Figs. 5.2 and 5.3). The valley of Beni Derkoul drains into the Maâmala River, a tributary of the south-flowing Audour River (Fig. 5.1). In the upper sections of the catchment two valleys drain from SE to NW, with direction shifting to E-W approximately 3km upstream from the village of Beni Derkoul (Figs. 5.3 and 5.4). The lower section of the valley is 1km wide and is characterized be a semi-flat hummocky surface that contrasts with the 30 to 60° bedrock slopes (Figs. 5.2 and 5.4).

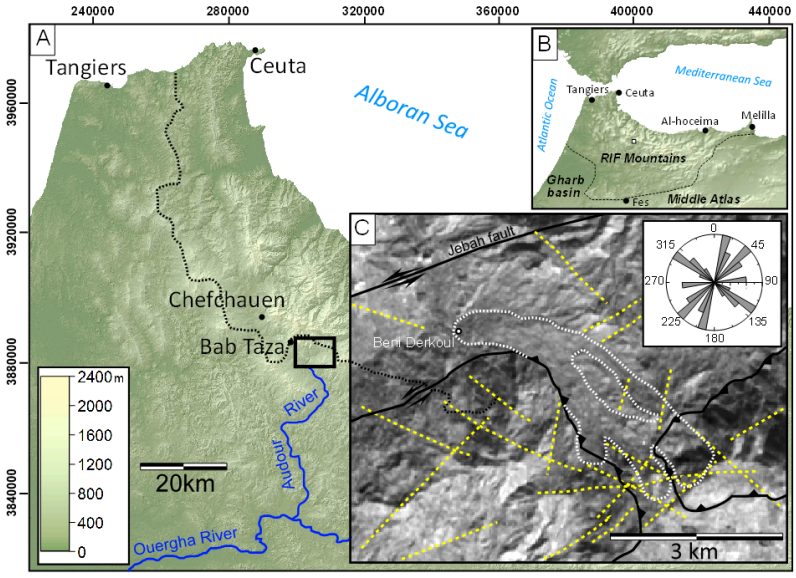


Figure 5.1 – Location of the Beni Derkoul landslide in the context of the Rif.
A) Overview of the northern Rif Mountains and location of the study area. Dashed black line marks the position of the main drainage divide; B) Location and overview of the Rif Mountain; C) Landsat 7 (Band 5) of the study area. Dashed white line indicates the limits of the Beni Derkoul landslide; Yellow dashed lines - tectonic lineaments; Black lines - Faults.

The critical topographic and tectonic setting in which the Beni Derkoul landslide occurs is in accordance with the favourable predisposing conditions identified in section 3 of this work, controlling the distribution of large (>1km^2) bedrock failures. Specifically, it is located in the western-end of the Tiziren thrust front, where the compact sandstones of the Tiziren and Beni Ider units overthrust the marl and clay domain of the Tanger Unit. Furthermore, slope deformation occurs in close proximity (≈7km) to the Jebah Fault, a sector defined by Benchekroun et al. (2013) as being subjected to the highest seismic accelerations (0.27-0.33g) in the northern Rif.

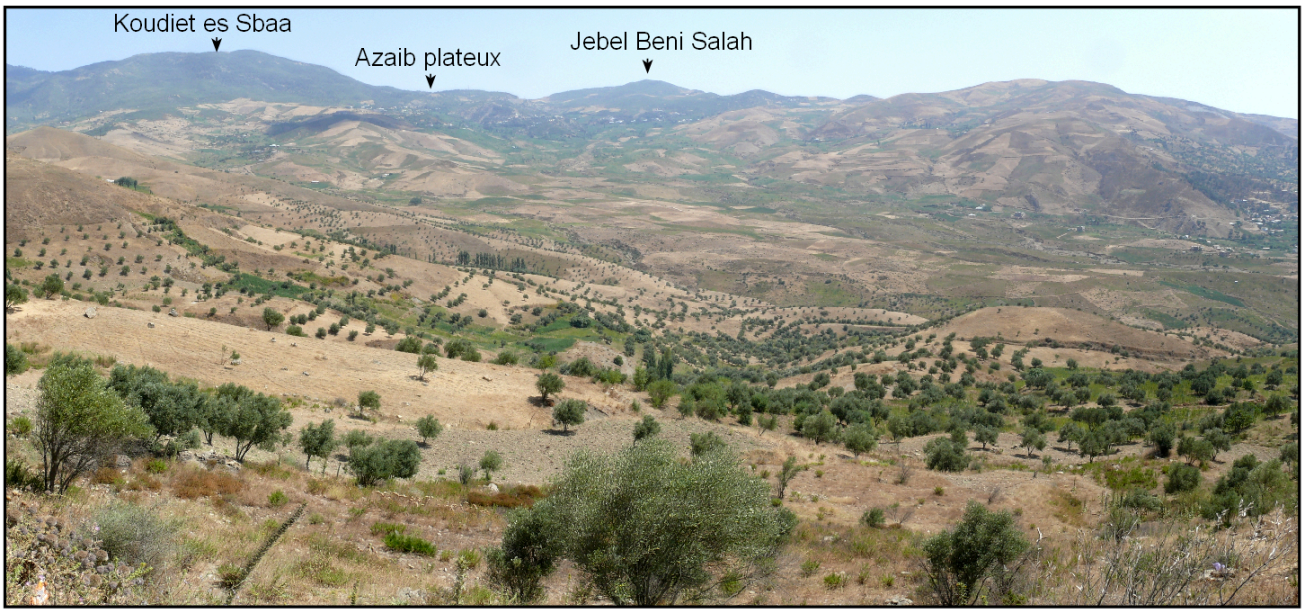


Figure 5.2 - Overview of the Beni Derkoul valley looking south.

The Beni Derkoul landslide occurs in the contact between the Mauritanian nappe and the Tanger Unit (Fig.3). The contact between nappes is established by N135 and N85 trending thrust faults dipping to the north and north-east. From a structural point of view, the Mauritanian nappe is subdivided into the Jebel Tisiren and the Beni Ider nappes. The Tiziren Unit starts with a pre-flysch sequence (≈200m thick) consisting of marly-limestone of Berriasian-Valanginian age, followed upward by graded siliciclastic layers with clay intercalations (~250m) of Hauterivian-Barremian age (Durand-Delga et al. 1999), a dominantly clay unit of Barremian - early Aptian age (~50m) and a turbiditic succession comprised of thick graded sandstone beds of late Aptian-middle Albian age (Durand-Delga et al. 1999) (~600m).

The Beni Ider nappe starts with Upper Eocene marls and breccias (≈100m), which are overlain by thick Middle-Upper Oligocene micaceous sandstones intercalated with thin clay beds (≈300m) (Kornprobst et al. 1980; Chalouan et. al. 2008) (Fig.3).

In the study area the Tanger Unit is composed of a thick Cenomanian-Senonian marly-pelitic sequence with sandstone and limestone intercalations (Lespinasse et al. 1978). It begins with a marly-clay sequence (≈150m) composed of thin limestone and sandstone beds of Cenomanian age and is followed up by a ≈350m thick sequence (Turonian-Senonian) composed of marls and black shales with thin limestone intercalations (Kornprobst et al. 1980).

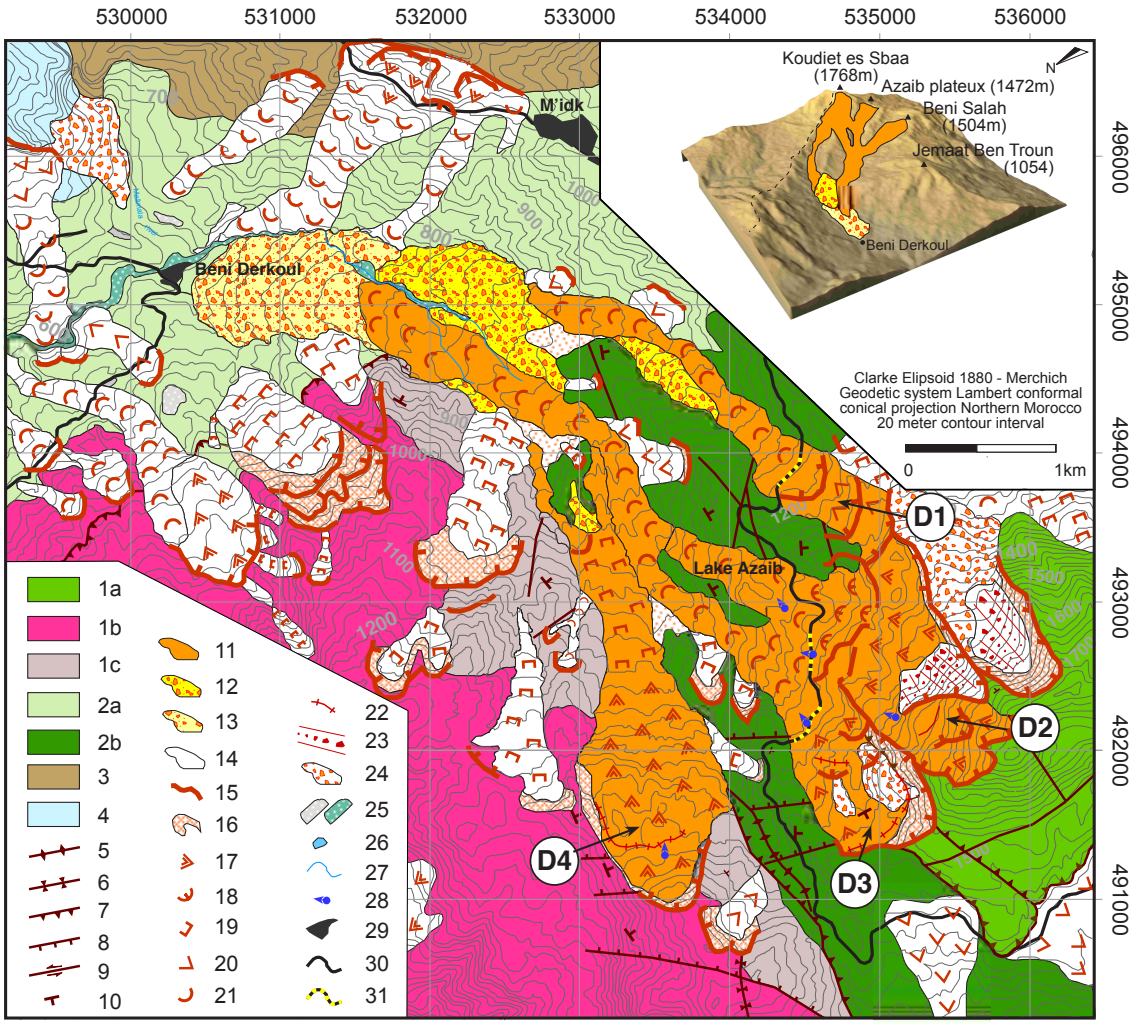


Figure 5.3 Simplified geomorphological map of the Beni Derkoul landslide.

1a) Tiziren Unit; 1b) Upper Beni IderUpper Tanger; 3) Lower Tanger; 4) Upper Beni Ider Unit; 5) Lower Beni Ider Unit; 6) Ametrass Unit; 7) Dorsal Calcaire; 8) Anticline; 9) Syncline; 10) Thrust fault; 11) Normal fault; 12) Strike-slip fault; 13) Bedrock attitude; 14) Beni Derkoul active landslide; 15) Landslide Unit 2; 16) Landslide Unit 1; 17) Secondary landslide; 18) Landslide scarp; 19) Detachment area; 20) Area affected by deep-seated deformation; 21) Complex slide; 22) Translational slide; 23) Rotational slide; 24) Flow; 25) Trench; 26) Scree deposit; 27) Rockslide deposit; 28) Fluvial and flood-plain terrace; 29) Landslide lake; 30) Seasonal stream; 31) Source; 32) Village; 33) Road; 34) Road affected by fracture opening. Inset shows 3D sketch of the landslide. Inset shows 3D view of the Beni Derkoul valley.

5.3 Methods

5.3.1 Geological and geomorphological analysis

The methodological approach to study the Beni Derkoul landslide involved the analysis of terrain first-order derivates (slope, aspect, hill-shade) extracted from a digital elevation model (DEM) (pixel size ≈20m) (Fig. 5.4) and the interpretation of 1:40,000 aerial photos (Agence Nationale de la Conservation Foncière, du Cadastre et de la Cartographie, ANCFCC) and satellite images (Google-Earth image archive), coupled with field observations and mapping. The combination of the information extracted from these sources enabled the creation of the geomorphological map of the Beni Derkoul landslide (Fig. 5.3 and annex 2).

The digital elevation model was obtained through the interpolation of 1:25,000 scale topographic maps (ANCFCC). Digital stereographic interpretation and remote sensing of aerial photos and satellite images enabled the identification of gravitational landforms and distinct landslide units based on the terrain morphology and the reflectance of the surface geology. Furthermore, in order to detect changes in landscape morphology and dynamics that relate to landslide activity and to the progressive incision of the landslide mass by the fluvial system, we compared published topographical maps, aerial photos and satellite images, enabling the reconstruction of the evolution of the main drainage network system within the landslide body.

Landslide classification is according to the Cruden and Varnes (1996) classification scheme, recently updated by Hungr et al. (2014), and five main typologies were distinguished: rotational slide, translational slide, flow, complex (slide-flow; rotational-translational sliding) and deep-seated slope deformation. The later category indicates sectors were trenching and normal faulting in the crow area accommodates slope deformation and the horizontal component of the movement is non-existent or less evident.

5.3.2 Field sampling and laboratory techniques

The examination of the relationship between bedding plane attitude and topography is a key procedure in identifying and understanding the structural control on slope and landslide evolution (Grelle et al. 2011). Therefore, a detailed analysis of bedrock structure was performed. Bedrock outcrops and tectonic structures were identified from published data (Kornprobst et al. 1980) and analysing aerial photos and satellite images (Figs. 5.1 and 5.3). These were validated in the field and bedrock attitude and fault geometry data was collected for each structural unit (Fig. 5.5).

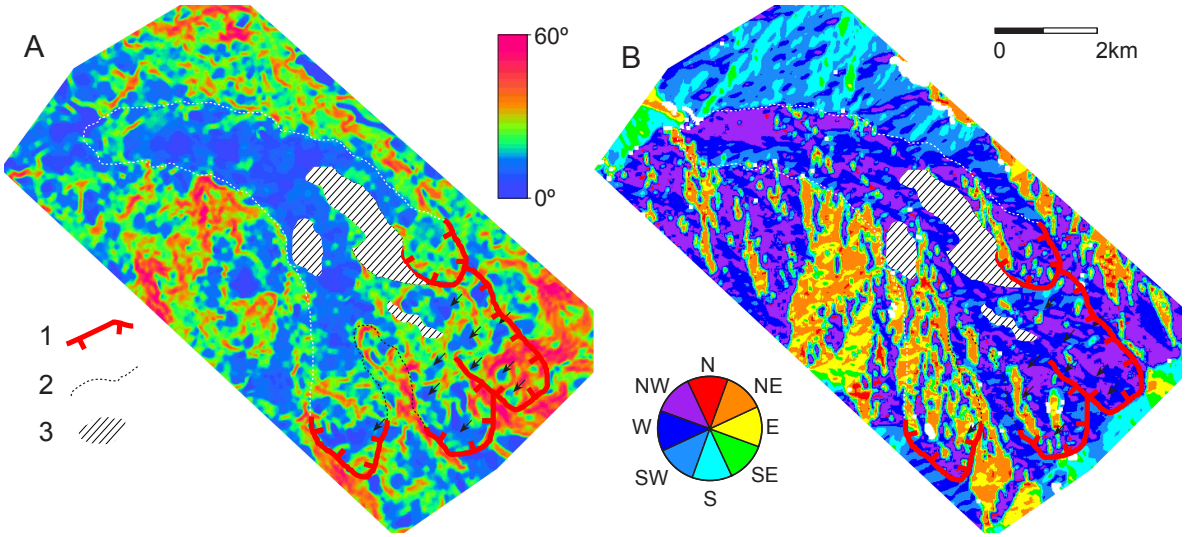


Figure 5.4 - DEM first order derivatives.
A) Slope; B) Aspect. 1) Landslide scarp; 2) Limit to the Beni Derkoul landslide; 3) Stable bedrock outcrops.

In order to gain insights into the behaviour of the clay and marly formations of the Tiziren, Tangier and Beni Ider units in response to water content, a total of 8 samples were collect and Atterberg limits were calculated following the Liquid limit and Plastic limit-Plasticity Index methods T 89-76 and T 90-70, respectively (Table 5.1) (Liu and Evett 1997). Furthermore, undrained and residual shear strength data was collected at each site using a T 174 pocket vane, which is particularly suitable for soft to medium cohesive soils. Measurements were collected at minimum and maximum depths of 30 and 80cm and during winter and spring months to ensure maximum bedrock saturation (Table 5.1).

Downslope from Lake Azaib a road cut showing two sequences of paleolake levels was found (Figs. 5.3 and 5.12). Charcoal samples were collected for AMS 14C dating performed at the Beta Analytic Laboratory. Results are presented in table 5.2. Dates are reported as radiocarbon years before present (present = AD 1950). By international convention, the modern reference standard was 95% for the 14C activity of the National Institute of Standards and Technology (NIST) Oxalic Acis (SRM 4990C) and calculated using the Libby 14C half-life (5568 years). Quoted errors represent 1 relative standard deviation statistics (68% probability) counting errors based on the combined measurements of the sample, background, and modern reference standards. Measured 13C/12C ratios (delta 13C) were calculated relative to the PDB-1 standard. The Conventional Radiocarbon Age represents the measured Radiocarbon Age corrected for isotopic fractionation, calculated using 13C. Calibration was performed using the Calib Rv 7.0.2 by Stuiver and Reimer, (1986) (version 5.0) following the dataset found in the work of Hughen et al. (2004) and Hutchinson et al. (2004).

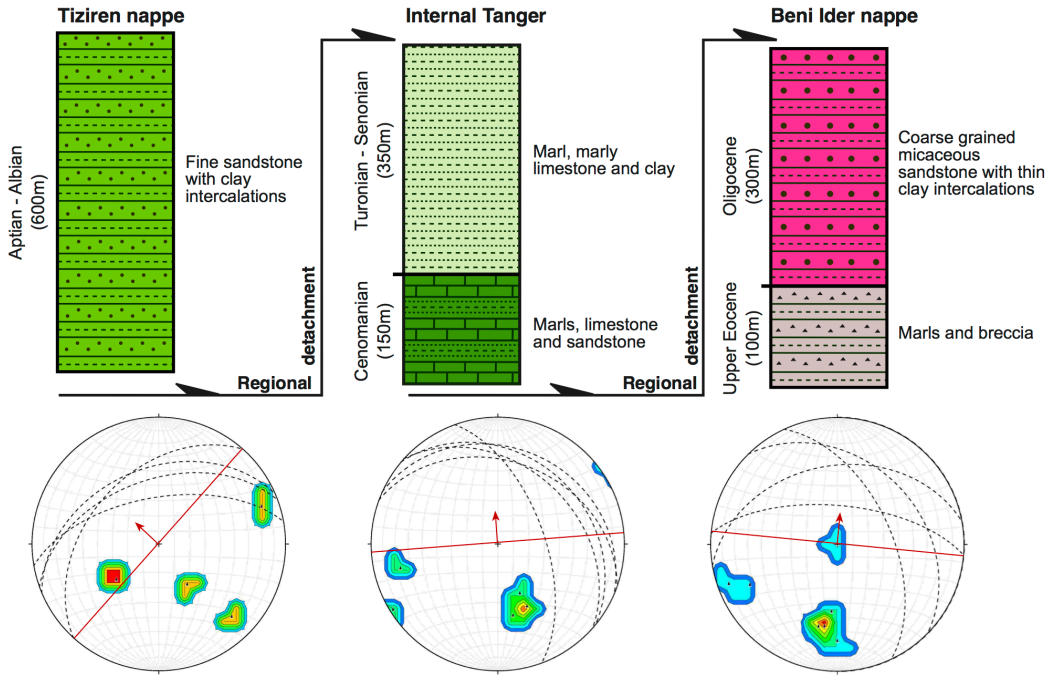


Figure 5.5 - Stratigraphy of stable bedrock units.
Stratigraphy of stable bedrock units adapted from Kornprobst et al. (1980) and bedrock attitude and poles to faults for each structural unit. Red line indicates the orientation of the main landslide scarp; arrow indicated the landslide propagation azimuth in the detachment area.

Table 5.1 - Shear strength and Atterber limits for the bedrock samples.

Sample	Lithology	Unit	Undrained shear strength		Residual shear strength		Atterberg		
			Avg	Std	Avg	Std	Liquid limit	Plastic limit	Pasticity Index
1	Marl	Lower Beni Ider	6.20	0.83	1.00	0.22	48.92	27.61	21.31
2	Marly-clay	Lower Tanger	5.55	0.85	1.73	0.50	54.89	30.05	24.84
3	Marly-clay	Lower Tanger	5.83	0.71	1.22	0.48	52.24	28.51	23.73
4	Clay	Upper Tanger	3.29	1.03	1.04	0.32	59.14	12.22	46.92
5	Clay	Upper Tanger	3.67	0.41	0.92	0.44	62.62	12.32	50.3
6	Clay	Upper Tanger	3.54	0.98	0.45	0.27	62.83	14.3	48.53
7	Clay	Upper Tanger	3.37	1.37	0.90	0.33	63.44	15.3	48.14
8	Clay	Tiziren	-	-	-	-	53.94	26.11	27.83

5.3.3 Landslide morphometry and depth estimation

Landslide morphometric properties (planimetric area, perimeter, runout length, landslide height, runout slope, width and length of rupture area) were extracted from the cartographic and digital terrain data following the definitions of the IAEG Commission on Landslides (1990) (Table 5.3).

Table 5.2 - Conventional and calibrated AMS 14C ages of the Azaib paleolake sediments (AUD-Area Under the Curve).

Road cut	Level	Dated material	Measured Radiocarbon age	13C/12C ratio	Conventional radiocarbon age (yr BP)	68% (1σ) cal age ranges	68% (1σ) AUD	95% (2σ) cal age ranges	95% (2σ) AUD
1	L2	Peat	6070±30	-25.8 **o/oo**	6070±30	6890-6968 Cal BP	1	6800 - 6815 Cal BP 6846-7006 Cal BP 7134-7137 Cal BP	0.023 0.975 0.002
1	L4	Charcoal	5850±30	-23.8 **o/oo**	5870±30	6664-6726 Cal BP	1	6636-6752 Cal BP 6765-6775 Cal BP	0.985 0,015
2	L2	Charcoal	5400±40	-24.4 **o/oo**	5410±40	6195-6046 Cal BP; 6200-6278 Cal BP	0.011; 0.989	66025-6046 Cal BP 6066-6077 Cal BP 6115-6152 Cal BP 6175-6296 Cal BP	0.021 0.009 0.069 0.901
2	L8	Charcoal	5380±40	-25.2 **o/oo**	5380±40	6122-6146 Cal BP; 6178-6223 Cal BP; 6229-6276 Cal BP	0.160; 0.425; 0.415	6280-6170 Cal BP 6160-6110 Cal BP 6080-6010 Cal BP	0.163 0.185 0.652
2	L14	Charcoal	5470±40	-24.0 **o/oo**	5490±40	6217-6237 Cal BP; 6272-6316 Cal BP	0.203; 0.797	6209-6254 Cal BP 6260-6352 Cal BP 6366-6396 Cal BP	0.213 0.692 0.094

Table 5.3 - Morphometric properties and depth estimation of the landslide sectors.
Morphometric properties and depth estimation of the landslide sectors (Fig. 3 and 10 for location). D1 through D4) detachment sectors; U1 and U2) Landslide units positioned in the lower section of the Beni Derkoul Valley; W) Width; L) Length; W/L) Width/Length ratio; H) Height; D) Depth; R^2) Coefficient of determination; R) Runout.

Landslide sectors	Detachment area						Runout area					Total	
	W	L	W/L	H	D	R^2	W	L	W/L	D	R^2	R	H
D1	495	580	0.85	400	35±10	0.98	415	1880	0.22	10±2	0.94	2460	430
D2	695	1080	0.64	940	60±15	0.93	805	1625	0.50	20±5	0.93	2705	545
D3	715	965	0.74	700	100±15	0.96	605	1425	0.42	8±2	0.89	2390	418
D2/D3	-	-	-	-	-	-	670	5600	0.12	8±2	0.91	5615	-
D4	950	960	0.99	315	70±15	0.93	910	1690	0.54	20±5	0.92	2650	425
U1	-	-	-	-	-		-	-	-	30±10	0.89	-	-
U2	-	-	-	-	-		-	-	-	30±5	0.88	-	-

In the absence of geotechnical and borehole data, the definition of a landslide structural model is limited by the inability to pinpoint the depth of the failure plain. Nonetheless, significant effort has been placed in the definition of conceptual landslide models combining surface (morphological and geological) observations and remote sensing data (e.g. Carter and Bentley 1985; Bishop 1999).

Following the limitation imposed by the available DEM, the absence of landslide displacement vectors and rates and the lack of geophysical and borehole data, we adopted a simplified method for an approximate calculation of the depth of the failure surface. Assuming landslide scarp degradation to be minimal, we use its slope as a proxy to the subsurface rupture plane dip. Using reference points within the runout area (e.g. stable bedrock outcrops, bedding planes, potential surfacing of the rupture surface) we used a 2nd order polynomial fit to define the approximate

depth of the failure surface with 5% confidence intervals. Based on the uncertainty behind the method in use, we limited the analysis to 2nd degree polynomial adjustments as it produces smoother and rectilinear profiles (Fig. 5.6).

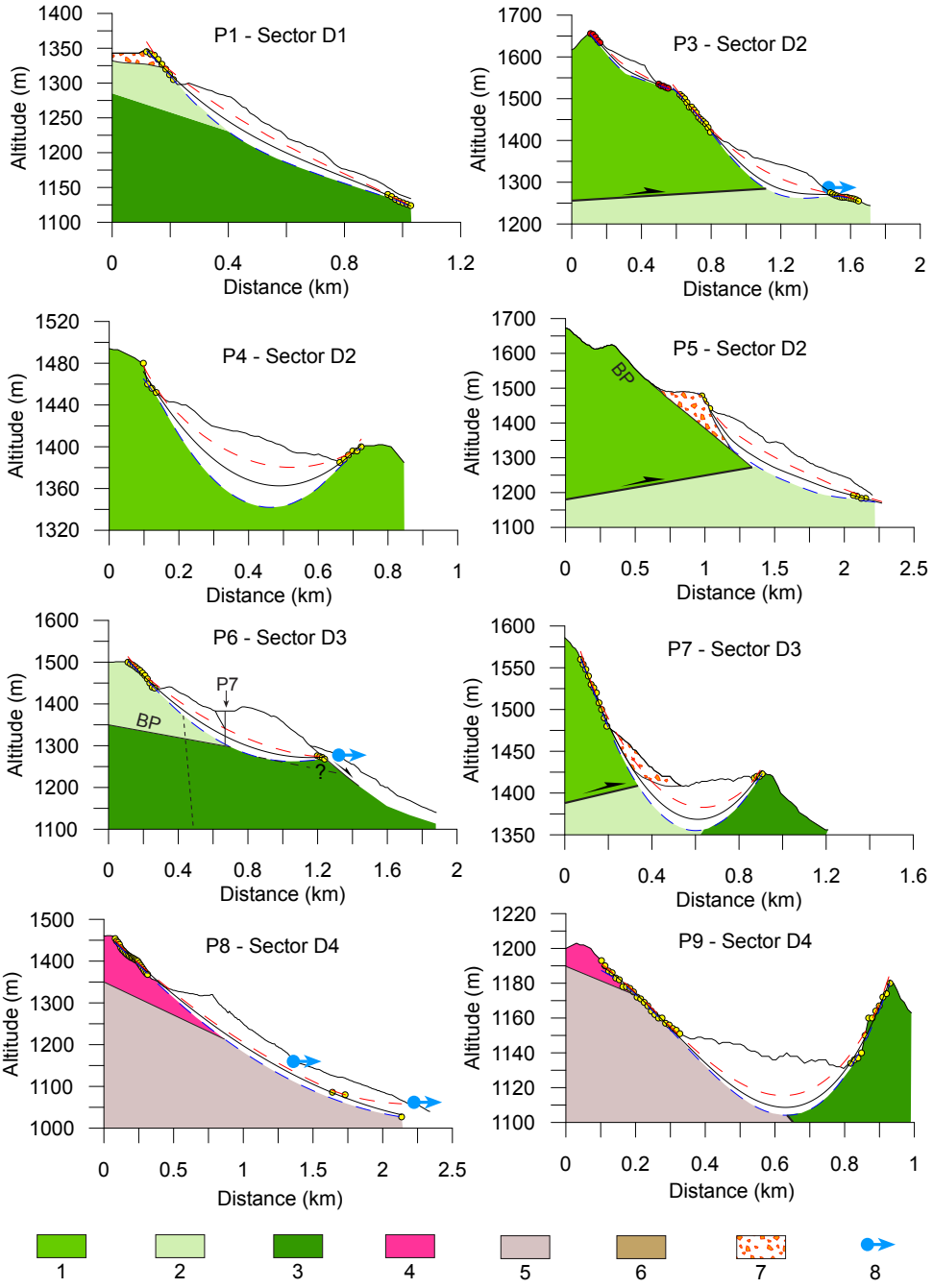


Figure 5.6 Longitudinal and transverse profiles.
Profiles of the landslide mass (Fig.8 for location) and 2nd order polynomial fit to reference points (see text for explanation) with 5% confidence intervals. 1) Tiziren Unit; 2) Upper Tanger Unit; 3) Lower Tanger Unit; 4) Upper Beni Ider Unit; 5) Lower Beni Ider Unit; 6) Ametrasse Unit; 7) Rockslide deposit; 8) water source. BP = bedding plane.

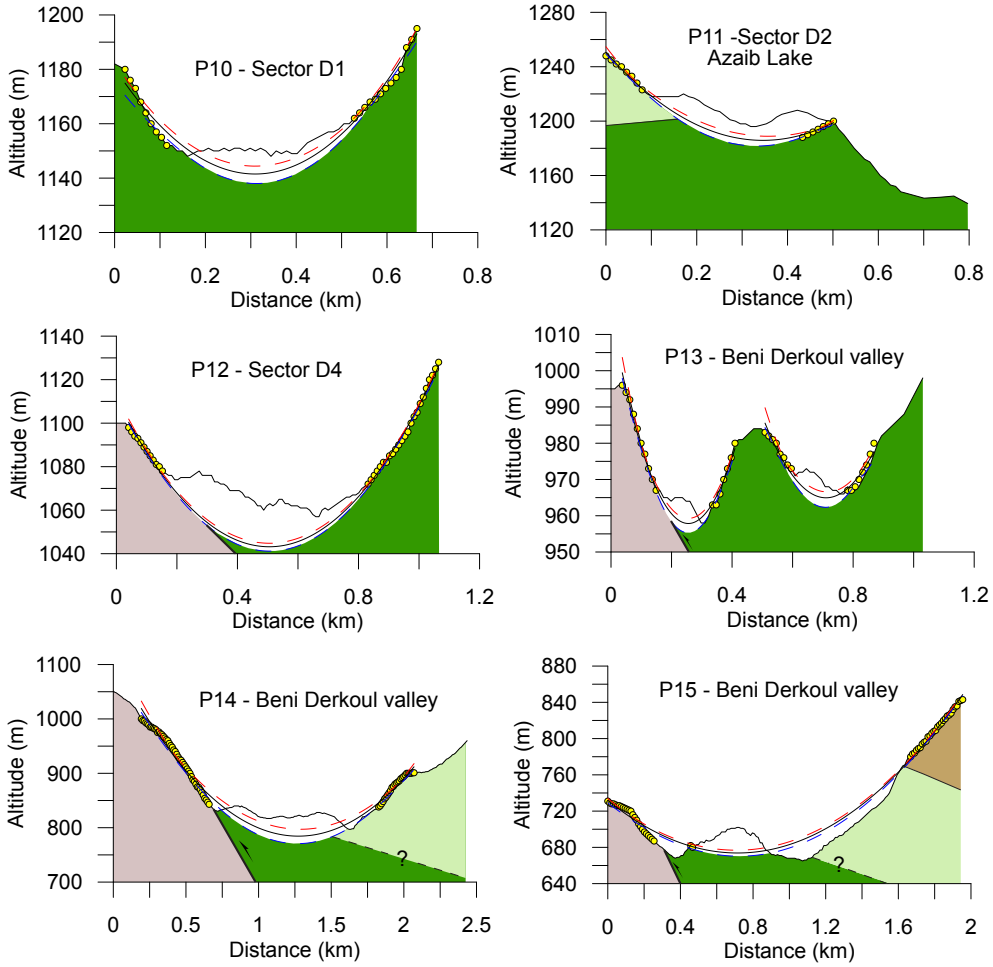


Figure 5.6 – (continued)

The shape of valley cross-section profiles has been used to describe landscape morphology in fluvial and glacial settings (e.g. Svensson 1959; Sugden and John 1976; Hirano and Aniya 1988; Baker 1990; Schumm et al. 1995). Several authors presented power-law and polynomial functions to approximate valley cross-sections and estimate valley sediment infill (Wheeler 1984; James 1996; Rasemann et al. 2004). From the use of polynomial functions Rasemann et al. (2004) noted that the modelled cross section is significantly influenced by the chosen polynomial order. The authors concluded that the fourth-order polynomial adjustment fitted to the rock wall showed accurate results and were capable of representing smaller irregularities associated to rock falls. Nonetheless, the authors suggest the use of lower (2^{nd} and 3^{rd}order) polynomials that generate a smoother and flatter curve, therefore accounting for differences in morphology over time.

In order to retrieve information on the landslide depth in the runout area we analysed the longitudinal and cross-section profiles of the landslide mass and of the valley walls of the Beni Derkoul valley. We extracted transverse profiles in the middle and lower section of the valley (Fig.

5.6 and 5.7 for location) and bedrock outcrops were used as control points for the application of the polynomial fit. Sectors affected by landsliding or within the landslide units were excluded. Moreover, along the lower section of the Beni Derkoul and Maâmala River valleys it is possible to find perched strath terraces that relate to the Quaternary river incision history. In order to better characterize the paleo-landslide topography we use these geomorphic markers as references to stability phases in the evolution of the fluvial system and compare their altitudinal distribution with the altitude of the calculated landslide depth and knick zones along the longitudinal profiles of the fluvial channels that margin the landslide body (Figs. 5.7 and 5.10).

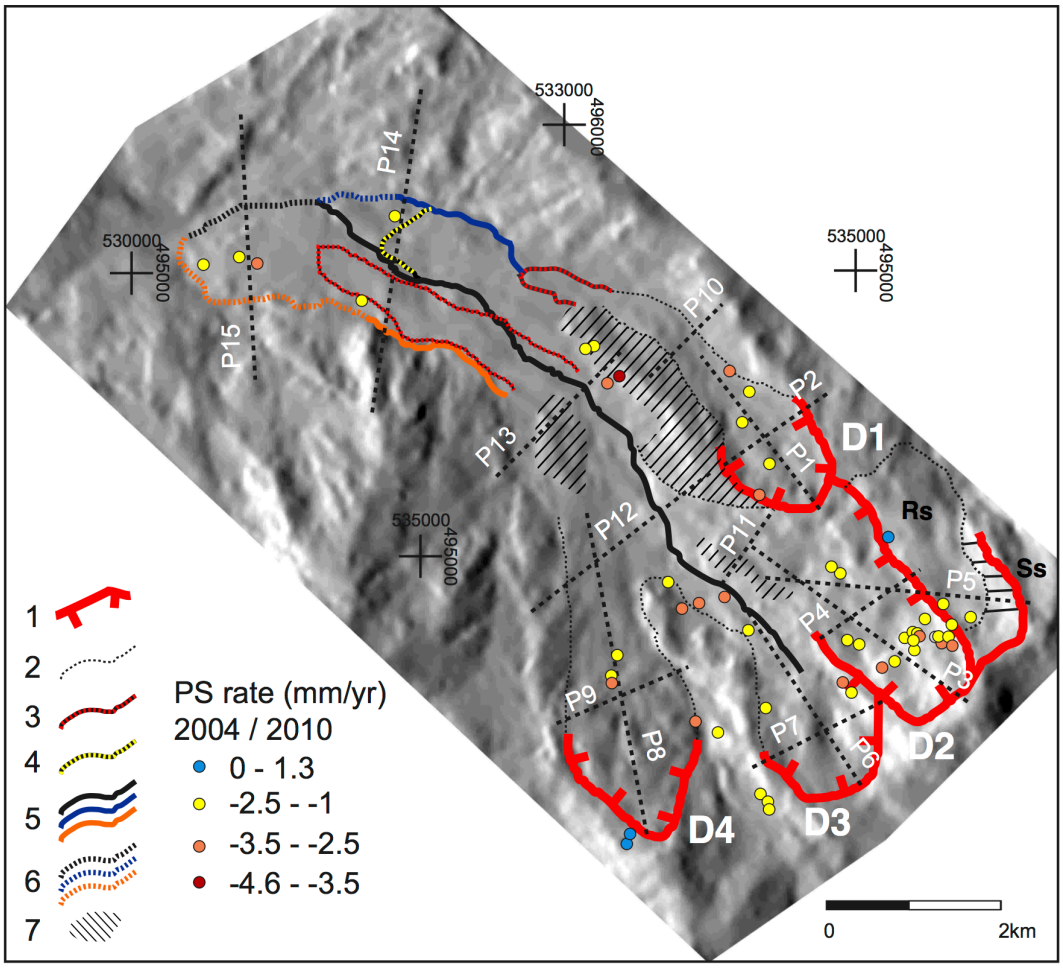


Figure 5.7 - Shaded relief image of the Beni Derkoul landslide.
Location of the profiles presented on figure 5.6 and of the streams segments used in the analysis of longitudinal profiles. Colored circles are persistent scatterers produced for this study. References D1 through D4 identify the main detachment areas (see text for explanation). Rs – rockslide deposit; Ss – structural surface. 1) Landslide scarp; 2) Limits of the Beni Derkoul landslide; 3) Frontal lobe of the active landslide; 4) Frontal section of landslide Unit 2; 5 and 6) Streams analyzed in figure 11; 5) Streams flowing on surface deposit; 6) Bedrock streams; 7) Stable bedrock outcrops.

5.3.4 Persistent scatterer interferometry

Taking advantage of the result from the application of the PSInSar technique presented in the previouse section we analize the spatial distribution of PSs within the landslide mass to detect and better characterize present-day activity. Persistent Scatterers (PSs) used in this study are shown in figure 5.7. Furthermore, climatic data for the SAR image timeframe was collected from the stations of Bab Taza and Chefchauen in order to aid data interpretation.

5.4 Results

5.4.1 Bedrock structure and mechanical properties

The structural setting of the area is somehow complex due to the presence of thrust faults separating tectonic nappes. The regional structure of the area is the result of two main tectonic phases (Ait Brahim et al. 2002): (i) early-Miocene NE-SW compression controlled by N50°E to N90°E-trending sinistral and N20°E to N160°E-trending dextral strike-slip faults; ii) late-Miocene through Quaternary N – S to N140°E compression controlled by N170°E to N20°E trending sinistral and N90°E to N140°E- trending dextral strike-slip faults.

Locally, the upper Beni Derkoul valley is affected by three fault sets that relate to the tectonic evolution of the mountain belt. The most important structures affecting the main detachment area are the Tiziren and Beni Ider thrusts and a set of sub-vertical NW-SE to NNW-SSE and NE-SW to W-E oriented structures (Figs. 5.1, 5.3 and 5.5).

Bedrock units within the detachment area of the landslide were analysed. Within the study area only the upper sequences of the Tiziren Unit are involved in gravitational failure, being composed of thick graded sandstone beds (≈1.5m) with thin (max. 30cm) mudstone intercalations. Stable bedrock outcrops dip towards the north-west with an attitude of N222, 40N to N260, 60N and are dissected by NW-SE and ENE-WSW trending faults (Fig. 5.5).

The Beni Ider Unit crops out further to the west. It starts with a marly and breccia sequence approximately 100m thick and is overlain by thick-bedded micaceous sandstones with thin clay intercalations.

The Tanger Unit begins with a marly-clay sequence (≈150m) with intercalations of limestone and sandstone beds (max. 50cm thick) and is followed up by a thick grey and yellow coloured clay unit with marly intercalations. The structure strikes approximately NW-SE dipping to the north-east (Fig. 5.5). Bedrock outcrops belonging to Upper Tanger Unit occur within the landslide mass (Fig. 5.3).

Stratification strikes approximately NW-SE and dip to the north-east, consistently reproducing the geometry of the Tanger Unit within stable sectors.

The liquid limit for the samples collected in this study are well above the threshold of 35% (Table 5.1), which indicates a high expansion potential of the clays within the Tanger, Tiziren and Beni Ider units. The large liquid limit further indicates high compressibility and high shrink-swell tendencies, particularly for the Upper Tanger clays. By plotting above the A'line, the plasticity chart (Fig. 5.8) reveals the presence of clay of medium to high plasticity. Atterberg limit calculations are in accordance with field pocket vane testing, showing that the Upper Tanger clays display the lowest shear strength values of the dataset (Table 5.1).

5.4.2 Landslide geomorphology

The active portion of the Beni Derkoul landslide covers an area of 3.2km^2 and has a maximum runout of 5.6km. Its detachment area is positioned along the northern flank of the Koudiet es Sbaa and Beni Salah peaks and the Azaib plateaux. Landslide detachment is characterized by complex deep-seated slope deformation associated to four departure areas (D1, D2, D3 and D4 in Fig. 5.3) affecting the Tisiren, Tanger and Beni Ider units, as well as a ~30-40m thick rockslide deposit. The main landslide scarps strike N53, N27, N57 and N71 for the detachment areas D1 through D4, respectively (Figs. 5.3 and 5.5).

The detachment and runout areas of the Beni Derkoul landslide show width-length ratios ranging

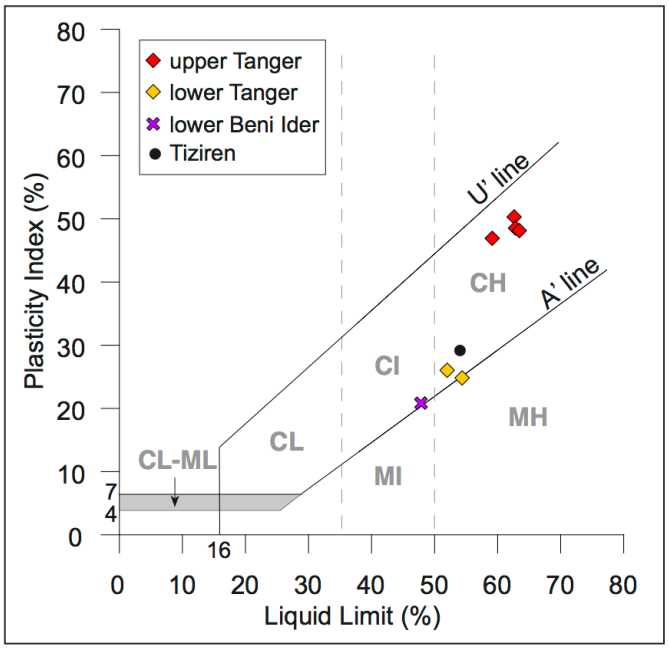


Figure 5.8 - Plasticity chart for the bedrock clay samples.

from 0.64 to 0.99 and 0.12 to 0.54, respectively (Table 5.3). The largest total runout height difference between scar and toe occurs within sectors D2 (900m) and D3 (700m). Nonetheless, height difference for the detachment area is highest for sector D1 and D2, and lowest for sector D3 (Table 5.3).

Deformation on sector D1 begins at the elevation of 1420m asl on the northern edge of the divide, affecting the lower and upper stratigraphic sequences of the Tanger Unit. It shows characteristic of a deep-seated complex slide propagating to N330, presenting three circular scarps with a maximum vertical offset of 30m.

Deformation along sector D2 affects the stratigraphic sections of the Tiziren and Upper Tanger Unit and a ~40m thick rockslide deposit (Fig. 5.3 and 5.9). The rockslide scarp is preserved along the top of Koudiet es Sbaa exposing a structurally-controlled failure surface facing north-west (Figs. 3 and 10). Slope deformation appears to post-date the rockslide event as testified by the existence of an offset of over 40m within the rockslide deposit (Fig. 5.3 and 5.9). The rupture zone for sector D2 is defined by a triangular scarp facing north-west and by a complex hummocky topography extending from elevations of 1700 asl to approximately 1300m asl (Fig. 5.3). From the top of Koudiet es Sbaa, three morphological steps associated with deep-seated gravitational normal faulting gradually lower topography (Figs. 5.3 and 5.4).

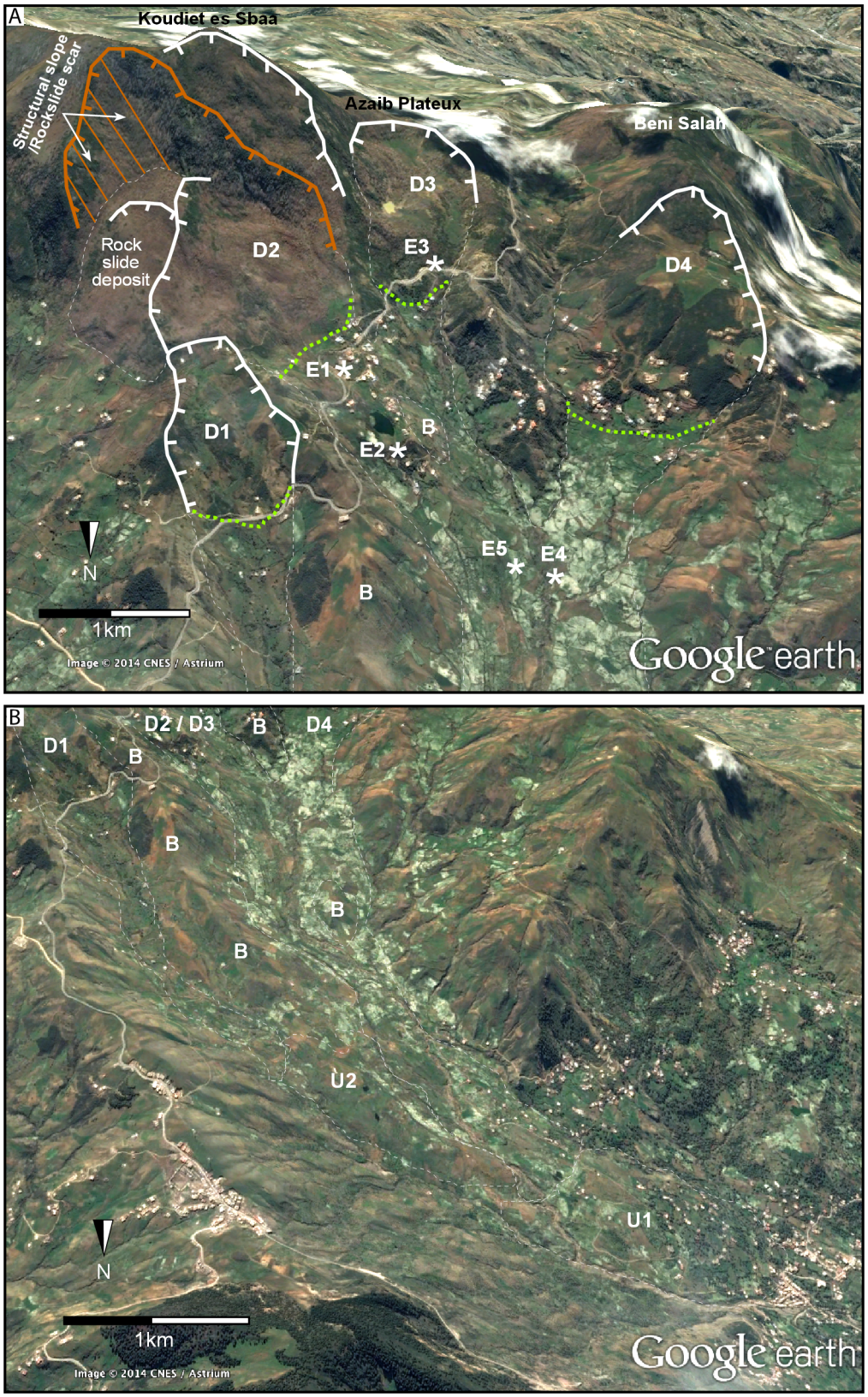


Figure 5.9 – Bird-eye view of the Beni Derkoul landslide.
Google Earth image of the Beni Derkoul landslide. D1 through D4 identify the main detachment areas (see text for explanation); B) Bedrock; E1) Azaib café road-cut; E2) Lake Azaib road-cut; E3) Village of Azaib road-cut; E4 and E5) Taghfart gully; U1 and U2) Landslide units.

Further southwest, along the top of the Azaib plateau, sector D3 experiences slope deformation through deep-seated normal faulting and trench opening affecting the upper stratigraphic units of the Tanger nappe and a ~30m-thick rockslide deposit resulting from the collapse of the Tiziren thrust front (Figs. 5.3 and 5.9). Similarly to sector D2, deep-seated deformation seems to post-date the rockslide event, as testified by the presence of slide scarps and trenches offsetting the deposit downslope from the main detachment zone. The transition between the areas affected by deep-seated deformation and earth-flow along sectors D2 and D3 is marked by the occurrence of water sources along a probable gravitational thrust, following the stratigraphic limit between the Upper and Lower Tanger Units.

Sector D4 is located further to the west along the northern flank of Jebel Beni Salah. Slope deformation affects the upper and lower stratigraphic unis of the Beni Ider nappe.

Downslope from the main detachment areas, landslide kinematics changes progressively from deep-seated failure to flow while penetrating the valley of Beni Derkoul. Valley morphology results from the coalescence of landslide masses descending from the upper sectors of the catchment, presenting successive slope breaks on which small lakes and poorly drained areas can be found (Figs. 5.3 and 5.9).

The lower section of the Beni Derkoul valley is 1km wide and presents a semi-flat hummocky surface that contrasts with the 30° to 60° valley slopes carved into the bedrock (Fig. 5.4). Valley orientation shifts from SE - NW to E – W approximately 2.5km east of the village of Beni Derkoul. At this point, the presence of a morphological step (15-20m) leading to a semi-flat hummocky surface (2° - 3° slope) between 750 and 820m marks the transition between two landslide deposition units: Unit 1 (U1) and Unit 2 (U2) (Figs. 5.3 and 5.9). The sedimentary characteristics of U1 and U2 are similar, being composed of angular to sub-rounded sandstone blocks in a sandy-clay matrix. Deposits are strongly heterometric with sandstone blocks ranging from 0.003 to 8m^3, showing evidences of inverse grading with larger blocks occurring on top.

5.4.3 Landslide depth estimation

The estimated depth of the landslide rupture plane was obtained through 2nd order polynomial fit of reference points positioned along the longitudinal and transverse profiles of the landslide mass (Fig. 5.6 and Table 3). We used 5% confidence intervals as proxies to the measured uncertainty. All plots show determination coefficients (R^2) above 0.88. Maximum landslide depths range from 100m±15m in sector D3 to 35m±10m in sector D1.

The depth of the failure surface at sector D1 was estimated based on the morphology and slope of the upper scarp and on the estimated depth of the landslide mass in the runout area. Polynomial fit shows a maximum depth of 35m±10m.

The detachment area D2 is composed of two sectors affecting the Tiziren Unit. The first step occurs close to the top of the Koudiet es Sbaa and is associated with a secondary failure of the Tiziren front. The depth of the detachment surface was modelled based on the morphology and slope of the landslide scar and reaching a maximum depth of 30m ±10m. The second and third steps are limited to the rockslide deposit. To analyse the geometry of failure we have taken into account the thickness of the deposit and the geometry of the rockslide rupture surface. The rupture plane for the rockslide deposit follows a bedding surface of the Tiziren sandstones with an attitude of N45W, 60N (Fig. 10). Taking into account the geometry of both failure planes and assuming that slope deformation mobilizes the complete rockslide sequence we estimate a maximum depth of 70m±15m (Fig. 5.6).

Sector D3 affects the upper stratigraphic sequence of the Tanger Unit. Field evidence indicates that the slide surface follows the contact between the upper and lower sequences of the Tanger Unit. Taking into account both the geometry of failure and the attitude of the bedrock units and the presence of water sources occurring along the frontal section of the detachment zone we estimate that the failure plane reaches a maximum depth of 100m±15m (Fig. 5.6).

Deformation on sector D4 displaces the upper and lower stratigraphic units of the Beni Ider nappe. The geometry of the failure plane consistently follows the contact between the upper and lower sequences reaching a maximum estimated depth of 70m±15m (Fig. 5.6).

Slope deformation downslope from the main detachment areas shifts from deep-seated failure to a dominant flow component. The landslide masses flowing from sectors D1 through D4 penetrate the valley of Beni Derkoul fossilizing pre-existing valley topography. The depth of the debris infilling the lower sections of the valley was estimated using a 2^{nd} degree polynomial fit to the valley slopes carved on bedrock. A maximum thickness of 20m±5m occurs in association to the debris detached from sectors D2 and D4. Valley infill originating from sectors D1 and D3 reaches a maximum estimated thickness of 8m±2m (Fig. 5.6).

The lower sector of the Beni Derkoul valley occupied by landslide deposition units 1 and 2 was also analysed. Longitudinal profiles of the gully incision along the margins and central section of U1 and U2 (Fig. 5.3 and 5.10) were created to inspect the magnitude of incision and estimate the thickness of the landslide deposits. Furthermore, we used bedrock carved valley slope and stable bedrock

outcrops along the margins of the valley bottom to estimate the thickness of accumulated debris from transverse valley profiles.

Longitudinal profiles reveal the presence of two knick zones positioned at 900 and 750m asl (Fig. 5.10). The first knick zone occurs between Unit 2 and Unit 1 at an approximate altitude of 900m asl. The second knick zone occurs at 730m asl and is carved into the Tanger nappe. Above and below the first knick (up to 850m asl) the gully runs on top the landslide deposit presenting 8 to 10 meter of incision. Below 850m asl the gully channels are carved into bedrock, running up to 30 meters below the top of Unit 1, providing a rough estimate to the thickness of the debris along the margins of the deposit. We obtained similar results taking into account the transverse valley profiles, with a maximum thickness of 30m±10m and a determination coefficient (R^2) of 0.90 for a 2nd degree polynomial fit (Fig. 5.6 and Table 3). Furthermore, considering the elevation of the fluvial terraces along the Maâmala River we observe that the upper levees coincide with the elevation of the second knick zone (Figs. 5.10 and 5.11).

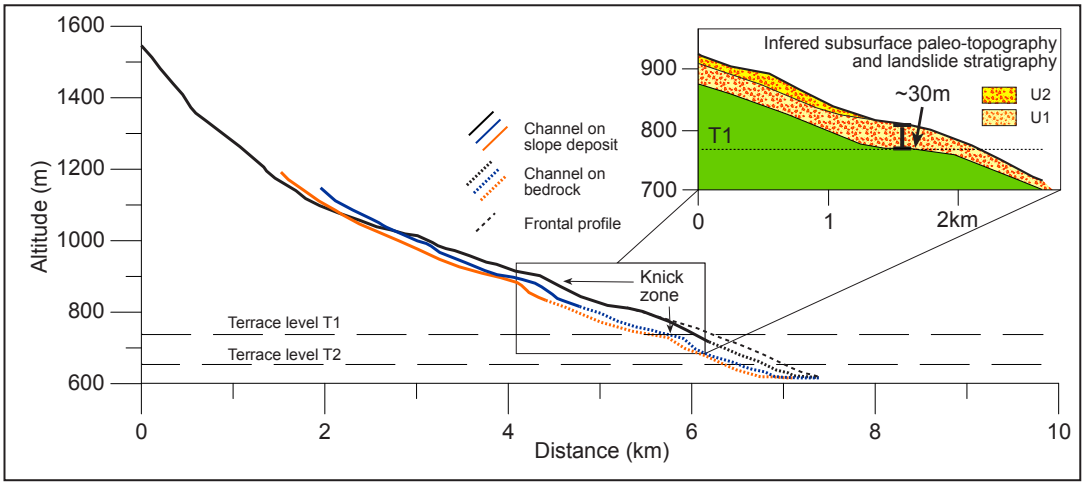


Figure 5.10 - Longitudinal profiles of the streams incising the landslide body, inferred subsurface paleo-topography and landslide stratigraphy.

5.4.4 Slope tectonics

The term slope tectonics is adopted in this section following the work of Jaboyedoff et al. (2011) describing deformation that occurs in response to gravity, topography and the geological setting and generates features that can be compared to those created by tectonic processes. In the context of the Beni Derkoul landslide most of these structures are masked by vegetation or covered by superficial deposits. The privileged spots to study slope tectonics are located along road-cuts and along the margins and central section of the Beni Derkoul valley, where seasonal torrential gullies expose the internal structure of the landslide (locations on Fig. 5.9).

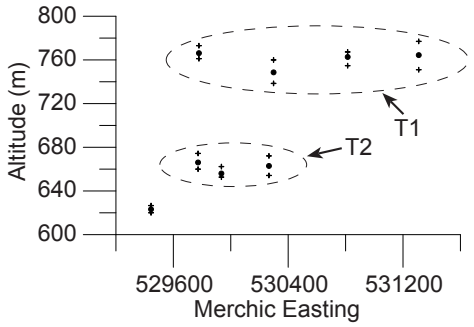


Figure 5.11 - Altitudinal distribution of the fluvial terraces of the Maâmala River.

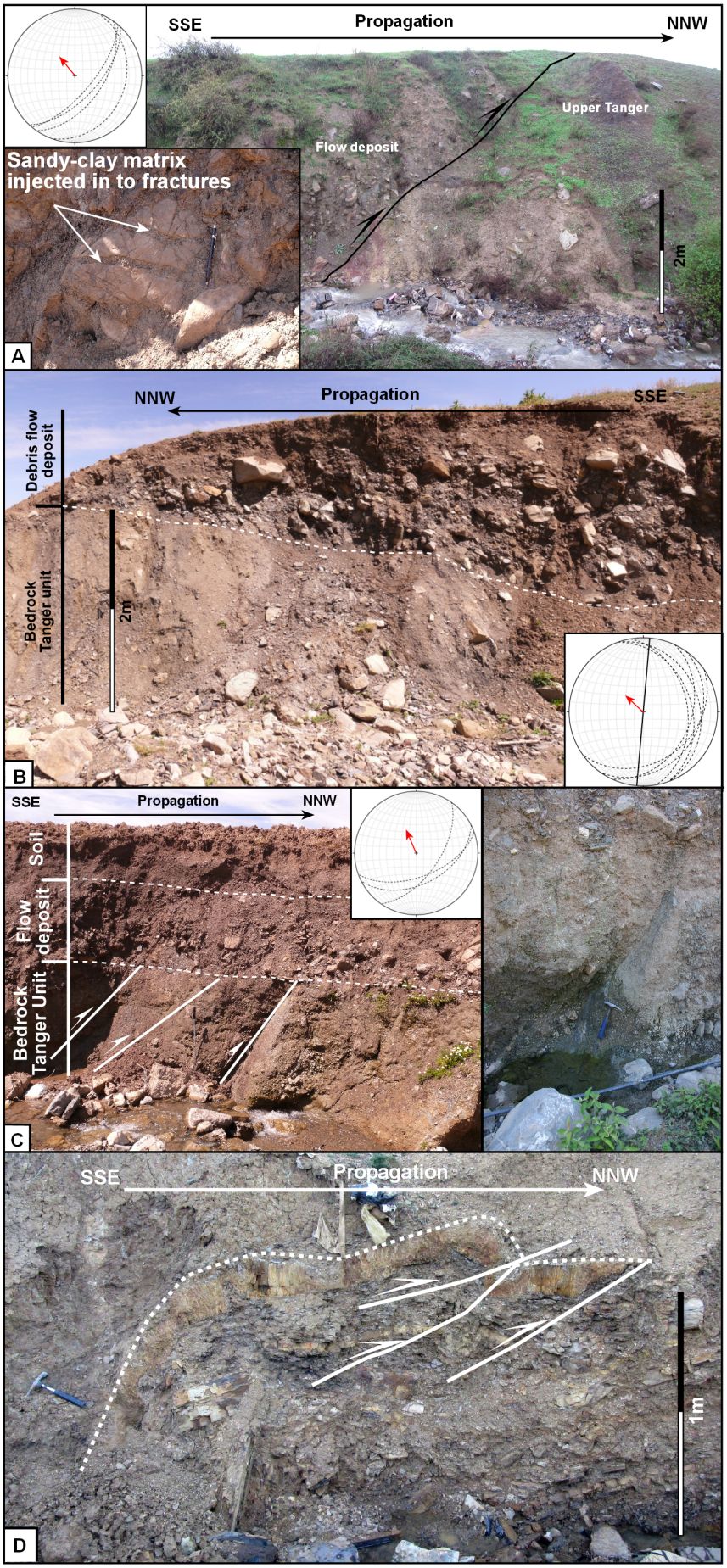
5.4.5 Taghfart gully sections

The Taghfart gully incises the western and eastern end of landslide bodies detaching from sectors D4 and D3, respectively (E4 and E5 in Fig. 5.9 and Fig. 5.12A and B). On the western branch (E4; Fig. 12A and B), a deposit (5m thick) containing angular to sub-rounded sandstone and limestone blocks in an heterometric sand and clay matrix, superimposes the upper Tanger Unit through a N75,58S trending thrust fault. The larger and flatter blocks display imbrication, with flat block surfaces presenting N40,69S attitude (stereoplot in Fig. 5.12A) indicating a general N310 propagation direction; furthermore, fractured blocks are injected with the involving sandy-clay matrix (inset Fig.12A). The underlying Tanger clays presents N5,90E striking foliation.

The eastern branch (E5; Fig. 5.12C) of the Taghfart gully exposes a similar, but thinner and undeformed, sequence superimposed to the Tanger clays. Foliation within the Tanger clays strikes N70 to N82,65E and is affected by three faults striking N35,60S, N63,48S and N70,58S.

5.4.6 Village of Azaib section

The structure of the landslide is further exposed along the walls of the gully that flows north from sector D3, showing a deformed sequence of the upper Tanger Unit (Fig. 5.12D). At this site, bedding in stable bedrock outcrops strikes N310,38N. The exposure shows a sequence of marls and clay beds deformed into an asymmetric monocline fold with the axial plane striking N60,45N. The northern limb is deformed by high angle reverse faulting striking N65,18S.


SSE
Propagation
NNW
Upper Tanger
Flow deposit
2m
Sandy-clay matrix
injected in to fractures
A
NNW
Propagation
SSE
Debris flow
deposit
Bedrock
Tanger unit
2m
B
SSE
Propagation
NNW
Soil
Flow
deposit
Bedrock
Tanger Unit
C
SSE
Propagation
NNW
1m
D

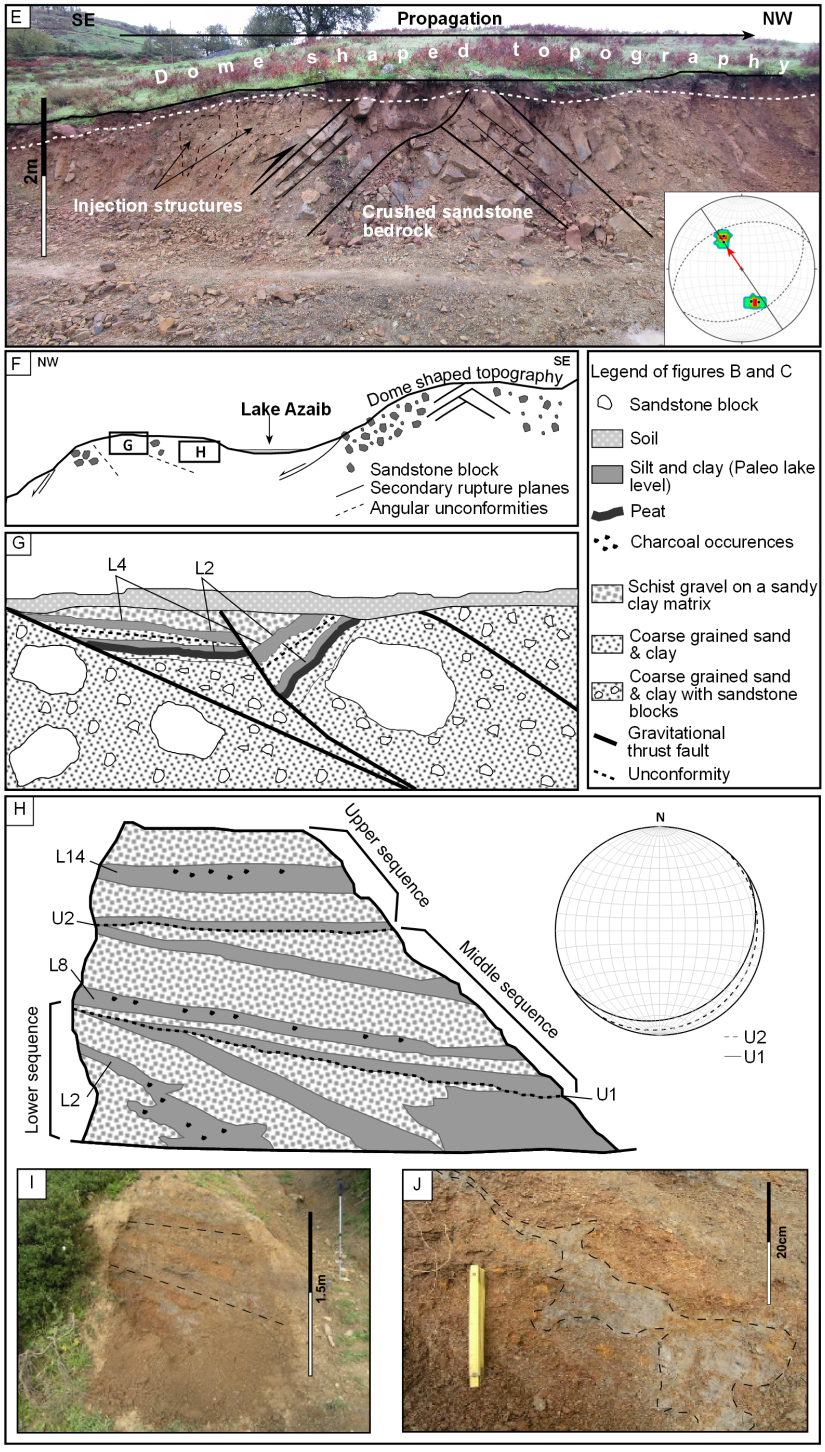


Figure 5.12 - Slope tectonic structures of the Beni Derkoul landslide.
A and B) Exposure of the western Targhfart gully. Equal area stereoplots show flat clasts attitude (projected as planes); Solid line for bedrock foliation and red arrow for the propagation azimuth of the landslide mass. C) Exposure of the eastern Targhfart gully. Equal area stereoplots show fault attitude; D) Azaib Village road-cut. Dotted white line points to the upper limit of a deformed schist bed. E) Azaib café road-cut. Stereoplot shows bedding attitude and poles to fractures measured in the fold core. F) Lake Azaib roadcut. Position of the roadcuts G and H relatively to Lake Azaib; G) Roadcut 1; H) Roadcut 2. Equal area projection of unconformities. I and J) Photos of the deformation on section H and close-up of the flame structures identified in the lower sediment level.

5.4.7 Azaib Café road-cut

Downslope from sector D2 a road-cut exposes a chevron-like fold (hinge striking N55) deforming sandstones belonging to the Tiziren Unit (Figs. 5.12E). The fold is thrusted in the hinge line along N50,38S shear planes that coincide with bedding of the sandstone. The core of the fold is highly shattered showing rock fracturing along N48, 47S and N247, 58N structures. Bedding disappears to the north-west and south-east of the fold giving place to a sandy-clay deposit with angular sandstone blocks. To the south-east of the fold plume-like structures with fine sandstone and schist clasts pinching to the base of the road-cut, occur.

5.4.8 Lake Azaib road-cut

Lake Azaib is the largest seasonal water body within the Beni Derkoul landslide. It is located in the transition between the upper sector affected by deep-seated failure and the lower sector dominated by flow. A road located downslope from Lake Azaib (Fig. 5.12F-J) exposes two road-cuts (~2m thick) showing deformed layers of silty-clay, gravel and peat.

Road-cut 1 (Fig. 5.12G) shows two sequences composed of five levels of alternating grey silty-clay and yellow fine-grained sand. The upper and lower silty-clay levels are separated by an angular unconformity and deformed along a N28, 64E gravitational structure. Peat and charcoal collected from levels 2 and 4 yielded calibrated AMS^{14}C age (1σ) ranges of 6,890-6,968 Cal BP and 6,664-6,726 Cal BP, respectively (Table 5.2). The top of the sequence is covered with a 15-centimeter schist gravel bed.

Road-cut 2 (Fig. 5.12H) is composed of 15 layers of alternating angular to sub-rounded schist gravel (clast size = 1 to 4 cm) in a sandy-clay matrix with no internal stratification and grey silty-clay levels containing millimetre-sized charcoal fragments. Two angular unconformities plunging to the SSE allow the definition of three sedimentary sequences. Bed deformation increases from top to bottom. The lower sedimentary unit shows syn-sedimentary deformation (flame structures) (Fig. 5.12J). Charcoal collected from levels 2, 8 and 14 yielded the following calibrated AMS^{14}C age (1σ) ranges: L2 – 6,195-6,046 Cal BP; 6,200-6,278 Cal BP; L8 – 6,122-6,146 Cal BP; 6,178-6,223 Cal BP; 6,229-6,276 Cal BP; L14– 6,217-6,237 Cal BP; 6,272-6,316 Cal BP (Table 5.2).

5.5 Evidence for present-day activity

Geomorphic evidence of present-day activity of the Beni Derkoul landslide is concentrated along the detachment areas, particularly in sectors D2 and D3. At these sites, open tension gashes striking

perpendicular to the propagation azimuth are common (Fig. 5.13). Furthermore, fracturing on buildings and along the national road further emphasizes the recent nature of the landslide reactivation (Fig. 5.13).

Persistent scatterer data for the Beni Derkoul landslide shows deformation ranging from -4.6 to 1.3 mm/yr (Fig. 5.7). PSs distribution is generally dispersed and provides little information on surface motion. The highest and most consistent PSs concentration occurs within sector D2 with deformation values ranging from -3.5 to -2.5mm/yr.

5.6 Interpretation and discussion

Previous work (Kornprobst et al. 1980; Chaouki 1991) mapped the Beni Derkoul landslide as a single event of late-Pleistocene age (Soltanian in Moroccan chronology), resulting from the coalescence of debris detached from rupture areas placed at elevations of 900-1300m asl. Nonetheless, our data indicates that active slope deformation extends further upslope affecting the Tiziren, Beni Ider and Tanger units along the drainage divide of the Beni Derkoul valley. Furthermore, terrain morphology point out to the existence of two landslide units that relate to earlier stages of landslide evolution. In the next sections we will interpret and discuss the obtained results to the main geomorphological features that were identified: I) the active Beni Derkoul landslide; II) landslide units 1 and 2.

5.6.1 Active Beni Derkoul landslide

5.6.2 Structural, lithological and tectonic control

The first observation regarding the imposed structural control on landslide initiation is related with the coherence between the attitude of sedimentary bedding and the main propagation azimuth of the landslide masses detaching from sectors D1 through D4 (Fig. 5.3; section 2). The most striking evidence of bedding control on landslide triggering occurs in the rockslide events in sectors D2 and D4, were failure occurs along bedding planes of the Tiziren and Beni Ider unit, respectively. Deformation on sector D1 and D3 is oblique to local bedrock attitude but our data suggests that the failure surface is established along the contact between the upper and lower stratigraphic units of the Tanger nappe.

The lithological control on bedrock failure is clearly outlined by the mechanical properties of the clay formations, which present high plasticity and low shear strength. The liquid limit for the collected samples is well above the threshold of 35% indicating a high expansion potential of the clays, as well as indicates high compressibility and high shrink-swell tendency. Taking into account

these observations, we conclude that gravitational deformation of the Beni Derkoul landslide occurs in response to the presence of high plasticity clays beds. These occur as lateral facies variations within geological units and create sharp rheological transitions between nappes. The critical position and geometry of these beds, underlying compact bedrock units and displaying a sub-parallel geometry to the local slope, creates the necessary condition for the observed slope instability.

Inherited tectonic structures, particularly the ones striking perpendicular and oblique to the main detachment areas, aid to define rock compartments prone to failure. This is particularly evident for the landslide scarps of rockslide events along the flank of the Koudiet es Sbaa and within sectors D3 and D4, where faults striking W-E to WNW-ESE and dipping to the north are spatially coherent with trench opening and gravitational normal faulting inside the landslide mass (Fig. 5.3).

5.6.3 Landslide kinematics and slope tectonics

The study of landslide kinematics is based on interpretation of surface geomorphology and analysis of the internal structure of the landslide mass exposed along road-cuts and gully incisions.

Within the main detachment areas slope deformation is accommodated through high-angle reverse faulting leading to formation of step-like morphologies where small lakes and poorly drained areas are found. Based on the geometry of the preserved surface landslide features and on the maximum observed offset the estimated depth of the presumed failure surface shows plausible results for all four sectors. Nonetheless, irregularities associated with internal buckling of the landslide mass of due to the presence of compact bedrock units are not detected and further studies should be performed (e.g. electric resistivity).

The transition between sectors affected by deep-seated slope deformation and flow movement is marked by the presence of water sources, providing a good indicator to the surfacing of the main or secondary shear planes. Moreover, based on the inferred depth of shear surfaces, the transition between the two sectors is also accompanied by a drastic reduction in the thickness of the debris involved in gravitational failure.

The structure of the landslide masses descending from the peaks of the Koudiet es Sbaa, Azaib Plateux and Beni Salah was analysed. Downslope from sector D2 an anticline fold of sandstone beds was identified. The fact that this structure is located in context of the Tanger Unit allows us to interpret it as deformation of detached bedded material from the flank of the Koudiet es Sbaa. Moreover, the fact that structural folding is consistent with the dome-shaped topography (Fig.

5.12E) indicates probable contemporary formation. This notion is further validated by the fact that both the fold and bedrock fracture geometries are consistent with N120 trending **σ**1 compression, which is in accordance with the propagation azimuth of the landslide mass. The presence of plume-like structures may be interpreted as injected material associated with high water content and formed in response to the compressive component associated with landslide propagation.

A similar fold structure is found along the gully that flows north from sector D3, showing a deformed sequence of the Upper Tanger Unit. The exposure shows an asymmetric monocline fold with the axial plane striking N60, 45N that is consistent with the north-northwest trending propagation azimuth of the landslide. Furthermore, the presence of high angle reverse faulting striking N65, 18S further indicates the existence of a horizontal component in landslide propagation.

Field observations along the Taghfart gully provide information on deformation occurring downslope from sectors D3 and D4. The presence of foliation within the Tanger clays striking perpendicular to the propagation azimuth in both sectors is a good indicator that bedrock units are involved in failure. The back tilting of the overlying slope deposit accompanied by the presence of block imbrication and matrix injection in block fractures are in accordance with north trending **σ**1 compression in association with translational sliding from sector D4. Furthermore, the geometry of the faults identified along the eastern branch of the Taghfart gully may correspond to internal thrusts detaching from the basal failure plane.

5.6.4 Middle Holocene activity and the Lake Azaib sedimentary record

The only available age constraints to the activity of the Beni Derkoul landslide were obtained from the Lake Azaib sedimentary record. Although the lake sediments only record landslide activity sourcing from sector D2, it provides evidence to the nature and magnitude of deformation within a short period of the Holocene.

The road-cut exposures of Lake Azaib displays a sedimentary sequence composed of alternations of silty-clay, coarse-grained sand and gravel layers. The absence of stratification within sandy-gravel beds indicates that sediment deposition is most probably related to single geomorphic events associated with erosion and surface wash in response to intense precipitation events. The silty-clay levels are interpreted as paleo-lake sediments corresponding to phases of landslide stability and fine sedimentation.

One of the main issues regarding landslide activity reconstruction from paleolacustrine data interpretation relates to the fact that sediment deposition within ponds and lakes post-dates slope

deformation, therefore providing minimum ages for a landslide event. In the case of Lake Azaib's sedimentary record, dating of lake sediments provides minimum ages for five reactivations (six if we take into account the present Azaib lake level) occurring between 6,868 Cal BP and 6,046 Cal BP (Table 5.2).

The oldest lake record placed at 6868 Cal BP has a 2cm thick peat level. Although several factors contribute to peat formation (e.g. temperature, soil saturation, rainfall-evaporation ratio), its presence within the oldest dated record outlines the presence of a higher temperature-humidity regime towards the establishment of climatic optimum. Furthermore, the absence of peat in the overlying levels testifies to a drastic shift in the climatic conditions. Nonetheless, due to the absence of previous records, the timeframe between the landslide event and lake deposition is presently unconstrained.

The existence of an angular unconformity between levels 2 and 4 on road-cut 1 provides evidence to a minor reactivation event, with tilting of level 1 to the south. The intense deformation and tilting of both levels along a south dipping gravitational fault testifies to a reactivation event with a dominant horizontal component.

In road-cut 2, the three sedimentary sequences divided by angular unconformities provide evidence to three reactivations of the Koudiet Sbaa landslide. For this particular case, the overlapping age intervals (Table 5.2) probably result from re-sedimentation processes, making it difficult to establish a time frame for the deformation events. Nevertheless, we can infer that in the 6,278 Cal BP to 6,046 Cal BP period three reactivations took place. The presence of flame structures in the lower sedimentary levels, interpreted as paleoseismites, is an indicator of paleoseismic activity in the region (Fig. 5.12J). Although similar structures could be formed in response to vertical gravitational loading or pressure associated with landslide movement, the close proximity to the surface, together with the fact that flame structures are limited to one sedimentary sequence, favours the interpretation of a syn-sedimentary deformation in response to seismic ground acceleration. Furthermore, the fact that a similar schist-gravel unit occurs on top and bottom of road-cuts 1 and 2 respectively, leads to associate the deformation of the oldest units within sequence 1 with this paleoseismic event. The younger reactivation stages represented by lower magnitude deformation displayed by the upper sedimentary sequences of road-cut 2 most probably fits into a deformation pattern produced by creep.

Holocene climate variability in northern Morocco is relatively well constrained through the study of lake sediments (Damnati 2000) and pollen analyses (Reille 1977; Lamb et al. 1995; Cheddadi et al.

1998, 2009; Jalut et al. 2000, 2009). A clear climatic contrast is observed between the early and late Holocene, with precipitation being closer to present-day values after 5.3ka Cal BP (Cheddadi et al. 1998) (Fig. 5.14). Mean annual rainfall reached maximum values around 3.2 Cal BP. The lowest mean annual precipitation occurs at 9.5 Cal BP and at 6800 Cal BP (Fig. 5.14). Summer and winter temperatures were 2.5°C and 1°C above present day values for the period between 10000 and 6000 Cal BP. Between 6500 and 5700 Cal BP summer and winter temperatures displayed a drastic decrease, reaching values similar to those experienced nowadays.

Previous investigations suggest that wet and colder intervals from Lateglacial to the present have influenced slope evolution through increased landslide activity (e.g. Goudie 1992; Panizza et al. 1996; Dikau and Schrott 1999; Bertolini et al. 2004; Schmidt and Dikau 2004; Soldati et al. 2004; Bigot-Cormier et al. 2005). Nonetheless, when searching for landslide events as a feedback mechanism to climate change, data interpretation is hampered by the fact that both earthquake and extreme meteorological events (e.g. intense precipitation events; snow melt) also produce spatial and temporal clustering of landslide on a regional scale.

In what concerns the Lake Azaib record, taking into account present knowledge on the Holocene climate variability in northern Morocco, it is possible to say that, with the exception of the oldest lake level for which a minimum age is provided, landslide reactivations are decoupled from the main humid phases. Furthermore, according to the data produced by Cheddadi et al. (1998) the Azaib Lake record begins in one of the driest phases of middle-Holocene (-100mm than present-day values) with the upper sedimentary sequences occurring in a period of increasing mean annual precipitation and decreasing winter/summer temperature towards present-day values (Fig. 5.14).

These observations favour the association of the first reactivation events to triggering mechanisms other than the unique action of precipitation and hydrological processes. Due to the fact that the Beni Derkoul landslide occurs in close proximity (≈7km) to the Jebah Fault (Fig. 5.1), a sector defined by Benchekroun et al. (2013) as being subject to one of the highest seismic accelerations (0.27-0.33g) in the northern Rif, it is plausible to assume earthquake activity as candidate to landslide triggering. The presence of paleoseismic structures within the Azaib sedimentary sequence further supports these observations.

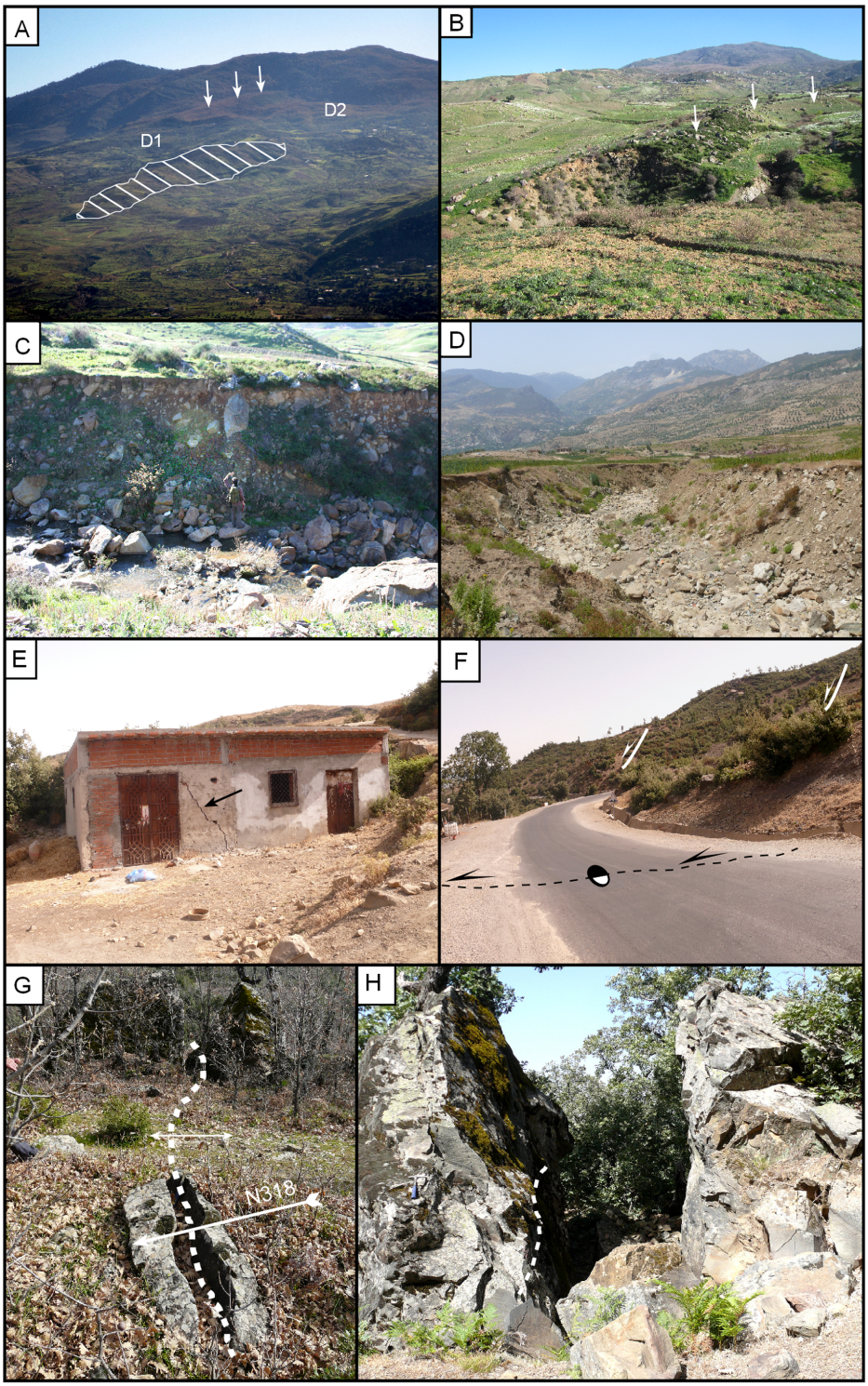


Figure 5.13 - Geomorphic features of past and present-day activity.
A) Detachment area D2. Arrows indicate the landslide scarp affecting the rockslide deposit; B) Lateral landslide ridge; C) Flow- slide deposit containing sandstone blocks embedded into remobilized clay of the upper Tanger unit; D) Gully incision of landslide Unit 2; E) Fractures on houses of the village of Azaib downslope from sector D2; F) Road deformation; G and H) Trench opening at the top of sector D3.

5.6.5 Present-day activity

As it was documented on section 4 the identification of Persistent scatterer data is hampered by several constrains (Hanssen 2005; Colesanti and Wasowski 2006; Crosetto et al. 2008; Cigna et al. 2012): I) problems associated with the geometrical visibility between local topography and the Line Of Sight (LOS) orientation; II) the presence of vegetation which causes temporal decorrelation and limits the identification of PSs; and III) landslides moving at rates exceeding the employed SAR wavelengths and satellite revisiting times, which in the cases of the images used in this study (ERS/Envisat) may not exceed 15cm/yr. Furthermore, within remote areas, data acquisition is hindered by the fact that PSs are not always evenly distributed within the landslide body, but gathered around particular sites where reflectance is consistently captured by the satellite.

The present-day movement of the Beni Derkoul landslide expressed as high velocity PSs (Fig. 5.7) is consistent with the internal limits of the landslide. Nonetheless, the low number of PSs and the presence of data voids within the landslide surface limit data interpretation. Therefore, the nature of reactivation is difficult to discern when simply referring to PSs data and further data needs to be collected.

Persistent scatterers showing higher point concentration with consistent deformation rates occur within sector D2. According to surface geomorphology (Fig. 5.3), PSs are associated with scree deposits occurring along the main slide scarp. Slope deformation might be related to the gravitational adjustment of large blocks in response to a very slow (2-3mm/yr) movement of the landslide. The fact that PSs data was not acquired for the frontal section of sector D2 suggests that the vertical component of deformation is dominant. Furthermore, taking into account the estimated depth of the failure plane (70m±15m), it is likely that slope deformation rates of 3mm/yr might be accommodated along the detachment planes and not reproduce horizontal propagation.

An interesting observation regards the analysis of the rainfall data for the SAR image timeframe. Climatic data shows that the winter months between 2004/2005 and 2008/2009 were characterized by average precipitations bellow 200mm (Fig. 5.15). Nevertheless, rainfall registered during the winter period of 2009/2010 at the station of Chefchauen was well above average, reaching 567mm in December 2009 and 200mm on January 2010 distributed over a period of twelve days. While the Bab Taza meteorological station is the closest to the Beni Derkoul landslide, rainfall data is unavailable for December 2009 and January 2010. Taking into account data from both stations, a strong correlation (R^2=0.89) for the monthly rainfall of winter months is observed (Fig. 5.15). This allows us to estimate the amount of rainfall at the Bab Taza station based on a linear regression fit,

which provides nearly 1210mm of rainfall for the same twelve-day period. A similar situation occurred in December 1963 with rainfall reaching 1120mm in 20 days, amounting to values of over 110mm/day in a five-day period (Reille 1977).

Although this only provides a rough estimate to the probable amount of rainfall falling in the Bab Taza area, it is interesting to observe that during this period several landslide occurred and partial reactivations were identified in the Beni Derkoul landslide. Specifically, the most common evidences were small fractures opening in house walls and road deformation at the base of sectors D2 and D3. Taking into account the PSs data it is plausible to assume that the majority of the observed deformation occurred during this period.

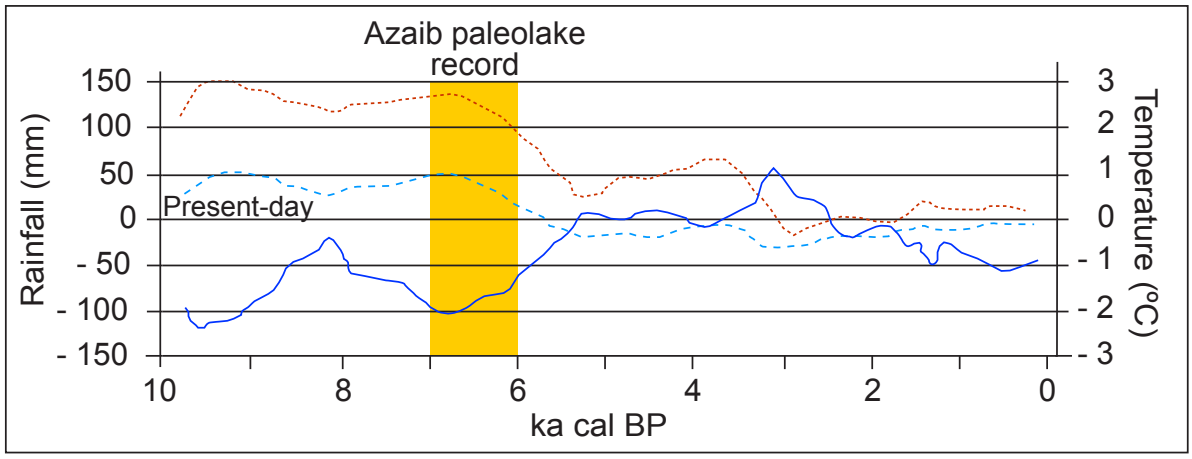


Figure 5.14 - Reconstructed climatic parameters according to present-day conditions (adapted from Cheddadi et al., 1998).
Blue line – Annual rainfall (mm); Red dotted line – July temperature; Dashed blue line – January temperature.

5.6.6 Landslide deposition units 1 and 2: record of past landslide activity

Geomorphological analysis of the lower section of the Beni Derkoul valley enabled the identification of a morphological step of 20m within the landslide debris. A similar feature is found along the longitudinal profiles of the gullies that margin the landslide deposit. Above the first morphological step (around 900m asl) gully incision is established within the landslide deposit. Below, the thalweg exposes the bedrock sequences of the Tanger Unit. Nonetheless, up and downstream from the first referenced morphological step the sedimentary composition and structure of the deposit is visually identical, showing an heterometric texture composed of large sandstone blocks in a sandy clay matrix with inverse grading.

Differences in terrain morphology point to the existence of two landslide deposition units. Landslide unit 2, while resulting from similar geomorphic processes, post-dates Landslide unit 1 and covers the later creating a morphological step of approximately 15-20m in the sector that corresponds to

the frontal lobe of the accumulation (Fig. 5.10). These observations are supported by the presence of knicks along the longitudinal profiles consistently reproducing the surface geomorphology. The comparable nature of the surface deposits is explained by the fact that both landslide units share similar sources.

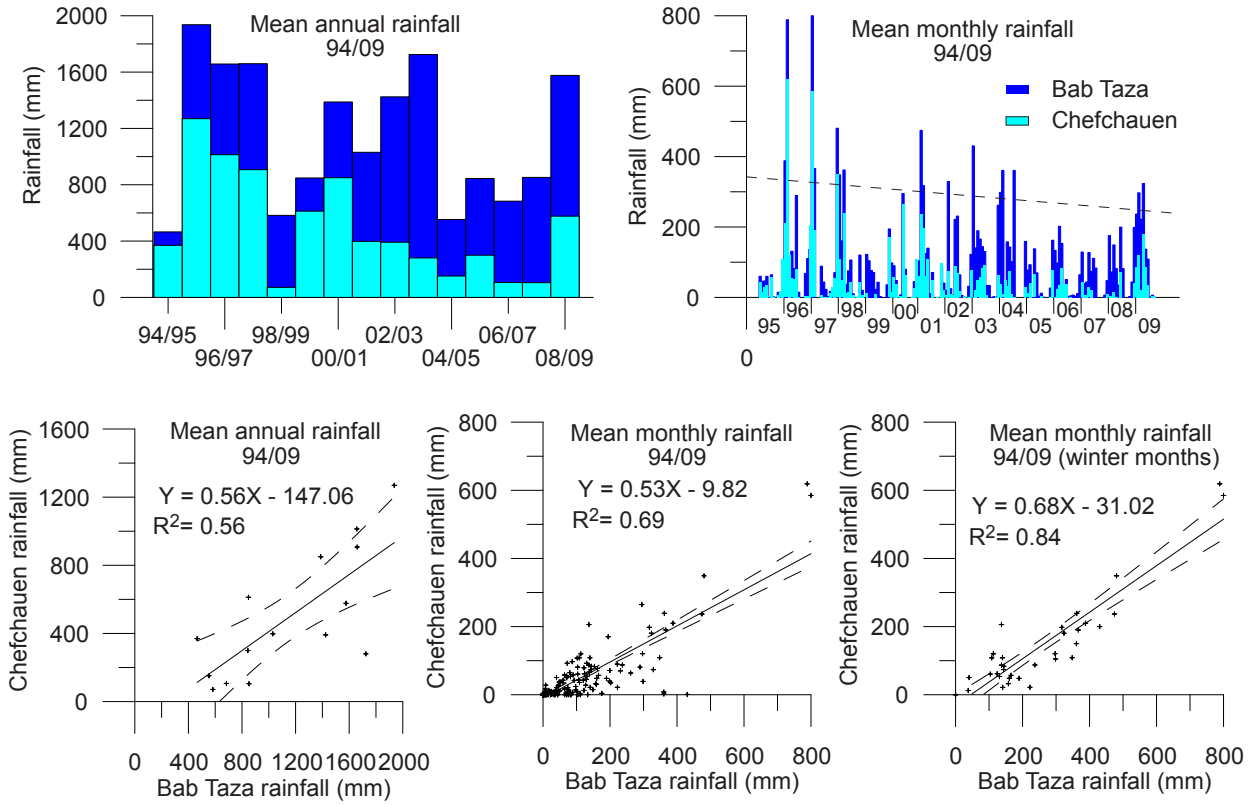


Figure 5.15 – Precipitation and data correlationa for the meteorological stations of Bab Taza and Chefchauen for the SAR image timeframe.

Estimations for the valley infill point to nearly 30m±20m of debris. An interesting observation relies on the fact that the altitude of the base of Unit 1 matches the altitude of the Upper-Pleistocene fluvial strath terraces of the Maamala River, positioned at approximately 730m asl (Fig. 5.11). Moreover, the lower knicks along the gullies that margin the landslide deposit are carved into bedrock and occur within the same elevation window. The altitudinal consistency between the base of Unit 1 and the fluvial terraces along the Maâmala River, suggests that the landslide mass adapted to a pre-existing topography that relates to the late-Pleistocene evolution of the Maâmala River (Figs. 5.10 and 5.11). Nonetheless, the fact that Unit 1 overlaps a paleofluvial level provides no indication to the age of the deposit, as it might be chronologically decoupled. Furthermore, due to the fact that the landslide debris could overlap an unknown thickness of fluvial sediments raises the question to whether the estimations of landslide thickness could be overestimated.

5.7 Conclusion

The Beni Derkoul landslide is a complex deep-seated failure comprising four main detachment areas and a runout sector extending over 5km. Along the lower sections of the valley, two landslide deposits testify to past landslide activity. Slope deformation in the detachment area is strongly controlled by bedrock structure and lithology. The consistency between the structure of the bedrock units and the topography of the flanks of the Koudiet es Sbaa and Beni Salah peaks, together with the presence of high plasticity clays are determining factors for slope instability phenomena. In this context, the geometry and depth of the failure planes is controlled by E-W to NW-SE trending tectonic structures, by the depth at which the marly and clay formations occur beneath the compact sandstone of the Beni Ider and Tiziren units and the geometrical consistency between bedrock attitude and surface slope and aspect.

The complexity of the evolution of the Beni Derkoul landslide is testified by the presence of two landslide units within the lower section of the valley. Furthermore, the altitudinal consistency between the estimated depth of landslide unit 1 and the fluvial terraces along the Maâmala River, suggests that during the earliest stages of landslide activity it adapted to a pre-existing topography that relates to the late-Pleistocene evolution of the Maâmala River.

The age of the initial failure is not determined in this study. Nonetheless, five Middle Holocene reactivations were identified, for which minimum AMS radiocarbon ages were obtained. From a kinematical perspective, the first three events are associated with a downward propagation of the landslide mass as evidenced by the deformation of paleolake sediments along NE-SW trending gravitational structures and presenting evidence of plaeoseismic activity. The geometry of the upper and most recent levels fits into a pattern of deformation associated with creeping. Furthermore, according to Holocene climatic reconstructions, the age constrains for the landslide reactivations are placed during one of the driest and hottest phases of the Holocene, which suggests that slope deformation is decoupled from the Holocene climatic trends.

Present-day landslide activity is characterized by trench opening within the main detachment areas. Tension fractures in man-made structures outline the recent nature of the activity. The analysis of climatic data for the 2004-2009 period showed that during the winter of 2009-2010 the region received estimated rainfall amounts of over 1000mm in a period of twelve days. Although evidence of slow movement was identified during this period it is unclear if the nature of reactivations is related to partial/secondary failures. Moreover, since estimated rupture surface depths reach 35 to 100m in the detachment sectors, the low deformation rates acquired through persistent scatterer

technique (max. 3mm/yr) may in fact be accommodated through internal deformation of the landslide mass and not produce any relevant horizontal landslide propagation.

Although several problems remain to be answered, our results question the ability of present-day rainfall patterns to trigger the reactivation of the total Beni Derkoul landslide without the aid of an earthquake event. The fact that this landslide is located in an area of high seismic acceleration and shows paleoseismic evidences associated with geomorphic marker of slope instability, leads us to associate landslide triggering with cyclic earthquake events. Furthermore, due to the presence of high plasticity clays as one of the main predisposing condition controlling slope deformation and taking into account the relevant flow component in the runout area we are tempted to place the initial triggering during the humid phases of the Upper-Pleistocene Lower Holocene boundary, in response to either, or the combination of, heavy and prolonged rainfall, seasonal or climate-induced snow melting and seismic activity. In fact, during the last pluvial phase at the end of the Pleistocene, the Rif Mountains experienced heavy rainfall and permanent snow cover along the highest peaks, with geomorphic evidence of frost action processes and periglacial activity include stratified slope deposits and nivation hollows extending to a minimum altitude of 1000 and 1650m asl, respectively (Maurer 1968).

6 Concluding remarks

Similarly to what has been reported for other mountain belts, the topography of the Rif Mountains expresses an ongoing competition between tectonic, climatic and erosion processes. Using a multidisciplinary approach, we up scaled from the application of geomorphometric tools to study the topography of the northern Rif, to a detailed analysis of the geomorphological and geological conditions of a large bedrock failure. Throughout this study we successfully identified the main factors controlling the spatial variability of topographic relief and magnitude of large bedrock failures.

Objective 1 – To detect spatial variations in landscape morphometry reflecting the interference of post-Tortonian tectonic activity and analyse the role of bedrock in sustaining relief conditions.

The topography of the Rif was inspected through two time-scale dependent morphometric approaches focusing on the identification of tectonic and bedrock related influences on the physiography of the Rif. Our results show that spatial variations in tectonic uplift and bedrock strength tend to control the way the drainage system evolves through bedrock incision and regressive erosion. Morphotectonic evidences of surface uplift and tectonically induced drainage network incision are concentrated along the Internal Domain and the southern sector of the Ketama Unit, defining two zones of distinct deformation limited by the Jebah and Nekor faults. These observations are in accordance with the current tectonic models proposed for the maghrebian region.

Nonetheless, while significant detailed geological and tectonic information is available for the Internal Domain, the majority of the mountain belt lacks information on measured uplift rates. One of the possible procedures to fill-in this gap will be to focus on the analysis of Quaternary fluvial deposits to further elaborate on the nature and intensity of tectonic processes responsible for the uplift of the Rif belt.

Objective 2 – To analyze the statistical and spatial distribution of large bedrock failures

One of the most relevant contributions of this work is the establishment of the first landslide inventory for the northern whole northern Rif Mountains. By performing a detailed analysis of aerial photos at the scale of 1:40,000 and satellite images within free only servers such as Google-Earth and Bing we were able to identify more than 10,000 landslides ranging in size from $3x10^{-5}$ to 9,4 × 10^6 km^2. Nonetheless, the completeness of the inventory below 0.01km^2 is questioned due to spatial variation in image quality.

The statistical properties of the inventory were analysed through the pdf. While the power-law fit to the distribution between 0.01 and 1km^2 is in accordance with the statistical data of other regional and complete landslide inventories (Mallamud et al., 2004a), above the threshold value of 1km^2 the distribution drops along a distinct power-law fit. Taking into account that large landslides tend to sustain the action of erosional processes over smaller landslides, it is unlikely that our dataset expresses an incompleteness of the inventory for the upper–end of the distribution. Furthermore, taking into account landslide density estimatimates through the application of the Getis-Ord method, a similar trend is obtained showing high landslide clustering above a similar threshold value of 1km^2. The fact that landslides tend to occur in association with distinctive surface bedrock conditions is most probably an expression of critical triggering and predisposing conditions (either than lithology), capable of producing high magnitude, low frequency events. In fact, the integration of tectonic data shows that large bedrock failures tend to occur within the hanging-wall of the thrust fronts of the Rif and close proximity to NE-SW trending active faults, in association to areas with a mean local relief above 1000m. The increase in number of large bedrock failures along areas subjected to the highest seismic acceleration values supports this observation, with potentially high magnitude earthquakes effectively producing large scale slope deformation through rock shattering of highly and deeply fractured bedrock units positioned along the hanging-wall of the Rif thrust fronts.

Taking advantage of the existing inventory, future studies should try to perform a detailed analysis of the geometry and chronology of large and very large failures in order to provide information on the volumetric and spatio-temporal contribution of bedrock landslides to the degradation of mountain topography. Furthermore, with the increasing availability of high-resolution digital terrain

data it will be interesting to reassess the topographic signature of large bedrock failures within the morphostructural domain of the Tanger Unit.

Objective 3 – To refine the activity status of large bedrock failures and detect slow gravitational movement using the PSInSAR technique

In this section we performed a slope instability analysis through the integration of persistent scatterers obtained from SAR image modeling for a 6-year period (2004-2010). The distribution of PSs was analyzed taking into account terrain first order derivatives, bedrock lithology and landslide distribution. Furthermore, the activity status of the inventory was refined through the application of the PSI matrix approach (Cigna et al. 2012) and the PSI-Hotspot and Cluster analysis (Lui et al. 2011). Slope deformation expressed as high velocity hotspots is consistent with sectors previously identified with deep-seated slope deformation. Furthermore, field and PSs data suggests that during the triggering event of 2009/2010 larger landslides tended to suffer only partial reactivations, either through the slow downward propagation of a secondary landslide mass or through the sliding along its margins, while smaller landslides (<0.05km^2) suffered reactivation along significant portions of the landslide body. This fact potentially expresses the dependency between landslide size and the ability of a precipitation event to produce a reactivation. Nevertheless, our conclusions are hindered by the fact that PSs are not always evenly distributed within large landslide bodies, but gathered around particular sites where reflectance is consistently captured by the satellite. This is particularly evident in the Atress, Agni Beni Boufra, Tiarta and El Marhza landslides. Furthermore, the low terrain roughness and the low frequency of terrain features capable of producing PSs-like within smaller landslides disables any link between landslide size and triggering in response to heavy and prolonged rainfall events. The nature of partial reactivations of large landslides is therefore difficult to discern when simply referring to PSs data and further field data collection and detailed geomorphological mapping should be performed.
Future studies should focus on exploiting SAR missions employing higher temporal frequencies, as the Sentinel-1 mission. For particular landslide cases, the approach could involve the application of conventional single interferograms techniques of Ground-Based InSAR techniques (Antonello et al. 2004), which can extend the velocity range to include faster phenomena.

Objective 4 – To study a large bedrock failure located within a critical topographic, tectonic and geological context as defined in section 3.

The Beni Derkoul landslide occurs within the critical topographic, tectonic and geological context of the Tiziren thrust front and approximately 7km south to the Jebah Fault, a sector subjected to the highest seismic accelerations in the northern Rif. We performed a detailed geological and geomorphological analysis of the landslide features combining field and laboratory techniques. Among the obtained results, the highlight of this investigation is the identification of five reactivations between 6,868 Cal BP and 6,046 Cal BP (with probable seismic triggering for the first event), which are apparently decoupled from the main humid phases of the Holocene. Although several problems remain unanswered, our results clearly outline the role of seismic activity in the triggering and reactivation of the Beni Derkoul landslide.

Future studies should focus on use of geophysical tools (e.g. electric resistivity) in order to better constrain the depth of the failure planes. Furthermore, as potential paleosesimic features have been identified, it is plausible to assume that several landslides in the vicinity of the Beni Derkoul valley were reactivated or triggered in response to this seismic event. For this reason, future studies should focus on extending the analysis to other landslides in the region. Coring of lake sediments along with analysis of paleosols should be performed in order to better constrain the history of landslide reactivations.

References

Agliardi, F., Crosta, G., Zanchi, A., (2001). Structural constraints on deep-seated slope deformation kinematics. *Engineering Geology* 59, 83-102.

Ahnert, F. (1970). Functional relationship between denudation, relief, and uplift in large mid-latitude drainage basins. *American Journal of Science 268*, 243-263.

Aït Brahim L, Chotin P, Hinaj S, Abdelouafi A, El Adraoui A, Nakcha C, Dhont D, Charroud, M, Sossey Alaoui F., Amrhar M, Bouaza A, Tabyaoui H, Chaouni A (2002). Paleostress evolution in the Moroccan African margin from Triassic to Present. *Tectonophysics* 357, 87-205

Ait Brahim, L. & Sossey, A.F. (2003). Utilisation de la télédétection pour l'analyse de la fracturation du domaine interne rifain (Maroc): relation avec la répartition des sources. *Télédétection* 3(1), 33-47.

Aït Brahim, L., Chotin, P., Hinaj, S., Abdelouafi, A., El Adraoui, A., Nakcha, C., Dhont, D., Charroud, M., Sossey Aloui, F., Amrhar, M., Bouaza, A., Tabyaoui, H. & Chaouni, A. (2002). Paleostress evolution in the Moroccan African margin from Triassic to Present. *Tectonophysics* 357, 187-205.

Akoglu, A.M., Cakir, Z., Meghraoui, M., Belabbes, S.O.E.A.S., Ergintav, S., Serdar, A., (2006). The 1994–2004 Al Hoceima (Morocco) earthquake sequence: conjugate fault ruptures deduced from InSAR. *Earth Planet Science Letters* 252, 467–480.

Andeweg, B. & Cloetingh, S. (2001). Evidence for an active sinistral shear zone in the western Alboran region. *Terra Nova* 13, 44-50.

Andrieux, J. (1971). La structure du Rif central. Notes et Mémoires du Sérvice Géologique du Maroc, 235: 155 p.Andrieux, J. (1973) Sur le metamorphisme des zones externes du Rif, L'Arc de Gibraltar. *Bulletin de la Société Géologique de France* 15, 106–107.

Azzouz, O., El Fellah, B., Chalouan, A. (2002). Processus de glissement dans le Massif de Bokoya (Rif interne, Maroc) : exemple de Cala Bonita. *Bulletin de l'Institut scientifique*, Rabat, section Sciences de la Terre, 24, 33-40.

Baker, V.R. (1990). Spring Sapping and Valley Network Development. In: Higgins, C. and D. Coates (Eds.), Groundwater Geomorphology: The Role of Subsurface Water in Earth-Surface Processes and Landforms. Special Papers, *Geological Society of America*, Boulder, 252, 235-265.

Barton, N.R., Lien, R. and Lunde, J. (1974). Engineering classification of rock masses for the design of tunnel support. *Rock Mechanics* 6(4), 189-239.

Baum, R.L., and Reid, M.E. (1995). Geology, hydrology, and mechanics of a slow-moving, clay-rich landslide, Honolulu, Hawaii. *Geological Society of America Reviews in Engineering Geology*, 10, 79-105.

Benchekroun, S., Iben Brahim, A., El mouraouah, A., Ouadif, L. & Baba, K. (2013). Maximum Magnitudes and Accelerations Determination in the Rif Mountain Belt, Northern Morocco. *International Journal of Engineering Inventions*, Volume 2, 6, e-ISSN: 2278-7461.

Bendkik, A. & Chenakeb M. (2004). Carte géologique du Maroc – Sidi Kacem: 1/50 000, Ministère de l'energie et des mines, Direction de la Géologie, *Service Géologique du Maroc*, nº 386, Rabat.

Benites, R.A., Haines, A.J., (1994). Quantification of seismic wavefield amplification by topographic features. *Research Report to the Earthquake Commission*, New Zealand. 108 pp.

Benmakhlouf, M., Galindo-Zaldívar, J., Chalouan, A., Sanz de Galdeano, C., Ahmamou, M., López-Garrido, A.C. (2012). Inversion of transfer faults: The Jebha–Chrafate fault (Rif, Morocco). *Journal of African Earth Sciences*, 73-74 (2012), 33–43.

Benmakhlouf, M., Galindo-Zaldívar, J., Chalouan, A., Sanz de Galdeano, C., Ahmamou, M. & López-Garrido, A.C. (2005). Kinematics and paleostresses in the Jebha–Chrafate transcurrent fault (northern Rif, Morocco). *Geogaceta* 38, 71-74.

Bertolini, G., Casagli, N., Ermini, L. and Malaguti, C. (2004). Radiocarbon data on Lateglacial and Holocene landslides in the Northern Appenines. *Natural Hazards*, 31, 645-662.

Bezzeghoud, M., Buforn, E., (1999). Source Parameters of the 1992 Melilla (Spain, Mw = 4.8), 1994 Alhoceima (Morocco, Mw = 5.8), and 1994 Mascara (Algeria, Mw - 5.7) Earthquakes and Seismotectonic Implications. *Bulletin of the Seismological Society of America*, 89, 2, 359 – 372.

Bianchini, S.; Cigna, F.; Righini, G.; Proietti, C.; Casagli, N. (2012). Landslide HotSpot Mapping by means of Persistent Scatterer Interferometry. *Environmental Earth Science*, DOI 10.1007/s12665-012-1559-5

Bigot-Cormier, F., Braucher, R., Bourles, D. (2005). Chronological constrains on processes leading to large active landslides. *Earth and Planetary Science Letters*, 235 (1-2), 141-150.

Bishop, K. M., (1999). Determination of translational landslide slip surface depth using balanced cross sections. *Environmental and Engineering Geoscience*, 5, 147-156.

Bouhdadi, S. (1994). Carte géologique du Maroc - Zoumi: 1/50 000. Ministère de l'energie et des mines, Direction de la Géologie, *Service Géologique du Maroc*, nº 386, Rabat.

Bourgois, J., Mauffret, A., Ammar, A. & Demnati, A. (1992). Multichannel seismic data imaging of inversion tectonics of the Alboran Ridge (western Mediterranean Sea). Geo-Marine Letters 12: 117-122.

Brardinoni, F. and Church, M. (2004). Representing the landslide magnitude-frequency relation. Capilano River Basin, British Columbia, *Earth Surface Processes and Landforms*, 29, 115–124.

Brookfield, M.E. (1998). The evolution of the great river systems of southern Asia during the Cenozoic India-Asia collision: rivers draining southwards. *Geomorphology* 22, 285–312.

Burbank, D. W. & Anderson, R. S. (2001). Tectonic Geomorphology. *Blackwell Science*, Malden, 274 pp.

Burbank, D.W. (1992). Characteristic size of relief. *Nature* 359, 483-484.

Burbank, D.W., Leland, J., Fielding, E., Anderson, R.S., Brozovic, N., Reid, M.R. & Duncan, C. (1996). Bedrock incision, rock uplift and threshold hillslopes in the northwestern Himalayas. *Nature* 379, 505–510.

Calabro, M. D.; Schmidt, D. A.; and Roering, J. J., (2010). An examination of seasonal deformation at the Portuguese Bend landslide, southern California, using radar interferometry. *Journal Geophysical Research*, Vol. 115, F02020, p. 10. doi: 10.1029/2009JF001214.

Carrara, A., Guzzetti, F., Cardinali, M., Reichenbach, P., (1999). Use of GIS technology in the prediction and monitoring of landslide hazard. *Natural Hazards* 20, 117–135.

Carson, M.A., & Kirkby, M.J. (1972). Hillslope form and process, *Cambridge University Press*, Cambridge, 475 pp.

Carter, M., Bentley, S. P., (1985). The geometry of slip surfaces beneath landslides: Predictions from surface measurements. *Canadian Geotechnical Journal* 22, 234–238.

Cascini, L., Fornaro, G. & Peduto, D. (2010). Advanced low- and full-resolution DInSAR map generation for slow-moving landslide analysis at different scales. *Engineering Geology*,

doi:10.1016/j.enggeo. 2010.01.003. now available online at: http://dx.doi. org/10.1016/j.enggeo. 2010.01.003.

Catalão, J., G. Nico, R. Hanssen, C. Catita (2011). Merging GPS and atmospherically corrected InSAR data to map 3D terrain displacement velocity. *IEEE Transactions on Geoscience and Remote Sensing*, Volume: 49, Issue: 6, Part: 2, 2354 – 2360.

Chalouan, A. & Michard, A. (1990). The Ghomarides nappes, Rif coastal range, Morocco: a Variscan chip in the Alpine belt. *Tectonics* 9, 1565–1583.

Chalouan, A., Michard, A., El Kadiri, Kh., Negro, D., Frizon de Lamotte, D., Soto,J.I. and Saddiqi, O. (2008). The Rif Belt, in Michard, A., Saddiqi, O., Chalouan, A. and Frizon de Lamotte, D. (Eds.). Continental Evolution: The Geology of Morocco Structure, Stratigraphy, and Tectonics of the Africa-Atlantic-Mediterranean Triple Junction, Springer, Lecture Notes in Earth Sciences, Volume 116/2008, 203-302.

Chalouan, A., Michard, A., Feinberg, H., Montigny, R. & Saddiqi, O. (2001). The Rif mountain building (Morocco): a new tectonic scenario. *Bulletin de la Société Géologique de France* 172, 603–616.

Chalouan, A., Saji, R., Michard, A. & Bally, A.W. (1997). Neogene tectonic evolution of the Southwestern Alboran Basin as inferred from seismic data off Morocco. *American Association of Petroleum Geologists Bulletin* 81, 1161-1184.

Champagnac, J., Molnar, P., Sue, C. & Herman, F. (2012). Tectonics, Climate, and Mountain Topography. *Journal of Geophysical Research* 117, B02403, Doi: 10.1029/2011jb008348.

Chaouki, A. (1991). *Les mouvements de terrain et les risques associés dans la region de Bab-Taza (Rif occidental)*. PhD thesis, Universite Louis Pasteur de Strasbourg.

Cheddadi, R., Fady, B., François, L., Hajar, L., Suc, J.-P., Huang, K., Demateau, M., Vendramin, G., Ortu, E. (2009). Putative glacial refugia of Cedrus atlantica deduced from Quaternary pollen records and modern genetic diversity. *Journal of Biogeography* 36, 1361-1371.

Cheddadi, R., Lamb, H.F., Guiot, J., Van Der Kaars, S. (1998). Holocene Climatic Change in Morocco: a Quantitative Reconstruction From Pollen Data. *Climate Dynamics* 14, 883-890.

Chen, Y.C., Sung, Q. & Cheng, K.Y. (2003). Along-strike variations of morphotectonic features in the Western Foothills of Taiwan: tectonic implications based on stream gradient and hypsometric analysis. *Geomorphology* 56, 109–137.

Chenakeb M., Bendkik A. (2004). Carte géologique du Maroc : Beni Ammar - Echelle 1/50 000, Ministère de l'energie et des mines, Direction de la Géologie, *Service Géologique du Maroc*, nº 428, Rabat.

Choubert G., Faure-Muret A. (1984). Carte géologique du Rif : Al Hoceima - Echelle 1/50 000, Ministère de l'energie et des mines, Direction de la Géologie, *Service Géologique du Maroc*, nº 302, Rabat.

Choubert G., Faure-Muret A., Frizon De Lamotte D. (1987). Carte géologique du Rif : Rouadi – Echelle : 1/50 000, Ministère de l'energie et des mines, Direction de la Géologie, *Service Géologique du Maroc*, nº 347, Rabat.

Cigna, F., Bianchini, S., Casagli, N. (2012). How to assess landslide activity and intensity with Persistent Scatterer Interferometry (PSI): the PSI-based matrix approach. *Landslides*, DOI 10.1007/s10346-012-0335-7.

Clarke, B.A. & Burbank, D.W. (2010). Bedrock fracturing, threshold hillslopes, and limits to the magnitude of bedrock landslides. *Earth and Planetary Science Letters* 297, 577–586.

Colesanti, C., Ferretti, A., Prati, C., Rocca, F. (2003). Monitoring landslides and tectonic motions with the Permanent Scatterers Technique. *Engineering Geology*, 68, 3-14.

Colesanti, C., Wasowski, J. (2006). Investigating landslides with space-borne Synthetic Aperture Radar (SAR) interferometry. *Engineering Geology*. 88, 173 – 199.

Comas, M.C., Garcia-Dueñas, V. & Jurado, M.J. (1992). Neogene tectonic evolution of the Alboran Sea from MCS data. *Geo- Marine Letters*, 12, 157-164.

Cornéea, JJ., Muncha, P., Melinte-Dobrinescub, M, Ben Moussa, A., Quillévéré, F., Drinia, H., Azdimousa, A., Touhamic, A.O., Merzerauda, G., Fauquetteg, S., Corsini, M., Moissette, P., Feddi, N. (2014). The Early Pliocene reflooding in the Western Mediterranean: New insights from the rias of the Internal Rif, Morocco. *Comptes Rendus Geoscience*, 346, 90-98.

Corominas, J.; Moya, J.; Ledesma, A.; Lloret, A.; and Gili, J. A. (2005). Prediction of ground displacements and velocities from groundwater level changes at the Vallcebre landslide (Eastern Pyrenees, Spain): *Landslides*, 2, 83–96.

Corsinia, M., Münchb, P.H., Melinte-Dobrinescud, M.C., Ben Moussag, A., Quillévéréf, F., Drinia, H., Azdimousa, A., Touhami, A.O., Merzeraud, G., Fauquette, S., Corsini, M., Moissette, P. & Feddi, N.

(2014). The Early Pliocene reflooding in the Western Mediterranean: New insights from the rias of the Internal Rif, Morocco. *C. R. Geoscience* 346, 90–98.

Crosetto, M., Biescas, E., Duro, J., Closa, J., Arnaud, A. (2008). Generation of Advanced ERS and Envisat Interferometric SAR Products Using the Stable Point Network Technique. *Photogrammetric Engineering & Remote Sensing*, 74 (4), 443–450.

Crozier, M.J., Deimel, M.S., Simon, J.S. (1995). Investigation of earthquake triggering for large deep-seated landslides, Taranaki, New Zealand. *Quaternary International* 25, 65-73, doi: 10.1016/1040-6182(94)00036-5.

Cruden, D.M., Varnes, D.J., (1996). Landslide types and processes. In: Turner, A.K., Schuster, R.L. (Eds.), *Landslides, Investigation and Mitigation*, Special Report 247. Transportation Research Board, Washington D.C., pp. 36–75.

Damnati, B. (2000). Holocene lake record in the Northern Hemisphere of Africa. Journal of African Earth Sciences 31(2), 253–262.

Davis, L.L., West, L.R. (1973). Observed effects of topography on ground motion. *Bulletin of Seismological Society of America* 63, 283–298.

Deffontaines, B., Chotin, P., Ait Brahim, I. & Rozanov, M. (1992). Investigation of active faults in Morocco using morphometric methods and drainage pattern analysis. *Geol. Rund*. 81, 199-210.

Deffontaines, B.L., Angelier, J.-C., Carvalho, J. & Rudant, J. P. (1994). New geomorphic data on the active Taiwan orogen: A multisource approach. *Journal of Geophysical Research* 99, 20243-20266.

Densmore, A.L., Dawers, N.H., Gupta, S. & Guidon, R. (2005). What sets topographic relief in extensional footwalls? *Geology* 33, 453-456.

Dewitte, O., and Demoulin, A., (2005). Morphometry and kinematics of landslides inferred from precise DTMs in West Belgium. *Natural Hazards and Earth System Sciences*, 5(2), 259-265.

Didoon, J. (2004). Carte géologique du Maroc – Souk Larbaa Beni Hessane: 1/50 000, Ministère de l'énergie et des mines, Direction de la Géologie, *Service Géologique du Maroc*, nº 454, Rabat.

Dikau, R. and Schrott, L. (1999). The temporal stability and activity of landslides in Europe with respect to climate change (TESLEC): main objectives and results. *Geomorphology*, 30 (1999), 1–12.

Duggen, S., Hoernle, K., Van den Bogaard, P. & Harris, C. (2004). Magmatic evolution of the Alboran region: the role of subduction in forming the Western Mediterranean and causing the Messinian Salinity Crisis. *Earth and Planetary Science Letters* 218, 91–108.

Durand Delga, M., Hottinger, L., Marcais, J., Mattauer, M., Milliard, Y. & Suter, G., (1962). Données actuelles sur la structure du Rif, Livre à la mémoire du professeur Fallot, Mémoires hors série. *Société Géologique de France*, Tome 1, Paris, 399-442.

Durand-Delga, M., Escalier des Orres, P., Fernex, F., (1962). Sur la presence de Jurassique et d'Oligocéne a l'ouest de Carthagene (Espagne meridionale). *Comptes Rendus de l'Académie des Sciences de Paris* 255, 1753-1755.

Durand-Delga M., Didon J. (1984a). Carte géologique du Rif : Ksar Es Srhir - Echelle 1/50 000, Ministère de l'energie et des mines, Direction de la Géologie, *Service Géologique du Maroc*, nº 295, Rabat.

Durand-Delga M., Didon J. (1984b). Carte géologique du Rif : Melloussa - Echelle 1/50 000, Ministère de l'energie et des mines, Direction de la Géologie, *Service Géologique du Maroc*, nº 296, Rabat.

Durand-Delga, M., Gardin, S., Olivier, Ph. (1999). Datation des Flyschs éocrétacés maurétaniens des Maghrébides: la formation du Jbel Tisirène. *Comptes Rendus de l'Académie des Sciences de Paris*, 328, 701–709.

Dury, G. H. (1951). Quantitative measurement of available relief and depth of dissection. *Geol.Mag.* 88, 339-343.

El Fellah, B., Azzouz, O. & Asebriy, L. (1996). Sikha d'Asfalou; exemple de glissement littoral sur la côte méditerranéenne de Bokoya entre Torrès et Bades (Rif, Maroc). *ORSTOM*, réseau érosion, Bull. 16, 222-230.

El Kadiri Kh., (1992). Description de nouvelles espèces de radiolaires jurassiques de la Dorsale calcaire externe (Rif, Maroc). *Revue Espagnol de Paleontologia*, numero extra, 37–48.

El Khattabi, J., Carlier, E., (2004). Tectonic and hydrodynamic control of landslides in the northern area of the Central Rif, Morocco. *Engineering Geology*, 71, 255–264.

Fadil, A., Vernant, P., McClusky, S., Reilinger, R., Gomez, F., Sari, D.B., Mourabit, T., Feigl, K. & Barazangi, M. (2006). Active tectonics of the western Mediterranean: Geodetic evidence for roll

back of a delaminated subcontinental lithospheric slab beneath the Rif Mountains, Morocco. *Geology* 34 (7), 529-532.

Faleh, Al. and Sadiki, A. (2002). Glissement rotationnel de Dhar El Harrag : exemple d'instabilité de terrain dans le Prérif central (Maroc). *Bulletin de l'Institut scientifique*, Rabat, section Sciences de la Terre, 2002, 24, 41-48.

Faleh, A., Sadiki, A., Akdim, B. and Haloui, B. (2002). Application des analyses minéralogiques et géotechniques des argiles dans l'étude des glissements de terrains: exemples du Prérif Central (Maroc Septentrional). *Papeles de Geografia*, 35, 115-128.

Farina, P.; Colombo, D.; Fumagalli, A.; Marks, F.; Moretti. S. (2006). Permanent Scatterers for landslide investigations: outcomes from the ESA-SLAM project, *Engineering Geology*, 88, 200-217.

Faure-Muret, A. and Morel, J.L. (1992). Carte Néotectonique du Maroc 1: 100.000. Feuille 1: Provinces du Nord. *Notes et mémoire du Service Géologique du Maroc* 368.

Ferretti, A., Prati, C., Rocca, F. (2001). Permanent Scatterers in SAR Interferometry. IEEE *Transactions on Geoscience and Remote Sensing*, VOL. 39, 1.

Fielding, E., Isacks, B., Barazangi, M. & Duncan, C. (1994). How flat is Tibet? *Geology* 22, 163–167.

Garcia, R. A. C. (2012). *Metodologias de Avaliação da Perigosidade e Risco associado a movimentos de vertente. Aplicação na bacia do rio Alenquer*. Dissertação de doutoramento em Geografia na Especialidade em Geografia Física.

Geli, L., Bard, P.Y. & Jullen, B. 1988. The effect of topography on earth- quake ground motion: a review and new results, *Bulletin of the Seismological Society of America*, 78, 42–63.

Gensous, B., Tesson, M. & Winnock, E. (1986). La marge meridionale de la mer d'Alboran: caractères structuro- sédimentaires et évolution récente. *Marine Geology* 72, 341-370.

Getis, A.and Ord, J.K., (1992). The Analysis of Spatial Association by Use of Distance Statistics. *Geographical Analysis* 24, 189-206.

Goudie, A., (1992). Environmental Change, Third edition. Clarendon Press, Oxford, 329 pp.

Grelle, G., Revellino, P., Donnarumma, A., Guadagno, F.M. (2011). Bedding control on landslides: a methodological approach for computer-aided mapping analysis. *Natural Hazards and Earth System Science* 11, 1395–1409.

Guthrie, R.H., Evans, S.G., (2004). Magnitude and frequency of landslides triggered by a storm event, Loughborough Inlet, British Columbia. *Natural Hazards and Earth System Science* 4, 475–483.

Guzzetti, F.; Ardizzone, F.; Cardinali, M.; Rossi, M.; Valigi, D. (2009). Landslide volumes and landslide mobilization rates in Umbria, central Italy. *Earth and Planetary Science Letters*, 279, 222 – 229.

Guzzetti, F.; Mondini, A. C.; Cardinali, M.; Fiorucci, F.; Santangelo, M.; Chang, K. T. (2012). Landslide inventory maps: new tools for and old problem. *Earth-Science Reviews*, 112, 42 - 66. doi: 10.1016/j.earscirev.2012.02.001

Guzzetti, F., Ardizzone, F., Cardinali, M., Galli, M., Reichenbach, P., Rossi, M. (2008). Distribution of landslides in the Upper Tiber River basin, central Italy. *Geomorphology* 96, 105–122.

Guzzetti, F., Cardinali, M., Reichenbach, P. (1996). The influence of structural setting and lithology on landslide type and pattern. *Environmental and Engineering Geoscience* 2, 531–555.

Guzzetti, F., Cardinali, M., Reichenbach, P., Carrara, A., (2000). Comparing landslide maps: a case study in the upper Tiber River Basin, Central Italy. *Environmental Management* 25 (3), 247–363.

Guzzetti, F., Carrara, A., Cardinali, M., Reichenbach, P., (1999). Landslide hazard evaluation: a review of current techniques and their application in a multi-scale study. *Geomorphology* 31, 181–216.

Guzzetti, F., Malamud, B.D., Turcotte, D.L., Reichenbach, P., (2002). Power-law correlations of landslide areas in Central Italy*. Earth and Planetary Science Letters* 195, 169–183.

Guzzetti, F., Reichenbach, P., Cardinali, M., Galli, M., Ardizzone, F., (2005). Probabilistic landslide hazard assessment at the basin scale. *Geomorphology* 72, 272–299.

Hack, J.T. (1957). Studies of longitudinal profiles in Virginia and Maryland. *USGS Professional Papers* 294-B, Washington DC, 46–97.

Hack, T. J. (1973). Stream-profile analysis and stream-gradient index. *Journal of Research of the U.S. Geological Survey* 1(4), 421–429.

Hanssen, R. (2001). *Radar interferometry, data interpretation and error analysis*. Kluwer Academic Publishers.

Herrera, G.; Davalillo, J.C.; Mulas, J.; Cooksley, G.; Monserrat, O.; Pancioli, V. (2009). Mapping and monitoring geomorphological processes in mountainous areas usin PSI data: Central Pyrenees case study. *Natural Hazards and Earth System Sciences*, 9, 1587-1598.

Hijmans, R.J., S.E. Cameron, J.L. Parra, P.G. Jones and A. Jarvis (2005). Very high resolution interpolated climate surfaces for global land areas. *International Journal of Climatology* 25, 1965-1978.

Hirano, M., M. Aniya, (1988). A rational explanation of cross-profile morphology for glacial valleys and of glacial valley development. *Earth Surface and Processes* 13, 707-716.

Hoek, E., Brown, E.T. (1997). Practical estimates of rock mass strength. *International Journal of Rock Mechanics and Mining Sciences & Geomechanics Abstracts* 34, 1165–1186.

Hooper, A., Zebker, H., Segall, P., Kampes, B. (2009). A new method for measuring deformation on volcanoes and other natural terrains using InSAR persistent scatteres. *Geophysical Research Letters*, 31(23), L23611.

Horton, R.E. (1932). Drainage basin characteristics. *EOS Trans*. 13, 350–361.

Hovius N, Stark CP, Hao-Tsu C, Jinn-Chuan L. (2000). Supply and removal of sediment in a landslide-dominated mountain belt: Central Range, Taiwan. *Journal of Geology* 108, 73–89.

Hovius, N., P. Meunier (2012). Earthquake ground motion and the pattern of seismically induced landslides. In: Cleague, J.J. and Stead, D. (ed). *Landslides, Types, Mecanisms and Modelling*, Cambridge University Press, 408p.

Hovius, N., Stark, C.P., Allen, P.A., (1997). Sediment flux from a mountain belt derived by landslide mapping: *Geology* 25, 231–234.

Hughen, K.A., Baillie, M.G.L., Bard, E., Bayliss, A., Beck, J.W., Bertrand, C.J.H., Blackwell, P.G., Buck, C.E., Burr, G.S., Cutler, K.B., Damon, P.E., Edwards, R.L., Fairbanks, R.G., Friedrich, M., Guilderson, T.P., Kromer, B., McCormac, F.G., Manning, S.W., Bronk Ramsey, C., Reimer, P.J., Reimer, R.W., Remmele, S., Southon, J.R., Stuiver, M., Talamo, S., Taylor, F.W., van der Plicht, J., Weyhenmeyer, C.E. (2004). Marine04 Marine radiocarbon age calibration, 26 - 0 ka BP. *Radiocarbon* 46, 1059-1086.

Hungr, O., Leroueil, S., Picarelli, L., (2014). The Varnes classification of landslide types, an update. *Landslides* 11, 167–194.

Hurtrez, J.E., Lucazeau, F., Lavé, J. & Avouac, J.P. (1999). Investigation of the relationship between basin morphology, tectonic uplift, and denudation from the study of an active fold belt in the Siwalik Hills, central Nepal. *Journal of Geophysical Research: Solid Earth* 104(B6), 12779-12796.

Hutchinson, I., James, T. S., Reimer, P. J., Bornhold, B. D., and Clague, J. J. (2004). Marine and limnic radiocarbon reservoir corrections for studies of late- and postglacial environments in Georgia Basin and Puget Lowland, British Columbia, Canada and Washington, USA. *Quaternary Research* 61, 193-203.

Hutchinson, J.N., (1986). A sliding-consolidation model for flow slides. *Canadian Geotechnical Journal* 23, 115-126.

IAEG Commission on Landslides, (1990). Suggested nomenclature for landslides. *Bulletin of the International Association of Engineering Geology* 41, 13-16.

Imaizumi, F., Sidle, R.C. and Kamei, R. (2008). Effects of forest harvesting on the occurrence of landslides and debris flows in steep terrain of central Japan. *Earth Surface Processes and Landforms*, 33, 827–840.

Innes, J. L. (1083). Debris flows. *Progress in Physical Geography* 7, 469–501.

Iribarren, L., Verges, J. & Fernandez, M. (2009). Sediment supply from the Betic-Rif orogeny to basins through Neogene. *Tectonophysics* 475(1), 68-84.

Iverson, R. M. and Major, J. J. (1987). Rainfall, groundwater flow, and seasonal motion at Minor Creek landslide, northwestern California: Physical interpretation of empirical relations. *Geological Society of America Bulletin*, Vol. 99, pp. 579–594.

Jabour, N., Kasmi, M., Menzhi, M., Birouk, A., Hni, L., Hahou, Y., Timoulali, Y., Badrane, S., (2004). The February 24th, 2004 Al Hoceima earthquake. *European-Mediterranean Seismological Centre Newsletter*, 21, 7–10.

Jaboyedoff, M. (ed.) (2011). *Slope Tectonics*. Geological Society, London, Special Publications, 351.

Jalut, G., Dedoubat, J. J., Fontugne, M. & Otto, T. (2009). Holocene circum-Mediterranean vegetation changes: Climate forcing and human impact. *Quaternary International*, 200, 4-18. doi:10.1016/j.quaint.2008.03.012.

Jalut, G., Esteban-Amat, A., Bonnet, L., Gauquelin, T., Fontugne, M., (2000). Holocene climatic changes in the Western Mediterranean, from south-east France to south-east Spain. *Palaeogeography, Palaeoclimatology, Palaeoecology* 160, 255–290.

James, L. A., (1996). Polynomial and power functions for glacial valley cross-section morphology. *Earth Surface Processes and Landforms* 21(5), 413-432.

Jarvis, R.S. (1976). Stream orientation structures in drainage networks. *Journal of Geology* 84, 563-582.

Jordan, G. (2003). Morphometric analysis and tectonic interpretation of digital terrain data: A case study. *Earth Surface Processes and Landforms* 28, 807-822.

Kadiri, Kh., Linares, A. & Oloriz, F. (1992). La Dorsale calcaire rifaine (Maroc septentrional): évolution stratigraphique et géodynamique durant le Jurassique-Crétacé. *Notes Mémoire Service Géologique du Maroc* 336, 217–265.

Keefer, D.K., (1984). Landslides caused by earthquake. *Bulletin of the Geological Society of America* 95 (4), 406-421.

Keller, E.A. and Pinter, N. (1996) *Active Tectonics*. Prentice Hall, Upper Saddle River, NJ.

Khattacha, D., Houaria, M.R., Corcheteb, V., Chourakb, M., El Gouta, R., Ghazalad, H., (2013). Main crustal discontinuities of Morocco derived from gravity data. *Journal of Geodynamics* 68, 37–48.

Kirby, E. & Whipple, K. X. (2001). Quantifying differential rock-uplift rates via stream profile analysis. *Geology* 29(5), 415–418.

Koons, P.O., (1989). The topographic evolution of collisional mountain belts: a numerical look at the Southern Alps, New Zealand. *American Journal of Science* 289, 1041–1069.

Kornprobst J. (1980). Carte géologique du Rif : Bou Ahmed - Echelle 1/50 000, Ministère de l'energie et des mines, Direction de la Géologie*, Service Géologique du Maroc*, nº 289, Rabat.

Kornprobst J., Wildi W., Nold M., Gutnie M., Lespinasse P. (1980). Carte géologique du Rif : Bab Taza - Echelle 1/50 000, Ministère de l'energie et des mines, Direction de la Géologie, S*ervice Géologique du Maroc*, nº 288, Rabat.

Korup, O. & Densmore, A.L. and Schlunegger, F. (2010). The role of landslides in mountain range evolution. *Geomorphology*, 120, 70 – 90.

Korup, O., (2005a). Geomorphic imprint of landslides on alpine river systems, southwest New Zealand. *Earth Surface Processes and Landforms* 30, 783–800.

Korup, O., (2005b). Distribution of landslides in southwest New Zealand. *Landslides* 2, 43–51.

Kuhni, A. and Pfiffner, O.A. (2001). The relief of the Swiss Alps and adjacent areas and its relation to lithology and structure: topographic analysis from a 250-m DEM. *Geomorphology* 41, 285-307.

Lamb, H.F., Eicher, U., Switsur, V.R., (1989). An 18,000-year record of vegetation, lake-level and climatic change from Tigalmamine, Middle Atlas, Marocco. *Journal of Biogeography* 16: 65-74.

Lamb, H.F., van der Kaars, S., (1995). Vegetational response to Holocene climatic change: pollen and palaeolimnological data from the Middle Atlas, Morocco. *The Holocene* 5, 400– 408.

Lang, A., Moya, J., Corominas, J., Schrott, L., Dikau, R. (1999). Classic and new dating methods for assessing the temporal occurrence of mass movements. *Geomorphology* 30, 33-52.

Larsen, I.J., Montgomery, D.R., Korup, O., (2010). Landslide erosion controlled by hillslope material. *Nature Geoscience* 3, 247–251.

Lavé, J., and Avouac, J.P. (2001). Fluvial incision and tectonic uplift across the Himalayas of Central Nepal. *Journal of Geophysical Research* 106, 26, 561-26,592, 2001.

Leblanc D., Feinberg H. Coll., Lorenz H.G (1986). Carte géologique du Rif: Aknoul - Echelle 1/50 000, Ministère de l'energie et des mines, Direction de la Géologie, *Service Géologique du Maroc*, nº 345, Rabat.

Leblanc D., Feinberg H. Coll., Lorenz H.G. Coll (1983). Carte géologique du Rif : Taïneste - Echelle 1/50 000, Ministère de l'energie et des mines, Direction de la Géologie, *Service Géologique du Maroc*, nº 224, Rabat.

Lespinasse P., (1975). *Géologie des zones externes et des flyschs entre Chaouen et Zoumi (Centre de la Chaıne rifaine, Maroc)*. Thèse Doctorat, Université de Paris & Marie Curie, Paris, 1975, 247p.

Lespinasse, P., Magne J. Coll., Suter G. (col.) (1978). Carte géologique du Rif : Beni Ahmed – Echelle : 1/50 000, Ministère de l'energie et des mines, Direction de la Géologie, *Service Géologique du Maroc*, nº 257, Rabat.

Lespinasse, P., Magne J. Coll., Suter G. (col.) (1978). Carte géologique du Rif : Beni Ahmed – Echelle : 1/50 000, Ministère de l'energie et des mines, Direction de la Géologie, *Service Géologique du Maroc*, nº 257, Rabat.

Lespinasse, P., Magne, J., Suter, G., (1978). Carte Geologique du Rif: Beni Ahmed – Scale 1:50 000. *Service Géologique du Maroc*, Royaume du Maroc.

Liu, C., Evett, J., 1997. *Soil and Foundation*, 6th ed. Prentice Hall, USA.

Loget, N., Driessche, J.V.D (2006). On the origin of the Strait of Gibraltar. *Sedimentary Geology* 188–189, 341–356.

Lonergan, L. and White, N., (1997). Origin of the Betic-Rif mountain belt. *Tectonics,* 16: 504-522.

Lu P, Casagli N, Catani F, Tofani V (2012). Persistent Scatterers Interferometry Hotspot and Cluster Analysis (PSI-HCA) for detection of extremely slow-moving landslides. *International Journal of Remote Sensing* 33(2),466–489.

Malamud, B.D., Turcotte, D.L., Guzzetti, F., Reichenbach, P. (2004a). Landslide inventories and their statistical properties. *Earth Surface Processes Landforms*, 29, 687–711.

Malamud, B.D., Turcotte, D.L., Guzzetti, F. and Reichenbach, P. (2004b). Landslides, earthquakes and erosion. *Earth and Planetary Science Letters*, 229, 45-59.

Mansour, M. & Ait Brahim, L., (2005). Apport de la télédétection radar et du mnt à l'analyse de la fracturation et la dynamique des versants dans la région de bab-taza, rif, Maroc. *Télédétection,* Vol. 5, n°1-2-3, 95-103.

Margaa, K. (1994). *Essai de cartographie des risques naturels : Application à l'aménagement de la région d'Al Hoceima (Rif, Nord- Maroc).* Thèse de doctorat, Université de Franche-Comté, Besançon. 196p.

Mariotti, M. & Milliès-Lacroix, A., (1963). Etude des zones de terrains instables. Route principale nº39, entre Bab Taza et Bab Berred, *S.E.G.M*., Géo. R. P. nº3, 65p.

Mastere, M., Ait Brahim, L., Elfahchouch, N., Guelzim, E., Mansour, M., Abdelouafi, A. (2009). Synergie de la photogrammétrie numérique et du MNT à l'étude Spatiotemporelle des mouvements de terrain : Application à la coulée de pierres d'Amtrass, Maroc Nord Occidental. *Journées d'Animation Scientifique*, AUF.

Mauffret, A., Ammar, A., Gorini, C. and Jabour, H. (2007). The Alboran Sea (Western Mediterranean) revisited with a view from the Moroccan Margin. *Terra Nova*, 19, 195-203.

Maurer, G., (1962). L'evolution des versants dans le Rif occidental: deux exemples de cartographie géomorphologique. *R. Géogr. Maroc*, nº1-2, 63-66.

Maurer, G., (1968). Les montagens du Rif central – étude géomorphologique. Travaux Institute Scientifique, *Série géologie et geographie physique* Nº14, Rabat, 499p.

Meghraoui, M., Pondrelli, S. (2012). Active faulting and transpression tectonics along the plate boundary in North Africa. *Annals of Geophysics*, 55, 5.

Meghraoui, M., Morel, J.L., Andrieux, J., Dahmani, M. (1996). Tectonique plio-quaternaire de la chaine tello-rifaine et de la mer d'Alboran. Une zone complex de convergence continent-continent. *Bulletin Société Géologique de France*, 167 (1), 141-157.

Meisina, C.; Zucca, F.; Notti, D.; Colombo, A.; Cucchi, A.; Savio, G.; Giannico, C.; Bianchi, M. (2008). Geological interpretation of PSInSAR data at regional scale. *Sensors* 8, 7469‐7492. DOI: 10.3390/s8117469.

Merritts, D.J., Vincent, K.R., (1989). Geomorphic response of coastal streams to low, intermediate, and high rates of uplift, Mendocino triple junction region, northern California. *Geological Society of America Bulletin* 101, 1373–1388.

Meunier, P., Hovius, N. & Haines, J.A. (2008). Regional patterns of earthquake-triggered landslides and their relation to ground motion, *Geophysical Research Letters*, Vol. 34, L20408, doi: 10.1029/2007GL031337.

Meunier, P., Hovius, N. & Haines, J.A. (2008). Topographic site effects and the location of earthquake induced landslides. *Earth and Planetary Science Letters*, 275, 221–232.

Michard A. Negro F., Saddiqi O., Bouybaouene M.L., Chalouan A., Montigny R., Goffé B. (2006). Pressure- temperature-time constraints on the Maghrebide mountain building: evidence from the Rif-Betic transect (Morocco, Spain), Algerian correlations, and geodynamic implications, *C. R. Geosci*. 338, 92–114.

Milliès-Lacroix, A. (1965). L'instabilité des versant dans le domaine rifain. *R. Géom. Dyn*., nº 7, 8, 9, 97-109.

Milliès-Lacroix, A. (1968). Les glissements de terrain. Présentation d'une carte prévisionnelle des mouvements de masse dans le Rif (Maroc septentrional). *Mines et Géologie* (27), 43-53.

Molnar, P., Anderson, R.S., Anderson, S.P. (2007). Tectonics, fracturing of rock, and erosion. *Journal of Geophysical Research*, Vol. 112, F03014, doi:10.1029/2005JF000433.

Montgomery, D. R. (2001). Slope distributions, threshold hillslopes, and steady-state topography, *American Journal of Sciences* 301, 432 – 454.

Montgomery, D. R., and M. T. Brandon (2002). Topographic controls on erosion rates in tectonically active mountain ranges. *Earth & Planetary Science Letters* 201 (3 – 4), 481 – 489.

Morel, J.L. (1987). *Evolution récente de l'orogène rifain et de son avant pays depuis la fin de la mise en place des nappes (Rif, Maroc)*. Thèse d'Etat, Univ. Orsay, 584 p.

Morel, J.L, Julien, M., Chanteux, P., Roche, G. (1992). Carte des movement récents du Rif. *Notes et mémoire du Service Géologique du Maroc*, 365.

Morel, J.L. (1989). Etats de contrainte et cinématique de la chaîne rifaine (Maroc) du Tortonien à l'actuel. *Geodynamica Acta*, 3: 283-294.

Morel, J.L. & Meghraoui, M. (1996). Goringe-Alboran-Tell tectonic zone: A transpression system along the Africa-Eurasia plate boundary. *Geology* 24, no. 8, p. 755–758.

Morley, C. (1993). Discussion of origins of hinterland basins to the Rif-Betic Cordillera and Carpathians. *Tectonophysics* 226, 359-376.

Negro, F., De Sigoyer, J., Goffé, B., Saddiqi, O., Villa, I.M., (2008). Tectonic evolution of the Betic–Rif arc: New constraints from 40Ar/39Ar dating on white micas in the Temsamane units (External Rif, northern Morocco), *Lithos*, vol. 106, 93-109.

Nico, G.; Oliveira, S.; Catalão, J.; Zêzere, J.L. (2009a) – Statistical assessment of Persistent Scatteres location in diferente landslide prone geological units. *Geophysical Research Abstracts.* Vol. 11. EGU2009- 8011. EGU General Assembly 2009.

Nold M., Uttinger J., Wildi W., (1981). Géologie de la Dorsale calcaire entre Tétouan et Assifane (Rif interne, Maroc), *Notes Mémoire Service Géologique du Maroc* 300, 1–233.

Oliveira, S.O., Zêzere, J.L., Catalão, J., Nico, G. (2014). The contribution of PSInSAR interferometry to landslide hazard in weak rock-dominated areas. *Landslides*, DOI 10.1007/s10346-014-0522-9.

Olivier Ph., (1981– 1982). L'accident de Jebha-Chrafate (Rif, Maroc), *Revue Géologie Dynamique et Géographie Physique*, 22, 201–212.

Ord, J.K. and Getis, A., (1995). Local Spatial Autocorrelation Statistics: Distributional Issues and an Application, *Geographical Analysis*, 27, 286-306.

Panizza, M., Pasuto, A., Silvano, S., Soldati, M., (1996). Temporal occurrence and activity of landslides in the area of Cortina d'Ampezzo (Dolomites Italy). *Geomorphology* 15, 311– 326.

Parker, R.S and Schumn, S.A. (1982). Experimental study of drainage networks. In Bryan, R and Yair, A., eds., Badland geomorphology and piping. *Geo Abstracts* Ltd., Norwich, p. 153-168.

Pelletier, J. D., Engelder, T., Comeau, D., Hudson, A., Leclerc, M., Youberg, A., And Diniega, S., (2009). Tectonic And Structural Control Of Fluvial Channel Morphology In Metamorphic Core Complexes: The Example Of The Catalina-Rincon Core Complex, Arizona. *Geosphere*, 5, 363-384.

Pelletier, J.D., Malamud, B.D., Blodgett, T., Turcotte, D.L. (1997). Scale-invariance of soil moisture variability and its implications for the frequency–size distribution of landslides. *Engineering Geology*, 48, 255–268.

Pike, R. J., and Wilson, S. E. (1971). Elevation relief ratio, hypsometric integral, and geomorphic area-altitude analysis. *Geological Society of America Bulletin*, 82, 1079-1084.

Platt, J.P. & Vissers, R.L.M. (1989). Extensional collapse of thickened continental lithosphere: A working hypothesis for the Alboran Sea and Gibraltar Arc. *Geology*, 17, 540-543.

Qi, S. W., Xu, Q., Lan, H. X., Zhang, B., and Liu, J. Y. (2010). Spatial dis- tribution analysis of landslides triggered by 2008.5.12 Wenchuan Earthquake, China, *Engeneering Geology*, 116, 95–108.

Rampnoux, J.P., Angelier, J., Colleta, B., Fudral, S., Guillemin, M., Pierre, G., (1979). Sur l'évolution néotectonique du Maroc septentrional*. Géologie Méditerranéenne* 6, 439–464.

Rasemann, S., Schmidt, J., Schrott, L., Dikau, R. (2004). Geomorphometry in mountain terrain. In: M.P. Bishop and J.F. Shroder (Eds.), GIS & Mountain Geomorphology, *Springer*, Berlin, 101–145.

Reille, M., (1977). Contribution pollenanalytique à l'histoire holocène de la végétation des montagnes du Rif (Maroc septentrional). Recherches Françaises sur le Quaternaire, INQUA 1977, *Association Française pour l'Etude du Quaternaire* 1(50), 53–76.

Righini, G.; Pancioli, V.; Casagli, N. (2012). Updating landslide inventory maps using Persistent Scatterer Interferometry (PSI). *International Journal of Remote Sensing*. 33(7), 2068-2096.

Rigon, R., Rodriguez-Iturbe, I., Maritan, A., Giacometti, A., Tarboton, D.G. and Rinaldo A. (1996). On Hack's law. *Water Resources Research*, 32 (11), 3367–3374.

Ritter, J.B. & Gardner, T.W., (1993). Hydrologic evolution of drainage basins disturbed by surface mining, central Pennsylvania. *Geological Society of America Bulletin*, v. 105, 101-115.

Rockwell, T.K., E.A. Keller, and G.R. Dembroff (1988). Quaternary rate of folding of the Ventura Avenue anticline, western Transverse Ranges, southern California. *Geological Society of America Bulletin*, 100, 850-858.

Roe, G. H., D. R. Montgomery, and B. Hallet (2002). Effects of orographic precipitation variations on the concavity of steady-state river profiles, *Geology*, 30(2), 143–146.

Roe, G. H., D. R. Montgomery, and B. Hallet (2003). Orographic precipitation and the relief of mountain ranges, *Journal of Geophysical Research* 108 (B6), 2315, doi:10.1029/2001JB001521.

Roering, J.J., Kirchner, J.W., Dietrich, W.E. (2005). Characterizing structural and lithologic controls on deep-seated landsliding: Implications for topographic relief and landscape evolution in the Oregon Coast Range, USA, *Geological Society of America Bulletin*, 117, 654-668.

Rogers, N.W., Selby, M.J., (1980). Mechanisms of shallow translational landsliding during summer rainstorms: North Island, New Zealand. *Geografiska Annaler* 62, 11-21.

Romagnya, A., Münch, P.H., Cornée, J.J., Corsini, M., Azdimousa, A., Melinte-Dobrinescu, M.C., Drinia, H., Bonno, M., Arnaud, N., Monié, P., Quillévéré, F. and Ben Moussa, A. (2014). Late Miocene to present-day exhumation and uplift of the Internal Zone of the Rif chain: Insights from low temperature thermochronometry and basin analysis. *Journal of Geodynamics* 77 (2014), 39–55.

Rouai, M., Jaaidi, E.B., (2003). Scaling properties of landslides in the Rif mountains of Morocco. *Engineering Geology* 68, 353–359.

Sanz de Galdeano C., El Kadiri K., Simancas J.F., Hlila R., López-Garrido A.C., El Mrihi A., Chalouan A., (2006). Palaeogeographical reconstruction of the Malaguide-Ghomaride Complex (Internal Betic-Rifian Zone) based on Carboniferous granitoid pebble provenance. *Geologica Carpathica* 57, 327–336.

Sanz de Galdeano, C., Vera, J. A. (1992). Stratigraphic record and paleogeographical contex of the Neogene basins in the Betic Cordillera, Spain. *Basin Research*, 4, 21-26.

Sato, P.H., Hasegawa, H., Fujiwara, S., Tobita, M., Koarai, M., Une, H., Iwahashi, J., (2007). Interpretation of landslide distribution triggered by the 2005 northern Pakistan earthquake using SPOT 5 imagery. *Landslides* 4, 113–122.

Schmidt, J. & R. Dikau (2004). Modeling historical climate variability and slope stability. *Geomorphology*, 60, 433-447.

Schulz, W. H.; Mckenna, J. P.; Kibler, J. D.; and Biavati, G. (2009). Relations between hydrology and velocity of a contin- uously moving landslide—evidence of pore-pressure feedback regulating landslide motion?: *Landslides*, 6, 181–190.

Schumm, S. (1956). Evolution of drainage systems and slopes in badland at Perth Amboy, New Jersey. *Bulletin of Geological Society of America*, 67, 597-646.

Schumm, S.A. (1965). Quaternary paleohydrology. The Quaternary of the United States. vol. for VII *Congress INQUA*. 793-949.

Schumm, S.A., Boyd, K.F., Wolff, C.G., Spitz, W.J. (1995). A ground-water sapping landscape in the Florida Panhandle. *Geomorphology* 12, 281-297.

Selby, M.J. (1992). *Hillslope Materials and Processes*. University Press, Oxford.

Serpelloni, E., Vannucci, G., Pondrelli, S., Argnani, A., Casula, G., Anzidei, M., Baldi, P. and Gasperini, P. (2007). Kinematics of the Western Africa-Eurasia plates boundary from focal mechanisms and GPS data. *Geophysical Journal International*, 169, 1180-1200.

Shroder, J.F. (1998). Slope failure and denudation in the western Himalaya. *Geomorphology*, 26, pp. 81–106.

Sklar, L.S., Dietrich, W.E. (2001). Sediment and rock strength controls on river incision into bedrock. *Geology*, v.29, no.12.

Soeters, R., van Westen, C.J. (1996). Slope instability recognition, analysis and zonation. In: Turner, A.K., Schuster, R.L. (Eds.), *Landslide Investigation and Mitigation*. National Research Council, Transportation Research Board Special Report, vol. 247, 129–177.

Soldati, M., Borgatti, L. (2009). Paleoclimatic significance of Holocene slope instability in the Dolomites (Italy). *Geografia Fisica e Dinamica Quaternaria* 32, 83-88.

Soldati, M., Corsini, A., Pasuto, A. (2004). Landslides and climate change in the Italian Dolomites since the Lateglacial. *Catena* 55(2), 141–161.

Spudich, P., Hellweg, M., and Lee, W. H. K. (1996). Directional topographic site response at Tarzana observed in aftershocks of the 1994 Northridge, California, earthquake: Implications for mainshock motions, *Bulletin of the Seismological Society of America* 86 (11), S193–S208.

Stark C.P. & Hovius N. (2001). The characterization of landslide size distributions. *Geophysical Research Letters* 28, 1091–1094.

Stark, C. & Guzzetti, F. (2009). Landslide rupture and the probability distribution of mobilized debris volumes. *Journal of Geophysical Research* 114, F00A02.

Stolar, D. B., S. D. Willett, and G. H. Roe (2006). Climatic and tectonic forcing of a critical orogen, in Tectonics, Climate, and Landscape Evolution. Penrose Conferece Services, *Special Papers Geological Society of America*, 398, 241 – 250.

Stolar, D.B., Willett, S.D., Montgomery, D.R. (2007). Characterization of topographic steady state in Taiwan. *Earth and Planetary Science Letters* 261 (2007), 421–431.

Strahler, A.N. (1952). Hypsometric (area-altitude) analysis of erosional topography. Bulletin of the *Geological Society of America*, 63, 1117-1142.

Stuiver, M., and Reimer, P. J. (1986). A computer program for radiocarbon age calibration, *Radiocarbon* 28, 1022-1030.

Sugden, D.E., John, B.S. (1976). *Glaciers and Landscape: A Geomorphologic Approach*. Arnold, London, 376 pp.

Summerfield, M.A. and Hulton, N.J. (1994). Natural controls of fluvial denudation rates in major world drainage basins. *Journal of Geophysical Research*, 99 (B7), 13871-13883.

Suter G. (1966a). Carte géologique du Rif : région du Moyen Ouerrha : Rhafsaï – Kelaa des Slès – Echelle : 1/50 000, Ministère de l'energie et des mines, Direction de la Géologie, *Service Géologique du Maroc*, nº 164, Rabat.

Suter G. (1966b). Carte géologique du Rif : région du Moyen Ouerrha : Tafrannt de l'Ouerrha - Moulay- Bou-Chta – Echelle : 1/50 000, Ministère de l'energie et des mines, Direction de la Géologie, *Service Géologique du Maroc*, nº 165, Rabat.

Suter G., (1980a). Carte geologique du Rif, 1/500.000, Notes et Mémoire, *Service Géologiques du Maroc*, 245a.

Suter G., (1980b). Carte structurale du Rif, 1/500.000, Notes et Mémoire, *Service Géologiques du Maroc*, 245b.

Suter G., Mattauer, M. (1967). Carte géologique du Rif : région du Moyen Ouerrha : Taounate – Aïn Aïcha – Echelle : 1/50 000, Ministère de l'energie et des mines, Direction de la Géologie, Service Géologique du Maroc, nº 166, Rabat.

Suter, G. (1990). Carte géologique du Rif : Terwal - Oulad Aïssa – Echelle : 1/50 000, Ministère de l'energie et des mines, Direction de la Géologie, *Service Géologique du Maroc*, nº 224, Rabat.

Svensson, H. (1959). Is the cross-section of a glacial valley a parabola? *Journal of Glaciology* 3, 362-363.

Tahayt, A. (2008). *Apport des mesures de la géodésie spatiale dans l"étude des déformations tectoniques actuelles dans la Méditerrané occidentale*. Doctorat en Sciences (Maroc) Doctorat de L'université de Toulouse (France), Géophysique et Sismotectonique, Université Toulouse III, Toulouse.

Thomas, M.F. (1999). Evidence for high-energy landforming events of the central African plateau: eastern province, Zambia. *Zeitschrift für Geomorphologie* N.F. 43(3), 273–297.

Van Laningham, S., A. Meigs, and C. Goldfinger (2006). The effects of rock uplift and rock resistance on river morphology in a subduction zone forearc, Oregon, USA. *Earth Surface Processes and Landforms*, 31(10), 1257–1279, doi:10.1002/esp.1326.

Varnes, D.J., (1978). Slope movement types and processes. In: Schuster, R.L. and Krizek, R.J. (Eds.) *Landslides: Analysis and Control*, pp. 11–33 (Washington, DC: Transportation Research Board).

Varnes, D.J., IAEG Commission on Landslides and other Mass- Movements (1984). Landslide Hazard Zonation: A Review of Principles and Practice. *The UNESCO Press*, Paris. 63 pp.

Varnes, D.J., Radbruch-Hall, D., Savage, W.Z. (1989). Topographic and structural conditions in areas of gravitational spreading of ridges in the western United States. *US Geological Survey*, Professional, vol. 1496.

Vidal J.C., Wernli, R. & Busnardo, R. (1983). Carte géologique du Rif : Dhar Souk - Echelle 1/50 000, Ministère de l'energie et des mines, Direction de la Géologie, *Service Géologique du Maroc*, nº 298, Rabat.

Vogt, J., (1984). Mouvements de terrain associés aux séismes en Afrique du Nord. In: Méditerranée, Troisièmesérie, Tome 51. *Actes du colloque - Effets des séismessur les reliefs de forte énergie*, 43-48.

Wheeler, D.A., (1984). Using parabolas to describe the cross-sections of glaciated valleys. *Earth Surface Processes and Landforms*, 9(4), 391-394.

Whipple, K. X., and G. E. Tucker (1999). Dynamics of the stream power river incision model: Implications for height limits of mountain ranges, landscape response time scales, and research needs. *Journal of Geophysical Research*, 104, 17,661–674.

Whipple, K. X., E. Kirby, and S. H. Brocklehurst (1999). Geomorphic limits to climate-induced increases in topographic relief. *Nature*, 401, 39–43.

Wildi W., Nold M., Uttinger J., (1977). La Dorsale Calcaire entre Tetouan et Assifane (Rif interne, Maroc). *Eclogae Geol. Helv.* 70 (1977), 371–415.

Wildi, W., Wernli, R., (1977). Stratigraphie et micropaléontologie des sédiments pliocènes de l'Wadi Laou (côte méditerranéenne marocaine). *Archives des Sciences Genève* 30, 213–228.

Willett, S.D., (1999). Orogeny and orography: the effects of erosion on the structure of mountain belts. *Journal of Geophysical Research* 104, 28957–28981.

Willett, S.D.& Schlunegger, F.& Picotti, V. (2006). Messinian climate change and erosional destruction of the central European Alps. *Geology*, vol. 34, 613-616

Woodside, J.M. and Maldonado, A. (1992). Styles of compressional neotectonics in the eastern Alboran Sea. *Geo- Marine Letters*, 12, 111-116.

Zaghloul M.N. (2002). *La sédimentation silico-clastique Oligo-Miocéne de type "flysch" dans le Rif, Maroc: évolution et corrélations à l'échelle de la chaine maghrébine*. Thèse Doctorat, Université de Tétouan, 329p.

Zaprowski, B. J., F. J. Pazzaglia, and E. B. Evenson (2005). Climatic influences on profile concavity and river incision. *Journal of Geophysical Research* 110, F03004, doi:10.1029/2004JF000138.

Zeck, H.P. (1996). Betic-Rif orogeny: subduction of Mesozoic Tethys lithosphere under eastward drifting Iberia, slab detach- ment shortly before 22 Ma, and subsequent uplift and extensional tectonics. *Tectonophysics*, 254, 1-16.

Zêzere, J.L., Faleh, A., Sadiki, A., Garcia, R.A.C., Oliveira, S.C. (2009). Modelação da susceptibilidade a deslizamentos na bacia do Oued Sra (Rif central, Marrocos) com métodos estatísticos bi-variados. *Publicações da Associação Portuguesa de Geomorfólogos*, Volume VI, APGEOM, Braga, p.203-210.

Zovoili, E., Konstantinidi, E., Koukouvelas, I.K. (2004). Tectonic geomorphology of escarpments: the cases of Kompotades and Nea Anchialos faults. *Bulletin of the Geological Society of Greece* 36, 1716–1725.

Annexes

Landslide inventory of the Northern Rif Mountains

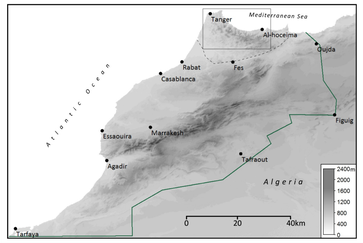
A regional overview of large gravitational processes

Fonseca, A.F. (1) , Zêzere, J.L. (1), Madeira, J. (2), Bouchta, E.F. (3)

1 – RISKam–CEG/IGOT, Universidade de Lisboa, Portugal, E–mail: a.fonseca@campus.ul.pt. zezere@campus.ul.pt
2 – LATTEX–IDL (LA), Departamento de Geologia, Faculdade de Ciências, Universidade de Lisboa, Portugal, E–mail: jmadeira@fc.ul.pt
3 – Laboratoire de Géomorphologie et de Cartographie, Institut Scientifique, Université Mohamed V –Agdal, Rabat, Morocco, E–mail: elfellah@israbat.ac.ma

U.T.M Coordinate System
Zone 30N
Internacional Elipsoid – European Datum

0 20 40 60 80 km



Landslide typology

Landslide > 0.05km2

Landslide < 0.05km2

Slide
- Active
- Relict

Flow
- Active
- Relict

Complex
- Active
- Relict

Hillslope affected by DSGSD

Undefined tipology

Probable landslide

Map symbols

City/Village

Motorway

Road

Railway

Elevation

2500m
2000
1500
1000
500
0

© Journal of Maps, 2014

Alboran Sea

Ceuta
Tanger-Medina
Tetouan
Oued Laou
Chefchaouen
Bab Taza
Ksar-el-Kebir
Souk El Arba Du Gharb
Zoumi
Bni Ahmed
Bab Berred
Ketama
Taghzout
Targha
Taounate
Tainaste
Thar Es-Souk
Aknoul
Nekkour
Torres el Kal'a
Boudinar
Al Hoceima
Ertebha

-660000 -640000 -620000 -600000 -580000 -560000 -540000 -520000 -500000 -480000 -460000 -440000 -420000 -400000

4280000 4260000 4240000 4220000 4200000 4180000 4160000 4140000 4120000 4100000

GEOMORPHOLOGICAL MAP OF THE BENI DERKOUL LANDSLIDE (NORTHERN RIF, MOROCCO)

Fonseca, A.F.[1]; Zêzere, J.L.[1]; Madeira, J.[2]; Bouchta, E.F.[3]

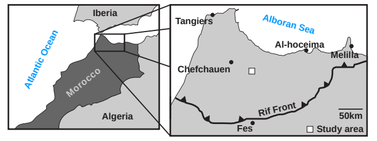
1 - Fonseca, A.F., Zêzere, J.L. - Centro de Estudos Geográficos e Instituto de Geografia e Ordenamento do Território da Universidade de Lisboa, Portugal, a.fonseca@campus.ul.pt; zezere@campus.ul.pt

2 - Madeira, J. - Faculdade de Ciências da Universidade de Lisboa, Departamento de Geologia e Instituto Dom Luiz, Portugal, jmadeira@fc.ul.pt.

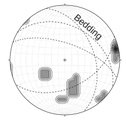
3 - Bouchta, El Fellah, Laboratoire de Géomorphologie et de Cartographie, Institut Scientifique, Université MohamedV-Agdal, Rabat, Morocco, elfellah@israbat.ac.ma

0 1 2km

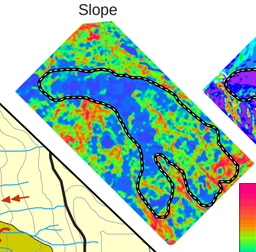
Clarke Elipsoid 1880 - Merchich Geodetic system
Lambert conformal conical projection - Northern Morocco
20 meter contour line interval



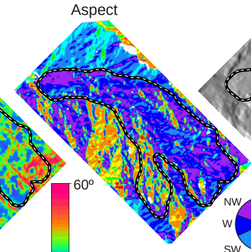
Poles to faults
(Landslide detachment area)



Slope

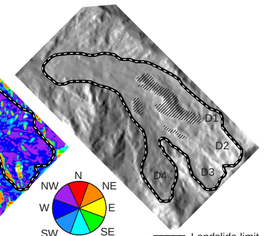


Aspect



60º
0º

Hillshade



Landslide limit
Bedrock

The digital elevation model and terrain first order derivative (aspect, slope and hillshade) were obtained from the interpolation of contour and point data extracted from the 1:25,000 topographic maps of the Rif (Agence Nationale de la Conservation Foncière, du Cadastre et de la Cartographie, ANCFCC)

© Journal of Maps

Bedrock lithology

- Beni Ider nappe - Flysch, sandstone and clay (Oligocene)
- Beni Ider nappe - Red coloured marls (Eocene)
- Ametrasse Unit - Marls (Eocene)
- Internal Tanger - Marls, black-shale and microbreccia (Turonian)
- Internal Tanger - Marls and pelites with sandstone intercalations (Senonian)
- Tiziren Unit - Sandstone and fine pelitic levels (Barremian-Albian)
- Dorsal Calcaire - Compact limestone (upper Jurassic)

Tectonic elements

- Thrust fault
- Normal fault
- Strike-slip fault
- Anticline
- Sincline
- Bedrock attitude

Structural landforms

- Edge of structural scarp

Gravity-induced slope landforms and deposits

- Landslide scarp
- Beni Derkoul active landslide
- Beni Derkoul landslide unit 1
- Beni Derkoul landslide unit 2
- Secondary landslide body
- Detachment area
- Area afected by deep--seated slope deformation
- Rotacional slide
- Translational slide
- Flow
- Complex slide
- Small landslide
- Reverse slope
- Gravitational thrust Certain/Probable
- Gravitational folding
- Trench
- Frontal lobe
- Pressure ridge
- Rockslide
- Scree slope
- Coluvial deposit

Fluvial landforms and deposits

- Gully
- Paleo stream trace
- Active flood area
- Terrace (late Pleistocene)
- Terrace (Pleistocene?)

Hidrography

- Perennial/Seasonal stream
- Source
- Lake

Anthropogenic landforms

- Village
- House
- Paved road
- Unpaved road

Beni Derkoul
M'idk
Maarnala river
Azaib
Azaib plateaux
1472
Koudiet es Sbaa
1768
Jebel Beni Salah
1504
1323
1102
700
600
800
900
1000
1100
1200
1300
1400
1500
1600
1700

530000 531000 532000 533000 534000 535000 536000

4496000 4495000 4494000 4493000 4492000 4491000

Submited paper: Fonseca, A.F., Zêzere, J.L., Madeira, J., El Felah, B. (submited). Geomorphological map of the Beni Derkoul landslide. Journal of maps, Taylor and Francis.